UC San Diego

UC San Diego Electronic Theses and Dissertations

Title

Experimental simulations of explosive loading on structural components : reinforced concrete columns with advanced composite jackets

Permalink

https://escholarship.org/uc/item/9k51d32c

Author

Rodríguez-Nikl, Tonatiuh

Publication Date

2006

Peer reviewed|Thesis/dissertation

eScholarship.org Powered by the California Digital Library
University of California

UNIVERSITY OF CALIFORNIA, SAN DIEGO

Experimental Simulations of Explosive Loading on Structural Components: Reinforced Concrete Columns with Advanced Composite Jackets

A dissertation submitted in partial satisfaction of the
requirements for the degree Doctor of Philosophy

in

Structural Engineering

by

Tonatiuh Rodríguez-Nikl

Committee in charge:

Professor Gilbert A. Hegemier, Chair
Professor David J. Benson
Professor Vistasp M. Karbhari
Professor Vitali Nesterenko
Professor José Restrepo
Professor Frieder Seible

2006

Copyright
Tonatiuh Rodríguez-Nikl, 2006
All rights reserved.

The dissertation of Tonatiuh Rodríguez-Nikl is approved, and it is acceptable in quality and form for publication on microfilm:

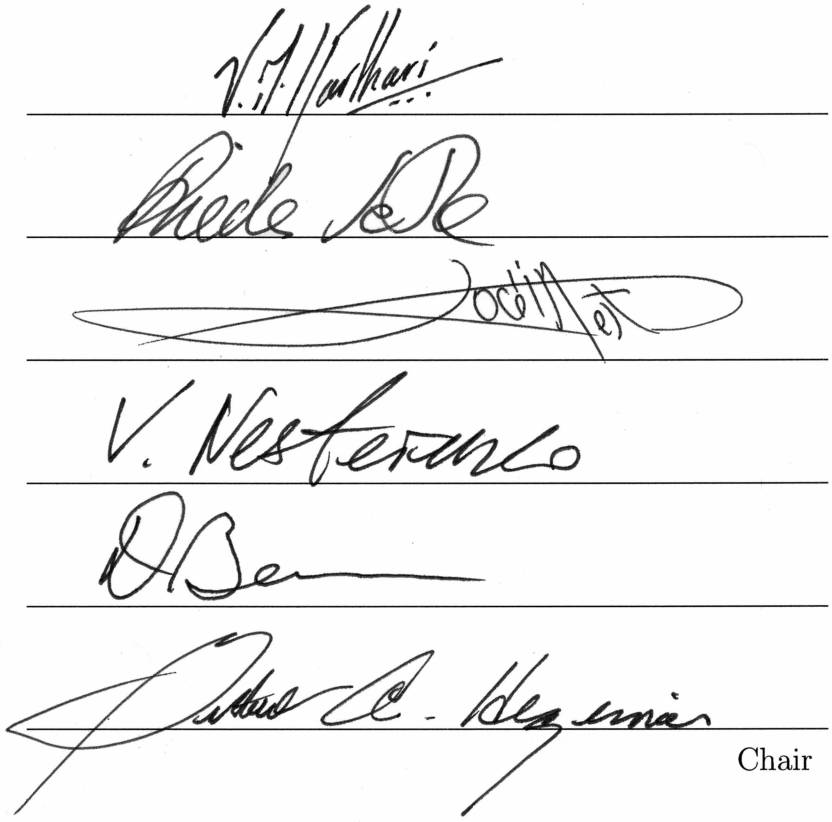

Chair

University of California, San Diego

2006

Mi abuelo, el ingeniero Francisco Rodríguez Peralta, me ha enseñado desde niño no sólo lo que es ser un buen ingeniero sino también lo que es ser un buen hombre. Durante más años de los que yo he vivido, él le ha dedicado su vida a la ingeniería y al bienestar y la educación de su familia. Por lo tanto no dudo que este acontecimiento signifique más para él que para mí. Esta tesis doctoral se la dedico a él con sumo cariño.

TABLE OF CONTENTS

LIST OF ABBREVIATIONS

ACI American Concrete Institute

ANFO Ammonium Nitrate and Fuel Oil

ASTM ASTM International (American Society for Testing and Materials)

BG Blast Generator

Caltrans California Department of Transportation

CFRP Carbon Fiber Reinforced Polymer

COR Coefficient of Restitution

CSS Carbon Shell System

DB Divine Buffalo

DSI Dywidag-Systems International

DTRA Defense Threat Reduction Agency

FAT Factory Acceptance Test

FRP Fiber Reinforced Polymer

GZ Ground Zero

ICP Integrated Circuit - Piezoelectric

K&C Karagozian & Case

LVDT Linear Variable Displacement Transducer

MOCA 4,4-Methylene-Bis-Orthochloroaniline

MTS MTS Systems Corporation

NA Not Available

NSF National Science Foundation

o.c. on center

PVC Polyvinyl Chloride

RC Reinforced Concrete

SAT Site Acceptance Test

SDOF Single Degree of Freedom

SEP Seismic Energy Products

SI Système International d'Unités

SRMD Structural Response Modification Device

TEMA Track Eye Motion Analysis

TNT Trinitrotoluene

TSWG Technical Support Working Group

UCSD University of California, San Diego

LIST OF SYMBOLS

Lower Case Latin Characters

a Acceleration

a_n Acceleration recorded at n^{th} instrument

b Column width

c_r Coefficient of restitution

c_1 Constant for shear thinning model

c_2 Constant for shear thinning model

c_3 Constant for shear thinning model

c_4 Constant for shear thinning model

c_5 Constant for shear thinning model

c_6 Constant for shear thinning model

d Programmer deformation

d_o Programmer deformation at beginning of unloading

f Force

f_b Baseline programmer curve

f_{bl} Baseline loading curve for programmer

f_{bu} Baseline unloading curve for programmer

f'_c Ultimate stress of concrete

$\tilde{f}$ Equivalent SDOF external force

$\tilde{f}_i$ Equivalent SDOF internal spring force

f_o Programmer force at beginning of unloading

g Acceleration of gravity

h Column depth

i Specific impulse

i_r Maximum normally-reflected specific impulse

i_s Maximum side-on specific impulse

$\bar{i}$ Equivalent specific impulse

$\bar{i}_r$ Equivalent normally-reflected specific impulse

k Spring stiffness

$\tilde{k}$ Equivalent SDOF spring stiffness

m Mass per unit length

m_1 Mass per unit length of BGs

m_2 Mass per unit length of specimen

p Pressure

p_n Pressure over tributary area of n^{th} instrument

p_r Peak normally-reflected pressure

p_s Peak side-on pressure

p_{gi} Incident pressure at point T

$\bar{p}$ Equivalent uniform pressure

$\hat{p}_{gi}$ Estimate of p_{gi}

t Time

t_a Time of arrival of shock front

t_d Pulse duration

t_{d^+} Duration of positive phase

t_{d^-} Duration of negative phase

t_r Ramp time

t^* End of programmer loading phase

v Deflection of column in transverse direction

$v_{s,\max}$ Maximum static deflection

$v_{\max}$ Maximum deflection

v Velocity

v_{1i} Initial velocity of mass 1 in two body collision

v_{1f} Final velocity of mass 1 in two body collision

v_{2i} Initial velocity of mass 2 in two body collision

v_{2f} Final velocity of mass 2 in two body collision

v_o Parameter to describe incoming BG velocity

w Load per unit length on column

w_i Resistance function

w_s Equivalent static load for force recovery

x Coordinate along longitudinal axis of column

x_{bn} Bottom coordinate of n^{th} instrument

x_{tn} Top coordinate of n^{th} instrument

y Coordinate along axis of collision

y_1 Position of mass M_1

y_2 Position of mass M_2

z Time component of deflection v

$\dot{z}_o$ Initial value of $\dot{z}$

Upper Case Latin Characters

A Area of programmer

A_o Initial area of programmer

C_f SDOF coefficient for equivalent force

C_{fn} Equivalent uniform load coefficient for n^{th} instrument

C_k SDOF coefficient for equivalent stiffness

C_m SDOF coefficient for equivalent mass

D Characteristic dimension of explosive

E Spring modulus

E_1 Spring modulus in Maxwell element for standard solid model

E_2 Spring modulus in lone spring for standard solid model

EI Flexural beam stiffness

EI_g Gross section flexural stiffness

F_d Dynamic modification factor

F_{dl} Dynamic modification factor for loading

F_{du} Dynamic modification factor for unloading

H_c Height of charge

H_t Height to a point on the target

I Impulse

L Column length

L_n Tributary length of n^{th} instrument

L_u Unloaded length in 3-BG configurations

M Mass

M_1 Mass of mass 1 in two-body collision

M_2 Mass of mass 2 in two-body collision

M_{bg} Mass of BG impacting mass

$\tilde{M}$ Equivalent SDOF mass

$\tilde{M}_1$ Equivalent BG mass in SDOF calculation

$\tilde{M}_2$ Equivalent specimen mass in SDOF calculation

$\mathcal{M}$ Bending moment

N Number of locations at which load is measured

R Standoff distance from charge to target

R_d Diagonal distance from charge to point T

R_g Horizontal standoff distance

$\hat{R}_d$ Estimate of R_d

T Point on ground immediately in front of target

T_n Natural period of vibration

W TNT-Equivalent weight of explosive

W_e Weight of explosive

Z Scaled distance

$\hat{Z}$ Fictitious scaled distance

Greek Characters

α Angle of incidence

α_g Angle of incidence at T

$\hat{\alpha}_g$ Estimate of α_g

β Reflected pressure increase factor

$\hat{\beta}$ Estimate of β

γ Nondimensionalized deformation rate $\dot{d}/(30\,\mathrm{m/s})$

δv Variation of deflection

δz Variation of time component of deflection

Δt Time step

ΔH Heat of detonation of TNT

ΔH_e Heat of detonation of explosive

ε Strain

ε_d Strain in dashpot

ε_s Strain in spring

$\dot{\varepsilon}_o$ Constant strain rate

η Viscous constant

η_o Viscosity at low strain rates.

η_∞ Viscosity at large strain rates

λ Scaling constant for Hopkinson-Cranz Equivalence

κ_1 Coefficient for loading curve f_{bl}

κ_2 Exponent for loading curve f_{bl}

κ_3 Coefficient for unloading curve f_{bu}

κ_4 Coefficient for exponent of unloading curve f_{bu}

κ_5 Coefficient for exponent of unloading curve f_{bu}

κ_6 Coefficient for dynamic factor F_{dl}

κ_7 Exponent for dynamic factor F_{dl}

κ_8 Coefficient for dynamic factor F_{du}

ν Poisson's ratio

ξ Parameter in Friedlander equation

ρ_v Volumetric mass density of concrete

σ Stress

σ_d Stress in dashpot

σ_s Stress in spring

σ_m Stress in Maxwell Element

τ_o Initial programmer thickness

ϕ Curvature

ψ Shape function for SDOF analysis, spatial component of deflection v

ψ_{ff} Shape function for beam with fixed ends

ψ_n Shape function describing location of n^{th} instrument

ψ_{pp} Shape function for beam with pinned ends

ψ_1 Shape function describing distribution of BG velocities

General Notation

$\dot{(\cdot)}$ Differentiation with respect to time

$(\cdot)'$ Differentiation with respect to variable other than time

$\tilde{(\cdot)}$ SDOF equivalent quantity

$\bar{(\cdot)}$ Quantity related to equivalent uniform load

$\hat{(\cdot)}$ Estimated or fictitious quantity

$\delta(\cdot)$ Variation of a variable

$(\cdot)_{j+1}$ or $(\cdot)_j$ Iteration on a variable

$(\cdot)_{\max}$ Maximum value

$(\cdot)_o$ Initial or reference value

LIST OF TABLES

LIST OF FIGURES

ACKNOWLEDGEMENTS

Above all else, I offer the warmest appreciation to my parents, M.A. Nikl and F.M. Rodríguez y Vázquez, for so many years of invaluable support, love, and encouragement without which, without exaggeration, my academic success would simply not have been possible.

I thank my friends, especially A. Lang and J. Collins, who have supported me wonderfully during the final months of writing, which have been difficult for reasons far beyond the academic.

I have benefitted from countless collaborations both within UCSD and without; I thank them all: colleagues, professors, laboratory staff, and extramural collaborators, especially G. Gurtman, J. Sallay, and M. Gram, whose work has directly informed mine.

I give a special mention to V.M. Cruz Atienza, for the thoroughness of his bachelor's thesis, a standard of quality towards which I'll always strive.

I thank my advisor Prof. G. Hegemier and my committee for their professional expertise, and TSWG, DTRA and NSF for funding me over the course of my graduate career.

I thank my reviewers, especially J. Keiser for extensive commentary (some of it quite funny), J. Sallay for insightful comments on Chapter 5, and J. Collins.

Lastly, I extend appreciation to developers of *the GIMP* and LaTeX for software I used extensively and freely, and to the website convertit.com for helping me manage the translation from our archaic but quaint system of units.

J., I've thought many hours about what to write here, for you've been by far the most important part of my life during these years in graduate school; try as I might, I simply don't have the words.

VITA

1993	Awarded U.C. Berkeley Chancellor's Scholarship
1997	Bachelor of Science, with Honors University of California, Berkeley Civil Engineering
1997	Awarded National Science Foundation Fellowship
1998	Master of Science University of California, Berkeley Civil and Environmental Engineering Structural Engineering, Mechanics, and Materials
1999–2000	Engineer II. Wiss, Janney, Elstner Associates, Inc. Emmeryville, California
2000–2006	Research Assistant University of California, San Diego
2002	Engineer III. Wiss, Janney, Elstner Associates, Inc. Emmeryville, California
2002–2003	Teaching Assistant University of California, San Diego
2006	Doctor of Philosophy University of California, San Diego Structural Engineering

PUBLICATIONS

Hegemier, Seible, Rodriguez-Nikl, Lee, Budek and Dieckmann (2002). FRP-based blast retrofit design strategies - Laboratory tests on rectangular RC columns. Research report SSRP-2002/04, UCSD Department of Structural Engineering.

Hegemier, Seible, Lee, and Rodriguez-Nikl (2003). FRP-based blast retrofit design strategies - Laboratory tests on rectangular RC columns - Part II. Research report SSRP-2002/17, UCSD Department of Structural Engineering.

Hegemier, Seible, Rodriguez-Nikl, and Arnett (2006). Blast mitigation of critical infrastructure components and systems. In *Proceedings of the Second fib Congress*, Naples, Italy.

ABSTRACT OF THE DISSERTATION

Experimental Simulations of Explosive Loading on Structural Components:
Reinforced Concrete Columns with Advanced Composite Jackets

by

Tonatiuh Rodríguez-Nikl
Doctor of Philosophy in Structural Engineering
University of California, San Diego, 2006
Professor Gilbert A. Hegemier, Chair

The dissertation responds to the need for efficient techniques for testing and validating protective technologies to resist explosive loading on civil structures; the newly-developed Explosive Loading Laboratory allows investigators to simulate explosive blast loading at a lower cost and with better data than when using real explosives. Analytical tools are developed for the new laboratory and comparisons between real and simulated explosive tests confirm that the two are equivalent. These developments provide future investigators with confidence in the simulated blast methodology and tools to predict results and analyze the data, thus setting the stage for decades of fruitful research in a nascent field of simulated explosive testing.

The simulated blast load is applied via specially designed apparatuses called blast generators, each of which is made of a high speed actuator that accelerates an impacting module towards the specimen. An elastomeric pad, called the programmer, on the front of the impacting module provides a blast-like pressure pulse to the specimen. The entire setup is housed in a post-tensioned, self-reacting, reinforced concrete reaction structure.

An inaugural series of tests on column specimens provides data on structural behavior and on the functioning of the laboratory. New methods of data analysis are developed: the equivalent uniform load method reduces the load recorded

on multiple channels to a single, rationally-derived value, and the equivalent charge method translates the experimental results to an equivalent real scenario. Because there is no fireball to obscure the specimen during the blast, the verbal descriptions and video stills herein are the first-ever visual record of structural behavior under blast loading.

The laboratory results are corroborated with field test data via qualitative comparisons and demand-damage plots to demonstrate the validity of simulated blast testing. A methodology is developed for quickly and easily determining the necessary velocity of the impacting module to deliver a desired impulse to the specimen. Load-deformation programmer data are collected and a phenomenological model of programmer behavior is derived for use in detailed pre-test analyses, including finite element implementations. Both tools are derived theoretically, calibrated to experimental data, and verified against independent experimental data.

1 Background

Terrorism has become one of the most important topics in political discourse, both domestically and globally. The United States has suffered significant attacks against its foreign installations in recent decades. Among them are attacks against the US embassy and Marine Corps barracks in Lebanon (1983), the Khobar Towers military complex near Dhahran, Saudi Arabia (1996), the US embassies in Nairobi, Kenya and Dab es Salaam, Tanzania (1998), and the USS Cole in Yemen (2000). Since 1995 it has suffered significant attacks on its own soil: against the World Trade Center (1995), the Alfred P. Murrah Federal Building in Oklahoma City (1995), and the World Trade Center and Pentagon (2001). The attacks in 2001 seared the topic of *terrorism* firmly in the American mind-set.

The response to this threat includes intelligence, military, diplomatic, financial, propaganda, and technological approaches, the last of which is the motivation behind this work; the Technical Support Working Group (TSWG), an interagency group under the auspices of the Department of Defense, is the prime financier of this research program, which aims to develop protective technologies to harden critical infrastructure against explosive charges; the Explosive Loading Laboratory, headed by professors G. Hegemier and F. Seible, has been developed to experimentally validate promising hardening technologies without use of explosive materials and at a fraction of the cost and time investment of real blast tests.

The Explosive Loading Laboratory is designed to simulate with a high degree of control and accuracy the impulse delivered by an actual blast to a structure and to measure the structural response to the simulated blast load. It is the first

of its type in the world and testing at this facility promises to be more repeatable, controllable, affordable, safer, and quicker than testing with actual explosives. It allows investigators to see for the first time ever, the behavior that has heretofore been obscured by the fireball produced by the explosive charge. The data produced will assist in validating computational codes and hardening technologies.

The Explosive Loading Laboratory can simulate a wide range of blast threats, but the primary threat motivating this work is a vehicular bomb at curbside, a large load about a half ton in size separated from the target by little more than a sidewalk. It is capable of causing significant damage to and even a complete progressive collapse of an unprotected structure. The carbon fiber composite-based retrofit technologies addressed in this work are highly effective at preventing damage to a structure subjected to such an attack.

The dissertation is divided into five chapters. The first provides both technical and nontechnical context to and a firm theoretical framework for later developments. It may be read in its entirety at the outset or skimmed and used as a reference when needed.

The second chapter discusses the functional requirements, design, construction, and proof testing of the Explosive Loading Laboratory. I was the chief designer of the structural portion of the laboratory, was involved in all aspects of the facility design, and oversaw the entire construction process.

The third chapter presents the first-ever simulated blast test series. This test series was conducted on columns, whose protection is critical to preventing progressive structural collapse, the main cause of death in building bombings. Facility validation or *shakedown* tests were conducted first and were followed by the inaugural or *commissioning* tests. New data analysis methodologies are developed for application not only to the simulated blast tests but also to field tests with real explosives.

The fourth chapter lays the groundwork for future research efforts at the Explosive Loading Laboratory. First, the equivalence is established between the

effects of simulated and real blast loads to develop confidence in the explosive simulation concept. Next are developed two predictive analytical tools for future investigators to use the laboratory effectively. The first is a methodology for an investigator to predict the required settings for the Explosive Loading Laboratory quickly and easily, and the other is a characterization of the impact modules of the Explosive Loading Laboratory for inclusion into detailed analyses of the blast simulation process.

The fifth and final chapter summarizes and concludes the dissertation and discusses some ideas for future research. Appendices contain derivations and data not included in the main text.

1.A Fundamentals Related to Blast Loads on Structures

This section details how to determine the loads that an explosive charge will impart onto a structure based on the charge's composition and its geometrical relation to the target. It then concentrates on the building's response to these loads and on strategies employed to mitigate the damaging effects of an explosive attack. An overview at the global level that includes a discussion on progressive collapse motivates a detailed look at the response of columns and the use of carbon fiber composite jackets to strengthen them. After this, the equivalent single degree of freedom method, which is critical to later developments, is developed in detail. Advanced analytical techniques are then mentioned briefly.

1.A.1 Airblast Characteristics

The pressure load that a bomb imparts onto a structure is determined by the charge type, configuration, size, its distance from the target, also called the *standoff*, and its relation to reflecting surfaces. To predict the airblast characteristics in typical configurations, these parameters are converted to TNT-equivalent, normalized parameters for which extensive bodies of data exist. Only unconfined

standoff charges are discussed herein. These occur outdoors, in open spaces and are somewhat removed from the target, which is typical of a vehicular bomb attack. Confined explosions, such as those occurring in a closed room or a narrow alley are not discussed nor are satchel charges, which are in contact with the target during detonation. Also ignored are the effects of debris caused by the bomb detonation. Blast design manuals contain guidelines for calculating the effects of simple charge configurations; predicting detailed blast loads for arbitrary configurations can be performed by advanced computer codes.

The Tri-Service Manual [57], developed by the departments of the Army, Air Force and Navy is used widely in the industry. It is referred to by its Army report designation, TM 5-1300, or its Navy report designation, NAVFAC P-397. The Army Technical Manual TM 5-855-1 [56] is widely used as well and is codified into the computer program ConWep [24, 43], a design aid for the blast mitigation engineer. Among the references that provide overviews of the field are *Structural Design for Physical Security* [11] and *Blast and Ballistic Loading of Structures* [51]. The former contains an extensive reference list at the beginning of Chapter3. The following discussion draws from all these references.

TNT Equivalency

Despite the wide range of explosives that might be used to load a target, their waveforms are similar enough to compare them by converting the type, weight and configuration of an explosive to an equivalent weight of TNT of the same configuration.

The equivalent weight is calibrated so that a charge of TNT at a given distance produces the same effect as the actual charge at the same distance. For each charge type there are two different equivalent weight factors: one to equate peak pressure and the other to equate maximum impulse (the time integral of pressure). Which factor is used depends on whether the target is more sensitive to pressure or impulse; impulse governs the behavior of the columns discussed

Table 1.1: Equivalent Explosive Weight Factors [56]

Explosive	Equivalent Weight Factor	
	Pressure	Impulse
ANFO	0.82	0.82
Composition C-4	1.37	1.19

herein. This approach is useful in a design context where the exact composition of the explosive is often unknown in which case the engineer need not analyze the phenomena for each different explosive type, but can instead consider a generic explosive load that accounts for all the various possible explosives.

Usually, the equivalent weight of TNT is obtained from tabulated values based on airblast testing; these data are widely available for common explosives. The equivalent weight factors for two common explosives, Composition C-4 and Ammonium Nitrate / Fuel Oil (ANFO), are reproduced from TM-5-855-1 in Table 1.1 for both pressure and impulse equivalence. The equivalent weight of TNT is the weight of the explosive multiplied by the factor given in the table.

Alternatively, the equivalent weight of TNT can be estimated by comparing its heat of detonation with the heat of detonation of TNT as follows:

$$W = \frac{\Delta H_e}{\Delta H} W_e \tag{1.1}$$

where W is the equivalent weight of TNT, W_e is the weight of the actual explosive, ΔH_e is its heat of detonation, and ΔH is the heat of detonation of TNT. For a rough calculation, a "TNT equivalency factor of 1.3 will generally provide a reasonable and conservative estimate of the TNT charge weight of any high explosive. Such an estimate would result in a scaled distance within 9% when the equivalency factor is within 30% of the actual value" [37]. Scaled distance is described next.

Scaled Distance

The distance of an explosive from the site is converted to a quantity called the Hopkinson-Cranz or cube root scaled distance (Z):

$$Z = \frac{R}{\sqrt[3]{W}} \tag{1.2}$$

where W is the equivalent TNT charge weight[1] and R is the distance from the charge to the target (R is defined more precisely when the different geometrical configurations are introduced). This scaling was independently derived by B. Hopkinson in 1915 and C. Cranz in 1926 [cited in 37]. Although Z is called a scaled *distance*, this is incorrect because it is a parameter of dimension length divided by cube root of weight. However the cube root of weight is proportional to the cube root of volume and thus to a characteristic size D. The scaled distance is thus proportional to a non-dimensionalized distance R/D. The Hopkinson-Cranz scaling law postulates that a charge of size D and weight W at a distance R from the target produces the same peak pressure as one of size λD and weight $\lambda^3 W$ at a distance λR. It also states that the charge at λR will have duration $\lambda\, t_d$ and impulse $\lambda\, i$, where t_d and i are the duration and impulse of the charge at R. These equivalences are summarized in Table 1.2 (p. 7).

Geometrical Configuration

The geometry of a blast environment (Figure 1.1) is described primarily by the charge height H_c, its horizontal *standoff* from the target R_g, and the target height H_t. Point T is on the ground immediately in front of the target and ground zero (GZ) refers to the point on the ground immediately below the charge. R_d, the *diagonal* or *slant distance* from the charge to point T, and α_g, the *angle of incidence* at point T, are used in computing the airblast parameters in the air burst environment. Keep in mind that α_g is a specific angle of incidence whereas

[1] When using SI units the scaled distance Z is calculated with W being the charge mass, not its weight.

Table 1.2: Hopkinson-Cranz Equivalences

Parameter	Charge A	Charge B
Distance	R	λR
Size	D	λD
Weight	W	$\lambda^3 W$
Scaled distance	Z	Z
Pressure	p	p
Duration	t_d	λt_d
Impulse	i	λi

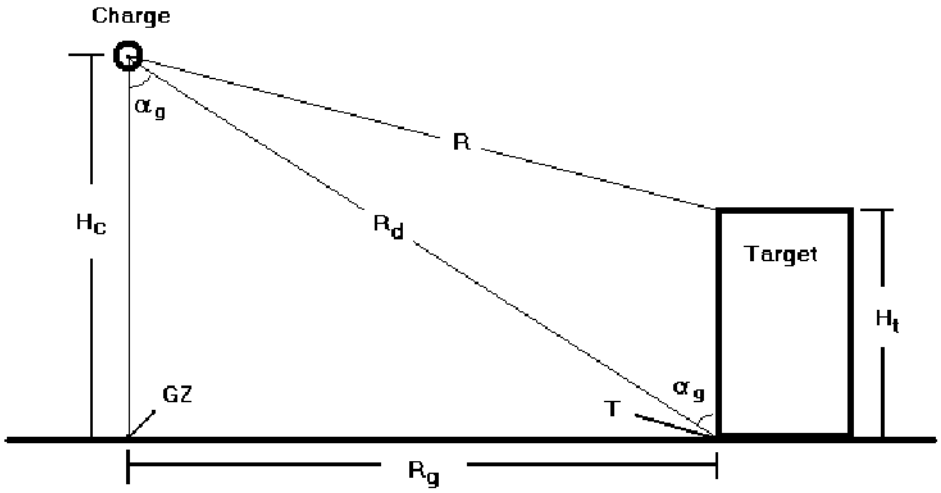

Figure 1.1: Geometry of a Blast Environment

α, which is introduced shortly, is the notation for an arbitrary angle of incidence. The distance R is the smallest standoff to the target.

When the charge detonates, the shock wave spreads spherically outward from the center of the charge.[2] What happens after that depends on the relative magnitudes of the charge height, target height and standoff. The three possible

[2]This may not be the case for specially-shaped charges. Charges of this type are not considered here.

configurations are *free air burst*, when the charge height is large and the *incident* wave hits the target directly; *ground burst*, when the charge is on the ground and reflects off it immediately; and *air burst*, when the charge is raised but the shock front reflects off the ground prior to arrival at the target.

In all cases, the pressure and impulse imparted to a surface (such as the ground or the target) depend on the surface's orientation to incident airflow. *Side-on* pressure and impulse are experienced when a surface is parallel to the direction of airflow and *normally-reflected* pressure and impulse are experienced when a surface is perpendicular to the direction of airflow; normally-reflected values are larger because of the momentum imparted by particle to the target upon reflection. The angle of incidence (α) quantifies the angle between airflow and the surface normal; $\alpha = 0°$ for normally-reflected airflow and $\alpha = 90°$ for side-on airflow. Relations exist to determine the pressure and impulse increases for angles of incidence between these two extremes.

Returning to the three possible geometrical configurations, free air burst occurs when the charge is so high off the ground ($H_c >> R_g$) that the *incident* shock wave hits the target before hitting the ground. Free air burst can occur when ordinance explodes above a target. For design, the spherical shape of the shock wave is simplified to a planar wave.[3] In free air burst R is the relevant standoff distance.

A ground burst occurs when the charge is on or very close to the ground ($H_c \approx 0$). In this case, the incident wave reflects immediately off the ground. The incident and *reflected* waves merge into a stronger shock wave that spreads hemispherically from the charge. For a perfectly reflective (infinitely rigid) surface the effective charge size is double the actual charge size. If significant cratering occurs underneath the charge, the effective charge size is approximately 1.8 times

[3]The assumption behind the plane wave simplification is that the standoff and angle of incidence vary little over the area of interest. Although they may vary greatly over the facade of a multi-story building, they will vary little over the target column that is immediately in front of the charge.

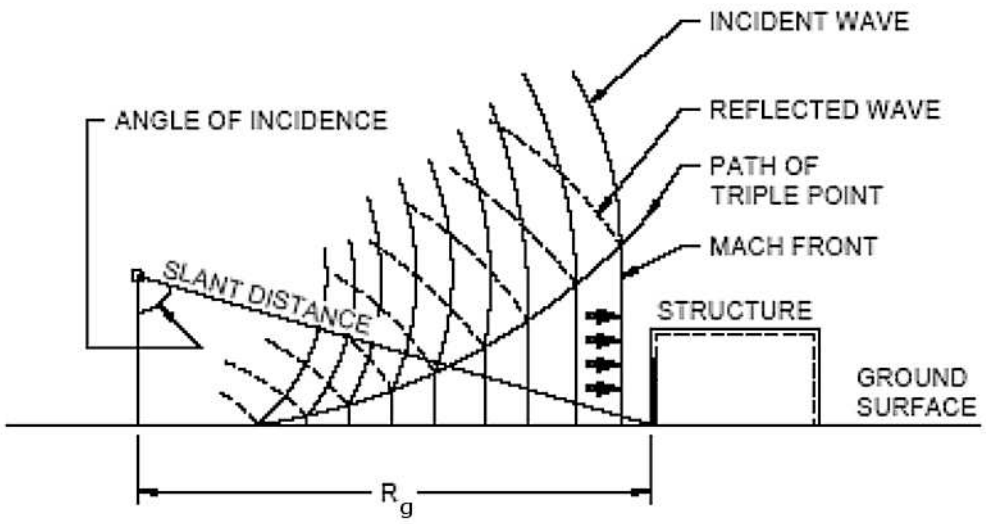

Figure 1.2: Air Burst Environment [57]

the original. A vehicular bomb may in some cases be considered a ground burst. As with free air burst, the hemispherical shape of the shock wave is usually simplified to a planar wave for design. In ground burst, the standoff distance is the horizontal distance R_g.

In between the two cases is air burst. This occurs when the charge is above ground but the incident wave reflects off the ground before it reaches the target. During air burst, a phenomenon called *Mach reflection* takes place, during which the incident and reflected waves merge to form the *Mach stem* or *Mach front*, a roughly vertical shock wave of greater pressure that travels horizontally (Figure 1.2). Whether Mach or *regular reflection* takes place depends on the angle at which the incident wave strikes the ground. Close to the charge, at low angles of incidence, the incident wave reflects from the ground in regular reflection, during which the incident wave, which travels diagonally downward, is ahead of the reflected wave, which travels diagonally upward. Beyond a critical angle of incidence (roughly 40° in air [51]) the mechanism of reflection changes to one that is described as skimming along rather than bouncing against the surface [51]. This allows the reflected wave to speed up sufficiently for it to merge with the incident

wave and form the Mach stem. The Mach stem grows in height as it travels further from the charge source. At the top of the Mach stem is the *triple point* above which the reflected wave still trails the incident wave. If the target height exceeds that of the Mach stem, the target will suffer a complex shock profile over its height: a single peak of increased pressure below the triple point and a double peak of lower pressure but increased duration above it. Usually the Mach stem is taller than the target, but it may be assumed to extend over the full height of the target; this is conservative in terms of peak pressure, but not necessarily so in terms of impulse.

Airblast Parameters

The time it takes from detonation to when the shock front arrives at the target is called the *arrival time* (t_a). At this time the pressure climbs almost instantly to the *maximum* or *peak pressure*. It then drops quickly to zero, below zero to the *minimum* or *peak negative pressure*, and then slowly back up to zero. The total time from when the shock front arrives to when the pressure returns to zero is the *pulse duration* (t_d), which can be divided into the *positive phase duration* (t_{d^+}) and the *negative phase duration* (t_{d^-}). A typical waveform produced by a high explosive is shown in Figure 1.3. Loads of the type that can damage columns have a negligible negative phase, and in such cases the waveform can be represented by the Friedlander equation

$$p(t) = p(0)\left(1 - \frac{t}{t_{d^+}}\right)\exp\left(-\xi(Z)\,\frac{t}{t_{d^+}}\right), \qquad 0 \le t \le t_{d^+} \tag{1.3}$$

where ξ depends on scaled distance and modulates the rate of decay [details in 51].

The integral of the pressure-time history is called the *specific impulse* (i) and the maximum specific impulse is reached at the end of the positive phase. A typical impulse profile produced by a high explosive is shown in Figure 1.4. In practice, the term "impulse," which is the integral of force, is often misused in place of "specific impulse," which is the integral of pressure. In addition, "impulse" is usually used in place of "maximum impulse." For the sake of simplicity and

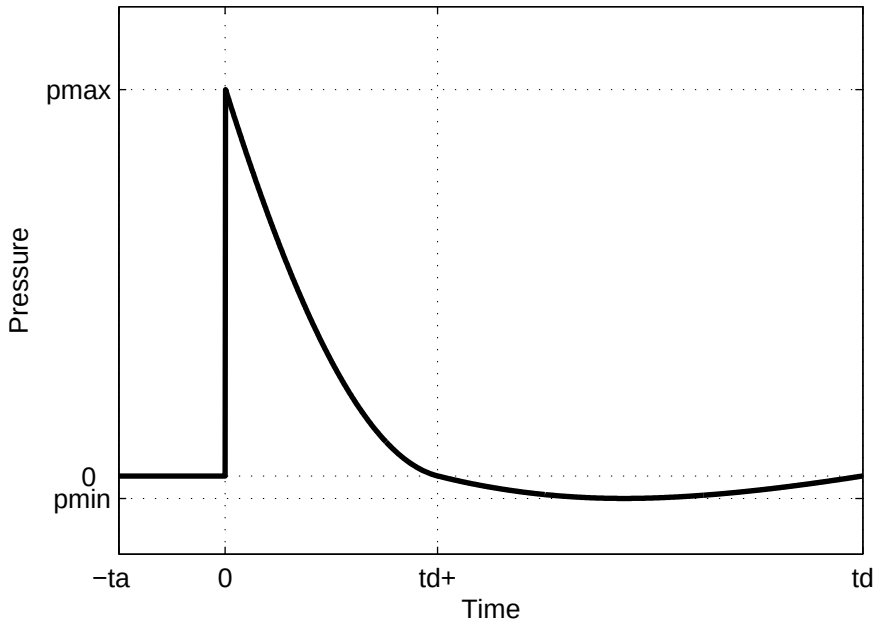

Figure 1.3: Typical Blast Pressure Time History

adherence to common usage, this practice is continued herein as long as there is no danger of ambiguity. Impulse is of high importance to this work because it is the most important parameter influencing the response of columns, much more so than peak pressure.

The design manuals TM 5-1300 and TM 5-855-1 and the software package ConWep contain tables and figures to determine values for these and other airblast parameters. The positive parameters for free air burst are determined from Figure 1.5 [57] (also in [24, 56]). This figure, which uses different notation than introduced in the text, is used to determine peak side-on pressure (p_s), peak normally-reflected pressure (p_r), maximum side-on specific impulse (i_s), maximum normally-reflected impulse (i_r), arrival time, positive phase duration, wave front speed, and positive phase wave length, all as functions of scaled distance. The positive parameters for ground burst are determined from Figure 1.6 [57] (also in [24, 56]). It contains the same information as does Figure 1.5 for free air burst.

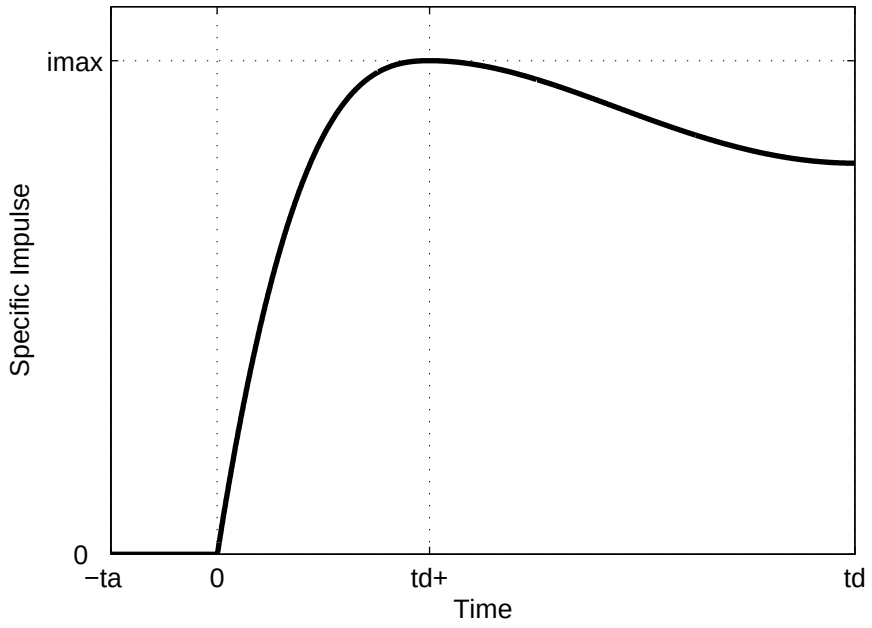

Figure 1.4: Typical Blast Impulse Time History

Peak pressure for an arbitrary angle of incidence is found using Figure 1.7 [24] (also in [56]). This figure is more detailed than the one provided by TM 5-1300, which does not account for the increase due to Mach reflection.

Calculating the shock wave parameters due to air burst is a two step process. First the pressure is determined in the Mach stem just prior to arrival at the target. Then an equivalent scaled distance corresponding to this pressure is calculated and used to obtain other airblast parameters. This is detailed in the following six step process: (1) using Equation (1.2) compute the scaled distance Z from the diagonal or slant distance R_d and the charge weight W; (2) using Z calculate the incident pressure on the ground p_{gi} from the relations for free air burst (e.g., Figure 1.5); (3) obtain the reflected pressure increase factor β from the angle of incidence relation (e.g., Figure 1.7) using p_{gi} and α_g, the angle of incidence at Point T; (4) compute $p_s = \beta\, p_{gi}$, the pressure in the Mach stem that will impart a side-on pressure to the target; (5) again using the relations for free air burst,

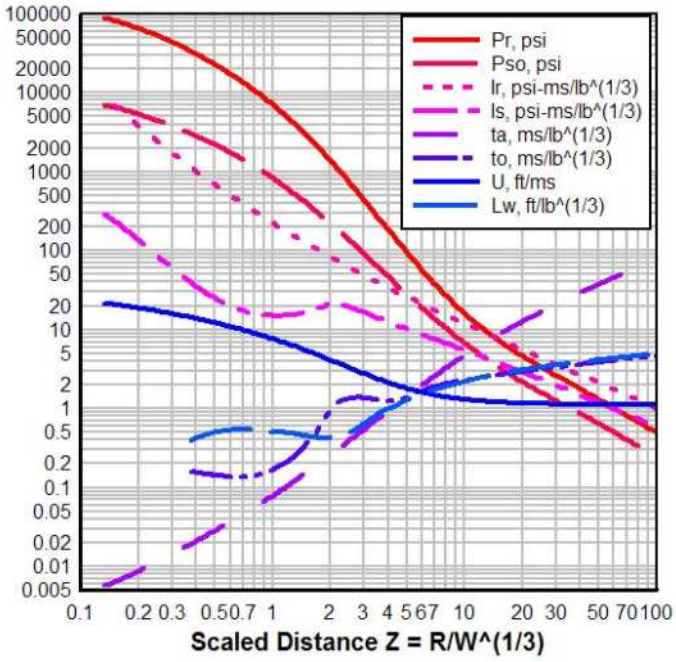

Figure 1.5: Positive Shock Parameters (Spherical Blast) [57]

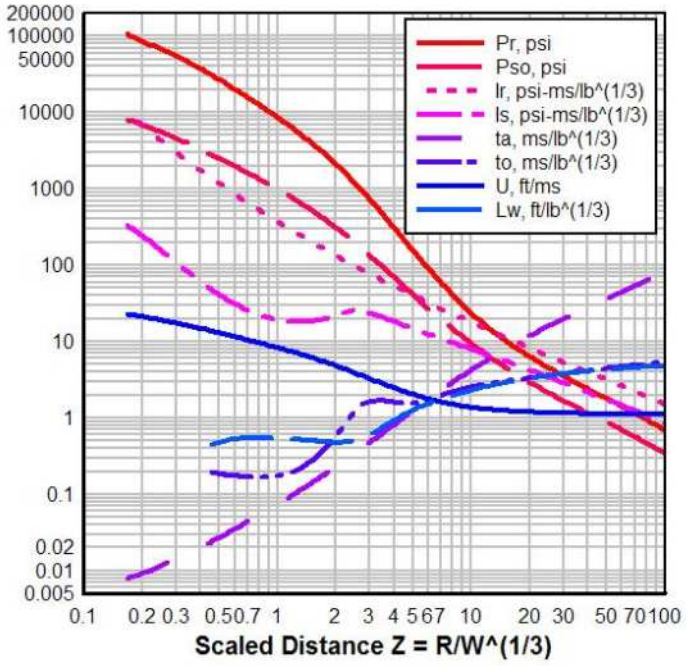

Figure 1.6: Positive Shock Parameters (Hemispherical Blast) [57]

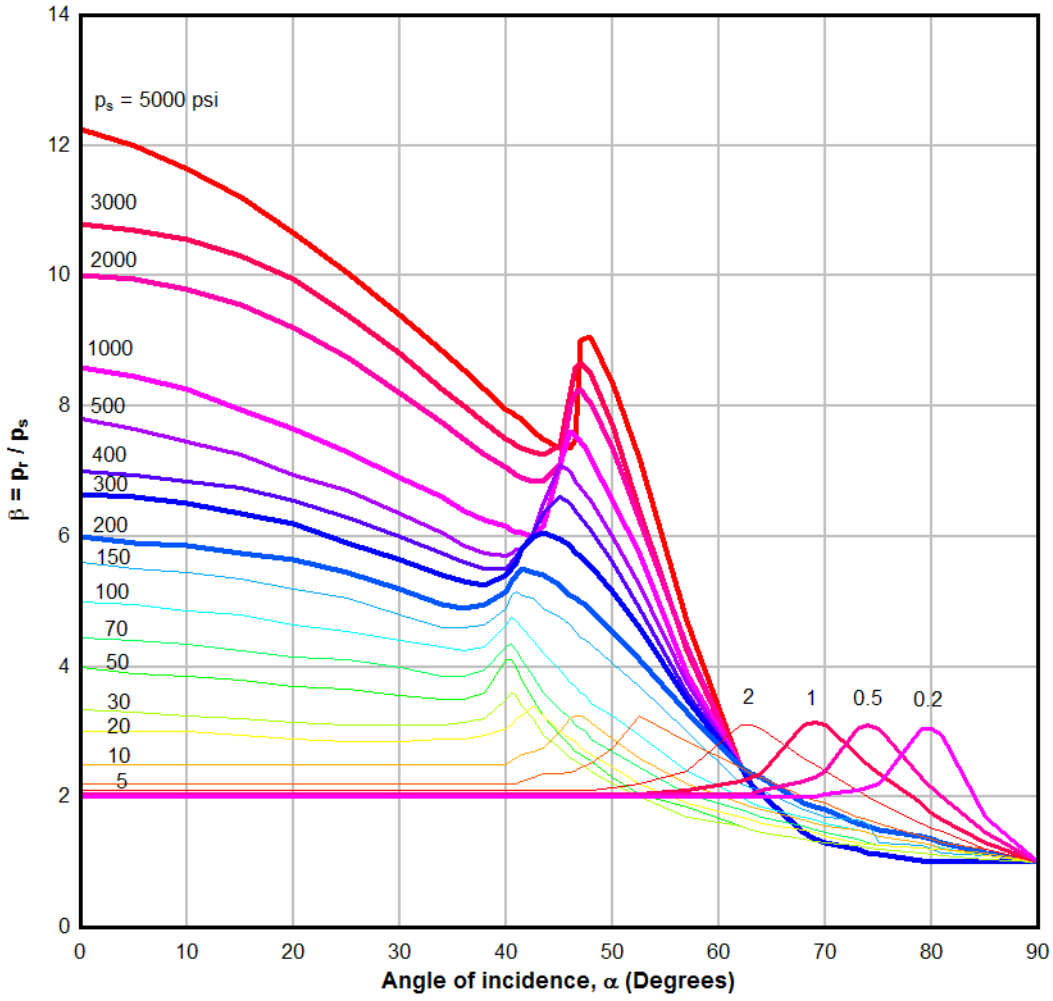

Figure 1.7: Pressure Increase Versus Angle of Incidence [24]

determine a fictitious scaled distance $\hat{Z}$ that corresponds to an incident pressure p_s; and (6) determine other airblast parameters from $\hat{Z}$ using the relations for free air burst.

Example

A column 10.75 ft (3.28 m) in length is loaded by a 1450 lb (658 kg) charge of ANFO placed 13 ft (3.96 m) away and raised 3 ft (0.91 m) off the ground. The column is facing the charge and thus will suffer normally-reflected pressure and impulse. We would like to determine the peak pressure, maximum impulse, arrival time, and pulse duration.

Because the charge height and standoff are of comparable magnitude, the blast environment is air burst; the blast wave will reflect from the ground and form a Mach stem. The equivalent weight of TNT is

$$W = 0.82 \cdot 1450\,\text{lb} = 1189\,\text{lb}\ (539.3\,\text{kg}) \tag{1.4}$$

thus

$$\sqrt[3]{W} = 10.59\,\text{lb}^{1/3}\ (8.140\,\text{kg}^{1/3}) \tag{1.5}$$

The diagonal distance from the charge to the point T is

$$R_d = \sqrt{(13\,\text{ft})^2 + (3\,\text{ft})^2} = 13.34\,\text{ft}\ (4.066\,\text{m}) \tag{1.6}$$

and

$$Z = \frac{R_d}{\sqrt[3]{W}} = 1.26\,\frac{\text{ft}}{\text{lb}^{1/3}}\ \left(0.50\,\frac{\text{m}}{\text{kg}^{1/3}}\right) \tag{1.7}$$

This value of Z determines the incident pressure at point T

$$p_{gi} = 564.3\,\text{psi}\ (3.890\,\text{MPa}) \tag{1.8}$$

The angle of incidence at point T is

$$\alpha_g = \tan^{-1}(13/3) = 77.01^\circ \tag{1.9}$$

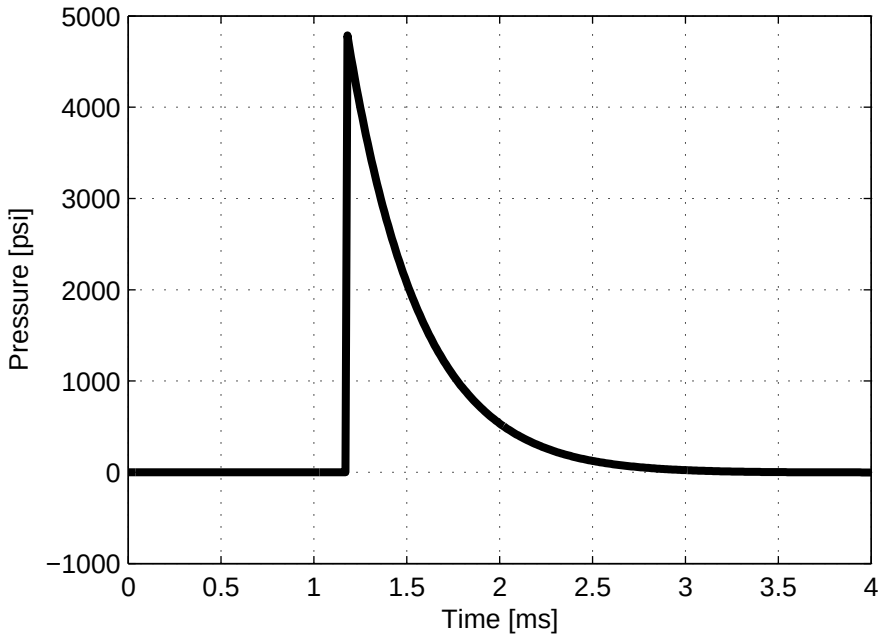

Figure 1.8: Pressure Time History for Airblast Example

and for these values of α_g and p_{gi} the increase factor in the Mach stem is $\beta = 1.070$, thus

$$p_s = 1.070 \cdot 564.3\,\text{psi} = 603.8\,\text{psi}\ (4.163\,\text{MPa}) \tag{1.10}$$

The fictitious scaled distance corresponding to p_s is $\hat{Z} = 1.21\,\text{ft/lb}^{1/3}$ $(0.48\,\text{m/kg}^{1/3})$ and for this scaled distance the airblast parameters are

$$p_r = 4788\,\text{psi}\ (33.01\,\text{MPa}) \tag{1.11}$$

$$i_r = 1814\,\text{psi·ms}\ (12.51\,\text{MPa·ms}) \tag{1.12}$$

$$t_a = 1.18\,\text{ms} \tag{1.13}$$

$$t_{d^+} = 2.43\,\text{ms} \tag{1.14}$$

Idealized pressure and impulse curves based on Equation (1.3) are shown in Figures 1.8 and 1.9. This result will be used in later chapters.

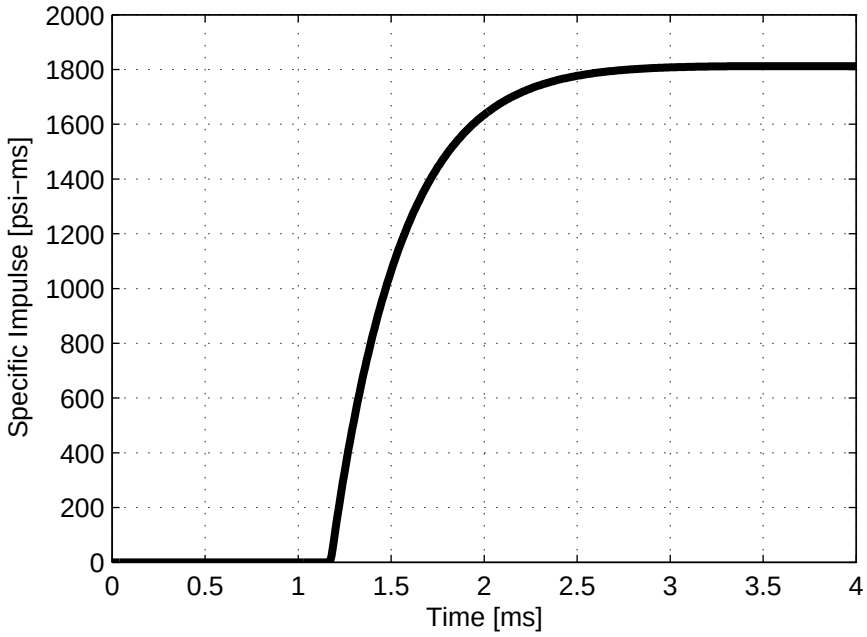

Figure 1.9: Impulse Time History for Airblast Example

1.A.2 Structural Response and Mitigation Strategies

Having derived the loads imparted to the structure how does the target respond, how and to what extent can it be damaged, and what can be done to mitigate the damage? Questions of this type motivate this section. The response to airblast occurs in two phases. During the first phase, the structure will suffer heavy local damage and personnel will be subjected to potentially fatal peak pressures and debris fields. After the shock wave has subsided the structure must redistribute the gravity loads around the damaged areas. If adequate alternate load paths do not exist, the structure will not be able to carry the gravity load and most or all of the building will fail in a *progressive collapse*. A structural failure of this type can cause more fatalities than the primary blast effects. Mitigation efforts generally aim at reducing the severity and likelihood of the threat by proper protection of the target's perimeter and at preventing progressive collapse by strengthening critical elements and providing global structural integrity.

There is a wealth of guidelines addressing these issues but no single, canonical work. TM5-1300 and TM5-855-1 provide guidelines about both structural response and mitigation as do the general references discussed above. Two other manuals, the US Air Force *Installation Force Protection Guide* [55] and the US Department of Defense *Minimum Antiterrorism Standards for Buildings* [54] discuss mitigation strategies in detail. Crawford et al. [12] and Krauthammer [28] discuss details of progressive collapse as does the British design code (cited in [28]). The response of retrofitted columns draws heavily from research in seismic engineering, e.g., Priestley et al. [44, § 8.2.2] and Seible et al. [48]. Morrill et al. [39] and Crawford et al. [12] discuss the extension of seismic standards to protect against blast loads. The following discussion draws from all these references. Global issues are discussed first, followed by the response of reinforced concrete columns and carbon fiber composite mitigation technologies.

Global Response and Mitigation

The basic philosophy in developing site mitigation efforts is that it is too costly to eliminate the risk completely; instead it must be reduced to within limits acceptable to the building owner given the budget and operational constraints. A mitigation effort requires a proper threat and vulnerability assessment; strategies are then developed and implemented to address the vulnerabilities.

Mitigation strategies for perimeter protection include increasing standoff via access controls and physical barriers; minimizing debris fields; improving the building layout by clustering buildings, placing critical facilities furthest from the threat, and avoiding architectural details such as reentrant corners that can intensify pressures; and establishing visual barriers to eliminate lines of sight from beyond the perimeters.

Mitigation strategies for progressive collapse involve strengthening critical elements, providing more ductility to critical elements, adding additional load paths and providing additional continuity to the gravity frame. In practice it is common to use the *missing member* analysis method to determine the response of the building during the static phase. This method assumes that only a single element, e.g. a column, is damaged during a blast. A static analysis of the building is then conducted with this member removed from the model. For instance, if a column were removed, the beams framing into it would have to support loads over a longer span than previously. A missing member analysis would determine whether or not they would be able to handle this additional load, and if not, whether the failure would propagate further. However, often more than one element has suffered damage, and even if the damage is limited to only one element, the joint region connecting that element to the rest of the structure is likely to be damaged as well, which would greatly reduce the continuity between surviving elements. Given these complexities, determining the potential structural behavior cannot be performed blindly and requires proper judgement and imagination on the part of the engineer. The simplifications involved in the missing member analysis may

render it inappropriate and a more detailed analysis may instead be needed. In either case it is important to determine whether or not the column survives the attack; this is addressed in the next section.

Local Response of Concrete Columns

As a column is accelerated laterally due to blast loading, the kinetic energy is absorbed - some into elastic behavior of the column and the rest into inelastic deformation. Ideally, the inelastic deformation is limited to ductile bending behavior. In this case, the column will be damaged but will likely be able to support the gravity load after the blast. However a bending mode cannot be developed unless the column is properly designed to carry the shear loads. If the shear capacity is inadequate, then the column will fail suddenly and catastrophically. Even if the column attains the desired bending mode, proper detailing in the plastic hinge has to be provided to ensure adequate ductility. On top of these requirements, the column must be stiff enough to limit displacements; if they are too large the column will become unstable due to softening behavior and second order instabilities. In total, five failure conditions will be considered: bending moment, diagonal shear, direct shear, confinement, and displacement. Of these, only direct shear is specific to blast. Strain rate strength enhancements can be included in capacity calculations. These rate enhancements are relatively small and do not exceed 1.25. Additional details can be found in TM 5-1300 and other references.

The bending moment capacity is determined from simple equations in the ACI-318 building code [2] or from a more detailed moment-curvature analysis. If the column has proper transverse reinforcement the core concrete will be confined, thus increasing its strength. Proper treatment of confinement is important and discussed below. Full bending capacity may also not be attained if rebar buckles or integrity of lap splices is lost inside the plastic hinge region. Proper confinement maintains bond across the lap splices and restrains rebar from buckling.

The bending behavior will only be developed if the column does not

otherwise fail in shear; if the shear capacity is breached first the column will lack ductility, fail catastrophically and be unable to sustain the gravity loads above it. Thus, design practice uses the concept of capacity design [42, § 1.4] whereby the required diagonal shear capacity is based on the moment capacity instead of the calculated shear demand. The total diagonal shear capacity is determined by contributions from the concrete, transverse reinforcement, and axial load. Various models exist for determining shear capacity such as that in ACI-318 and the more detailed model by Priestley et al. [44].

The only blast-specific failure mode is direct shear, which in this case is shear at the end of the column at the horizontal interface with the adjoining beams or slab. Direct shear capacity is determined by the strength of concrete and of reinforcement across the shear plane. Typically the direct shear capacity is much larger than diagonal shear or bending capacities and need only be considered if the other two are increased substantially.

Advanced Composite Jackets for Mitigation

Advanced composite materials consist of a reinforcement material embedded inside a matrix material. Fiber reinforced polymer (FRP) composites, which are made of thin reinforcement fibers such as carbon, aramid, and E-glass embedded in a polymer matrix material such epoxy are effective materials for construction applications. They are lighter and easier to transport than other jacketing technologies and have minimal architectural impact. Because the material is isotropic its engineering properties can be tailored to the needs of a particular situation. For instance, the fibers can be oriented exclusively along the hoop direction to enhance shear and confinement capacity without overly increasing bending moment capacity, which would then require yet another increase in shear capacity. In blast applications composite jackets may be damaged and weakened by the debris field and they might need to be protected either by extra jacket thickness or a protective covering. FRP jackets, especially carbon FRP (CFRP) jackets, have been studied

and successfully implemented since the late 1980s in seismic applications and more recently in blast applications (see Section 1.C).

FRP jackets are used to increase diagonal shear, confinement, displacement and bending moment capacities. Their design is discussed by Priestley et al. [44, § 8.2.2], Seible et al. [48], and Teng et al. [53]. The required FRP jacket thickness is determined individually for bending, shear and confinement actions; the total required jacket thickness is the sum of the three contributions. Design for shear capacity and integrity of the flexural hinge is based on limiting strains across the shear crack to maintain aggregate interlock. Design for confinement of the flexural hinge is based on providing sufficient confining force in the jacket.

The confinement behavior of FRP-jacketed reinforced concrete (RC) columns requires special attention. The well-known confinement model developed by Mander et al. [36] is not accurate for FRP-confined concrete. Because steel is ductile after yielding while FRPs are elastic up to failure, the model is derived on assumptions that are inadequate for FRP-confined concrete (Nanni and Bradford [40], Teng et al. [53]). Instead, FRP-specific confinement models must be used, e.g., Lee [31], Teng et al. [53]. Some jacket designs might expand as a function of their fiber orientations (Howie and Karbhari [23]); this peculiar structural behavior also affects the effective confinement.

Confinement on rectangular jackets is about half as effective as for circular jackets. Data on rectangular columns are limited to medium sized and relatively square columns and care must be taken when extrapolating to larger and more oblong cross section [44, 49]. Additional considerations need to be taken for rectangular columns with both FRP and steel transverse reinforcement, which have complex confinement zones (Wang and Restrepo [58]).

A technology for new construction has been proposed and successfully tested by Seible et al. [47]. This is a prefabricated carbon shell system (CSS) that functions both as formwork as well as longitudinal and transverse reinforcement. The shell can be used in addition to longitudinal rebar, with no longitudinal rebar

at all, or with only starter bars at the top and bottom. CSS jackets are prefabricated by filament winding under high quality control. The construction process is simplified and expedited because the jacket does not need to be removed as does ordinary formwork. This technology is simulated in the tests described in Chapter 3 by FRPs applied in the longitudinal and hoop directions by hand layup after casting. Because the jacket applied after concrete casting is similar but not identical to a CSS it is referred to a *pseudo-CSS* jacket.

1.A.3 Single Degree of Freedom Analysis Methods

In practice, there are two predominant methods to calculate the response of critical components to blast loads: (1) highly-detailed, physics-based, nonlinear, explicit, finite element codes (which will be discussed briefly below) and (2) a simpler equivalent single degree of freedom (SDOF) method. The SDOF method is frequently used in design practice; it is robust, well-studied and gives answers accurate enough for design with relatively minimal investment. It can be developed under linear elastic assumptions or extended to nonlinear behavior. The linear elastic assumption is frequently used because critical elements are often designed to remain nearly elastic under blast threats.

The equivalent SDOF method is an approximate solution to the partial differential equation governing the dynamic behavior of an Euler-Bernoulli beam.[4] The basic kinematic assumption in this well-known theory is that plane sections normal to the longitudinal axis of the undeformed beam remain plane when the beam is deformed. The approximate solution is based on an assumed deformation profile and is obtained by the method of calculus of variations.[5] Biggs [7] is a popular author in the blast field because he applies the SDOF method directly to blast applications, but a presentation of the SDOF method is part of most standard

[4]In practice, the Euler-Bernoulli beam formulation is used to adequately estimate failure even for specimens that suffer large, localized shear deformation, such as the as-built specimens treated herein. Although adequate for some applications, this approach is not free of error. More advanced methods are discussed in Section 1.A.4.

[5]See Gelfand and Fomin [16] for a treatment of calculus of variations.

structural dynamics textbook [9, 10].

Problem Statement

Consider a column of length L and mass per unit length $m(x)$. It is subject to a time-dependent, transverse load per unit length $w(x,t)$ and in response it develops an internal resisting bending moment $\mathcal{M}(x,t)$, where time is denoted by t. A coordinate system originates at the base of the column with the x-axis oriented along the longitudinal axis; the lateral column deflection $v(x,t)$ is oriented perpendicular to x. The internal resisting moment $\mathcal{M}$ is a function of curvature $\phi = v''/[1+(v')^2]^{3/2}$, which for small deformation is approximated by $\phi \approx v''$, where the prime indicates differentiation with respect to x. The governing differential equation for dynamic equilibrium of an Euler-Bernoulli beam is

$$m\,\ddot{v} + \mathcal{M}'' = w \qquad \forall x \in (0, L) \tag{1.15}$$

where the dot indicates differentiation with respect to time. Damping is not included because the maximum response occurs in the first quarter cycle of the time history, during which time the effect of damping is negligible. The column is initially undeformed and at rest

$$v(x,0) = 0 \qquad \forall x \in (0, L) \tag{1.16}$$

$$\dot{v}(x,0) = 0 \qquad \forall x \in (0, L) \tag{1.17}$$

and two different sets of boundary conditions will be considered: fixed ends and pinned ends. For fixed ends, both displacements and rotations must be zero at the boundaries

$$v(x,t) = 0, \qquad x = 0, L \tag{1.18}$$

$$v'(x,t) = 0, \qquad x = 0, L \tag{1.19}$$

while in the case of pinned ends, the displacements and bending moments are zero at the boundaries

$$v(x,t) = 0, \qquad x = 0, L \tag{1.20}$$

$$\mathcal{M}(x,t) = 0, \qquad x = 0, L \tag{1.21}$$

The approximate solution is found by separation of variables with the deflection being represented by its spatial and temporal components as follows:

$$v(x,t) = \psi(x) z(t) \tag{1.22}$$

In the SDOF method, the shape function ψ is assumed based on the expected deformed shape of the column. The shape function must satisfy the displacement and rotation boundary conditions (the *Dirichlet* or *essential* boundary conditions) but need not satisfy the moment boundary condition (the *Neumann* or *natural* boundary conditions). It is convenient, but not necessary, to normalize the shape function to a maximum value of one. In this way ψ represents the column shape and z the magnitude of deflection. The deflected shape of a uniformly and statically loaded elastic beam is a frequently adopted shape function.

Using calculus of variations, also known as the principle of virtual work, Equation 1.15 is satisfied in weak form

$$\int_0^L \left[m\,\ddot{v} + \mathcal{M}'' - w \right] \delta v \;\, \mathrm{d}x = 0 \tag{1.23}$$

where the variation of displacement takes the same form as the real displacement,

$$\delta v(x,t) = \psi(x)\, \delta z(t) \tag{1.24}$$

with δz being an arbitrary variation in time. Combining Equations (1.22), (1.23), and (1.24) yields

$$\left\{ \int_0^L m\,\psi^2\,\ddot{z} + \mathcal{M}''\,\psi - w\,\psi \;\, \mathrm{d}x \right\} \delta z = 0 \tag{1.25}$$

Because $\delta z(t)$ is arbitrary, the quantity in curly brackets must vanish; this yields the governing single degree of freedom equation

$$\tilde{M}\ddot{z}(t) + \tilde{f}_i(t) = \tilde{f}(t) \tag{1.26}$$

where $\tilde{M}$ is the equivalent mass, $\tilde{f}_i(t)$ is the equivalent internal force, and $\tilde{f}(t)$ is the equivalent external force and are equal to

$$\tilde{M} = \int_0^L m\,\psi^2\,\mathrm{d}x \tag{1.27}$$

$$\tilde{f}_i = \int_0^L \mathcal{M}''\,\psi\,\mathrm{d}x \tag{1.28}$$

$$\tilde{f} = \int_0^L w\,\psi\,\mathrm{d}x \tag{1.29}$$

In an alternative formulation, the expression for internal force is reworked to avoid second derivatives of bending moment. Integrating Equation (1.28) by parts twice yields

$$\tilde{f}_i = \Big[\mathcal{M}'\,\psi - \mathcal{M}\,\psi'\Big]_0^L + \int_0^L \mathcal{M}\,\psi''\,\mathrm{d}x \tag{1.30}$$

The boundary terms are identically equal to zero in both the pinned end and fixed end cases, yielding

$$\tilde{f}_i = \int_0^L \mathcal{M}\,\psi''\,\mathrm{d}x \tag{1.31}$$

as an alternate expression for the internal force.

The equivalent internal force is seldom expressed in terms of an internal resisting moment exactly as it is written here. Rather, in some cases it is expressed in terms of a nonlinear resistance function: a uniform resisting force per unit length w_i as a function of midspan displacement. TM 5-1300 provides guidance for determining the resistance function for a column based on its positive and negative moment capacities. In Euler-Bernoulli beam theory the distributed load is the second derivative of moment, so

$$\mathcal{M}''(t) = w_i(v(L/2,t)) \tag{1.32}$$

Thus for a specified resistance function, after substituting Equation (1.32) into Equation (1.28), the equivalent internal force simplifies to

$$\tilde{f}_i = w_i \int_0^L \psi\,\mathrm{d}x = C_f\,w_i\,L \tag{1.33}$$

The coefficient C_f depends on what shape function is specified (see Equations (1.47) and (1.48) and Table 1.3 below).

In other cases, e.g., the design of critical components that must not be damaged, the column may be treated as linear elastic. In this special case the moment is

$$\mathcal{M}(x,t) = EI(x)\, v''(x,t) = EI(x)\, \psi''(x)\, z(t) \tag{1.34}$$

where EI is the bending stiffness of the beam. Thus in the linear elastic case, after substituting Equation (1.34) into Equation (1.31), the resistance function simplifies to

$$\tilde{f}_i = \tilde{k}\, z \tag{1.35}$$

where the equivalent SDOF stiffness $\tilde{k}$ is

$$\tilde{k} = \int_0^L EI\, (\psi'')^2 \, \mathrm{d}x \tag{1.36}$$

In this case Equation (1.26) becomes

$$\tilde{M}\ddot{z} + \tilde{k}z = \tilde{f} \tag{1.37}$$

a second order linear differential equation with constant coefficients, which is the basic equation for undamped, forced vibration. If the pressure, column mass, and stiffness do not vary over the length, Equations (1.27), (1.36), and (1.29) simplify to

$$\tilde{M} = m \int_0^L \psi^2 \, \mathrm{d}x \tag{1.38}$$

$$\tilde{k} = EI \int_0^L (\psi'')^2 \, \mathrm{d}x \tag{1.39}$$

$$\tilde{f} = w \int_0^L \psi \, \mathrm{d}x \tag{1.40}$$

respectively, which involve integrating only the shape function. These are often written as

$$\tilde{M} = C_m\, m\, L \tag{1.41}$$

$$\tilde{k} = C_k \frac{EI}{L^3} \tag{1.42}$$

$$\tilde{f} = C_f\, w\, L \tag{1.43}$$

Table 1.3: Coefficients for Equivalent SDOF Analysis

Boundary	C_m	C_k	C_f
Pinned Ends	$\frac{3968}{7875} = 0.5039$	$\frac{6144}{125} = 49.15$	$\frac{16}{25} = 0.6400$
Fixed Ends	$\frac{128}{315} = 0.4063$	$\frac{1024}{5} = 204.8$	$\frac{8}{15} = 0.5333$

where

$$C_m = \frac{1}{L}\int_0^L \psi^2 \,\mathrm{d}x \tag{1.44}$$

$$C_k = L^3 \int_0^L \left(\psi''\right)^2 \,\mathrm{d}x \tag{1.45}$$

$$C_f = \frac{1}{L}\int_0^L \psi \,\mathrm{d}x \tag{1.46}$$

The shape function is often defined as the deflected shape of an elastic beam under uniform static loading:

$$\psi_{ff} = \frac{16x(L^3 - 2xL^2 + x^3)}{5L^4} \tag{1.47}$$

for a column with fixed ends and

$$\psi_{pp} = \frac{16x^2(L-x)^2}{L^4} \tag{1.48}$$

for a column with pinned ends. Strictly for convenience these equations have been normalized so that the maximum deflection is equal to unity. With the shape function explicitly defined, the coefficients C_m, C_k, and C_f can be calculated. These are tabulated for each set of boundary conditions in Table 1.3.

Solution

Finding a solution consists primarily in solving for the time-dependent quantity $z(t)$ in Equation (1.26) and using it to find the displacement $v(x,t)$ with Equation (1.22). Internal forces can be obtained in the linear elastic case by analyzing the column statically under the equivalent distributed load [9]

$$w_s(x,t) = \left(\frac{\tilde{k}}{\tilde{M}}\right) m(x)\,\psi(x)\,z(t) \tag{1.49}$$

Because the applied force is arbitrary, no general closed form solutions exist and $z(t)$ is typically obtained by numerical methods. Some analytical results exist for special and limiting cases such as linear-elastic structures with very long or very short periods relative to the load duration, as well as linear-elastic structures subject to idealized load descriptions. The structural period $T_n = 2\pi\sqrt{\tilde{M}/\tilde{k}}$ is found while solving the homogenous form of Equation (1.37).

If the blast pulse duration t_d is much longer than the natural period of the system, then the maximum response is reached well before the load diminishes. This regime is called *quasi-static*, which is somewhat of a misnomer. It is named quasi-static because if the load were applied smoothly and gradually so as to reach the maximum at time t_d then the dynamic effects would be negligible. However, if a force is applied suddenly and then maintained, the peak deflection is equal to twice the peak static deflection,

$$v_{\max} = 2\, v_{s,\max} \tag{1.50}$$

where the static deflection

$$v_s = \psi \frac{\tilde{f}}{\tilde{k}} \tag{1.51}$$

is the deflection that would be attained if the load were applied slowly. In practice this condition can be used with negligible error for any suddenly-applied pulse shape when $t_d \gtrsim 10\, T_n$; for a square pulse, the result is exact as long as $t_d > T_n/2$. Very stiff structures and faraway blasts with long durations fall in this regime.

At the other extreme, if $t_d << T_n$ then the maximum response is reached well after the load diminishes. This regime is called *impulsive*; only the impulse, not the pulse shape, is important. The maximum response is approximated by

$$v_{\max} = \pi \left(\frac{t_d}{T_n} \right) v_{s,\max} \tag{1.52}$$

with very good accuracy as long as $t_d/T_n \lesssim 1/4$. This approximation represents an upper bound to the actual response. Charges close to the target having short durations and flexible structures fall in this regime, as do many of the blast scenarios discussed in later chapters. That the pulse shape is not of primary importance

in the impulsive regime is of utmost importance to later developments of the Explosive Loading Laboratory.

In between these two extremes is the *dynamic* regime, where no such simplifications are possible and the response is calculated by explicitly solving the governing differential equation. Often, the blast pulse with measured peak pressure p and maximum impulse i is represented by an idealized triangular pulse of fictitious duration $2 \cdot i/p$. The literature contains analytical results for idealized pulse shapes such as this one [7, 9, 10, 51].

1.A.4 Advanced Analysis Methods

The SDOF method just presented is used in design practice because it is relatively simple and quick. It does lack accuracy, especially for members with significant inelastic action and those dominated by shear. To achieve greater detail, more advanced analysis methods must be used. An intermediate method is an SDOF solution of the differential equation using a Timoshenko beam formulation to more accurately account for shear deformation (Krauthammer et al. [29, 30]). The idea is promising but has not been widely used. Beyond this are advanced finite element codes.

Advanced finite element calculations of blast response can be very expensive, sometimes requiring supercomputers to complete the analyses in a reasonable time. Two approaches to advanced analysis are taken. One is a single step approach that computes the phenomena from the time of detonation through the end of structural response. It explicitly accounts for the interaction between the structure and the shock front. The other approach uses a finite element discrimination to solve the structural response and a different analysis to determine the loading on the structure (see for example Crawford et al. [13]). Interaction effects cannot be accounted for by this second approach. The blast effects can be calculated by a dedicated program such as BlastX [52] or by a general purpose finite element program. Popular finite element programs in the field include LS-DYNA [32] and

ABAQUS [1].

In the analysis of reinforced concrete structures, selection of the material model is the most critical step. Plasticity-based models are the most widely used. They can be quite effective, especially for confined concrete, which only develops small cracks and behaves as a continuum throughout the entire range of behavior. Plasticity models define a convex hypersurface in stress-strain space. This hypersurface is called the *yield surface*. If the stress state lies inside the yield surface the material is in the elastic regime. If the stress state lies on the yield surface it is in the plastic regime; the stress state is not allowed to fall outside the yield surface. The plastic regime is defined either by *associated flow* if the plastic strain rate is proportional to the gradient of the yield surface, or by *non-associated flow* if the plastic strain rate is proportional to the gradient of a different hypersurface (usually related in some way to the yield surface). The yield surface may evolve in time in a combination of *isotropic hardening* (a symmetric expansion of the yield surface) and *kinematic hardening* (a rigid shift of the yield surface). Typically the rate of hardening is controlled by the accumulation of a damage parameter, e.g., accumulated plastic strain. Yield surfaces are generally visualized in three-dimensional principal stress space. When viewed in this way the yield surface is (barring kinematic hardening) symmetric about the *hydrostat*, the axis of hydrostatic pressure. A planar cut normal to the hydrostat reveals *cross-sections* of the yield surface and a planar cut parallel to and including the hydrostat reveals *meridians* of the yield surface.[6]

Adequate plasticity models for concrete have yield surfaces with rounded triangular cross sections and curved meridians. The meridians are closed in tension and are usually open at the compression end. Abrupt corners in the yield surface are best avoided for numerical reasons. To agree with test data, a yield surface must be a function of three or more stress invariants. Contemporary models define hardening and softening behavior and are based on non-associated flow in an

[6]For an in depth treatment of plasticity theory, consult Chen [8], Kleiber [27], and Ottosen and Ristinmaa [41].

attempt to properly model dilatancy, which is critically important in passively confined concrete because it determines the confining stress.

Even with detailed plasticity models, modelling of unconfined concrete is still approximate. At late stages of damage a concrete specimen opens large macrocracks resulting in considerable softening. Not only do the cracks violate the continuum assumption inherent in plasticity theory, but the softening it engenders is numerically tedious. In addition, strictly speaking, softening is not a real material property so much as crack-induced structural changes that are lumped into material behavior [45]. Even so, plasticity models can be used to obtain realistic results for unconfined concrete structures, but careful attention to detail is advised when using them to avoid physically meaningless results.

A promising material model currently under development by Karagozian & Case is coded for use with several finite element codes including LS-DYNA (material 072R3, v. 971 beta). Malvar et al. [35] discuss the latest implementation and the history of its development. Additional details are available from Malvar et al. [34]. The model uses the five-parameter model by Willam and Warnke [1975, cited in 8] for the cross sections and defines its own meridians for the yield, ultimate and residual states. These surfaces are enhanced based on strain rate. A variable degree of associativity, which controls rate of dilation, is included in the model. The law governing the degree of associativity is physically-motivated; it depends on a comparison between aggregate size and volumetric strain [4]. The latest version includes automatic generation of seventy-two input parameters based solely on the concrete strength in compression for common concrete mixes.

1.B Fundamentals Related to Simulated Blast

The Explosive Loading Laboratory simulates blast effects by transferring momentum and energy during an inelastic collision between impacting masses and the specimen. On the front of these impacting masses is a polymer layer called

a *programmer* that is used to modulate the shape of the force acting during the collision. Polymers are known to be well modelled by viscoelastic material models. Thus, in the interest of later developments, relevant topics in both viscoelastic theory and collisions are presented here. While the discussion of viscoelastic theory serves as an inspiration for the programmer model developed in Chapter 4, it is most relevant to the ideas proposed in Chapter 5.

1.B.1 Viscoelastic Theory

A viscoelastic material is one with characteristics of both a viscous fluid and an elastic solid. It has time dependent behavior with the stress σ depending not only on the strain ε but also on the strain rate $\dot{\varepsilon}$. A viscoelastic material can be represented by any arrangement of springs and dashpots in what is called a *rheological* model. Any such combination of springs and dashpots can be represented mathematically by a linear combination of stress, strain, and their derivatives. In the springs the stress is proportional to the strain

$$\sigma_s = E\,\varepsilon_s \tag{1.53}$$

and in the dashpots the stress is proportional to the strain rate

$$\sigma_d = \eta\,\dot{\varepsilon}_d \tag{1.54}$$

where the subscripts s and d refer to the spring and dashpot, respectively, E is the spring constant with units of pressure and η the viscous constant with units of pressure multiplied by time.[7] It should be kept in mind that some materials may be best described with nonlinear springs and variable viscous constant, e.g., shear thinning materials whose viscous constant decreases at higher strain rates.

Viscoelastic materials exhibit behavior such as relaxation, creep and hysteresis. Relaxation is a reduction in stress during a period of constant strain. Creep

[7]Fundamentals of viscoelasticity not discussed in this section can be found in Ottosen and Ristinmaa [41].

is an increase in strain during a period of constant stress. Hysteresis is observed in stress-strain space when the loading path is different from the unloading path. The area between these two paths represents energy dissipated by the viscous elements.

Two basic rheological models are presented to illustrate relevant features of viscoelastic models and their governing equations: the Maxwell model, which consists in a spring connected to a dashpot in series, and the Kelvin-Voigt model, which consists in a spring connected to a dashpot in parallel. After this is discussed the standard solid model, a model useful for representing many solid materials. For each model the governing differential equation is derived and solved under a constant strain rate $\dot{\varepsilon}_o$, a result that is useful in numerical implementations. Each model is then subjected to a loading-relaxation cycle: first a loading ramp of duration t_r and strain rate $\dot{\varepsilon}_o$ is applied, and then the strain attained at the end of loading ($\dot{\varepsilon}_o\, t_r$) is held indefinitely. The results are plotted and compared to elucidate the behavior of each model.

Maxwell Model

In the Maxwell model, equilibrium requires that the stress in the spring and the dashpot be equal

$$\sigma = E\,\varepsilon_s = \eta\,\dot{\varepsilon}_d \tag{1.55}$$

while compatibility requires that the global strain be the sum of the strains in each element

$$\varepsilon = \varepsilon_s + \varepsilon_d \tag{1.56}$$

where the subscripts s and d denote the spring and the dashpot, respectively. Differentiating Equation (1.56) and substituting into it Equation (1.55) determines the governing differential equation for the Maxwell model:

$$\dot{\varepsilon} = \frac{\dot{\sigma}}{E} + \frac{\sigma}{\eta} \tag{1.57}$$

This is solved for a constant strain rate $\dot{\varepsilon}_o$ to obtain

$$\sigma = \dot{\varepsilon}_o\eta + (\sigma(0) - \dot{\varepsilon}_o\eta)\,\mathrm{e}^{\left(-\frac{E\,t}{\eta}\right)} \tag{1.58}$$

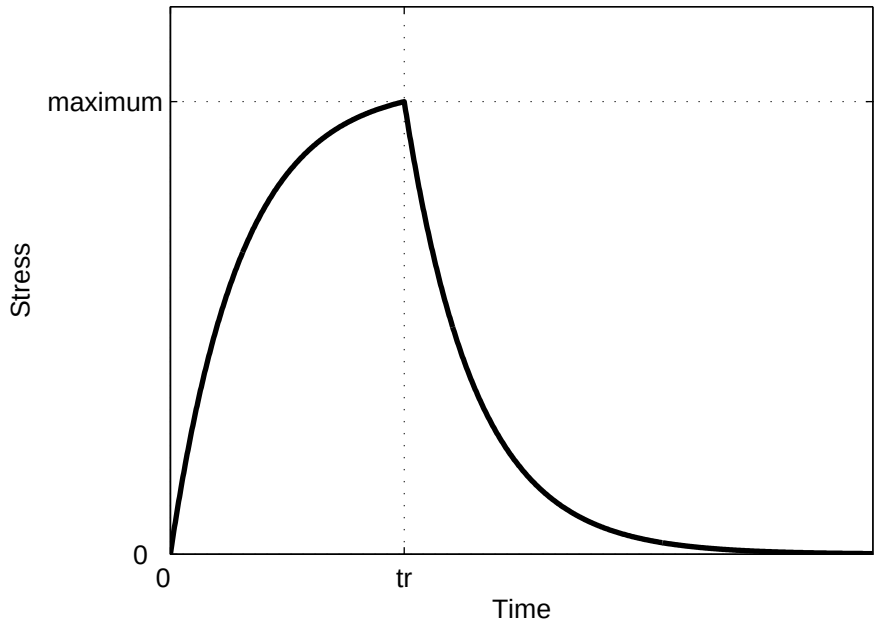

Figure 1.10: Maxwell Model Under Constant Rate Loading and Relaxation

This result can be used for relaxation by setting $\dot{\varepsilon}_o = 0$.

When a Maxwell material is loaded under a constant strain rate and then allowed to relax, it behaves as shown in Figure 1.10. The stress rate is initially $E\,\dot{\varepsilon}_o$ and it decays asymptotically to zero. The maximum stress, at most $\dot{\varepsilon}_o\eta$, is obtained at the end of loading. During relaxation, the stress drops asymptotically to zero.

Kelvin-Voigt Model

For the Kelvin-Voigt model the stress is the sum of the stresses in the spring and the dashpot, which directly yields the governing equation

$$\sigma = E\,\varepsilon_s + \eta\,\varepsilon_d \tag{1.59}$$

Under constant strain rate loading the stress is

$$\sigma = E\,(\varepsilon(0) + \dot{\varepsilon}_o\,t) + \eta\,\dot{\varepsilon}_o \tag{1.60}$$

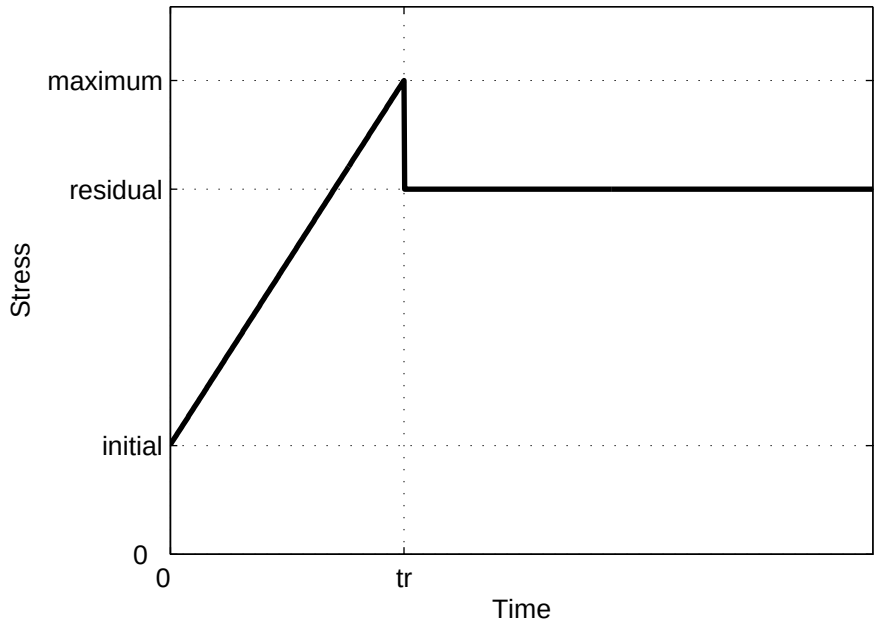

Figure 1.11: Kelvin-Voigt Model Under Constant Rate Loading and Relaxation

When a Kelvin-Voigt material is loaded under constant strain rate and then allowed to relax, it behaves as shown in Figure 1.11. The dashpot causes the initial stress to jump abruptly to $\dot{\varepsilon}_o\,\eta$. Stress increases at a constant rate $E\dot{\varepsilon}_o$. When loading ends, the force in the dashpot vanishes and the residual stress $E\,\dot{\varepsilon}_o\,t_r$ is determined solely by the strain accumulated in the spring.

Standard Solid Model

A more complicated model that behaves like many solid materials is the standard solid model, which has a lone spring connected in parallel with a Maxwell element.The governing differential equation is

$$\dot{\sigma} + \frac{E_1}{\eta}\,\sigma = (E_1 + E_2)\,\dot{\varepsilon} + \frac{E_1\,E_2}{\eta}\,\varepsilon \tag{1.61}$$

where E_1 is the spring modulus in the Maxwell element and E_2 is the spring modulus for the lone spring (derivation in Appendix A). Its behavior under constant

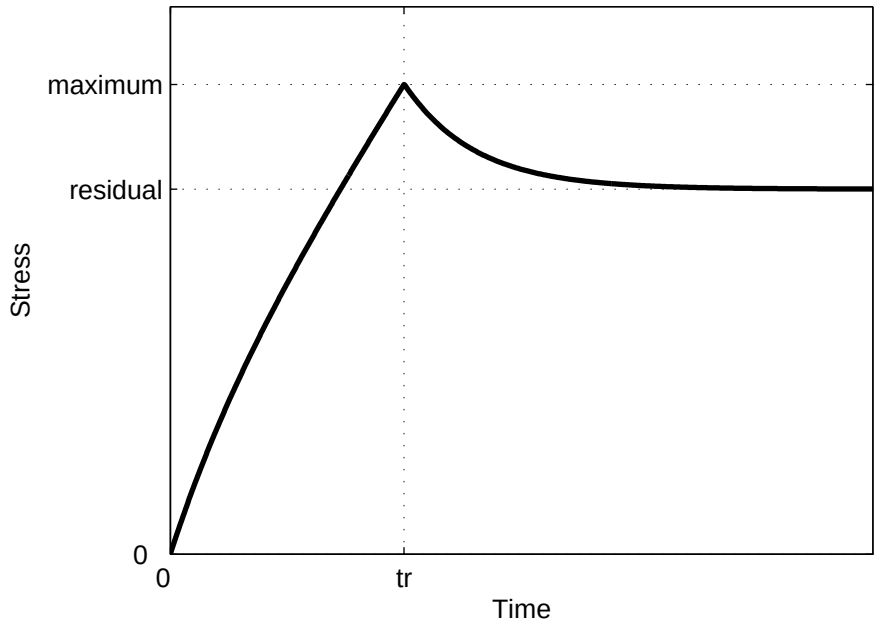

Figure 1.12: Standard Solid Model Under Constant Rate Loading and Relaxation

loading is like that of a Maxwell element (Equation (1.58)) with the addition of a spring term

$$\sigma = \dot{\varepsilon}_o \eta + (\sigma(0) - \dot{\varepsilon}_o \eta)\, \mathrm{e}^{\left(-\frac{E_1\, t}{\eta}\right)} + E_2\, (\varepsilon(0) + \dot{\varepsilon}_o\, t) \tag{1.62}$$

Under a loading-relaxation cycle the behavior displays the exponential decay of the Maxwell model and the residual stress of the Kelvin-Voigt model (Figure 1.12). The stress rate is initially $(E_1 + E_2)\, \dot{\varepsilon}_o$ and decays asymptotically to $E_2 \dot{\varepsilon}_o$. The maximum stress is attained at the end of loading, and the residual stress of $E_2 \dot{\varepsilon}_o\, t_r$ is reached asymptotically during relaxation.

1.B.2 One-Dimensional Collisions

A well-known application of Newtonian mechanics is to the inelastic collision of two masses travelling along a common linear path. A mass M_1 travels at initial velocity v_{1i} and approaches a mass M_2, which is travelling at an initial velocity $\mathsf{v}_{2i} < \mathsf{v}_{1i}$. After the collision, the masses are travelling at their final veloci-

ties, v_{1f} and v_{2f}, and $\mathsf{v}_{1f} \leq \mathsf{v}_{2f}$. During the collision of the two masses, momentum is conserved:

$$M_1\,\mathsf{v}_{1i} + M_2\,\mathsf{v}_{2i} = M_1\,\mathsf{v}_{1f} + M_2\,\mathsf{v}_{2f} \tag{1.63}$$

The material interaction between the two masses is described by an experimentally-determined parameter called the coefficient of restitution (COR) that relates the approach and separation velocities. The COR is defined as

$$c_r = \frac{\mathsf{v}_{2f} - \mathsf{v}_{1f}}{\mathsf{v}_{1i} - \mathsf{v}_{2i}} \tag{1.64}$$

It is equal to zero for a purely plastic collision and unity for an elastic collision. Solving Equations (1.63) and (1.64) simultaneously yields the solution for the final velocities:

$$\mathsf{v}_{1f} = \frac{\mathsf{v}_{1i}\,(M_1 - c_r\,M_2) + \mathsf{v}_{2i}\,M_2(1 + c_r)}{M_1 + M_2} \tag{1.65}$$

$$\mathsf{v}_{2f} = \frac{\mathsf{v}_{1i}\,M_1(1 + c_r) + \mathsf{v}_{2i}\,(M_2 - c_r\,M_1)}{M_1 + M_2} \tag{1.66}$$

During the collision a force of magnitude f acts equally and oppositely on each mass. For each mass, Newton's second law states that

$$f(t) = \frac{\mathrm{d}(M\mathsf{v}(t))}{\mathrm{d}t} \tag{1.67}$$

where the subscripts 1 and 2 have been omitted for clarity. Assuming constant mass M and integrating Equation (1.67) over the duration of contact determines the impulse I:

$$I = \int_0^{t_d} f(t)\,\mathrm{d}t = M(\mathsf{v}_f - \mathsf{v}_i) \tag{1.68}$$

This yields two equivalent ways of conceptualizing impulse, either as the time integral of the applied force or as the change in momentum of a mass during the application of said force. These results are used in Chapter 4.

1.C Previous Experimental Work

Divine Buffalo (DB) is a series of field tests with real explosives conducted under the auspices of the Technical Support Working Group and the De-

fense Threat Reduction Agency. It has been ongoing for many years and among the components tested are hardening technologies for columns. The column tests were carried out in large part by Karagozian & Case and are discussed briefly by Morrill et al. [39] and in somewhat more detail by Crawford et al. [12]. Data are available in the BLast Information Systems database [43], but these data are unfortunately not publicly available.[8] The test specimens reported in Chapter 3 are of the same design as the 14 in (356 mm) square columns tested in the DB test series.

The DB column tests were conducted both on columns in a four-story building (1999) and on isolated columns loaded into a specially-designed test rig (2001). In total, results are reported on fifty-three specimens, forty in-building columns and thirteen isolated components. Incipient damage was observed to occur at scaled distances smaller than $2.0\,\mathrm{ft/lb^{1/3}}$ ($0.79\,\mathrm{m/kg^{1/3}}$). To compare to damage in these tests to damage in tests described in later chapters, only similar columns are considered: CFRP- and non-retrofitted, 14 in (356 mm) square columns loaded at a scaled distance of $2.0\ \mathrm{ft/lb^{1/3}}$ or less. This limits the data to seven specimens (Table 1.4): three as-built, one with two CFPR wraps, two with six CFRP wraps, and one pseudo-CSS column. The specimen designation is the test number followed by the column designation where applicable.

The in-building tests, which included DB06 and DB08, were conducted at the CTS-1 facility at the White Sands Missile Range in New Mexico. These tests were proof-of-concept tests whose principal value was to verify the efficacy of CFRP jackets as a retrofit strategy for blast loads. The specimens were instrumented with pressure gauges and accelerometers, but the data were noisy and instrument failure before the end of the test was frequent. Photographs of the target columns in each of these tests (Figures 1.13 and 1.14) show a dramatic difference in the response of the two columns: while the as-built specimen failed dramatically in shear at both the top and bottom and suffered 10.5 in (267 mm) of residual deflection, the

[8]The academic literature in explosive testing of structural components is severely limited due in large part to national security concerns.

Table 1.4: Divine Buffalo Test Matrix

Specimen Designation	Weight [lb (kg)]		R [ft (m)]	z [ft/lb$^{1/3}$ (m/kg$^{1/3}$)]	Retrofit
	Actual	TNT			
DB06-1A3	1005 (456)	1284 (582)	13 (3.96)	1.20 (0.48)	None
DB06-2A3	1005 (456)	1284 (582)	18.2 (5.55)	1.67 (0.66)	None
DB08-1A2	966 (438)	1236 (561)	13 (3.96)	1.21 (0.48)	Pseudo-CSS
DB08-2A2	966 (438)	1236 (561)	20 (6.10)	1.86 (0.74)	6 Wraps
DB20	1450 (658)	1189 (539)	13 (3.96)	1.23 (0.49)	None
DB21	1450 (658)	1189 (539)	13 (3.96)	1.23 (0.49)	6 Wraps
DB22	1450 (658)	1189 (539)	13 (3.96)	1.23 (0.49)	2 Wraps

retrofitted specimen showed only minor damage at the column ends and suffered less than 1 in (25 mm) of residual deflection.

Identically designed specimens were tested on column specimens in a specially-designed test rig at Kirtland Air Force Base, New Mexico. The columns were instrumented with accelerometers, potentiometers, pressure gauges and load cells on the reaction structure. As with the CTS-1 tests, the data are of limited use because of noise and instrument failure, but the importance of the tests was in verifying the effectiveness of the retrofits. The columns behaved similarly to the in-building columns: the as-built specimen failed dramatically in shear and suffered 4.3 in (109 mm) of residual deflection, the two-wrap specimen failed at the bottom end and suffered 3.5 in (89 mm) of residual deflection, and the six-wrap specimen sustained minor damage and 1.75 in (44 mm) of residual deflection. All results are summarized in Table 1.5. The composite wrapped specimens showed surface pitting from ANFO fragments indicating the need to protect the jacket against debris. The maximum residual deflection reported typically occurs near midspan but sometimes occurs near the bottom end.

In conjunction with the DB component tests, quasi-static pushover tests

Figure 1.13: As-Built Specimen Post-Test (DB 6) [43]

Figure 1.14: Pseudo-CSS Specimen Post-Test (DB 8) [43]

Table 1.5: Divine Buffalo Test Results

Specimen	Res. Defl. [in (mm)]	Damage Summary
DB06-1A3	10.5 (267)	Major shear failure at both ends
DB06-2A3	0	Minor shear cracks at both ends
DB08-1A2	< 1 (25)	Minor jacket rupture at top and bottom
DB08-2A2	0	No damage
DB20	4.3 (109)	Major shear failure at both ends
DB21	1.75 (44)	Minor flexural damage
DB22	3.5 (89)	Major jacket rupture at bottom

were conducted by Hegemier et al. at UCSD [20, 22]. These tests were used to validate FRP retrofit options and to develop resistance functions. The results from the quasi-static tests are compare well to the DB results (see Crawford et al. [12], who did not cite the original work). The specimens tested and hardware used in the tests described in Chapter 3 were adapted from these quasi-static tests.

1.D Chapter Summary

The first chapter motivates the research by providing a conceptual framework in which to understand the results. There have been a number of attacks against United States installations at home and abroad. Included in the response to these attacks are defensive technologies to mitigate the damaging effects of such bomb attacks on buildings. To meet this need by experimentally testing promising designs, the Explosive Loading Laboratory, headed by principal investigators G. Hegemier and F. Seible, enables investigators to experimentally simulate blast loading on structural specimens at a lower cost and with better data than tests using real explosives.

The bulk of the first chapter discusses fundamentals related to later developments: blast loading on buildings, analysis methods including the single degree

of freedom method, viscoelastic theory, theory of collisions, and relevant experimental work. The equivalent single degree of freedom method and the discussion on collisions figure prominently in the new methods developed in Chapters 3 and 4. Previous field experiments are mentioned for comparison to the results described in Chapter 3. Other sections provide a sound technical background to developments throughout the dissertation.

2 Development of the Explosive Loading Laboratory

The Explosive Loading Laboratory is designed to simulate with a high degree of control and accuracy the impulse delivered by an actual blast to a structure and to measure the structural response to the simulated blast load. It is the first of its type in the world and testing at this facility promises to be more repeatable, controllable, affordable, safer, and quicker than testing with actual explosives. It allows investigators to see for the first time ever, the behavior that has heretofore been obscured by the fireball produced by the explosive charge. The data produced will assist in validating computational codes and hardening technologies. The Explosive Loading Laboratory is headed by professors G. Hegemier and F. Seible and is located in the Englekirk Center at the Elliot Field Station, 13 km from the main UCSD campus. The Englekirk Center is part of the Charles Lee Powell Structural Research Laboratories.

Simulated blast loads are produced by an array of *blast generators* (BGs). Each BG consists of an *impacting module* and a hydraulic actuator to accelerate it towards the specimen. The resulting collision between the impacting modules and the specimen imparts a controlled, blast-like impulse to the specimen. The impacting module consists in a mass attached to a textured polymer layer that has been termed the *programmer* and allows the investigator to control the force time history to which the specimen is subjected. The first generation of blast simulation hardware consists in four blast generators with two interchangeable

sets of impacting modules: one for column tests and the other for wall tests. To put the capacity of the BGs into perspective, the four impacting masses together weigh as much as a mid-size vehicle, and they can impact the specimen at highway speeds of up to 100 km/h.

The specimen and blast generators react against a self-equilibrating reaction structure that consists in a strong floor and two strong walls, all of which are highly post-tensioned. To prevent transmission of shock to the surrounding area, this reaction structure rests on rubber isolation bearings. There is a gap between the foundation and the superstructure to allow for movement and the test table is locked off when a test is not in progress. A secondary, non-isolated test floor provides a test area for supplementary testing. The facility was completed in March, 2005.

2.A Design

I was the chief designer for the main reaction structure working under engineer of record F. Seible. J. Restrepo and G. Hegemier served as technical advisors. C.S. Lee assisted with the process, especially with the development of design drawings. The rubber isolation bearings were detailed and fabricated by Seismic Energy Products of Alameda, California according to my design specifications. The blast generators were detailed and fabricated by MTS Systems Corporation of Eden Prairie, Minnesota according to performance specifications developed by the Explosive Loading Laboratory design team. This section details the design considerations for the foundation, superstructure, and BG components. These components are shown schematically in Figure 2.1. Items in this figure related to the test setup will be discussed in the following chapter.

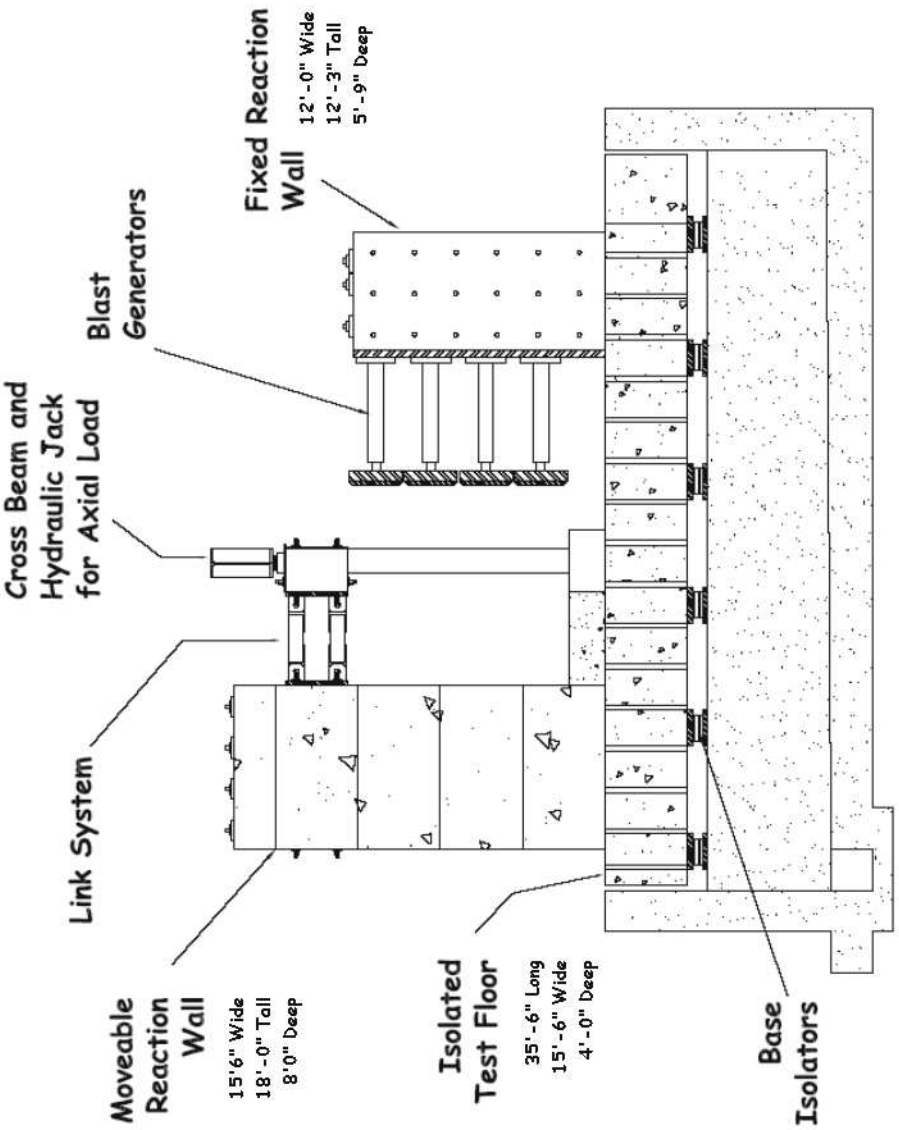

Figure 2.1: Overview of Explosive Loading Laboratory Facility with Test Setup

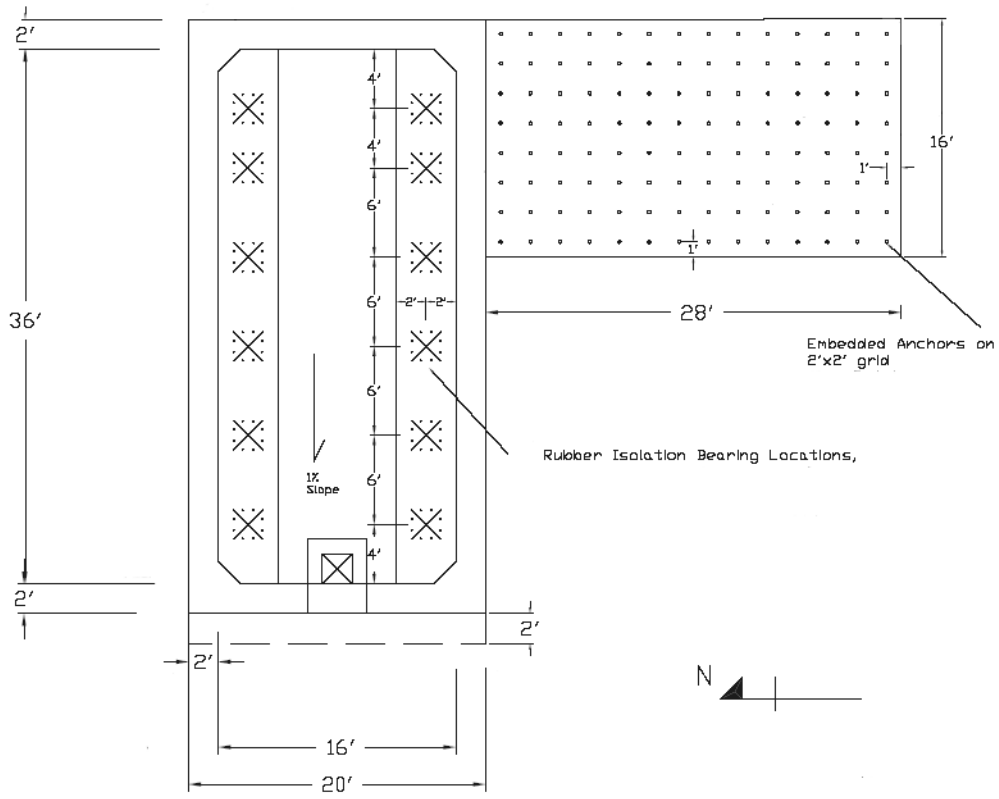

Figure 2.2: Foundation Plan

2.A.1 Foundation

The foundation supports the superstructure and provides access beneath the isolated slab. The foundation is shown in various figures; Figure 2.2 shows a plan view of the foundation along with the secondary slab (described later); Figure 2.3 is a longitudinal cut through the foundation at the sump (west end); and Figure 2.1 is a transverse cut that shows the superstructure in addition to the foundation.

The foundation was designed according to standard Load and Resistance Factor Design methods. Its main components are a mat slab, perimeter walls, isolator pedestals, rubber isolators, and a post-tensioned rim. The material specifications are: $f_c^{'} = 5000$ psi (34.5 MPa) for concrete, ASTM A615 grade 60 (420)

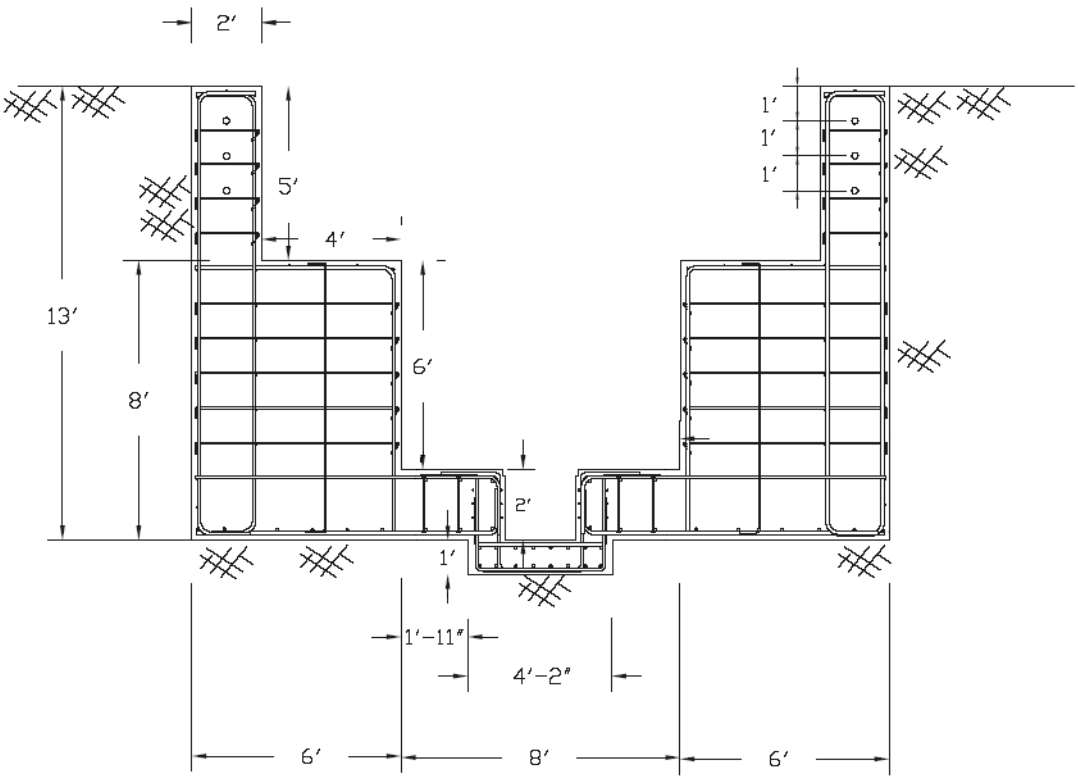

Figure 2.3: Foundation Longitudinal Section

rebar, and ASTM A416 grade 270 (1860) post-tensioning tendons [3, v. 01.04]. Clear cover is 3 in (76 mm) where exposed to earth and 2 in (51 mm) elsewhere.

The perimeter walls and isolator pedestals rest on a 20'-0" (6.10 m) × 40'-0" (12.19 m) × 2'-0" (610 mm) mat foundation reinforced with a top and bottom layer of reinforcement; each has #9 bars at 12 in (305 mm) on center (o.c.) in the longitudinal direction and at 6 in (152 mm) o.c. in the transverse direction. Additional #5 headed bars are placed in the through-thickness direction at 12 in (305 mm) o.c. in both directions. Actual slab thickness varies from 2'-0" (610 mm) to 2'-4" (711 mm) because it is sloped at 1% for drainage from east to west. The top of the slab is 11'-0" (3.35 m) below grade at its lowest point. A drainage sump is built into the slab at the west end.

Resting on the slab are 2'-0" (610 mm) thick walls around its entire perimeter. These function both as retaining walls and as shear walls to withstand seismic loads from the superstructure. The walls are designed with boundary elements containing twelve evenly spaced #9 longitudinal bars and two interior #4 headed ties in each direction in addition to the rest of the horizontal steel described next. Outside the boundary elements the wall is reinforced vertically with #9 bars at 12 in (305 mm) o.c. and horizontally with #6 bars at 12 in (305 mm) o.c. #3 ties are placed in the through-thickness direction at 12 in (305 mm) o.c. in both directions. The vertical bars are terminated in standard ninety degree bends in a special detail suggested by J. Restrepo; the transverse walls extend 2'-0" (610 mm) beyond the bottom of the slab providing additional anchorage length for the reinforcement. The west end of the slab uses the same detail but it was not possible to use it at the east end due to conflict with the pump house design.

The top of the walls are specially detailed to provide a continuous load path for lateral seismic loads. During seismic loading, the isolated slab can only make contact with the walls at one or two of the four corners at a time. A 45 in (1143 mm) × 25 in (635 mm) × 1 in (25.4 mm) galvanized steel plate is cast into

the wall corners at 45 degrees from either wall to provide a contact surface. When the facility is not used for testing, the slab is locked off to the foundation by hydraulic jacks bearing on these steel plates. The concentrated compressive forces on the plates cause tensile reactions that are counteracted with post-tensioning. Two tendons with seven 0.6 in (15.2 mm) diameter strands are used in the transverse direction and stressed to 308 kips (1370 kN) after seating. The longitudinal direction has three tendons with five 0.6 in (15.2 mm) diameter strands and stressed to 185 kips (823 kN) after seating. All tendons are grouted after stressing. The specified anchorage system, the Multistrand Anchorage System by Dywidag-Systems International (DSI), is manufactured with local zone reinforcement. General zone reinforcement is twelve #4 headed bars through the thickness of the wall arranged four bars at 12 in (305 mm) o.c. vertically by three bars at 6 in (152 mm) o.c. horizontally.

The isolators rest on pedestals that in turn rest on the top of the mat slab and extend from the longitudinal walls. The top of the pedestals are 5'-0" (1.52 m) below grade and they extend 4'-0" (1.22 m) from the inner edge of the perimeter walls. This leaves a corridor 8'-0" (2.44 m) wide × 7'-0" (2.13 m) tall (at its tallest) for laboratory staff to access the tie-down holes from underneath the slab. The pedestal is reinforced with a continuous bent #9 bar at 12 in (305 mm) o.c. along its inner edge and top. An additional vertical #5 bar runs along the center of the pedestal at 12 in (305 mm) o.c. Horizontal #6 bars at 12 in (305 mm) o.c. along the side and top of the pedestal. The through thickness wall steel specified above continues all the way to the inner edge of the pedestal. Anchor bolts for the isolators were cast into the pedestal, but the detail was changed during construction and these were removed and replaced with other anchors that were secured to the foundation with epoxy.

Seismic Energy Products (SEP) was provided two sets of factored vertical load and lateral deflection combinations to design the isolators; a force of 300 kips (1334 kN) at zero deflection and a force of 150 kips (667 kN) at 3 in (76 mm)

of deflection. The first set applies to when the table is locked off. It represents the worst case between large live loads during test setup and seismic overturning (seismic governs). The second set represents the testing scenario, during which testing equipment remains on the table, but due to testing-induced motion, the table might move up to three inches laterally. A minimum stiffness was provided to ensure that the BGs would not move the test table more than three inches, but this requirement did not drive the design.

The bearing delivered by SEP is 16 in (406 mm) in diameter and 8.020 in (203.7 mm) in height. The base plate is ASTM A36 steel [3, v. 01.04] and measures 27 in (686 mm) × 18 in (457 mm) × 1.5 in (38.1 mm). The top plate is ASTM A36 steel and measures 20 in (508 mm) × 20 in (508 mm) × 1 in (25 mm). It is oriented at 45° from the base plate and matches the alignment of a mating plate in the isolated slab. The rubber has a 59 duro A hardness (by ASTM D2240 [3, v. 09.01]), a tensile strength of 4028 psi (27.77 MPa), and an ultimate elongation of 630% (both by ASTM D412 [3, v. 09.01]). Each bearing was tested at the factory in Athens, Texas prior to shipment. The bearings were each loaded 450 kips (2002 kN) at zero deflection for five minutes and in a separate test were loaded to 150 kips (667 kN) and loaded cyclically to ± 3 in (76 mm). The measured lateral stiffness ranged from 5.7 (1.00) to 7.4 kips/in (1.30 kN/mm) and averaged 6.6 kips/in (1.16 kN/mm). "Each bearing was inspected for lack of rubber to steel bond, laminate placement faults and surface cracks wider and deeper than 0.08 [in (2.0 mm)]; no signs of such defects were observed" [50].

2.A.2 Reaction Structure

The main reaction structure is designed to have sufficient post-tensioning to develop no tension at all during testing. The inelastic behavior is ductile and the slab is stronger than the walls. There is a high uncertainty in design loads because of uncertainty in the types of testing that might take place throughout the lifetime of the facility; the facility is envisioned primarily for blast simulation tests, but

it is also intended for static tests, especially as residual capacity test of elements subjected to simulated blast. A slab depth of 4 ft (1219 mm) and post-tensioning stress of 1000 psi (6.89 MPa) were selected and capacity was then maximized subject to these constraints. Because the loading can be bidirectional, the slab design is equal in positive and negative bending. Specified material properties are self-compacting concrete with $f'_c = 5500$ psi (37.9 MPa), ASTM A615 grade 60 (420) mild steel and ASTM A722 Type II post-tensioning bars with a minimum ultimate tensile strength of 150 ksi (1035 MPa) [3, v. 01.04]. Clear cover is 2 in (51 mm) throughout. L. Bogdan from DSI provided recommendations for the post-tensioning system.

Isolated Slab

The slab is 35'-6" (10.8 m) × 15'-6" (4.72 m) in plan (Figure 2.4) and 4'-0" (1219 mm) thick. The length and width are such that a 3 in (76 mm) gap exists between the slab and the foundation walls. In the longitudinal direction (Figure 2.5) the slab is reinforced with twenty 2.5 in (64 mm) diameter grouted post-tensioning bars stressed to 462 kips (2055 kN) (after seating) and four layers (two top, two bottom) of sixteen #11 rebar. Three additional bars of the same size are located along each edge. Headed rebar is used to alleviate some of the congestion in the anchorage zone. No shear reinforcement is required in the slab. The post-tensioning force is transferred through a 13 in (330 mm) square × 2.5 in (64 mm) thick ASTM A36 bearing plate [3, v. 01.04]. The local anchorage zone is reinforced with a #5 spiral, 9 in (229 mm) in diameter, 24 in (610 mm) long, and at a 2 in (51 mm) pitch; while the general zone is reinforced by headed rebar in the transverse and through-thickness direction: four layers at 8 in (203 mm) o.c. each with sixteen #8 headed bars through the thickness and four #9 headed bars transversely.

The transverse reinforcement is all mild steel and consists in #9 headed bars at 8 in (203 mm) o.c. Galvanized steel pipe, 2.5 in (64 mm) in diameter, is

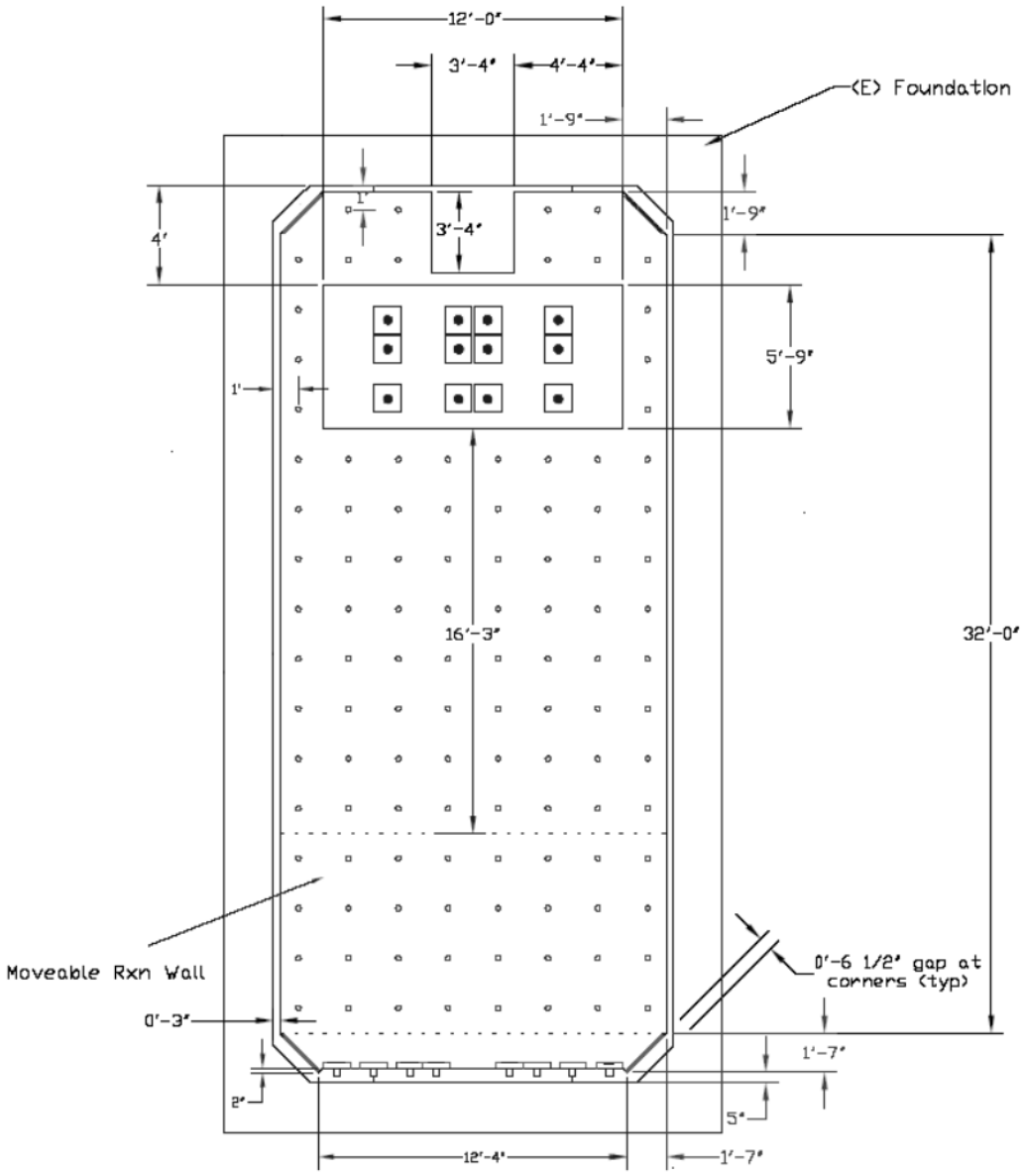

Figure 2.4: Isolated Slab Plan

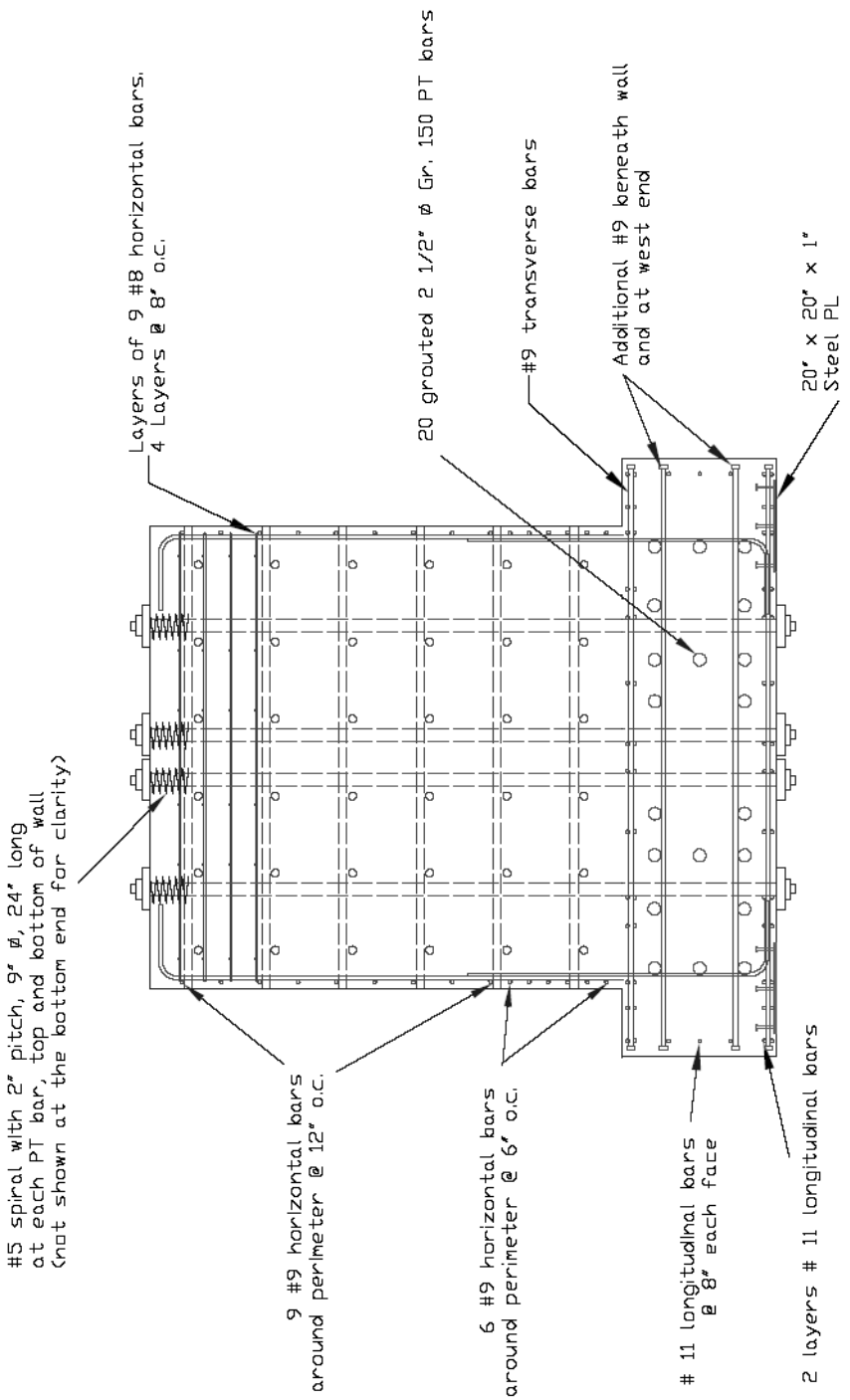

Figure 2.5: Isolated Slab Longitudinal Section at Fixed Wall

inserted through the thickness on a 2 ft (610 mm) × 2 ft (610 mm) grid to provide tie-down locations for testing hardware. Special details are designed at the four corners of the slab where the galvanized steel plates are located to match with the plates in the foundation and at the access opening at the east end of the slab. Starter bars and ducts are provided for the reinforcement in the fixed reaction wall. Steel plates with shear studs are embedded at the base of the slab to match the top plate of the isolators.

The nominal slab moment capacities in the longitudinal direction are 5244 ft·kip (7109 kN·m) at loss of compressive preload, 7763 ft·kip (10 525 kN·m) at first crack, and 30 127 ft·kip (40 846 kN·m) at ultimate. The moment-curvature behavior is ductile and is shown along with that of the two walls in Figure 2.6. The ultimate and post-peak capacity of the slab is greater than that of the walls, whose design is described next. Limits to loads during testing are determined by loss of preload, thus no force applied to a reaction wall may be allowed to cause more than 5244 ft·kip (7109 kN·m) of moment.

The shear is carried entirely by the concrete and because there is no steel shear reinforcement, the provisions of ACI 318 section 11.5.5 require that the factored shear demand be less than half the factored shear capacity of concrete. However, shear demand is very low because (1) lateral testing loads are self-reacting, thus causing no shear demand at all, and (2) the slab is supported all around by the isolators, thus drawing vertical loads directly to the support through compression struts without causing shear. Thus shear capacity is not a factor in determining the allowable loads during testing.

Fixed Reaction Wall

The fixed reaction wall will be used in two directions; the primary direction is in the longitudinal direction of the isolated slab and the other is perpendicular to that. The wall is 12'-0" (3.66 m) wide, 5'-9" (1.75 m) deep and 12'-3" (3.73 m) tall. It is reinforced with seventeen #9 bars on each of long faces and

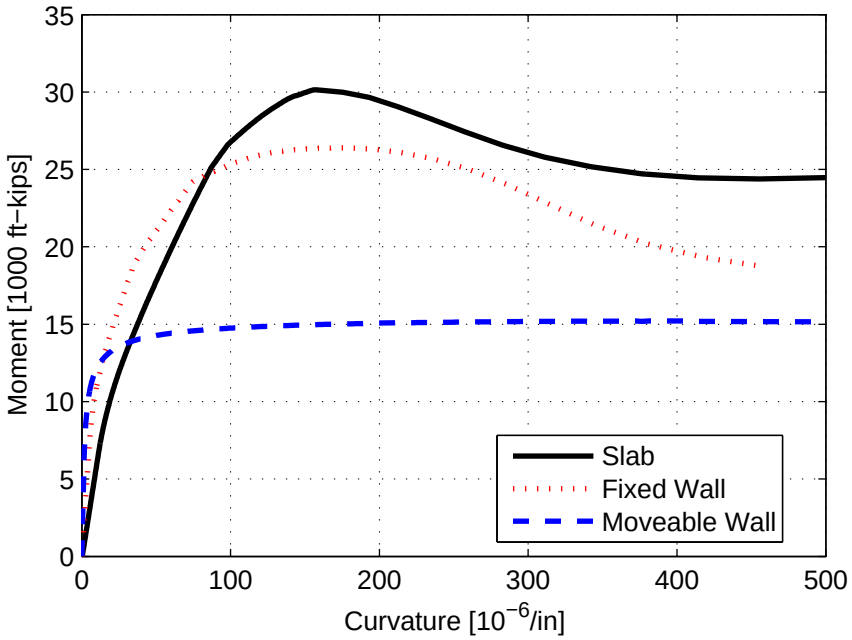

Figure 2.6: Moment-Curvature Behavior of Slab and Walls

eight #9 bars on each of the short faces (Figure 2.7). These bars are terminated with standard 90° bends at the top and bottom. There is a 4'-0" (1219 mm) lap splice in the vertical reinforcement at the base of the wall. The wall is reinforced horizontally on all sides with six # 9 bars at 6 in (152 mm) o.c. at the base, and nine #9 bars at 12 in (305 mm) o.c. along the rest of the height (Figure 2.5).

The wall is additionally reinforced in the vertical direction with twelve grouted, 2.5 in (64 mm) diameter post-tensioning bars stressed to 508 kips (2260 kN) after seating. The same 13 in (330 mm) square × 2.5 in (64 mm) thick ASTM A36 [3, v. 01.04] bearing plates are used as with the isolated slab. The local anchorage zone is reinforced with a 9 in (229 mm) diameter, 24 in (610 mm) long #5 spiral at a 2 in (51 mm) pitch at the top and bottom of each bar. The general zone at the top of the wall is reinforced (in addition to the horizontal reinforcement already described) with four layers of headed #8 reinforcement at 8 in (203 mm) o.c. Each layer has three bars in the long direction and six bars in the short direction.

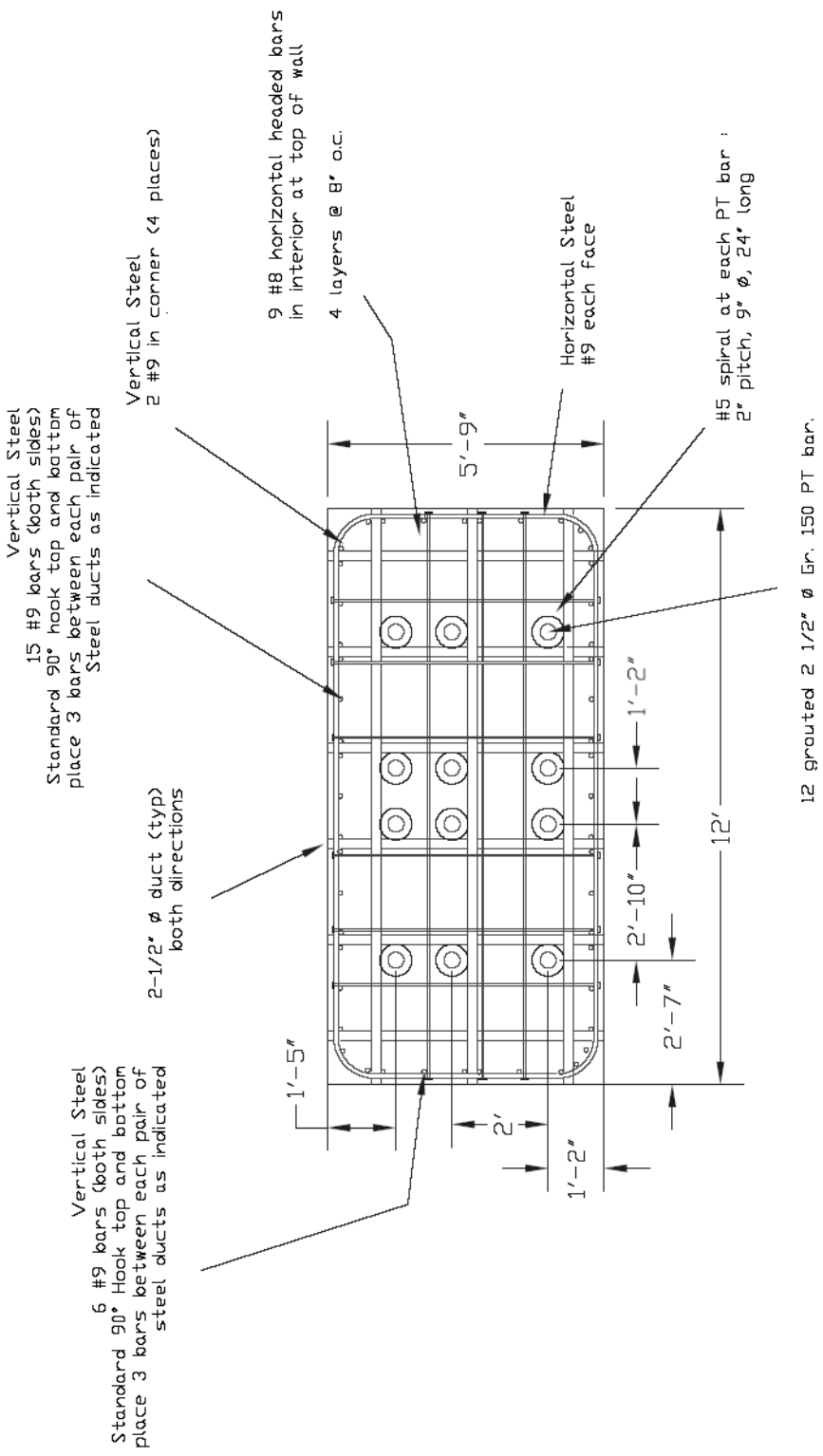

Figure 2.7: Fixed Wall Cross Section

The wall is fitted with 2.5 in (64 mm) diameter galvanized steel pipe in both directions to provide tie-down locations for lab hardware. The pipes in both directions are on a 2 ft (610 mm) × 2 ft (610 mm) grid. In the principal direction this grid starts 1'-0" (305 mm) above the slab, and in the other direction it starts 1'-3" (381 mm) above the slab.

The wall's moment capacities in the longitudinal direction are 4704 ft·kip (6378 kN·m) at loss of compressive preload, 8583 ft·kip (11 636 kN·m) at first crack and 26 394 ft·kip (35 785 kN·m) at ultimate. The moment-curvature behavior (Figure 2.6) is ductile. The wall's shear capacity is conservatively calculated at 1760 kips (7829 kN).

Moveable Reaction Wall

The moveable reaction wall is built as four separate blocks each 15'-6" (4.72 m) wide, 8'-0" (2.44 m) deep, and 4'-0" (1219 mm) tall. A bond breaker is used between each block to allow them to be moved and restacked elsewhere. The blocks have thirty-two tie ducts aligned with the ducts in the slab to accommodate ungrouted post tensioning rods. Twenty 1.75 in (44 mm) diameter rods post tensioned to 200 kips (890 kN) are used in the current configuration, but this can easily be changed in the future.

In plan, the block is reinforced with six layers of six #5 bars in each direction, and in elevation with #5 headed bars at 8 in (203 mm) o.c. evenly around the perimeter. A special top cap half as tall is reinforced in plan with three layers of reinforcement. Each layer has #5 bars around the perimeter and #8 bars elsewhere, seven in the longitudinal direction and three in the transverse direction. It is reinforced in elevation with #5 headed bars at 8 in (203 mm) o.c. evenly around the perimeter. Each tie duct is reinforced with an 8 in (203 mm) #5 spiral at a 2 in (51 mm) pitch.

The failure mechanism of the wall is different than usual because of the lack of bond between the blocks. The wall has a moment capacity of 5330 ft·kip

(7227 kN·m) at loss of compressive preload and an ultimate moment capacity of 15 186 ft·kip (20 589 kN·m). Moment-curvature plots are in Figure 2.6. Its shear capacity, based on frictional sliding, is 2400 kips (10 700 kN). Both the moment and shear capacities depend on the preload applied to the wall. Because the bars are ungrouted and the preload can be altered by lab staff, it must be verified prior to testing.

Secondary Strong Slab

The strong slab on grade is 28'-0" (8.53 m) long, 16'-0" (4.88 m) wide, and 3'-0" (914 mm) thick. It is reinforced in the longitudinal direction with three layers of #11 rebar at 12 in (305 mm) o.c. on both the top and bottom. Reinforcement in the transverse direction is a single #11 bar at 12 in (305 mm) o.c. At the edges of the slab, all bars terminate in a lap splice with a single U-bar with a 5'-0" (1524 mm) lap length. Threaded anchor points are located in the slab on a 2 ft (610 mm) × 2 ft (610 mm) grid aligned with the tie grid on the isolated slab and fixed wall. The secondary strong slab, built to provide an additional area for testing, is not used in these tests and is thus not discussed further.

2.A.3 Blast Generators

The blast generators (BGs) simulate the effect of airblast on a specimen. Their main parts are an actuator and an impacting module. The impacting module consists in a cuboid mass, in this case steel but it may be aluminum as well, attached to the programmer assembly, which is made up of the programmer proper bonded to a thin aluminum plate (Figure 2.8). There are four first-generation BGs. These can be assembled in any geometrical configuration and the impacting velocity can be set independently for each unit, thus allowing us to simulate a wide variety of blast scenarios.

The performance specifications for the blast generators were determined by the Explosive Loading Laboratory design team to ensure that the BGs could

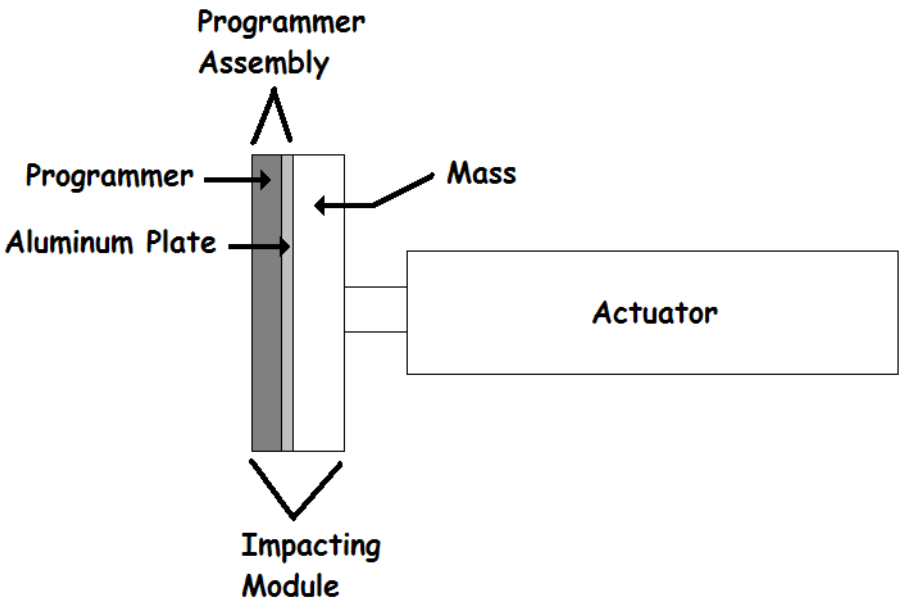

Figure 2.8: Blast Generator Components

produce sufficient impulse to damage a highly retrofitted column specimen and that the pressure time history would be similar to that of a real blast. The functional requirements were then developed in consultation with engineers from MTS [14]:

- Maximum Energy and Velocity: As per Table 2.1
- Repeatability of velocity: greater of 4% or 0.1 m/s
- Simultaneity of impact: $\pm$ 1 ms
- Pulse duration: 0.5 to 5 ms
- Maximum pressure on specimen face: 5000 psi (34.5 MPa)
- Soft initial stiffness to prevent overly-abrupt force initiation.

The quasi-static blast mitigation tests [20, 22] provide a point of physical comparison for the BG energy capacity. The force-deflection data from the six-wrap specimens determine that the specimen absorbed 210 kJ of mechanical

Table 2.1: BG Energy and Velocity Specification

Impacting Mass	Energy	Velocity
50 kg	30 kJ	34.6 m/s
100 kg	51 kJ	31.9 m/s
200 kg	76 kJ	27.6 m/s
400 kg	101 kJ	22.5 m/s

energy when pushed to a deflection far beyond what might be experienced in a real explosion. Perhaps half of this, or 100 kJ, might be absorbed in a blast that fails the specimen. In comparison, the energy capacity of four BGs with the column masses is 329 kJ. Up to two thirds of this may be lost due to the viscoelastic nature of the programmer (see Chapter 4), but even after losses the capacity of the BG group is sufficient to fail a highly reinforced specimen.

Actuator

The actuator is designed for high velocity. It has a 4 in (102 mm) diameter bore and a 36 in (914 mm) stroke. The active working stroke is about 20 in (508 mm); the remaining stroke is used for nitrogen compression and hydraulic cushions. At the end of the piston rod there are external threads for mounting the impacting mass. An internally-mounted Temposonic stroke transducer provides feedback for closed loop control of the actuator position during setup. During testing, the actuator operates in open-loop control. A close-coupled pressure accumulator provides the flow during the acceleration of the impacting mass. A second close-coupled return accumulator accepts the return flow after impact. The actuator is pictured in Figure 2.9 and a schematic of the hydraulic system is provided in Figure 2.10. The large cylinder in Figure 2.9 is the pressure accumulator, the small cylinder on the right is the return accumulator, and the piston rod is on the bottom left.

Figure 2.9: BG Actuator

A poppet valve on the compression end of the actuator controls the flow into the actuator. A linear variable displacement transducer (LVDT) provides position feedback for the poppet, which is controlled by a servo-valve. Peak flow is over 3000 gallons per minute (gpm) (11 400 L/min). Opening of this poppet valve initiates the testing sequence. The tension end of the actuator is filled with nitrogen gas. As the piston drives forward, it compresses the nitrogen chamber. This decelerates the actuator rod and forces it back to the retracted position after the test. A second poppet valve opens at the calculated time of impact allowing the actuator to retract. An LVDT provides position feedback for this poppet, which is also controlled by a servo-valve. Peak flow is about 1000 gpm (3685 L/min). The return accumulator receives the flow from the return poppet valve. A hydraulic cushion is built into the retract end of the actuator to prevent impact as the piston returns to its pre-test position.

The blast generators are served by an accumulator bank with a capacity

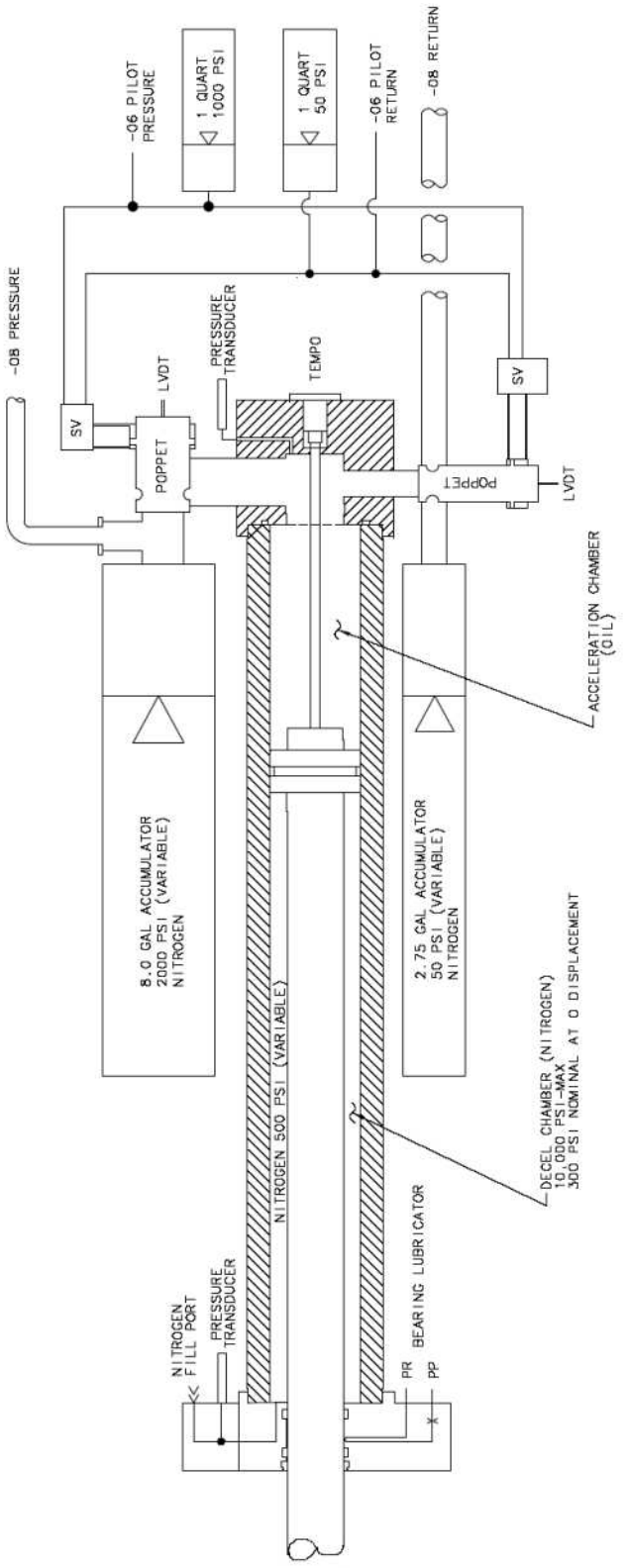

Figure 2.10: BG Actuator Hydraulic System (by MTS)

of 9500 L at a pressure of 35 MPa, and a surge tank with a 20 000 L capacity. These are all located in the main pump house, which services the outdoor shake table as well. The pilot pressure power supply provides 2000 psi (13.8 MPa) at 180 gpm (681 L/min) to the pilot valves on the blast generators, which control the position of the poppet valves.[1]

Impacting Module

The impacting module is made up of the programmer assembly that is bolted to a large steel mass that is bolted in turn to the actuator piston rod. It is attached to the rod with bolts that break away in case of excessive bending at the rod-mass interface, thus acting as a fuse to prevent damage to the main actuator components. The programmer assembly consists of a polymer layer with a specially-textured front side and an aluminum plate bonded to the backside. The aluminum plate connects the programmer to the steel mass. The entire mass impacting the specimen weighs 243 kg. This includes the weight of the steel plate (175 kg) and the programmer assembly (25.5 kg) as well as the weight of the piston rod and collar (42.4 kg). However, it does not include the weight of oil in the cylinder, which weighs an additional 6.8 kg at full extension.

The programmer (Figure 2.11) has a textured front surface that softens the initial stiffness. It is constructed from a polyurethane block of approximately 90 duro A hardness and a minimum resilience of 60%. It is bonded to a 0.5 in (13 mm) thick 6061-T651 aluminum backing plate with a minimum bond strength of 1000 psi (6.89 MPa). The main part of the polyurethane block measures 14 in (356 mm) wide × 30 in tall (762 mm) × 2 in (51 mm) thick. The textured surface consists in pyramids measuring 2.281 in (57.94 mm) square in plan × 0.37 in (9.4 mm) high. The aluminum substrate is bolted to the impacting mass.

[1]The wording in the preceding description of the actuator and hydraulic system is adapted from the description provided by MTS [14].

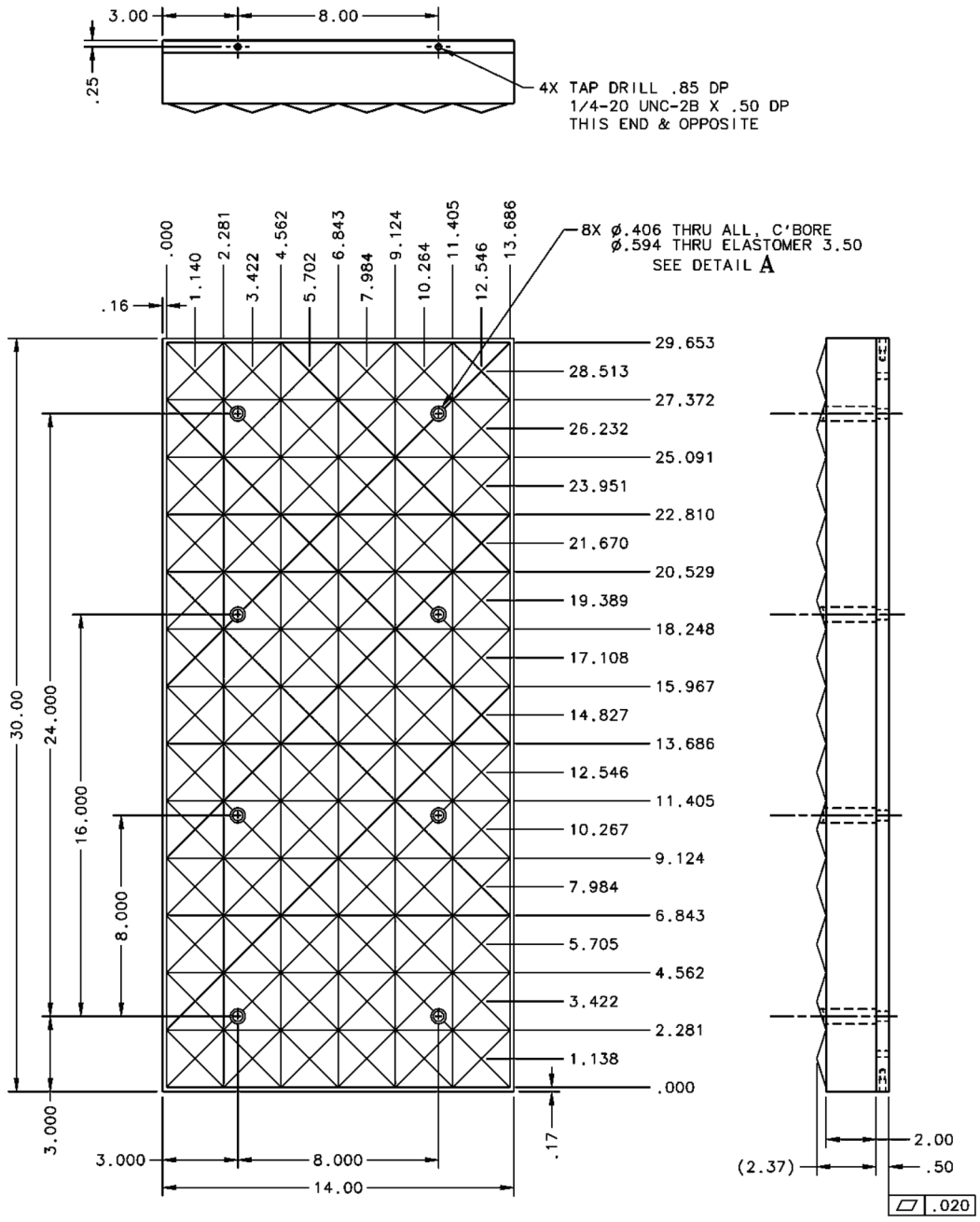

Figure 2.11: Programmer Assembly (by MTS)

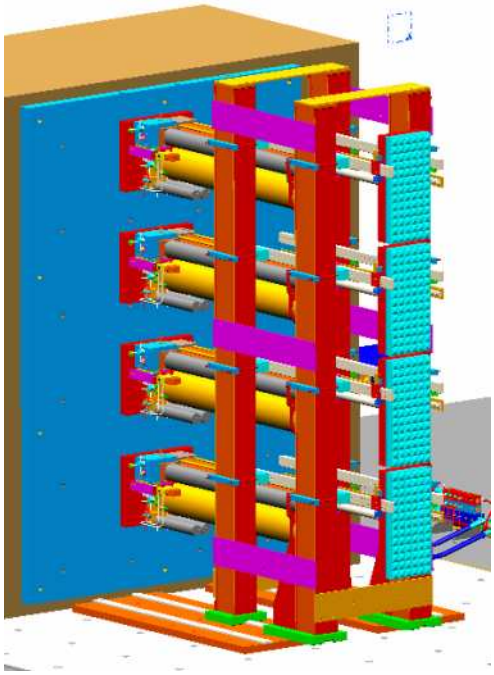

Figure 2.12: BG Tower (by MTS)

Support Systems

The entire BG assembly rests on a specially-designed tower (Figure 2.12) that supports and guides the BG array. The tower is necessary to support the weight of the impacting masses and to guide the impacting masses towards the specimen. The BG units are connected to the fixed reaction wall via a 3.5 in (89 mm) thick plate that is tied to the duct system in the wall.

MTS also developed the computer control system for setup and test operation of the BGs. This system controls the speed and timing of each BG independently, making it possible to impact the specimen with a complex loading. This system also functions as a data acquisition system for pressure, displacement and velocity transducers as well as BG accelerometers. These data are used for tuning the operation of the BGs; a separate data acquisition system (described in the following chapter) is used for data analysis.

2.B Construction

Construction of the facility occurred in tandem with construction of other facilities at the Englekirk Center that share the pump house and administrative facilities. Taylor Frager of San Diego, California was the general contractor on this phase, which lasted from July to September, 2003. While work on other parts of the site continued after this time, no on-site construction work took place for the explosive loading laboratory until July, 2004. The construction of the testing superstructure took place between July and November, 2004. Pacific Southwest Structures of La Mesa, California was the general contractor on this phase of the project. MTS completed delivery and installation of BG and other components in March, 2005.

Construction began in mid-2003. The excavation was finished by late July, 2003, at which time construction of the rebar cage for the slab, walls and isolator pedestals began. Concrete for the slab was placed in the first week of August as work on the rebar cage continued at higher elevations (Figure 2.13). The second lift of the foundation consisting in the isolator pedestals and lower walls, was completed in mid-August (Figure 2.14). Post-tensioning ducts were then placed, and the third and final lift was completed in early September. The rim of the foundation wall was post-tensioned in mid-September (Figure 2.15). In late September the excavation was filled and foundation work for the pump house commenced directly next to the foundation for the reaction structure. The finished foundation for the floating slab can be viewed from inside in Figure 2.16.

During the following months, as work progressed on the pump house, no work was done on the reaction structure. By late October, erection of the pump house's steel frame had begun. On October 25, 2003, the Cedar Fire, which devastated large areas of San Diego County, reached the construction site. Although the fire encroached on UCSD property and came within just a few meters of the Englekirk Center, our facility was undamaged and the construction delay was min-

Figure 2.13: Foundation Rebar Cage (12 Aug, 2003)

Figure 2.14: Isolator Pedestals and Upper Foundation Rebar (29 Aug, 2003)

Figure 2.15: Foundation Post-Tensioning (courtesy of C.S. Lee, 16 Sep, 2003)

Figure 2.16: Finished Foundation From Inside (3 Oct, 2003)

Figure 2.17: Installation of Accumulator Banks (5 Nov, 2003)

imal. In early November, grading for the perimeter access road commenced and the large hydraulic components: accumulator banks (Figure 2.17), surge tank and pumps were installed on site. By early December the pump house was largely finished.

The secondary strong floor was formed and concrete was placed by the end of July, 2004 (Figure 2.18), around which time the isolator bearings were delivered on site. By mid-August, the bearings were properly located but not yet secured (Figure 2.19), and falsework for the isolated strong slab was erected. Construction of the slab took place five feet (1.52 m) above its final elevation. Steel placement for the strong slab began in the first week of September (Figure 2.20, viewed from southwest corner showing anchorage zone reinforcement in foreground) and concrete was placed by the third week in the same month. Post-tensioning of the strong slab took place over four days at the end of the month (Figure 2.21).Once this was completed, the 150 t slab was carefully lowered into place with hydraulic

Figure 2.18: Secondary Slab (29 Jul, 2004)

jacks (Figure 2.22). Once it was at the proper location, the anchors were installed in the pedestal, the isolator bearings were attached to mating plates on the underside of the slab (Figure 2.23, showing isolator and a jack holding up the slab in the background) and a grout pad was cast underneath the bottom plate of each isolator bearing. Construction of the strong walls continued into October. Figure 2.24 shows the fixed wall prior to placement of pot-tensioning bars and Figure 2.25 shows the rebar cage for the first block of the moveable wall. By the end of the month, the fixed wall had been poured as had the first two slip-formed lifts of the moveable wall (Figure 2.26). Construction finished in November, 2004; Figure 2.27 shows the completed testing superstructure and Figure 2.28 shows the finished moveable wall during installation of BG hardware.

In February, 2005, MTS delivered and began installation the BGs together with the support frame, guidance system, hydraulic system components, and control system for the Explosive Loading Laboratory. Installation of these items was

Figure 2.19: Isolators in Position (10 Aug, 2003)

Figure 2.20: Main Slab Reinforcement (9 Sep, 2004)

Figure 2.21: Main Slab Post-Tensioning (27 Sep, 2004)

Figure 2.22: Main Slab Lowering (courtesy of L. Berman, 6 Oct, 2004)

Figure 2.23: Isolators and Jack (15 Oct, 2004)

Figure 2.24: Fixed Wall Reinforcement (15 Oct, 2004)

Figure 2.25: Moveable Block Reinforcement (15 Oct, 2004)

Figure 2.26: Two Blocks of Moveable Wall (2 Nov, 2004)

Figure 2.27: Completed Testing Superstructure (8 Feb, 2005)

Figure 2.28: Finished Moveable Wall (8 Feb, 2005)

completed in March, 2005. In total, 220 cubic yards (168 m^3) of concrete were placed in the foundation and 195 cubic yards (149 m^3) in the superstructure; the entire superstructure weighs 370 t. Over 15 million pounds (67 000 kN) of post-tensioning is used in the slab and fixed reaction wall, and another 4 million pounds (18 000 kN) in the moveable wall.

2.C Proof Testing

To verify the efficacy of the programmer material, bungee-accelerated drop tests were performed on October 6, 2004, at the MTS facilities. They were performed on an 11.5 in (292 mm) square, 85 duro A hardness programmer bonded to an aluminum plate (an early version of the material that would eventually become the programmer delivered to the Explosive Loading Laboratory). These tests generally confirmed that the programmer material would function as desired, but because the test rig suffered non-negligible and unmeasured acceleration and because the impact velocities were not measured, the data proved useless in anything but a qualitative sense [19]. Further data would be necessary to characterize the behavior of the programmer material. These additional data are reported and analyzed in Chapter 4.

MTS conducted factory acceptance tests (FAT) at their facilities in January, 2005. The main purpose of these tests was to verify that the BGs functioned properly before shipping them to the Explosive Testing Laboratory. The tests were conducted in a self-reacting steel frame that houses two BGs: the actual unit being tested and one set up to receive the impact of the first (see Figure 4.4, p. 169). The first unit had a programmer attached to the steel portion of the impacting mass while the second did not. Each BG was fired at various velocities, and data were collected from both actuators. Satisfied that the BGs could operate in the range of velocities required under the contract, MTS shipped the units to UCSD. The FAT also assisted in characterizing the programmer behavior; this is discussed

in Chapter 4.

Site acceptance tests (SATs) were conducted in March, 2005 on a highly fortified dummy column designed to receive repeated hits from the blast generator [14]. The SATs were intended primarily to evaluate, verify and calibrate the performance of the BGs, instrumentation and data acquisition systems. Testing was conducted on March 8, 9, 16, 17, and 18, 2005. In total, the dummy specimen was hit sixty-one times. All tests were conducted with the four BGs arranged vertically; from top to bottom the BGs were identified as 4D, 3C, 2B, and 1A.[2]

First, each BG was tested individually at 1000 psi (6.89 MPa) pilot pressure (one fifth of maximum) at incremental valve openings from 5% to 100% of maximum, which theoretically correspond to velocities of 1.7 to 9.2 m/s. These tests demonstrated that the BGs operated as specified and the behavior of each BG at the same settings was similar. As an example, the tests at 100% valve opening, which were conducted separately and are plotted together in Figure 2.29, show that the four pulses have practically identical shapes. Because the BGs that impact at the ends record a greater acceleration due to the stiffening effect of the boundary restraints, the peak accelerations are looked at in two different groupings, top/bottom (4D and 1A) and middle two (3C and 2B). The stiffening effect of the boundary restraints is discussed theoretically in Section 3.B.3. The top and bottom BGs reach maximum accelerations of 1037 and 1130 g, respectively, where g is the acceleration of gravity; the recorded peak accelerations differ by only 93 g. Each reading differs from the mean value of 1083.5 g by 4.2%. The middle two BGs reach peak accelerations of 928 and 941 g and differ by only 13 g. Each reading differs from the mean value of 934.5 g by 0.70%. The other SATs were similarly close. With the SAT results, we were convinced that each BG produces a controllable and repeatable acceleration trace and that the different BGs behave similarly at the same valve settings.

The acceleration trace is composed of a main signal that rises to the

[2]The reason for this numbering system will be explained in Chapter 3.

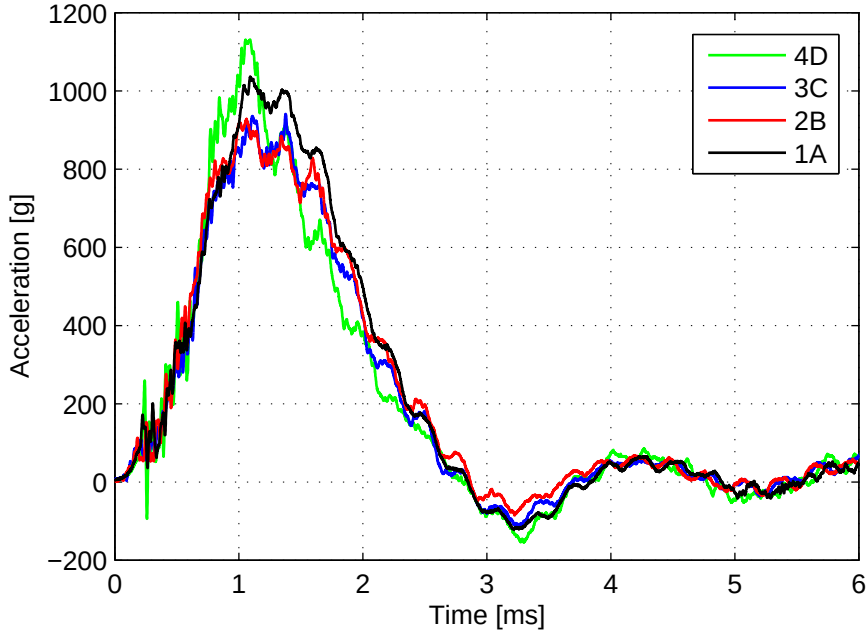

Figure 2.29: Individual SAT Tests (each test conducted separately)

peak in about 1 ms and then decays to zero. Superposed on this main signal are higher frequency ones, two of which are clearly visible, one at about 3.5 kHz and one at about 0.5 kHz. The slower of the two causes negative acceleration readings from about 2.8 ms to 3.7 ms and from about 4.8 ms to 5.4 ms. Because the contact condition between the programmer and the specimen cannot develop tension, these negative accelerations are not due to forces between the programmer and the specimen. Rather they represent vibration of some sort somewhere in the BG system. This phenomenon and its consequences are discussed further in Section 4.C.3. In brief, the problem is of secondary importance to this work because it is impulse, not acceleration, that is the important parameter governing specimen response; by good fortune the integration process used to calculate impulse acts as a filter for these higher frequency signals.

Once the results from the individual tests were satisfactory, the full array of 4 BGs was tested to calibrate the BGs so that the times of the acceleration

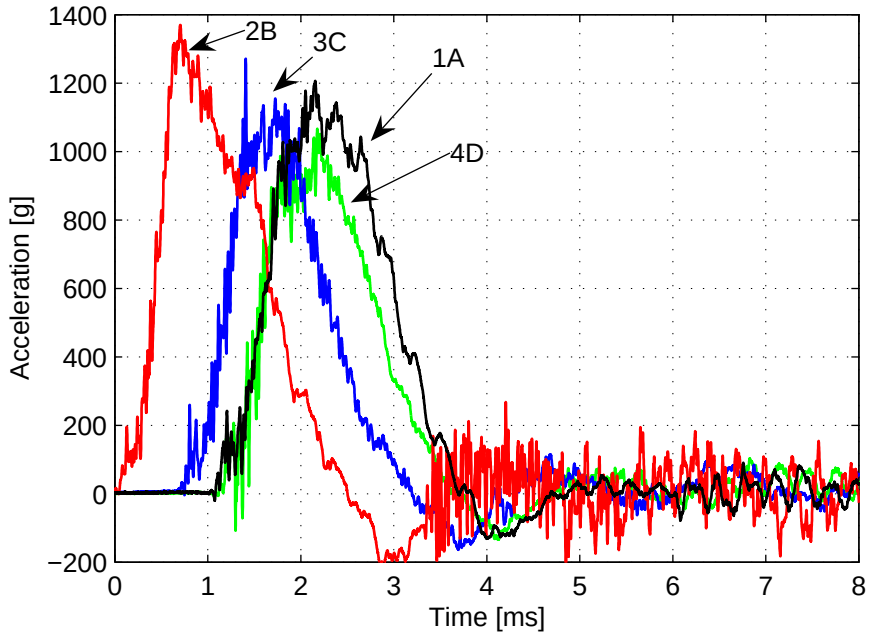

Figure 2.30: Site Acceptance Test: Four-BG Group

peaks would be separated by no more than 2.0 ms. The 4-BG array was tested at incremental valve openings at two different pilot pressures: at 1000 psi (6.89 MPa) from 5% to 100% valve opening and at 1550 psi (10.7 MPa) at 40% and 75% valve opening, which theoretically correspond to velocities from 1.7 to 12.0 m/s. Because of strength limitations in the reaction hardware these tests were conducted only up to approximately half of the maximum velocity capacity of the BGs. The pulse separation was not within specification in initial tests and different valve settings and warm-up procedures were tried to mitigate the problem. By the final test (Figure 2.30), the separation had been closed to 1.474 ms. Although this separation is within specification, we wished to reduce it further. The settings were refined in later tests and the separation was reduced to under 1 ms (see tests in Chapter 3).

The dummy specimen was designed to behave nearly elastically. At the end of the round of SATs, during which the dummy specimen suffered sixty-one

hits, it was showing some signs of degradation. However, it is still adequate for additional calibration tests if they are deemed necessary in the future.

2.D Chapter Summary

The second chapter covers the design, construction and proof testing of the Explosive Loading Laboratory, which took place between late 2002 and early 2005. The simulated blast load is applied via specially designed apparatuses called blast generators or BGs. Each BG is made of a high speed actuator that accelerates an impacting module towards the specimen. A polymer pad called the programmer, which is located on the front of the impacting module, is designed to provide a blast-like pressure pulse. The setup is housed in a self-reacting reaction structure that is isolated from the surrounding facilities. It is made of highly post-tensioned reinforced concrete and designed to suffer no tension during service. Proof tests of the BGs were conducted at the factory and once the facility was constructed, at the site. These tests are described not only to demonstrate that the BGs function as intended, but also to provide initial insight into the facility behavior and to present data that will be used in later chapters.

3 Simulated Blast Tests

Experimental blast tests with real explosives on structural components although useful and informative, are also costly, dangerous, and have data of limited use because of the destructive nature of the explosive. They can only be performed in dedicated facilities in remote locations and are very time consuming. In contrast, experimental tests using simulated blast promise to be less expensive, more informative, quicker to perform and safer.

This chapter presents the results from a series of simulated blast tests on as-built and retrofitted columns, which were conducted with two purposes in mind: studying the specimen behavior and obtaining data to calibrate the laboratory. The first section discusses fundamentals: setup, instrumentation, construction, and material data. The next addresses newly-developed data analysis methodologies, including the equivalent uniform load method, which is a powerful, new method that is used to analyze data from both simulated and real blast tests. Following this are results, which include stills from high speed video showing the specimen behavior during the blast. To date, this type of behavior has always been hidden from view by the fireball, and only post-mortem damage reports were possible. The verbal and video descriptions herein are the first-ever of specimens subjected to high-level blast-like loads. A short summary of results precedes the detailed test descriptions. This is the first time the results are publicly available; preliminary results were reported previously to the sponsoring agency [15].

Tests were conducted on seven specimens (Table 3.1) similar to those described in Section 1.C: four as-built, a pseudo-CSS, a six-wrap, and a two-wrap.

Table 3.1: Column Test Matrix

Test	Type	Axial Load	Desired Impact Velocity
2	As-Built	Yes	25 m/s
3	As-Built	No	12 m/s
4	Pseudo-CSS	Yes	19 m/s
5	Six-Wrap	Yes	Same as Test 4
6	Two-Wrap	Yes	irrespective
7	As-Built	No	of actual velocity
8	As-Built	Yes	attained

Test numbering begins at Test 2 because Test 1 was the designation used for the site acceptance tests. The first two tests, known as the *shakedown* tests, exercised the laboratory at higher levels than were possible in the site acceptance tests; the latter, known as the *commissioning* tests, studied different retrofit designs under similar loading. The axial load was varied in one of these tests.

3.A Preliminaries

This section describes details of the experimental setup. The reaction fixtures, axial load fixtures and blast generator (BG) arrangements are detailed first, followed by instrumentation details. Instrumentation includes a high speed data acquisition system, high speed video, accelerometers and displacement gauges. Finally, the specimen construction and material data are provided.

3.A.1 Setup

The columns are loaded with three or four BGs distributed over the height of the column. The impacting units, which were discussed in detail in Chapter 3 measure 14 in (356 mm) wide $\times$ 30 in (762 mm) tall and weigh 243 kg. The reaction

Figure 3.1: Link System

fixtures are similar to those used in previous quasi-static tests on blast-resistant designs conducted in 2000 and 2001 [20, 22].

The connection at the base of the column restrains all degrees of freedom. It is post-tensioned to the test floor (all post-tensioning for test fixtures is with 1-3/8 in (34.9 mm) diameter rods) and a concrete spacer block (1'-9" (533 mm) tall × 3'-0" (914 mm) wide × 4'-6" (1372 mm) long and also post-tensioned to the test floor) transfers shear forces from the footing to the reaction wall.

A more sophisticated restraint is used at the top of the column; a link system allows the column to move vertically while providing lateral and moment restraint (Figure 3.1). This mechanism is post-tensioned to the load stub and reaction wall. The hydraulic jacks are left in place under pressure during testing, thus providing the system with live post-tensioning; all other post-tensioned connections are locked-off mechanically.

An axial load is applied at the top of the load stub by three hydraulic

Figure 3.2: Hydraulic Jacks for Vertical Load

jacks (Figure 3.2). Once the appropriate axial load is applied (as determined by the pressure gauge reading multiplied by the contact area) the jacks are locked off mechanically. These jacks react against a steel frame that straddles the column and is post-tensioned to the test floor (Figure 3.3). This setup simulates the initial gravity load on the specimen. It also allows the axial load to increase as the column end moves upward due to arching action in compression, the so-called compression membrane effect. However, the axial load setup cannot develop tension, so if the column suffers large lateral deflections it will not develop second order tensile action, the so-called tension membrane effect, nor will it be vertically restrained.

Because the axial load frame straddles the column it obscures the specimen from a direct side view, which reduces the usefulness of the video record. When we were planning the tests it was clear that using an axial load system that blocks the specimen from view is sub-optimal. Ultimately, the decision to use was motivated by two non-scientific factors. First, instead of manufacturing a new axial load system, an existing load frame was used to allow us to complete the tests within the contracted time frame. (A new axial load system has now been developed for later tests.) Second, although it would have been possible to

Figure 3.3: Vertical Load Frame

test all specimens without the axial load, we wished to sidestep tangential discussions regarding whether or not tests without axial load are representative of real in-building conditions. In doing so we hoped to gain quicker acceptance of the blast simulation methodologies.

Tests 7 and 8, both of which were conducted on as-built specimens, provide one point of comparison on this matter. Test 7 was conducted without axial load. It was loaded with the equivalent of a 1230 lb (558 kg) charge of TNT at 14.3 ft (4.36 m) and suffered 3.33 in (85 mm) of residual deflection. In contrast, Test 8 was conducted with axial load. It was loaded with the equivalent of the same charge at 14.2 ft (4.33 m) (a slightly stronger load) and suffered 3.24 in (82 mm) of residual deflection (a slightly smaller deflection). That the column without axial restraint suffered a larger deflection at a lower load suggests strongly that the axial load condition indeed has an effect on the specimen's behavior. However, the small magnitude of the differences, even if completely attributable to the different axial

Table 3.2: BG Configurations 1 and 3

Height in (mm)	Slot	Configuration	
		1 (Test 2)	3 (Tests 4-8)
112.9 (2868)	D	4	3
80.6 (2047)	C	3	4
48.4 (1229)	B	2	2
16.1 (409)	A	1	1

load conditions, are small enough to suggest that the axial load condition does not have significant effects on the global structural behavior.

Three different BG configurations (Tables 3.2 and 3.3) were used during the column tests. Only one configuration was originally intended, but one of the BGs suffered damage during one of the tests and the configuration was adapted to avoid disruptions to the testing schedule. The first configuration is a 4-BG configuration, the second is a 3-BG configuration, and the third is again a 4-BG configuration almost identical to the first but with the position of the top two BGs reversed. To identify the various BG arrangements, each actuator was numbered 1 through 4, and each location was named A through D, from bottom to top. Each BG was identified with both its actuator number and its location. The single exception to this scheme was during the 3-BG configuration, in which case they were identified simply by the actuator number. Thus, for instance, the top-most BG in configuration 3 is referred to as "BG 3D," and the middle BG in configuration 2 is referred to simply as "BG 2."

3.A.2 Instrumentation

Data Acquisition System

A high speed data acquisition system from Hi-Techniques is used for data collection. This system samples at 14 bits and 1 MHz. At test time the data

Table 3.3: BG Configuration 2

Height in (mm)	Config. 2 Test 3
96.5 (2451)	4
64.5 (1638)	2
32.5 (826)	1

acquisition system had a capacity of 52 channels. It is externally triggered from the MTS controller that operates the BGs.

High Speed Video

High speed video is captured with a black and white Phantom v7.1 camera from Vision Research. It was set to record at a rate of 3000 frames per second at a resolution of 800 pixels $\times$ 600 pixels. The camera supports higher frame rates at the expense of lower resolution. The camera is externally triggered from the BG controller. The Track Eye Motion Analysis (TEMA) software package from Image Systems is used to obtain graphical displacement and velocity measurements from the video capture. The camera is placed on the right side of the column, centered on the front edge of the column at a height of about 2 m. High contrast targets are placed on the column to aid in graphical displacement measurements.

Displacement Potentiometers

Displacements are measured with linear potentiometers of various makes and models. Test floor displacements are measured using BEI Duncan Electronics model number 9615 (1.5 in (38 mm) stroke). Three instruments are used to capture the three planar degrees of freedom of the test table. One instrument is located on the north edge of the table 9'-3" (2.81 m) from the east edge, and measures north-south motion. Two instruments are located on the east edge 6'-0" (1.83 m)

Table 3.4: Potentiometer Locations [in (mm)]

Slot Number	Test 3		Tests 4-7	
3	118-1/4	(3004)	120	(3048)
4	107-1/2	(2731)	111	(2819)
5	86	(2184)	93	(2362)
6	64-1/2	(1638)	64-1/2	(1638)
7	43	(1092)	36	(914)
8	21-1/2	(546)	18	(457)
9	10-3/4	(273)	10	(254)

from the centerline, and measure east-west motion. These potentiometers recorded longitudinal motion of less than 0.15 in (3.8 mm) and negligible transverse or rotational motion.

Column displacements are measured at seven locations along the column height (Table 3.4); the locations are numbered 3-9.[1] Most displacements are measured with the SLS320 units from Penny+Giles (500 mm stroke); in Test 4 smaller units were used in slots 3, 5 and 8 while assessing different potentiometer arrays. These units are BEI Duncan Electronics model number 610 (10 in (254 mm) stroke). Column displacements were not measured in Tests 3 and 8.

Potentiometer readings on the specimen were generally unreliable for several reasons, the most important of which was insufficient strength of the rod connecting the potentiometer to the side of the column, which led to bending of the rod and confounding of the specimen displacements with connecting rod displacements. A second difficulty was dropouts in the data signal. In these instances, the potentiometer signal dropped to zero, presumably because shock vibration caused the slider and the fixed resistor to separate. This problem was partially alleviated in later tests by stiffening the potentiometer to off-axis motion with a sleeve

[1]Displacement locations 1 and 2 are on the load stub itself and were intended to measure load stub rotation. They were only used in Test 2.

that also protected the instrument against falling debris. The video record, when available, was more reliable for displacement measurements.

Shock Accelerometers

Accelerations are measured using Integrated Circuit - Piezoelectric (ICP) shock accelerometers from PCB Piezotronics. Accelerations on the impacting masses are measured with accelerometers installed on the back face of the unit approximately 200 m below the centroid.

The shock transmitted to the adjacent spaces is monitored with accelerometers mounted near the moveable wall, one on the table itself and the other directly across from it on the foundation. Peak accelerations between 20 g and 35 g were measured on the test table, while peak accelerations between 0.3 g and 3.5 g were measured on the surrounding foundation. The typical reduction in peak accelerations is about 94%, indicating a highly effective isolation system between the test table and foundation.

3.A.3 Construction

The seven specimens were built in March, 2005. They are identical in design to columns used in the Divine Buffalo test series and the quasi-static blast tests (see Section 1.C). They are 10'-9" (3277 mm) in clear height and 14 in (356 mm) square in cross section. The specified concrete strength is 5000 psi (34.5 MPa), and all rebar is ASTM A615 Grade 60 (420) [3, v. 01.04]. The column specimens are reinforced longitudinally with eight #8 rebar (3.2% reinforcement ratio) and #3 stirrups with 90 degree bends at 12-3/4 in (324 mm) on center; clear cover is 1-1/2 in (38 mm). The large stirrup spacing is typical of non-seismic design. In preparation for application of the CFRP jackets, all column corners were rounded to between 3/4 in (19 mm) and 1 in (25 mm) (even those that would not have a jacket applied). The footing at the base of the column and the load stub at the top are both highly reinforced, encased in a 1/4 in (6.4 mm)

thick steel jacket, and contain PVC sleeves used to attach the specimen to the lab floor and reaction structure. The specimens were constructed at the test site in three lifts (footing, column, and load stub) and after three weeks of concrete cure the composite retrofits were applied by hand lay-up by VSL (a subsidiary of the Structural Group). Three columns were jacketed with composite: one with two wraps in the hoop direction, one with six wraps in the hoop direction, and one with vertically-oriented strips bonded to the concrete and overlayed with six wraps in the hoop direction. A gap of 3/4 in (19 mm) was maintained between the jacket edges and horizontal surfaces of the footing and load stub.

The CFRP hoop wraps use the V-Wrap C220 carbon fabric system from VSL and the longitudinal CFRP reinforcement consists of pultruded carbon reinforced epoxy strips bonded to the column with a surface adhesive. As described by the vendor, the V-Wrap C220 is a unidirectional, 18 oz/yd^2 (0.61 kg/m^2) fabric made of T700 carbon fiber tows and encapsulated in a two-component, high-modulus, high-strength structural epoxy adhesive [5].

3.A.4 Material Testing

Concrete

Concrete cylinders were prepared, but early concrete strength was not measured due to procedural errors.[2] Available data are limited to 56-, 63-, and 112-day breaks, which include test-day breaks for Tests 7 and 8. Concrete strength values for these days are based on the mean of three tests conducted according to ASTM C39 [3, v. 04.02]. The missing test-day strengths are estimated based on a least squares fit of an ACI Committee 209 equation for Type I concrete [cited in 33]:

$$f'_c(t) = f'_c(28) \cdot \left(\frac{t}{4 + 0.85\,t} \right) \tag{3.1}$$

[2]Lab staff assignments were continually changed between the new Englekirk center and the other laboratories at the main campus. The test cylinders were made for 7-, 14-, 28-, and test-day concrete tests, but due to the confused logistical situation, the order to test them was lost.

Table 3.5: Test Day Concrete Strength

Test	Cast Date	f'_c [ksi (MPa)]
2 - As-Built	9 Mar	5.6 (39)
3 - As-Built	9 Mar	5.9 (41)
4 - Pseudo-CSS	9 Mar	6.1 (42)
5 - Six-Wrap	15 Mar	6.5 (45)
6 - Two-Wrap	15 Mar	6.7 (46)
7 - As-Built	9 Mar	6.26 (43.2)
8 - As-Built	15 Mar	6.91 (47.6)

where f'_c is the concrete strength in ksi (6.89 MPa) and the time t is in days. Based on the fit, the 28-day strength of the 9 March batch is 5.86 ksi (40.4 MPa) and of the 15 March batch is 6.27 ksi (43.2 MPa). Test day strengths are reported in Table 3.5. These are either estimates (reported to two significant figures) or test results (reported to three significant figures).

Composite

Vendor-supplied specifications for the wraps and strips are detailed in Tables 3.6, 3.7 and 3.8. The composite has a specified strength of 22.4 ksi (154 MPa) and stiffness of 12.9 Msi (88.9 GPa); these properties were derived from six laboratory tests on thirty samples. The strips have specified strength of 348 ksi (2400 MPa) and modulus of 19.0 Msi (131 GPa); no information was provided on the sample size for strips or for the surface adhesive [5].

A panel was cut from one of the column specimens after testing and tested according to ASTM D3039 [3, v. 15.03]. Because the behavior was elastic, the panel was assumed to be undamaged. The strength and stiffness values for this panel were noticeably lower than the specification. Not only was the fiber volume fraction lower than expected, the fibers were arranged in a wavy pattern as

Table 3.6: V-Wrap C220 Specification [5]

Property	Mean (Std. Dev.)	
	US Customary	SI
Tensile Strength	224 (28.7) ksi	1544 (198) MPa
Tensile Modulus	12.9 (1.74) Msi	89 (12) GPa
Elongation at Break	1.7 (0.67) %	
Ply Thickness	0.038 (0.0047) in	0.96 (0.12) mm
Strength per Unit Width	8.4 (0.55) kip/in	1.47 (0.096) kN/mm

Table 3.7: Longitudinal Strip Specification [5]

Property	US Customary	SI
Tensile Strength	348 ksi	2400 MPa
Tensile Modulus	19.0 Msi	131 GPa
Elongation at Break	1.87 %	
Thickness	0.055 in	1.4 mm
Width	3.94 in	100 mm

Table 3.8: Surface Adhesive Specification [5]

Property	US Customary	SI
Tensile Strength	3.5 ksi	24 MPa
Tensile Modulus	580 ksi	4 GPa
Strain	0.5 %	
Flexural Strength	5.8 ksi	40 MPa
Shear Strength	2.9 ksi	20 MPa
2-Day Bond Strength (moist cure)	2.5 ksi	17 MPa
2-Day Bond Strength (dry cure)	2.9 ksi	20 MPa
Direct Pull-off	All Failures in Concrete Substrate	

opposed to being straight and taut along the hoop direction. Both of these defects, which are due to poor installation by the contractor, can explain the discrepancy. Whether these results apply to all the jackets or only to the small test section is not known. Any future analysis of these specimens should keep in mind this uncertainty in the composite. No further conclusions are drawn regarding this except to emphasize the importance of quality control in CFRP retrofits.

3.B Data Analysis Methodologies

This section details ways in which the recorded data are reduced and analyzed. First, the duration of each BG's acceleration pulse is determined manually from the video and accelerometer records and impact velocity is determined from the video record with motion tracking software. Next is developed a new method of analysis that reduces the three or four individual acceleration data channels to a single representative uniform load. Lastly, to provide a physical comparison between the load imparted by the BGs and a real scenario, the equivalent uniform load is converted to an equivalent charge size and standoff.

3.B.1 Acceleration Pulse

The first step in the analysis is to properly identify the time during which the BG impact masses are in contact with the specimen. This is first done visually from the video record, which with a time resolution of 3000 frames per second, is able to resolve contact time to within $\pm$ 0.17 ms. The acceleration data are then examined visually to improve the estimate of contact time. The abrupt change in slope in the acceleration-time curve, which indicates contact with the specimen, is determined visually; The accuracy in this process is roughly $\pm$ 0.01 ms. The end of contact is determined exclusively from video or from a best guess when the video record is obscured from view by the vertical load frame. Thus the accuracy in identifying the end of contact is no better than $\pm$ 0.17 ms. Once the initial times

of contact are determined, the time base is reset so that $t = 0$ corresponds to the first impact. The video record shows that the programmer is uncompressed during the latter parts of contact, thus indicating that although the programmer and specimen are in contact, only a negligible force is being applied to the specimen.

Because the BGs are already accelerating when the data acquisition begins there is no way to identify the correct value of a baseline correction to the acceleration signal, thus none is applied. The error is small; a visual inspection of the data before and after the main pulse suggest that the baseline correction would be well under 1% of the peak recorded acceleration. In addition, for the reasons described next, neglecting the baseline correction of acceleration data has only a small effect on the quality of the calculated impulse.

A constant baseline error in the accelerations would result in a linearly increasing error in the impulse (because of integration); this error can dominate the signal at later times. However, because the majority of the impulse is delivered in a very short time, the error introduced to the impulse during this time is small. This insight is borne out by the data. Impulse curves rise quickly to a large value that is relatively insensitive to baseline correction.[3] The impulse curves then plateau briefly and after that different shapes are seen: some might stay steady, some might rise, some might fall, some may even see a second but smaller sharp rise. This behavior is governed by the baseline error and the BG forces during retraction, neither of which represents loading on the specimen. Thus, the results are presented with the acceleration records terminated at the end of the first sharp rise in impulse.

As illustrated in Section 2.C the acceleration records have high frequency signals superposed on the main signal. The source of these signals is not well-known. Possible sources include angular acceleration measured because the accelerometers are not on the center of gravity of the mass, shock waves travelling

[3]This was verified by applying a range of possible corrections and noting the minuscule change in the value of the first peak of impulse. The same exercise also demonstrated that the baseline correction has a large effect on the later part of the curve.

through the impacting mass, and shock waves travelling through the oil column in the actuator. No effort is made to preprocess the data to filter out this effect, thus the acceleration values are understood to contain a small error. However, it is the impulse, not the pressure that determines the response of the specimen. The integration process used to calculate impulse effectively filters out these high frequency vibrations. This topic is addressed further in Chapter 4.

The acceleration pulses are analyzed to obtain additional information about individual BG behavior and synchronization of the BG group as a whole. The following values are extracted from the data: maximum acceleration, time at which maximum acceleration occurs, maximum spread between acceleration peaks (should be less than 2.0 ms as per the specification), and maximum spread between initial impacts.

3.B.2 Impact Velocity

The impact velocity for each BG is determined from the video record using the TEMA software package. For each BG, a point is selected on the impact mass and the software records its displacement time history. The software then differentiates this displacement time-history to obtain a velocity time-history. The differentiation algorithm TEMA employs delivers velocity curves that are inconsistent with the contact times determined above; the time at which the velocity changes abruptly ought to be at the time of impact, but it is not. Presumably, this is due to a smoothing algorithm that averages over a number of points, thus blurring time resolution of abrupt events such as impact. The impact velocity is thus taken as the value just before the velocity curve drops abruptly irrespective of how it matches up to the actual contact time. To insure against any errors in the differentiation algorithm the displacement data were analyzed a second time by a linear interpolation of the initial portion of the displacement curve; in this case the slope of the interpolant is the contact velocity. TEMA's differentiation algorithm and linear interpolation produce consistent results. The accuracy of the

reported value for velocity at impact is approximately ± 0.1 m/s. The average of all the impact velocities is calculated and used as one of the aggregate values that characterize the behavior of the BG group.

3.B.3 Equivalent Uniform Load

In blast tests to date, researchers have reported pressure records measured at various locations on the specimen but no effort has been made to convert these separate channels into a single useful metric. Thus analysis of blast loads has been relatively informal and this makes comparisons across tests difficult. To make better sense of the numerous acceleration channels recorded in simulated blast tests, these are converted to a single time-history: an equivalent uniform pressure. This equivalent pressure is made to produce the same equivalent single degree of freedom (SDOF) force as does the actual load imparted to the structure. After processing the data in this way, any of a number of comparisons can be made between the characteristic time histories, e.g., peak pressures, pulse lengths, and impulse curves. The method developed in this section is derived for *any* specimen with the load recorded at N locations over its length. As such it is applicable not only to the simulated blast tests, but also to real blast tests in the field. This is a powerful, new method that can be used to make rigorous comparisons across any number of tests, as is done in Chapter 4.

In experiments in both the laboratory and the field, the load on the column is recorded at several data channels distributed along the height of the column; pressures are measured during field tests using real explosives, while in laboratory tests accelerations are recorded on the BG impacting masses. These numerous data channels are converted to a single time-history that produces the same equivalent SDOF force. The equation governing the equivalence is

$$\int_L p(x,t) \cdot \psi(x)\,\mathrm{d}x = \int_L \bar{p}(t) \cdot \psi(x)\,\mathrm{d}x \tag{3.2}$$

where $p(x,t)$ is the pressure recorded in an experiment, $\bar{p}(t)$ is the equivalent

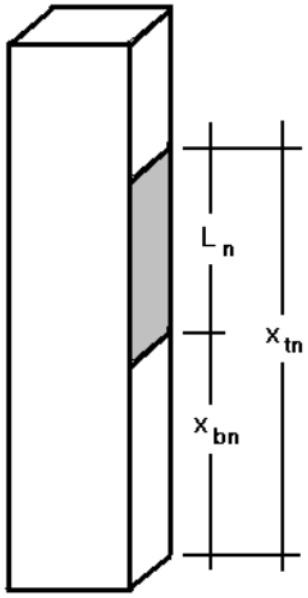

Figure 3.4: Tributary Area of a Single Sensor

uniform pressure, L is the length of the column, and $\psi(x)$ is the shape function defined previously in Section 1.A.3. By the methods presented in the same section, Equation (3.2) can be rewritten as

$$\int_L p(x,t) \cdot \psi(x)\,\mathrm{d}x = C_f \cdot \bar{p}(t) \cdot L \tag{3.3}$$

where C_f is the SDOF load coefficient for a beam with fixed ends.

Data are recorded at N discrete locations and it is assumed that each point on the column experiences the same pressure as that recorded at the instrument nearest to it. Thus the value recorded at each sensor determines a uniform load over a tributary area of length $L_n = x_{tn} - x_{bn}$ and width b, where x_{bn} and x_{tn} are, respectively, the bottom and top endpoints of the tributary area (Figure 3.4). Within this framework the experimental loading can be represented as

$$p(x,t) = \sum_{n=1}^{N} p_n(t) \cdot \psi_n(x) \tag{3.4}$$

where $p_n(t)$ is the pressure acting over the n^{th} tributary area, and

$$\psi_n(x) = \begin{cases} 1 & \text{if} \quad x_{bn} \leq x \leq x_{tn} \\ 0 & \text{otherwise} \end{cases} \tag{3.5}$$

The function ψ_n describes the location of the sensor. Substituting Equation (3.4) into Equation (3.3) and solving for $\bar{p}(t)$ yields

$$\bar{p}(t) = \frac{1}{C_f} \sum_{n=1}^{N} p_n(t) \cdot C_{fn} \tag{3.6}$$

where

$$C_{fn} = \frac{1}{L} \int_0^L \psi_n(x) \cdot \psi(x) \, \mathrm{d}x \tag{3.7}$$

or equivalently, using Equation (3.5)

$$C_{fn} = \frac{1}{L} \int_{x_{bn}}^{x_{tn}} \psi(x) \, \mathrm{d}x \tag{3.8}$$

These N coefficients represent the contribution of the load recorded at each sensor to exciting the assumed mode of vibration of the equivalent SDOF system.

It is important to realize that this approach is valid no matter what the inelastic behavior of the specimen might be. This is because the equivalent load is determined during the short time that the impulse is being delivered to the system. At this time, the column is still elastic and described well by a shape function derived from elastic analysis. Only later in the response does the column behave nonlinearly.

As a parenthetical note, earlier in this research program the equivalent pressure was calculated by simply averaging the total load over the total specimen area [15]. This method was effective at the time to obtain rough estimates of the impulse imparted to the specimen, but the error it introduces is too large for detailed and rigorous comparisons between field and laboratory tests; in the tests described next, discrepancies up to 22 percent between the old and new method have been observed. However, the old method is not so much incorrect as it is less refined, and in the special case that an equal load is applied over the entirety

Table 3.9: Four-BG Tests

Instrument	x_{tn}/L	x_{bn}/L	L_n/L	C_{fn}
D	1.00	0.75	0.25	0.05521
C	0.75	0.50	0.25	0.2125
B	0.50	0.25	0.25	0.2125
A	0.25	0.00	0.25	0.05521

Table 3.10: Three-BG Test

Instrument	x_{tn}/L	x_{bn}/L	L_n/L	C_{fn}
4	0.864	0.632	0.232	0.1298
2	0.616	0.384	0.232	0.2238
1	0.368	0.136	0.232	0.1298

of the specimen, as is ideally the case in the four-BG tests, the two methods give equal answers. Unfortunately, the magnitude of experimental error in impacting velocity and timing required the more accurate formulation.

To apply this method to the simulated blasts, the accelerations a_n recorded on the impact masses are converted to pressures by multiplying by the n^{th} BG impact mass M_n and dividing by its impact area (column width b times tributary length L_n). In this case the equivalent pressures in Equation (3.6) become

$$\bar{p}(t) = \frac{1}{C_f \cdot b} \sum_{n=1}^{N} \frac{M_n \cdot a_n(t) \cdot C_{fn}}{L_n} \tag{3.9}$$

In field tests, where pressures are recorded directly, the equivalent pressure is given by Equation (3.6).

The coefficients C_{fn} are calculated using $\psi = \psi_{ff}$ (Equation (1.47)). The coefficients are listed in Tables 3.9 and 3.10 for the four-BG and three-BG configurations, respectively. Once the equivalent uniform pressure is calculated, its integral, the equivalent specific impulse $\bar{\imath}$ is calculated as well. To characterize each experiment, the following quantities are calculated: peak equivalent pressure,

the time at which this peak occurs, the maximum equivalent specific impulse and the pulse length, which is defined as the time it take for the specific impulse to rise from 5% to 95% of the maximum.

3.B.4 Equivalent Charge

To give intuitive physical meaning to the results, the equivalent specific impulse $\bar{\imath}$ is treated as a normally-reflected specific impulse $\bar{\imath}_r$ and then converted to an *equivalent charge* that would have caused the same specific impulse. In Chapter 4 comparisons will be drawn between these tests and the Divine Buffalo field tests, thus the equivalent charge is modelled on a typical charge from these tests: an average charge size of 1230 lb raised 3 ft from the ground surface. The equivalent impulse is converted to a standoff distance at which this charge would have to be placed to produce the same impulse. The equivalent charge is derived in a process opposite from the example given in Section 1.A.1:

1. Obtain the equivalent reflected impulse $\bar{\imath}_r$ from the test data
2. Calculate the fictitious scaled distance $\hat{Z}$ corresponding to $\bar{\imath}_r$
3. Determine the side-on pressure p_s corresponding to $\hat{Z}$
4. Obtain an estimate of R_d: $\hat{R}_d = \hat{Z} \cdot \sqrt[3]{W}$
5. Obtain an estimate of α_g: $\hat{\alpha}_g = \cos^{-1}(H_c/\hat{R}_d)$
6. Determine the increase factor $\hat{\beta}$ using $\hat{\alpha}_g$ and p_s
7. Calculate an estimate of p_{gi}: $\hat{p}_{gi} = p_s/\hat{\beta}$
8. Determine the scaled distance Z corresponding to $\hat{p}_{gi}$
9. Calculate $R_d = Z \cdot \sqrt[3]{W}$
10. Compare R_d to $\hat{R}_d$

    If more accuracy is desired, set $\hat{R}_d = R_d$ and return to step (5)

11. Once the accuracy is sufficient, calculate $R_g = \sqrt{R_d^2 - H_c^2}$

For these tests no more than three iterations were required for convergence. The final value R_g is the horizontal distance of the charge from the target and is reported for each test. The three foot height is implied in but omitted from individual test descriptions.

3.C Test Results

A total of seven column specimens were tested under simulated airblast between March 29 and May 17, 2005. These tests proved the usefulness of blast simulation, further proved the usefulness of CFRP jackets in mitigating against blast loads, and provided data for characterizing the Explosive Loading Laboratory for future use. The tests provided high quality video data, including the first-ever recording of phenomena, e.g., development of shear cracks and spalling of cover concrete, that prior to these tests were obscured inside the fireball of an explosive. This being the first of its kind of testing, not all instrumentation and setups were ideal; relevant lessons have been drawn for future testing. This section provides an overview and a summary of the tests. Results from all seven tests are summarized in various tables: Table 3.11 focuses on measurements recorded on the BGs, Table 3.12 focuses on the equivalent pulse and charge size calculations, and Table 3.13 focuses on the specimen response.

The first two tests completed the shakedown test series, whose purpose was to calibrate the functioning of the test setup. These two tests evaluated the BGs at higher levels than were possible in the site acceptance test and were both on as-built specimens. In Test 2, the column specimen was hit at a very high load level of 2281 psi·ms (15.7 MPa·ms) and resulted in complete failure of the column. In Test 3, the column was hit at a moderate load level of 986 psi·ms (6.80 MPa·ms) and resulted in moderate damage. The load magnitudes and specimen behavior are consistent with those observed in previous explosive field tests.

Table 3.11: Summary of BG Measurements

Test	Spread [ms]		Avg. Impact Vel.	Peak Accel.	Last Contact
	Contact	Peaks	m/s	g	ms
2	2.39	2.79	26.0	6731	NA
3	1.73	1.84	11.8	1050	35.0
4	0.79	0.71	17.3	2254	22.8
5	0.84	0.79	17.1	1658	22.9
6	0.45	0.41	17.5	1876	24.9
7	0.43	1.32	17.3	3304	34.0
8	1.54	1.42	17.7	1834	33.9

Table 3.12: Summary of Equivalent Pulse Characteristics

Test	Peak Pressure			Impulse	Pulse Time	Equiv. Standoff
	psi (MPa)		ms	psi·ms (MPa·ms)	ms	ft (m)
2	3045 (21.0)	at	1.60	2281 (15.7)	3.13	11.6 (3.54)
3	839 (5.8)	at	1.15	986 (6.8)	3.21	20.0 (6.10)
4	1571 (10.8)	at	0.88	1609 (11.1)	2.43	14.3 (4.36)
5	1500 (10.3)	at	0.99	1617 (11.1)	2.55	14.2 (4.33)
6	1582 (10.9)	at	0.72	1623 (11.2)	2.32	14.2 (4.33)
7	2753 (19.0)	at	0.93	1598 (11.0)	2.01	14.3 (4.36)
8	1504 (10.4)	at	1.45	1616 (11.1)	3.39	14.2 (4.33)

Table 3.13: Summary of Specimen Response

Test	Peak Deflection in (mm)	ms	Res. Defl. in (mm)	Damage
2	Unknown at	198	17 (432)	Severe shear damage top & bottom
3	2.0 (51) at	14.2	0.44 (11)	Shear damage top & bottom
4	1.8 (46) at	8	0.38 (9.5)	Practically none
5	1.6 (41) at	9.0	0.63 (16)	Practically none
6	1.9 (48) at	9.4	0.8 (20)	Practically none
7	4.8 (122) at	41.7	3.33 (85)	Shear damage top & bottom
8	6.2 (157) at	47.6	3.24 (82)	Shear damage top & bottom

After the shakedown series was completed, the commissioning series tested five specimens at similar load level; the impacting velocity was just over 17 m/s, corresponding to an equivalent specific impulse between 1598 psi·ms (11.0 MPa·ms) and 1623 psi·ms (11.2 MPa·ms). Among the five columns were two as-built and three hardened specimens: one with a two-wrap jacket, one with a six-wrap jacket and one with a Pseudo-CSS. As expected, the retrofit options performed very well compared to the as-built specimens: whereas the as-built specimens suffered permanent deflection up to 6.2 in (157 mm), the retrofitted specimens limited this to under 1 in (25 mm).

Regarding the functioning of the BGs, the impacting velocity was well correlated with the impulse delivered to the specimen (less so with the peak acceleration and equivalent pressure). The 5%-95% pulse time is loosely correlated to the spread between BG impact times. This makes sense because the pulse time is roughly equal to the pulse time of a single BG plus the lag time between the first and last impact. However, the spread between impact times seems not to be correlated to any other variable, indicating that it is likely random, caused by such factors as tolerance errors and guide rail friction. The time of final contact is

lower for retrofitted specimens, perhaps because they are slightly stiffer or because the constitutive behavior between the polymer and concrete is different than between the polymer and composite. Additional investigation is needed to make any determinations in this matter.

Regarding instrumentation, the video record was the most reliable of the different types of instrumentation. Potentiometers can be used in the future, but these need to be connected to the specimen with stiffer rods, to prevent bending, embedded deeply into the core concrete, to prevent detachment in case the cover concrete spalls. The video targets need to be better secured to the specimen as well to make reliable recordings of the post-spalling kinematics of the concrete core. Currently they are adhered to the surface and when cover concrete spalls, the target becomes detached from the main specimen. Accelerometers need to be placed at the center of mass of the BGs to reduce the effect of impacting mass vibrations. Some changes have already been enacted in future tests; for instance, the axial load frame has been redesigned to provide a clear video record.

The remainder of the chapter describes the individual tests in detail: the initial setup, BG behavior, a physical description of the specimen behavior, calculation of descriptive metrics, and photographs both during and after the test. The descriptions and stills extracted from the video record are the first-ever of the response of structural specimens to blast loads.

3.C.1 Test 2, As-Built

Initial Setup

Test 2 was conducted on March 29, 2005 on an as-built column. This was the second shakedown test (the first was the site acceptance test discussed in Section 2.C). The impact masses were set to impact the specimen at 25 m/s. The column was set up with the axial load frame, the jacks were brought up to pressure and locked off mechanically once 100 kips (445 kN) of axial load had been imposed

Figure 3.5: Specimen Prior to Impact (Test 2, -1.6 ms)

on the column. Instrumentation was provided as per the instrumentation section for displacements, accelerations, and table movement. High speed video was also captured during the test. The BGs were arranged in configuration 1 for this test. The specimen is shown just prior to impact in Figure 3.5 (axial load frame in the foreground).

BG Behavior

The BGs impacted in the order 4D-3C-2B-1A, from top to bottom, with the first impact 51.71 ms after the data trigger. The peak measured acceleration is 6731 g (BG 4D) and the average of the impact velocities is 26.0 m/s. The total spread from first to last impact is 2.387 ms and from first to last peak is 2.790 ms. The latter value is outside the specification that the BG peaks be separated by no more than 2.00 ms. In response, the BGs were tuned further and the problem was eliminated in future tests. Acceleration traces are plotted in Figure 3.6 and impact

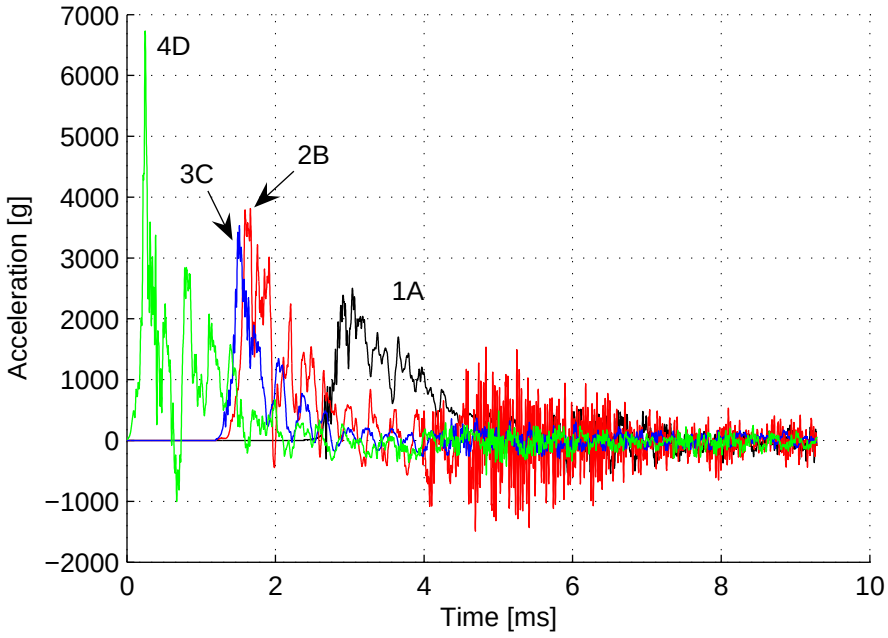

Figure 3.6: Accelerometer Readings (Test 2)

Table 3.14: BG Impact Details (Test 2)

BG	Impact Time ms	Impact Velocity m/s	Peak Time ms	Peak Value g
4D	0.000	27.2	0.247	6731
3C	1.199	26.9	1.516	3531
2B	1.204	25.7	1.664	3814
1A	2.387	24.0	3.037	2503
Average		26.0		

times, velocities and peak values are summarized in Table 3.14. Because the video camera's view of the specimen was obstructed by the vertical load frame, it was impossible to visually determine the end time of individual BG impacts; thus these are not reported.

The equivalent pressure pulse (Figure 3.7), shows a shape that is dis-

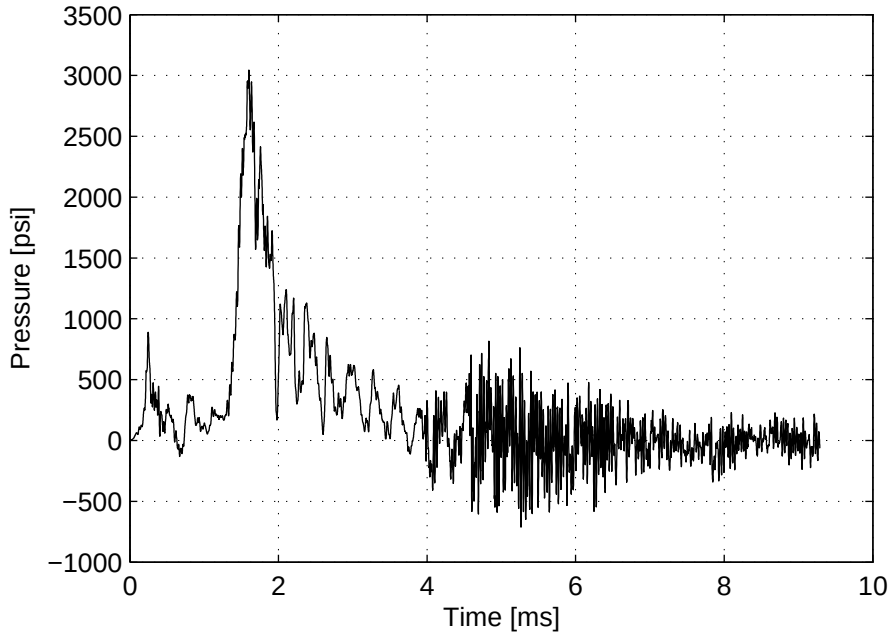

Figure 3.7: Equivalent Pressure (Test 2)

Table 3.15: Equivalent Pulse Characteristics (Test 2)

Peak Pressure			Impulse	Pulse Time	Equiv. Standoff
psi (MPa)		ms	psi·ms (MPa·ms)	ms	ft (m)
3045 (21.0)	at	1.60	2281 (15.7)	3.13	11.6 (3.54)

similar from an actual blast; there is an extra small pulse at the beginning of the record due to the early hit from BG 4D, which arrived 1.2 ms early. The maximum equivalent pressure of 3045 psi (21.0 MPa) was measured at 1.60 ms after impact. As with the equivalent pressure, the equivalent specific impulse (Figure 3.8) has an unusual shape at the beginning of the record. The maximum equivalent specific impulse is 2281 psi·ms (15.7 MPa·ms), which is equivalent to a 1230 lb (558 kg) TNT charge at 11.6 ft (3.54 m). The 5%-95% pulse time is 3.13 ms. These values are summarized in Table 3.15.

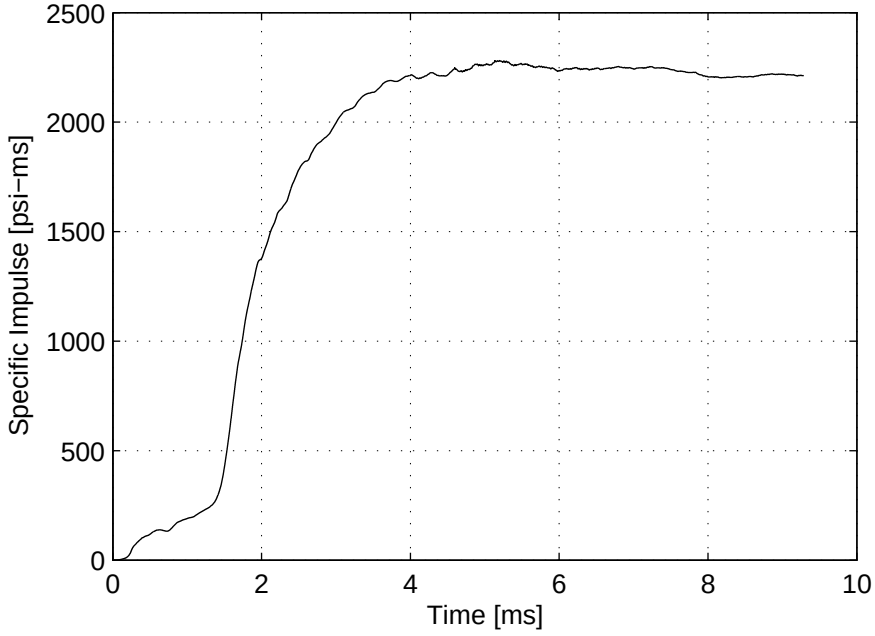

Figure 3.8: Equivalent Specific Impulse (Test 2)

Physical Description of Specimen Behavior

Shortly after impact, at 1.7 ms, the plastic brackets connecting the potentiometer rods to the back face of the column exploded when the shock wave travelling through the material reached them, which ruined the data collected from these devices because the potentiometer rods became detached from the specimen. Only potentiometers 1 and 2, on the load stub, and potentiometer 9, near the base of the column, survived intact. None would ultimately survive the test. At 4.7 ms the breakaway bolts on the BG masses began snapping due to excessive rotation of the masses relative to the rod.

Because of the location of the vertical load frame directly between the camera and the specimen, the early behavior was not visible. At 10.1 ms after impact the column had deflected sufficiently to where the back edge was once again visible. At this time spalling cracks were visible on the back face of the column, being most pronounced at mid-height. The BGs continued rotating as

the specimen deflected. At 11.4 ms BG 3C fell off its support rail. Eventually, the cantilevered load of this unsupported BG would bend the rod, requiring repairs. At 12.3 ms, the entire rear cover concrete was emerging from behind the load frame as a uniform mass, no longer attached to the rest of the column (Figure 3.9). As such, the lone surviving potentiometer was no longer measuring the main specimen behavior, but the cover concrete behavior in free flight.

Around 16 ms, axial deformation of the specimen became apparent. At 21.3 ms the load stub had dropped sufficiently to bear on BG 4D and displace its support rail. By 25.3 ms, the BG masses had reached the maximum rotation. The column was still travelling forward and the load stub was still descending, thus imposing an increasing second order moment onto the already failed column (Figures 3.10 and 3.11). At 198 ms, the maximum lateral and axial deflections were reached (Figure 3.12). Due to instrumentation failure it was not possible to determine the value of the maximum deflection. The axial deflection was stopped only by nonlinear behavior of the link system and residual stiffness of the rebar cage. The column rebounded slightly as the elastic portion of the deformation was recovered.

After the test, the column was seen to have two distinct regions of damage (Figure 3.13).The end regions - about 40 to 45 inches long - had cover concrete spalled off of all four sides, and heavily degraded core concrete, mostly due to the dynamic shear demand but also due to second order moment demands. The center of the column was relatively undeformed and suffered spalling only on the back end from the initial impact. A residual deflection of over 17 in (432 mm) was measured after the test. The two potentiometers intended to measure load stub rotation were also found to be damaged due to the large vertical deflection. Specimen response parameters are summarized in Table 3.16.

Figure 3.9: Rear Face Spalling (Test 2, 15.4 ms)

Figure 3.10: Column Failure (Test 2, 35.4 ms)

Figure 3.11: Column Failure Continues (Test 2, 112 ms)

Figure 3.12: Near Maximum Deflection (Test 2, 187 ms)

Figure 3.13: Specimen Post-Test (Test 2)

Table 3.16: Specimen Response (Test 2)

Peak Defl.	Res. Defl.	Damage
At 198 ms	17 in (432 mm)	Severe shear damage at top and bottom ends

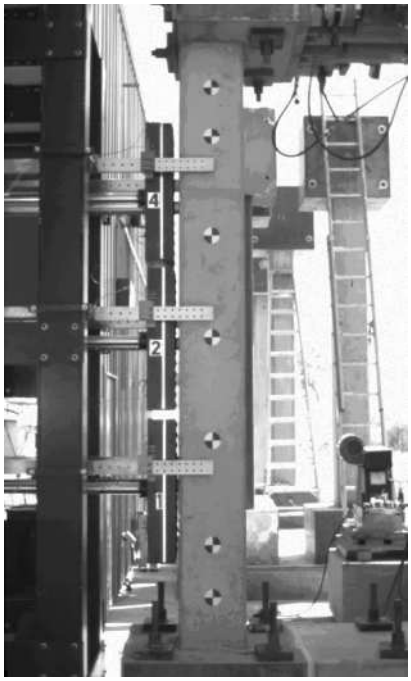

Figure 3.14: Specimen Prior to Impact (Test 3. -0.7 ms)

3.C.2 Test 3, As-Built

Initial Setup

Test 3 was conducted on April 7, 2005 on an as-built column. This was the last of the shakedown tests. The BGs were set to impact the specimen at 12 m/s. The column was set up without the axial load frame. For this test no instrumentation was provided except for high speed video and accelerometers on the BGs. Because of the damage suffered by BG 3 in the previous test, the BGs were arranged in configuration 2: a three BG setup. The specimen is shown just prior to impact in Figure 3.14.

BG Behavior

The BGs impacted in the order 1-2-4, from bottom to top. First impact was 50.67 ms after the data trigger. The peak measured acceleration is 1050 g

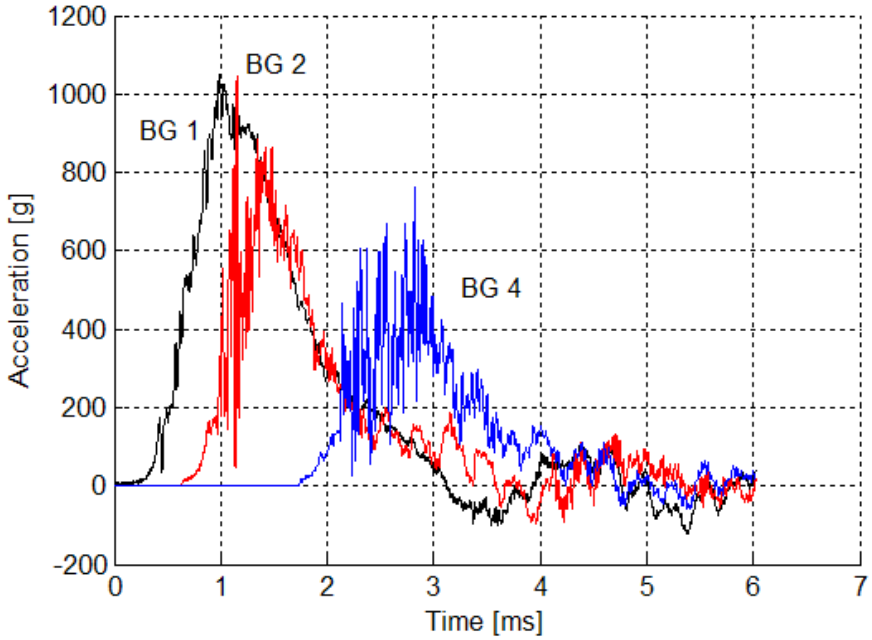

Figure 3.15: Accelerometer Readings (Test 3)

Table 3.17: BG Impact Details (Test 3)

BG	Impact Time ms	Impact Velocity m/s	Peak Time ms	Peak Value g	Last Contact ms
4	1.732	11.2	2.823	761	30.0
2	0.639	12.0	1.153	1044	35.0
1	0.000	12.2	0.985	1050	6.3
Average		11.8			

(BG 1), and the average of the impact velocities is 11.8 m/s. The total spread from first to last impact is 1.732 ms and from first to last peak is 1.838 ms. Acceleration traces are shown in Figure 3.15 and impact times, velocities and peak values are summarized in Table 3.17. The last contact times indicate that BGs 4 and 2 lingered on the specimen after impact.

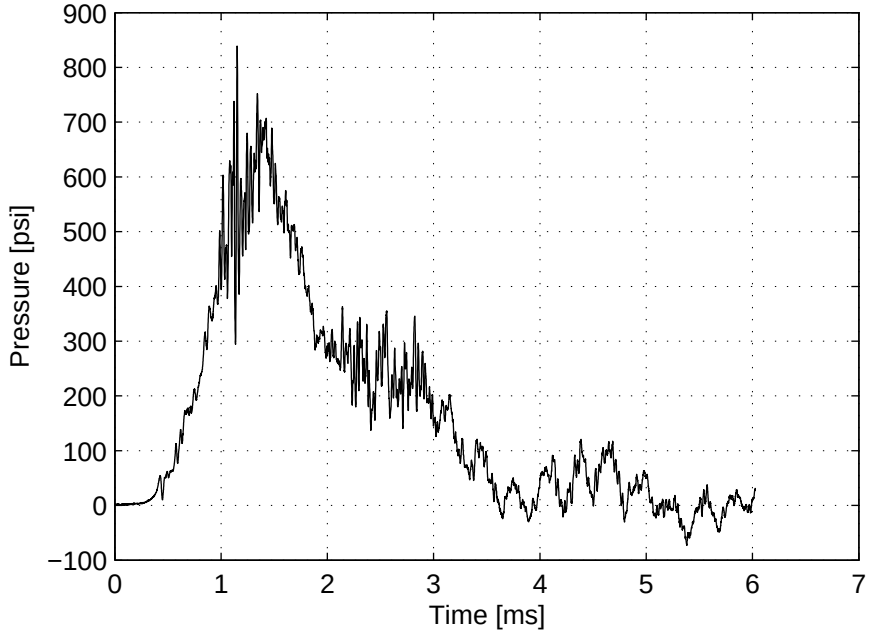

Figure 3.16: Equivalent Pressure (Test 3)

The equivalent pressure pulse (Figure 3.16) shows a slower initiation and a lower peak, but is otherwise consistent in shape with that of an actual blast. This is caused by the initial softness of the programmer and non-simultaneity of BG hits. The maximum equivalent pressure of 839 psi (5.78 MPa) was measured at 1.15 ms after impact. Although this value represents the actual peak in the data, it is due to a spurious peak. The actual peak is a little bit lower and later. Except for a slightly slower initiation, the shape of the equivalent impulse (Figure 3.17) is very similar to that of an actual explosive. The maximum equivalent specific impulse is 986 psi·ms (6.80 MPa·ms), which is equivalent to a 1230 lb (558 kg) charge of TNT at 20.0 ft (6.10 m). The 5%-95% pulse time is 3.21 ms. These values are summarized in Table 3.18.

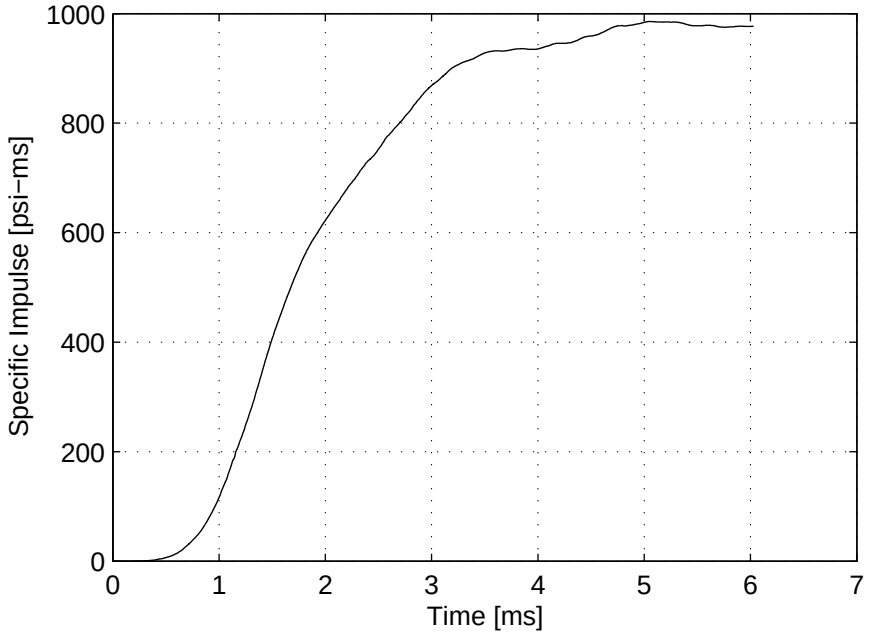

Figure 3.17: Equivalent Specific Impulse (Test 3)

Table 3.18: Equivalent Pulse Characteristics (Test 3)

Peak Pressure			Impulse	Pulse Time	Equiv. Standoff
psi (MPa)		ms	psi·ms (MPa·ms)	ms	ft (m)
839 (5.78)	at	1.15	986 (6.80)	3.21	20.0 (6.10)

Table 3.19: Specimen Response (Test 3)

Peak Deflection in (mm) ms	Res. Defl. in (mm)	Damage
2.0 (51) at 14.2	0.44 (11)	Shear damage at both ends; some spalling

Physical Description of Specimen Behavior

At 3.3 ms, a shear crack initiated from the center of BG 1 to the bottom compression toe. Shortly thereafter, at 3.7 ms a similar crack initiated at the top end. At the top end, additional shear cracks, parallel to the first, opened at 4.6 and 5.3 ms. The shear crack pattern at 6.0 ms is shown in Figure 3.18. Incipient crushing at the base of the column was seen at 7.0 ms. As the column deflected, the cracks expanded and at 11.3 ms the cover concrete at the back and sides in the top 30 in (762 mm) to 35 in (889 mm) of the column began spalling. The maximum deflection of 2.0 in (51 mm) was observed at 14.2 ms. This state of deformation is shown in the video capture at 14.4 ms (Figure 3.19). The spalling and crushing described above continued to progress (Figure 3.20) but unlike in the previous test, the column was able at all times to carry its own weight. At the end of the test, the column showed shear damage at both ends and some negligible flexural cracking on the back face. The residual deflection measured in the field is 7/16 in (11 mm). The overall view of the post-test column is show in Figure 3.21. Details of the damage at the top are shown in Figures 3.22 and 3.23 and at the base in Figures 3.24 and 3.25. Specimen response parameters are summarized in Table 3.19.

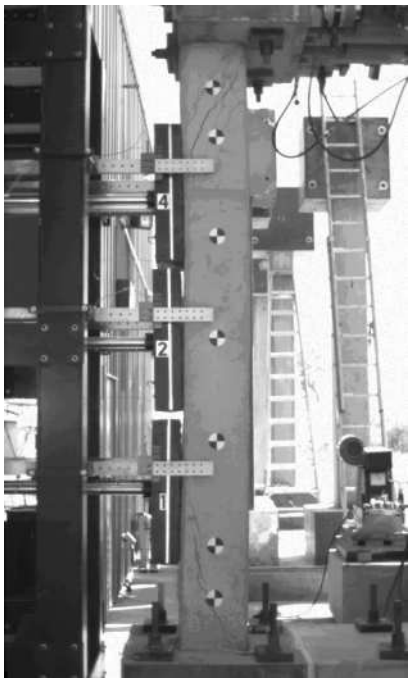

Figure 3.18: Initial Shear Crack Pattern (Test 3, 6.0 ms)

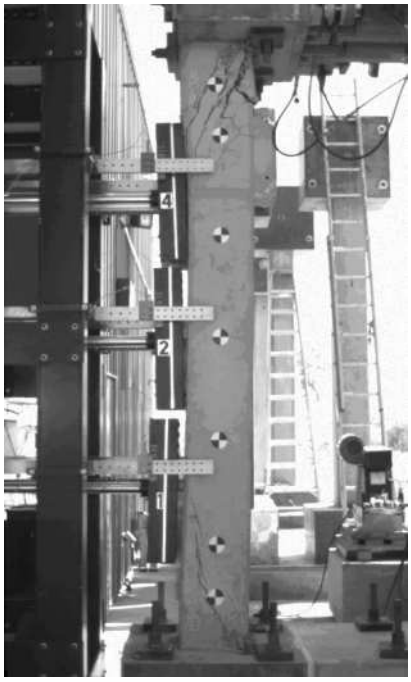

Figure 3.19: Shear Crack Pattern Progressing (Test 3, 14.4 ms)

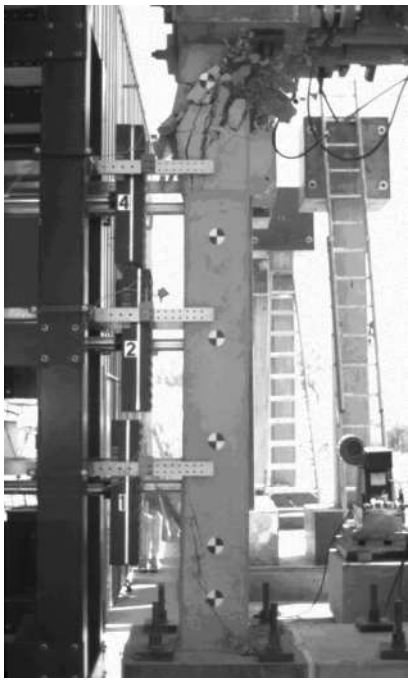

Figure 3.20: Advanced Damage Pattern (Test 3, 69.3 ms)

Figure 3.21: Specimen Post-Test (Test 3)

Figure 3.22: Damage Pattern Top Rear (Test 3)

Figure 3.23: Damage Pattern Top Right (Test 3)

Figure 3.24: Damage Pattern Bottom Right (Test 3)

Figure 3.25: Damage Pattern Bottom Left (Test 3)

3.C.3 Test 4, Pseudo-CSS

Initial Setup

Test 4 was conducted on April 14, 2005 on a column retrofitted with longitudinal carbon strips and six CFRP wraps in the hoop direction. This configuration was used to represent a carbon shell system (CSS) used in new construction applications. This was the first of the commissioning tests. It was planned to have the impact masses hit the specimen at 19 m/s. For the sake of consistency, all future commissioning tests would use the same BG settings irrespective of the actual velocity attained. The column was set up with the axial load frame, the jacks were brought up to pressure and locked off mechanically once 100 kips (445 kN) of axial load had been imposed on the column. Instrumentation was provided as per the instrumentation section for displacements, accelerations, and table movement. High speed video was also captured during the test. The repair on BG 3 was completed and the BGs were arranged in configuration 3 for this test. The specimen is shown just prior to impact in Figure 3.26 (axial load frame in the foreground).

BG Behavior

The BGs impacted in the order 1A-3D-4C-2B; bottom-most first then top to bottom after that. First impact was 55.50 ms after the data trigger. The peak measured acceleration is 2254 g (BG 4C), and the average of the impact velocities is 17.3 m/s - lower than the target. The total spread from first to last impact is 0.790 ms and from first to last peak is 0.712 ms, which is within the specification. Acceleration traces are shown in Figure 3.27 and impact times, velocities and peak values are summarized in Table 3.20. The last contact times indicate that while BG 1A hit cleanly, the other three lingered on the specimen after impact.

The equivalent pressure pulse (Figure 3.28) shows a slower initiation and a lower peak, but is otherwise consistent in shape with that of an actual blast. This is caused by the initial softness of the programmer and non-simultaneity of

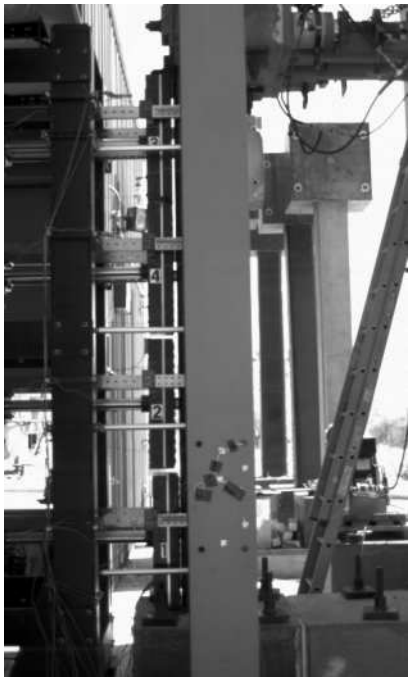

Figure 3.26: Specimen Prior to Impact (Test 4. -0.5 ms)

BG hits. The maximum equivalent pressure of 1571 psi (10.8 MPa) was measured at 0.88 ms after impact. Except for a slightly slower initiation, the shape of the equivalent impulse (Figure 3.29) is very similar to that of an actual explosive. The maximum equivalent specific impulse is 1609 psi·ms (11.1 MPa·ms), which is equivalent to a 1230 lb (558 kg) charge of TNT at 14.3 ft (4.36 m). The 5%-95% pulse time is 2.43 ms. These values are summarized in Table 3.21.

Physical Description of Specimen Behavior

The majority of the specimen behavior was blocked from view by the vertical load frame, thus the description of the test itself derives mostly from the collected data. Displacement measurements are difficult to make in large part due to the rod bending problem, discussed in depth in the instrumentation section, but because the BGs (except 1A) remain in contact with the specimen past the point of maximum deflection, the BG displacement measurements from the video capture

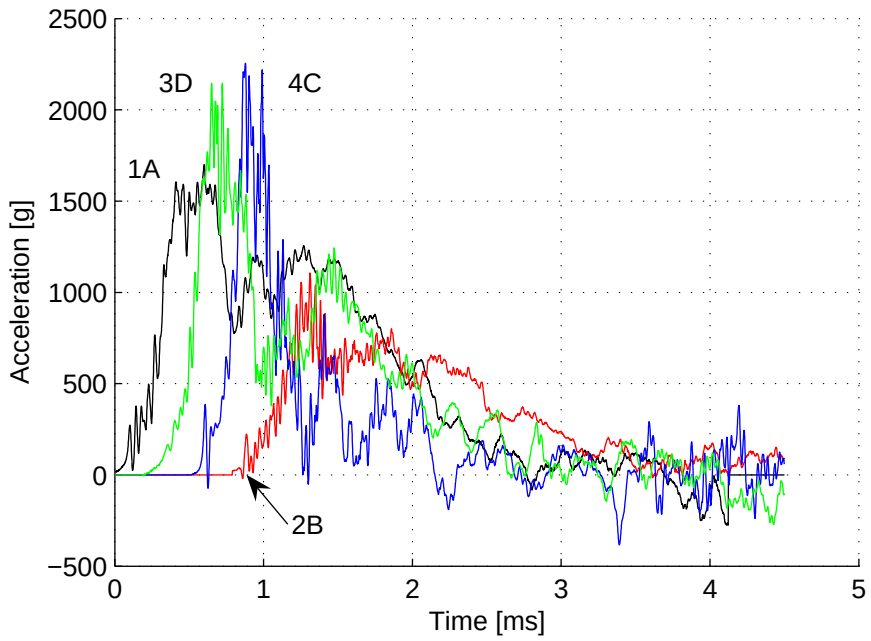

Figure 3.27: Accelerometer Readings (Test 4)

Table 3.20: BG Impact Details (Test 4)

BG	Impact Time ms	Impact Velocity m/s	Peak Time ms	Peak Value g	Last Contact ms
3D	0.190	17.5	0.651	2146	22.8
4C	0.510	17.0	0.877	2254	20.1
2B	0.790	17.3	1.312	1106	18.5
1A	0.000	17.6	0.600	1699	4.1
Average		17.3			

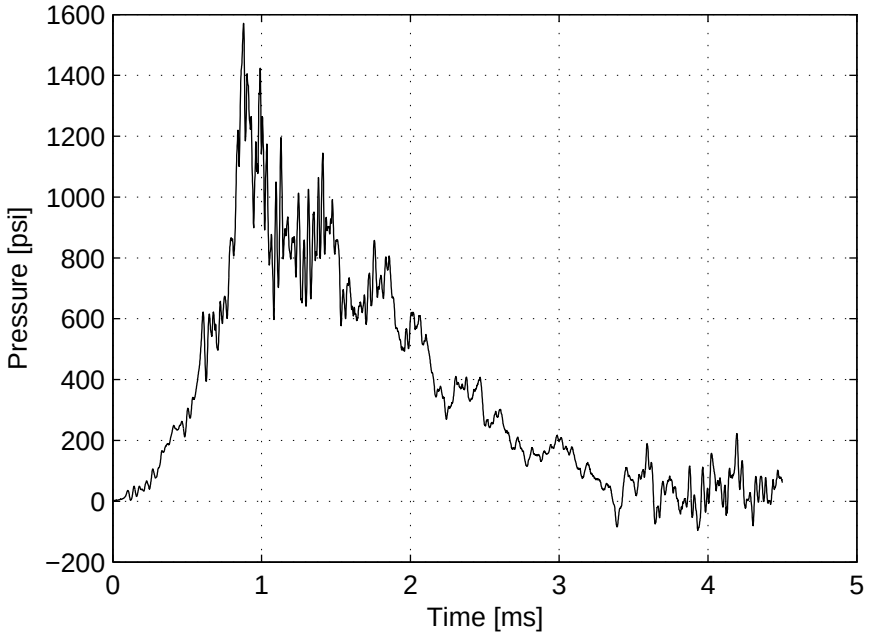

Figure 3.28: Equivalent Pressure (Test 4)

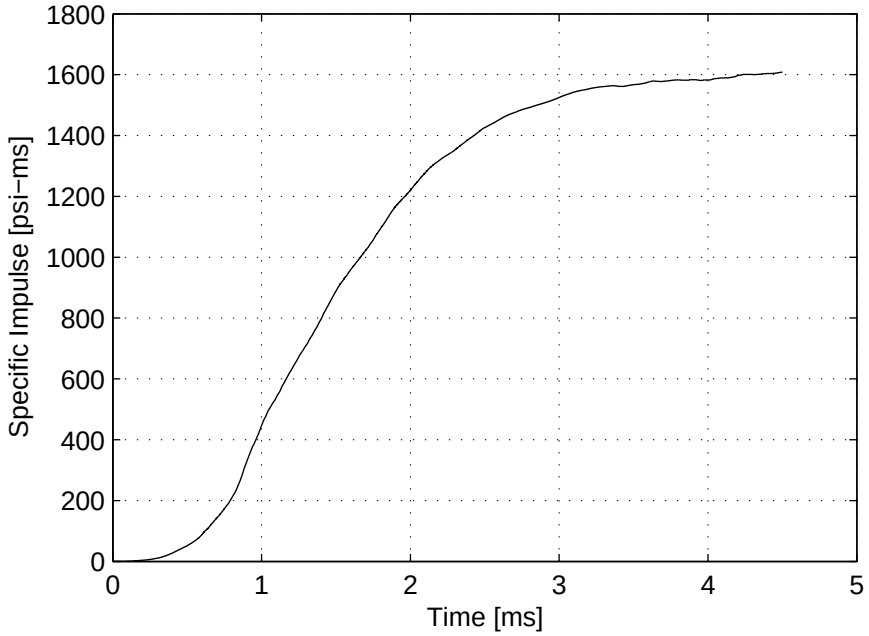

Figure 3.29: Equivalent Specific Impulse (Test 4)

Table 3.21: Equivalent Pulse Characteristics (Test 4)

Peak Pressure psi (MPa) ms	Impulse psi·ms (MPa·ms)	Pulse Time ms	Equiv. Standoff ft (m)
1571 (10.8) at 0.88	1609 (11.1)	2.43	14.3 (4.36)

Table 3.22: Specimen Response (Test 4)

Peak Defl. in (mm) ms	Res. Defl. in (mm)	Damage
1.8 (46) at 8 ms	0.38 in (9.5)	Practically none

can aid in estimating the maximum deflections. According to the potentiometer readings the maximum deflection is 1.6 in (41 mm) at 8 ms, and at the same time, according to the video estimate, the maximum deflection is 1.8 in (46 mm). The latter is considered more reliable, and the peak deflection (Figure 3.30) is taken as 1.8 in (46 mm) at 8.0 ms. Upon completion of the test, the residual displacement was measured at 3/8 in (9.5 mm). Hardly any damage was seen on the column indicating that the behavior was largely elastic and the retrofit worked very well. The only damage observed was some minor yield penetration into the footing (3.31) and horizontal cracks in the jacket no larger than 1/16 in (1.6 mm). Only a surface inspection of the composite was carried out. Specimen response parameters are summarized in Table 3.22.

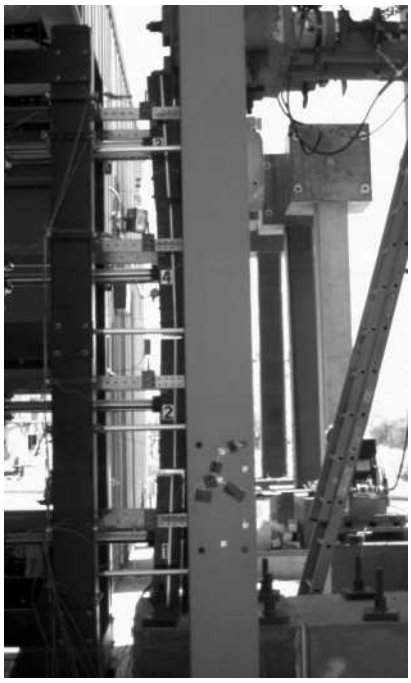

Figure 3.30: Maximum Deflection (Test 4, 8.1 ms)

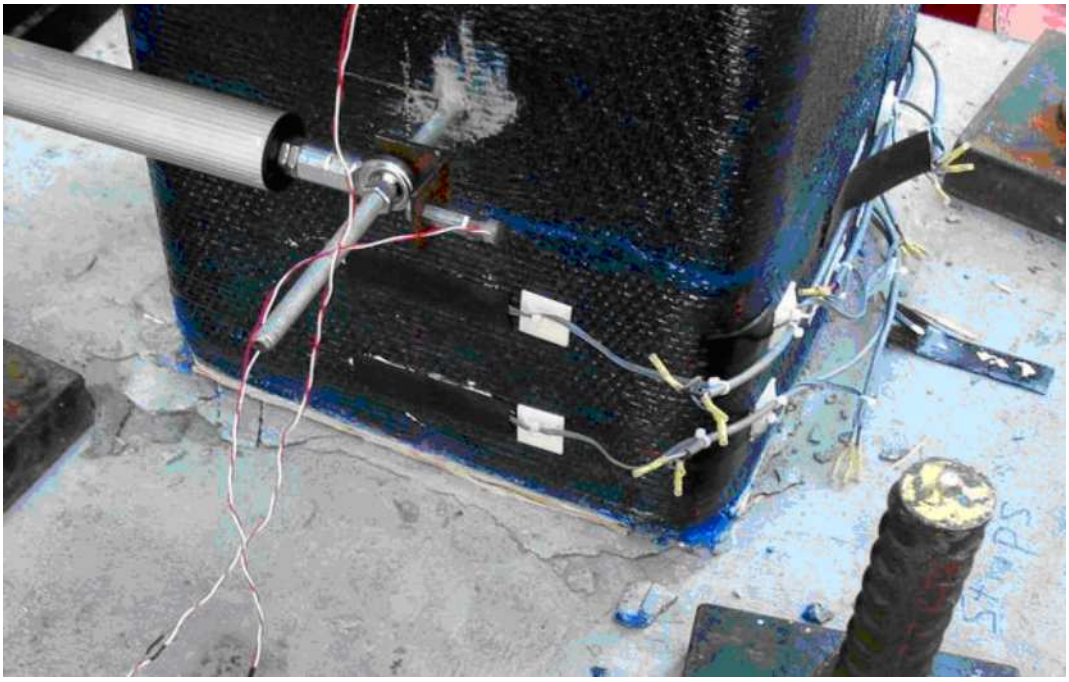

Figure 3.31: Yield Penetration (Test 4)

Figure 3.32: Specimen Prior to Impact (Test 5, -2.2 ms)

3.C.4 Test 5, Six-Wrap

Initial Setup

Test 5 was conducted on April 21, 2005 on a column retrofitted with a 6-layer CFRP jacket. This was the second of the column commissioning tests. For consistency across commissioning tests, the impact masses were set at the same settings as in the first such test (Test 4), and thus an average velocity of just over 17 m/s was targeted in this test. The column was set up with the axial load frame, the jacks were brought up to pressure and locked off mechanically once 100 kips (445 kN) of axial load had been imposed on the column. Instrumentation was provided as per the instrumentation section for displacements, accelerations, and table movement. High speed video was also captured during the test. The BGs were arranged in configuration 3 for this test. The specimen is shown just prior to impact in Figure 3.32 (axial load frame in the foreground).

Table 3.23: BG Impact Details (Test 5)

BG	Impact Time ms	Impact Velocity m/s	Peak Time ms	Peak Value g	Last Contact ms
3D	0.00	16.7	0.48	1658	22.6
4C	0.49	16.8	0.85	1458	22.9
2B	0.49	17.3	1.12	1427	22.2
1A	0.84	17.6	1.27	1427	21.2
Average		17.1			

BG Behavior

The BGs impacted in the order 3D-4C/2B-1A; from top to bottom with the center two impacting simultaneously. The first impact was 52.27 ms after the data trigger. The peak measured acceleration is 1658 g (BG 3D), and the average of the impact velocities is 17.1 m/s. The total spread from first to last impact is 0.840 ms and from first to last peak is 0.792 ms, which is within the specification. Acceleration traces are shown in Figure 3.33 and impact times, velocities and peak values are summarized in Table 3.23. Two of the accelerometers produced suspect data. The accelerometer on BG 4C had large spikes over ten times greater than seen in any other trace. These were removed manually. The accelerometer used on BG 1A reported a large pulse starting at about 1.5 ms that is unlike those seen in any other record. According to the video record it is likely that this is due to large angular acceleration of the impacting mass. This pulse was removed from the record. The traces shown in Figure 3.33 represent the best attempt at corrections, but for this test, the data from these two instruments need to be viewed with some suspicion. The last contact times indicate that all BGs lingered on the specimen after impact. The acceleration traces show that the simultaneity was good and that the pulse shapes, especially at the beginning of the record, were very similar.

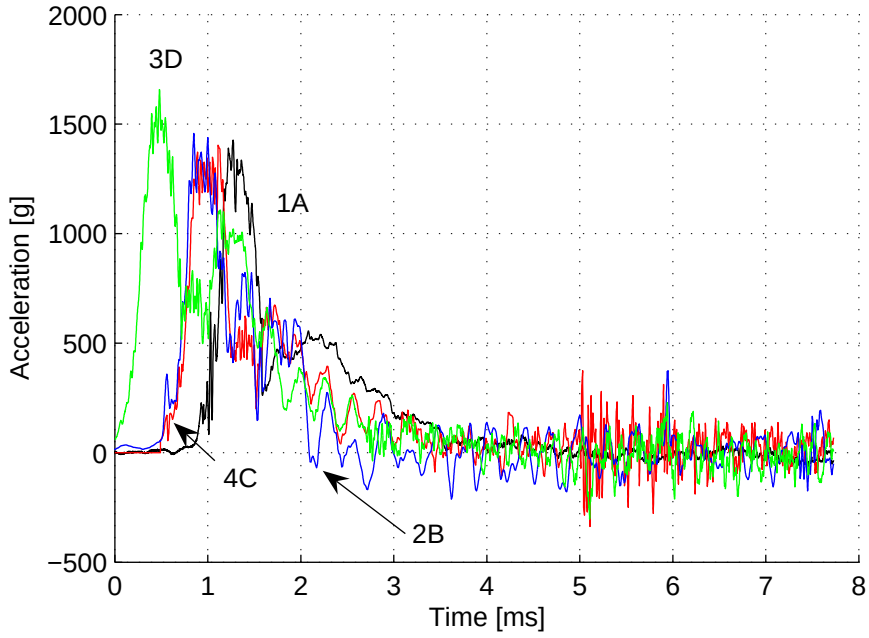

Figure 3.33: Accelerometer Readings (Test 5)

The equivalent pressure pulse (Figure 3.34) shows a slower initiation and a lower peak, but is otherwise consistent in shape with that of an actual blast. This is caused by the initial softness of the programmer and non-simultaneity of BG hits. The maximum equivalent pressure of 1500 psi (10.3 MPa) was measured at 0.99 ms after impact. Except for a slightly slower initiation, the shape of the equivalent impulse equivalent impulse (Figure 3.35) is very similar to that of an actual explosive. The maximum equivalent specific impulse is 1617 psi·ms (11.1 MPa·ms), which is equivalent to a 1230 lb (558 kg) charge of TNT at 14.2 ft (4.33 m). The 5%-95% pulse time is 2.55 ms. These values are summarized in Table 3.24.

Physical Description of Specimen Behavior

The majority of the specimen behavior was blocked from view by the vertical load frame, thus the description of the test itself comes mostly from the

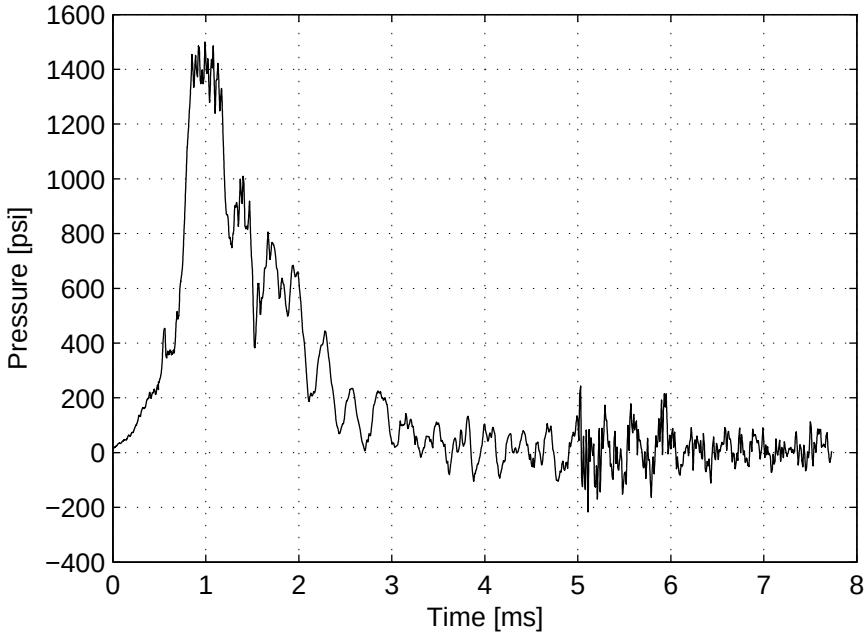

Figure 3.34: Equivalent Pressure (Test 5)

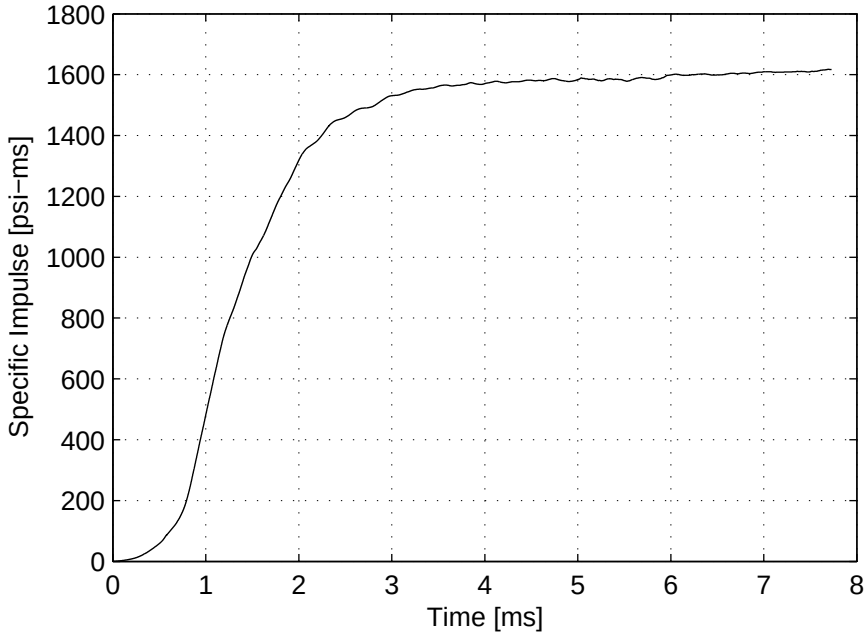

Figure 3.35: Equivalent Specific Impulse (Test 5)

Table 3.24: Equivalent Pulse Characteristics (Test 5)

Peak Pressure psi (MPa) ms	Impulse psi·ms (MPa·ms)	Pulse Time ms	Equiv. Standoff ft (m)
1500 (10.3) at 0.99	1617 (11.1)	2.55	14.2 (4.33)

Table 3.25: Specimen Response (Test 5)

Peak Defl. in (mm) ms	Res. Defl. in (mm)	Damage
1.6 (41) at 9.0	0.63 (16)	Practically None

collected data. Displacement measurements are difficult to make in large part due to the rod bending problem, discussed in depth in the instrumentation section, but because the BGs seem to remain in contact with the specimen past the point of maximum deflection, the BG displacement measurements from the video capture can aid in estimating the maximum deflections.

According to the potentiometer readings, the maximum deflection is 1.65 in (42 mm) at 15.7 ms, yet according to the video estimate, the maximum deflection is 1.6 in (41 mm) at 9.0 ms. It is assumed that the lag of the potentiometer peak response from that in the video is due exclusively to bending in the rods attaching the potentiometer to the specimen. Thus the maximum column response (Figure 3.36) is determined to have occurred at 9.0 ms with a peak displacement of 1.6 in (42 mm). The measured residual deflection is 5/8 in (16 mm). After the test hardly any damage was seen on the column indicating that the retrofit worked very well and that behavior was largely elastic. Some minor yield penetration was seen on the footing and some minor flexural cracking in the column was seen through openings in the horizontal fibers of the jacket. Only a surface inspection of the composite was carried out. The damage was so minor that it is very difficult to see in photographs. Specimen response parameters are summarized in Table 3.25.

Figure 3.36: Just Beyond Maximum Deflection (Test 5, 11.5 ms)

3.C.5 Test 6, Two-Wrap

Initial Setup

Test 6 was conducted on April 28, 2005 on a column retrofitted with a two-wrap CFRP jacket. This was the third of the column commissioning tests and the last of the retrofitted specimens. For consistency across commissioning tests, the impact masses were set at the same settings as in the first such test (Test 4), and thus an average velocity of just over 17 m/s was targeted in this test. The column was set up with the axial load frame, the jacks were brought up to pressure and locked off mechanically once 100 kips (445 kN) of axial load had been imposed on the column. Instrumentation was provided as per the instrumentation section for displacements, accelerations, and table movement. High speed video was also captured during the test. The BGs were arranged in configuration 3 for this test. The specimen is shown prior to impact in Figure 3.37 (axial load frame in the foreground).

BG Behavior

The BGs impacted in the order 1A-2B-3D-4C, with the first impact 51.88 ms after the data trigger. The peak measured acceleration is 1876 g (BG 3D), and the average of the impact velocities is 17.5 m/s. The total spread from first to last impact is 0.450 ms and from first to last peak is 0.406 ms, which is within the specification. Acceleration traces are shown in Figure 3.38 and impact times, velocities and peak values are summarized in Table 3.26. The last contact times indicate that all BGs lingered on the specimen after impact. The BG acceleration pulses show that all BGs hit with remarkably similar timing and pulse shapes at the beginning of the time-history.

The equivalent pressure pulse (Figure 3.39) shows a slower initiation and lower peak, but is otherwise consistent in shape with that of an actual blast. This is caused by the initial softness of the programmer and non-simultaneity of BG

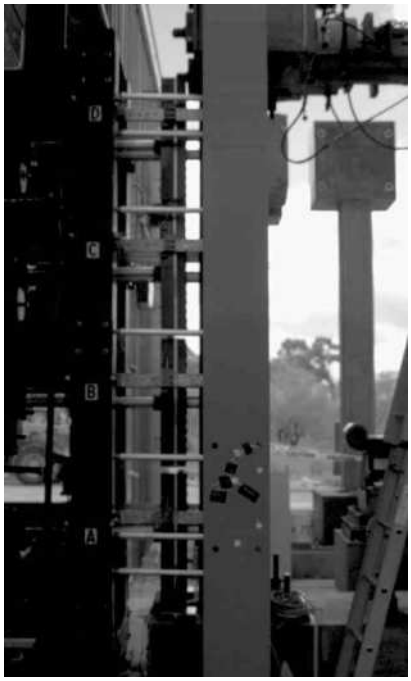

Figure 3.37: Specimen Prior to Impact (Test 6, -4.2 ms)

hits. The maximum equivalent pressure of 1582 psi (10.9) was measured at 0.72 ms after impact. Except for a slightly slower initiation, the shape of the equivalent impulse (Figure 3.40) is very similar to that of an actual explosive. The maximum equivalent specific impulse is 1623 psi·ms (11.2 psim), which is equivalent to a 1230 lb (558 kg) charge of TNT at 14.2 ft (4.33 m). The 5%-95% pulse time is 2.32 ms. These values are summarized in Table 3.27.

Physical Description of Specimen Behavior

The majority of the specimen behavior was blocked from view by the vertical load frame, thus the description of the test itself comes mostly from the collected data. Displacement measurements are difficult to make in large part due to the rod bending problem, discussed in depth in the instrumentation section, but because the BGs seem to remain in contact with the specimen past the point of maximum deflection, the BG displacement measurements from the video capture

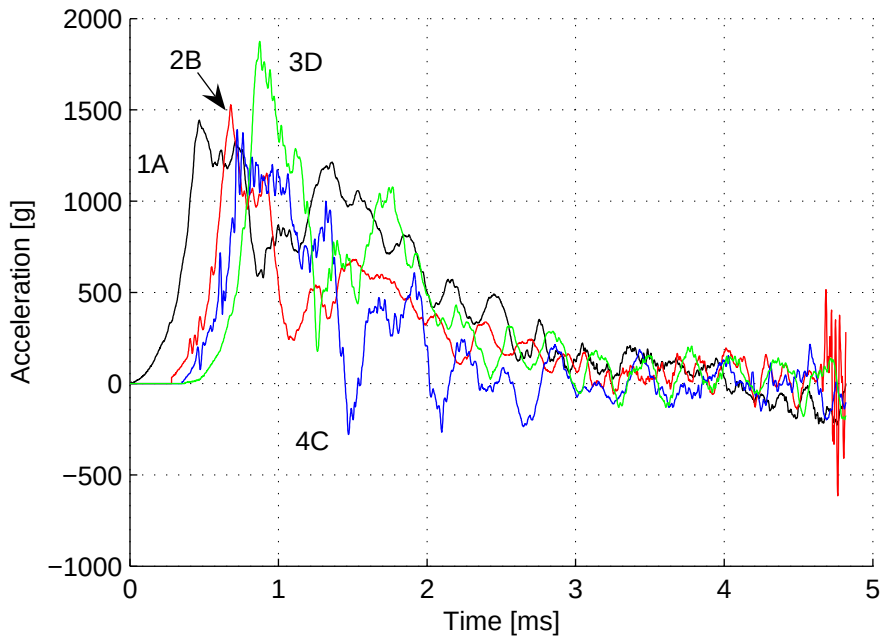

Figure 3.38: Accelerometer Readings (Test 6)

Table 3.26: BG Impact Details (Test 6)

BG	Impact Time ms	Impact Velocity m/s	Peak Time [ms]	Peak Value g	Last Contact ms
3D	0.370	17.3	0.874	1876	20.5
4C	0.450	17.0	0.723	1391	24.9
2B	0.280	17.9	0.679	1528	24.2
1A	0.000	17.9	0.468	1444	19.5
Average		17.5			

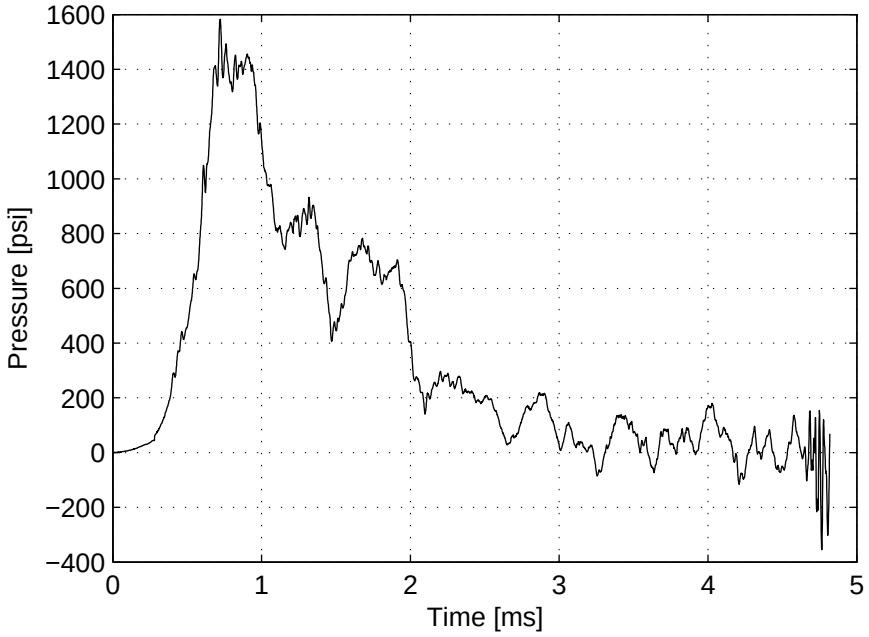

Figure 3.39: Equivalent Pressure (Test 6)

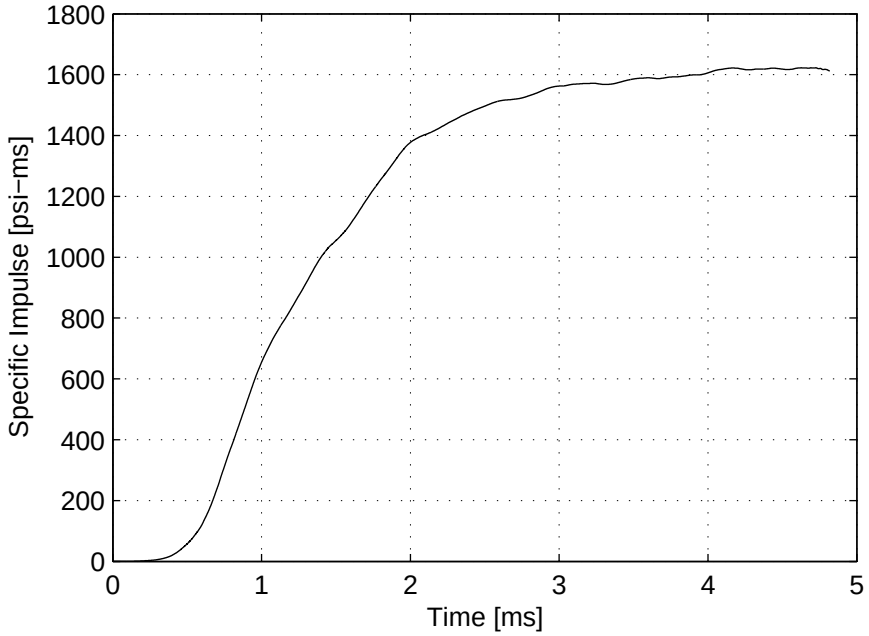

Figure 3.40: Equivalent Specific Impulse (Test 6)

Table 3.27: Equivalent Pulse Characteristics (Test 6)

Peak Pressure psi (MPa)	ms	Impulse psi·ms (MPa·ms)	Pulse Time ms	Equiv. Standoff ft (m)
1582 (10.9)	at 0.72	1623 (11.2)	2.32	14.2 (4.33)

Table 3.28: Specimen Response (Test 6)

Peak Defl. in (mm)	ms	Res. Defl. in (mm)	Damage
1.9 (48)	at 9.4	0.8 (20)	Practically none

can aid in estimating the maximum deflections.

According to the potentiometer readings the maximum deflection is 1.9 in (48 mm) at 17.4 ms, yet according to the video estimate, the maximum deflection is 1.9 in (48 mm) at 9.4 ms. The lag of the potentiometer peak response from that in the video is due to bending in the rods attaching the potentiometer to the specimen. Thus, the maximum column response (Figure 3.41) is determined to have occurred at 9.4 ms after impact, with a peak displacement of 1.9 in (48 mm). No field measurement of residual displacement was made and the potentiometer data are unreliable both because of the rod bending problem and because data collection stopped while the column was still vibrating. However, averaging peaks at the end of the potentiometer displacement trace suggests that the residual displacement is approximately 0.8 in (20 mm). After the test hardly any damage was seen on the column indicating that the retrofit worked very well and that behavior was largely elastic. Some minor yield penetration was seen on the footing and some minor flexural cracking in the column was seen through openings in the horizontal fibers of the jacket. Only a surface inspection of the composite was carried out. The damage is so minor that it is not easily visible in photographs, thus none are attached. Specimen response parameters are summarized in Table 3.28.

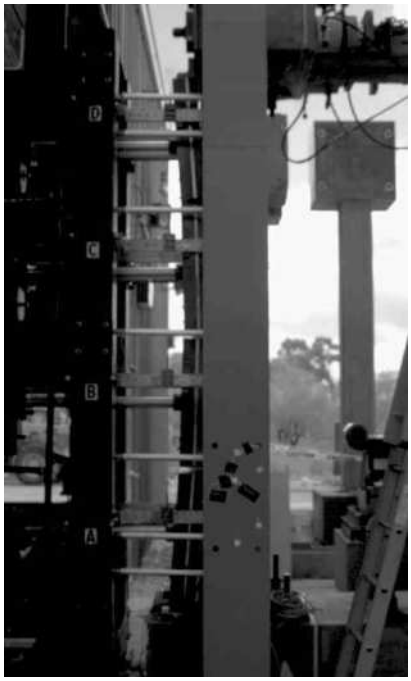

Figure 3.41: Maximum Column Deflection (Test 6, 9.4 ms)

Figure 3.42: Specimen Prior to Impact (Test 7, -2.7 ms)

3.C.6 Test 7, As-Built

Initial Setup

Test 7 was conducted on May 4, 2005 on an as-built column. This was the fourth of the column commissioning tests. For consistency across commissioning tests, the impact masses were set at the same settings as in the first such test (Test 4), and thus an average velocity of just over 17 m/s was targeted in this test. The column was set up without the axial load frame. Instrumentation was provided as per the instrumentation section for displacements, accelerations, and table movement. High speed video was also captured during the test. The BGs were arranged in configuration 3 for this test. The specimen is shown just prior to impact in Figure 3.42.

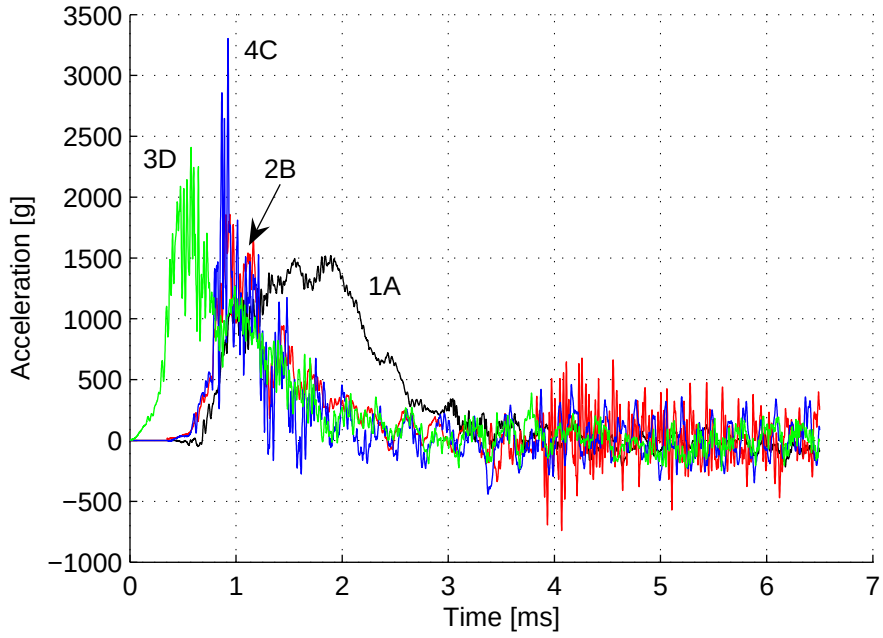

Figure 3.43: Accelerometer Readings (Test 7)

BG Behavior

The BGs impacted in the order 3D-4C/2B-1A; first the top, then the center two, and then the bottom. The first impact was 52.50 ms after the data trigger. The peak measured acceleration is 3304 g (BG 4C), and the average of the impact velocities is 17.3 m/s. The total spread from first to last impact is 0.430 ms and from first to last peak is 1.316 ms, which is within the specification. Acceleration traces are shown in Figure 3.43 and impact times, velocities and peak values are summarized in Table 3.29. The last contact times indicate that the center BGs lingered on the specimen after impact. The acceleration traces show that all BGs except 1A hit with remarkably similar timing and pulse shape at the beginning of the time-history.

The equivalent pressure pulse (Figure 3.44) shows a slower initiation and a lower peak, but is otherwise consistent in shape with that of an actual blast. This is caused by the initial softness of the programmer and non-simultaneity of

Table 3.29: BG Impact Details (Test 7)

BG	Impact Time ms	Impact Velocity m/s	Peak Time ms	Peak Value g	Last Contact ms
3D	0.00	17.2	0.576	2410	7.3
4C	0.36	17.0	0.925	3304	27.7
2B	0.35	17.2	0.942	1858	34.0
1A	0.43	17.6	1.892	1518	11.3
Average		17.3			

Table 3.30: Equivalent Pulse Characteristics (Test 7)

Peak Pressure psi (MPa)	ms	Impulse psi·ms (MPa·ms)	Pulse Time ms	Equiv. Standoff ft (m)
2753 (19.0)	at 0.93	1598 (11.0)	2.01	14.3 (4.36)

BG hits. The maximum equivalent pressure of 2753 psi (19.0 MPa) was measured at 0.93 ms after impact. Except for a slightly slower initiation, the shape of the equivalent impulse equivalent impulse (Figure 3.45) is very similar to that of an actual explosive. The maximum equivalent specific impulse is 1598 psi·ms (11.0 MPa·ms), which is equivalent to a 1230 lb (558 kg) charge of TNT at 14.3 ft (4.36 m). The 5%-95% pulse time is 2.01 ms. These values are summarized in Table 3.30.

Physical Description of Specimen Behavior

Because the axial load frame was not used, the specimen behavior was clearly visible from the high speed video capture. At 3.0 ms the first shear crack began to open at the top of the column and extended from approximately 30 in (762 mm) down from the load stub to the top compression toe. At 3.7 ms a crack

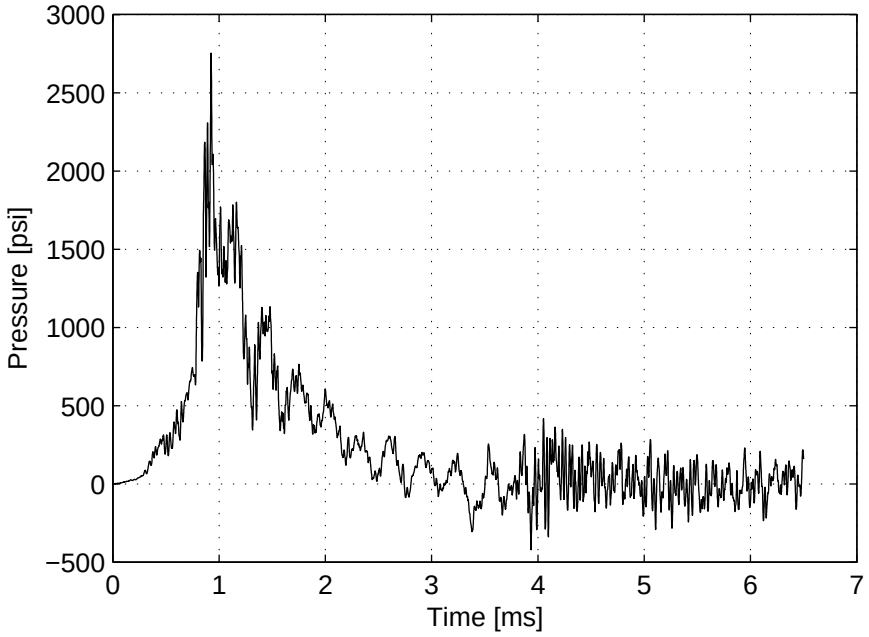

Figure 3.44: Equivalent Pressure (Test 7)

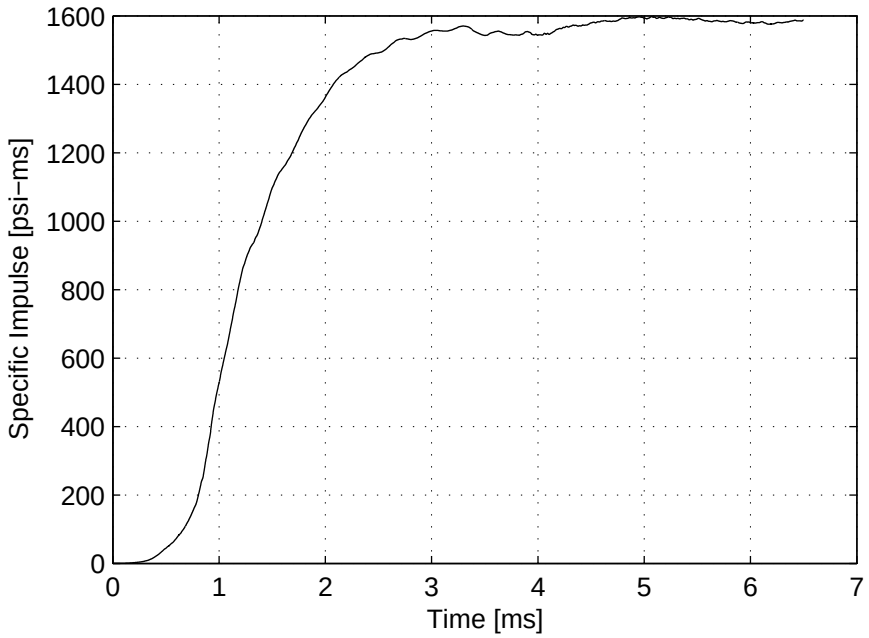

Figure 3.45: Equivalent Specific Impulse (Test 7)

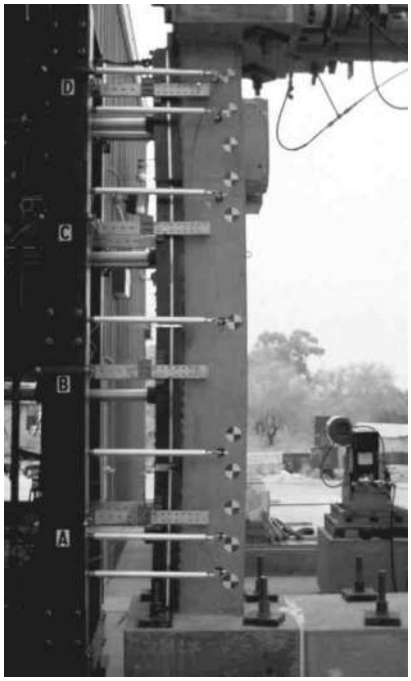

Figure 3.46: Initial Shear Cracks (Test 7, 3.7 ms)

opened at the base from approximately 25 in (635 mm) up from the footing to the bottom compression toe. At the same time, the top crack turned the corner and extended along the front cover concrete (Figure 3.46). At 4.3 ms, a second shear crack opened parallel to the one at the base, but about 35 in (889 mm) up from the first. At 6.7 ms, as the concrete degraded, secondary cracks opened in the vicinity of all the primary cracks described so far (Figure 3.47). At 9.0 ms the maximum upward axial deformation of 0.23 in (5.8 mm) was reached. At 7.3 ms the first of the BGs lost contact with the specimen. At 11.3 ms, the spalled cover concrete began to fall away from the column. The column descended axially and reached the initial location at 14.0 ms. At 19.3 ms, three small flexural cracks spaced at 6 in (152 mm) to 7 in (178 mm) opened at the center of the column. The last BG lost contact with the specimen at 34.0 ms and the maximum deflection of 4.81 in (122 mm) occurred at 41.7 ms (Figure 3.48). A dramatic sequence of progressive damage from 84 to 658 ms is shown in Figures 3.49, 3.50, and 3.51.

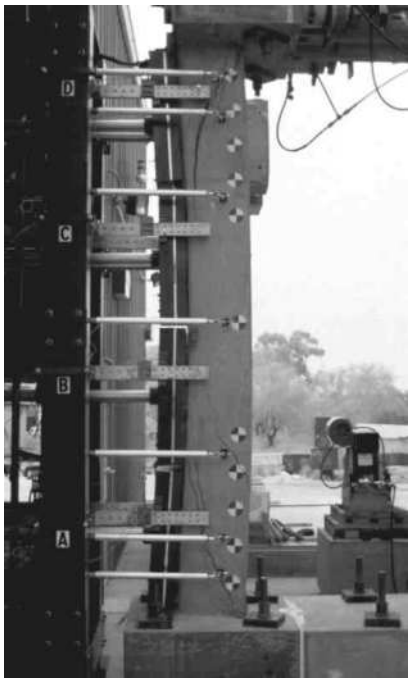

Figure 3.47: Progressing Shear Cracks (Test 7, 6.7 ms)

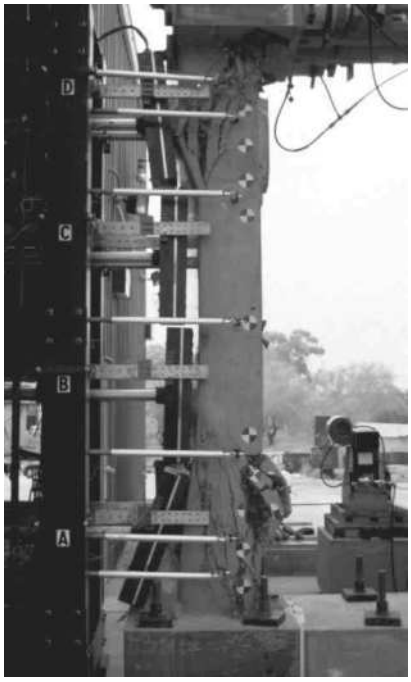

Figure 3.48: Progressing Shear Cracks (Test 7, 41.7 ms)

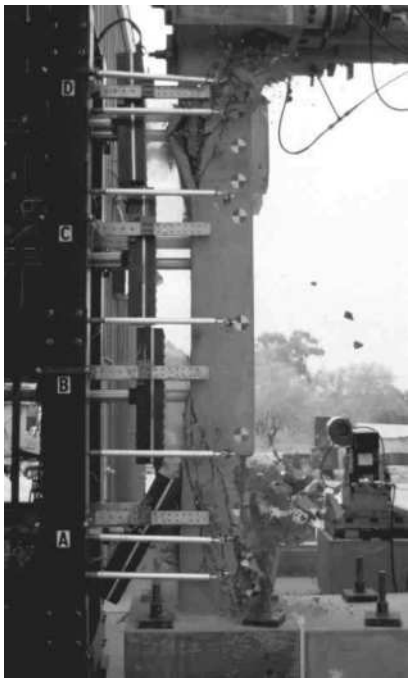

Figure 3.49: Advanced Damage (Test 7, 84.3 ms)

Figure 3.50: Advanced Damage (Test 7, 350 ms)

Figure 3.51: Advanced Damage (Test 7, 558 ms)

Table 3.31: Specimen Response (Test 7)

Peak Defl. in (mm)	ms	Res. Defl. in (mm)	Damage
4.8 (122)	at 41.7	3.33 (85)	Shear damage at top and bottom

At the end of the video capture (558 ms), the axial deflection was -0.27 in (-6.9 mm) and the horizontal deflection was 3.53 in (90 mm) while the residual deflection is 3.33 in (85 mm). The discrepancy is due to the video capture ending before the column stopped vibrating. A post-test investigation (Figure 3.52) exhibited two regions heavily damaged by the shear demand: one in the first 30 in (762 mm) at the top (Figure 3.53) and the other in the first 40 in (1016 mm) at the base (Figure 3.54). The center region was relatively undamaged with a center region exhibiting minor flexural cracking (Figure 3.55). Specimen response parameters are summarized in Table 3.31.

Figure 3.52: Specimen Post-Test (Test 7)

Figure 3.53: Top Damage Detail (Test 7)

Figure 3.54: Bottom Damage Detail (Test 7)

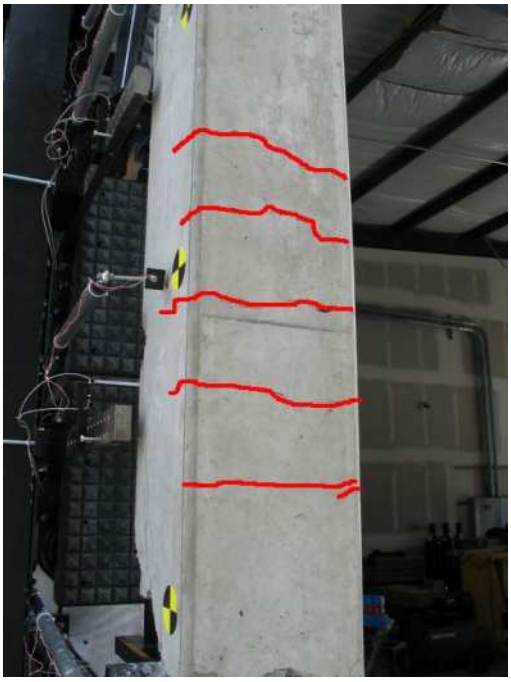

Figure 3.55: Flexural Cracks (Test 7)

Figure 3.56: Specimen Prior to Impact (Test 8, -6.1 ms)

3.C.7 Test 8, As-Built

Initial Setup

Test 8 was conducted on May 17, 2005 on an as-built column. This was the fifth and last of the column commissioning tests. For consistency across commissioning tests, the impact masses were set at the same settings as in the first such test (Test 4), and thus an average velocity of just over 17 m/s was targeted. The column was set up with the axial load frame, the jacks were brought up to pressure and locked off mechanically once 100 kips (445 kN) of axial load had been imposed on the column. Instrumentation was provided as per the instrumentation section for displacements, accelerations, and table movement. High speed video was also captured during the test. The BGs were arranged in configuration 3. The specimen is shown prior to impact in Figure 3.56 (axial load frame in the foreground).

BG Behavior

The BGs impacted in the order 3D-1A-4C-2B, with the first impact 52.360 ms after the data trigger. The peak measured acceleration is 1834 g (BG 3D), and the average of the impact velocities is 17.7 m/s. The total spread from first to last impact is 1.54 ms and from first to last peak is 1.416 ms, which is within the specification. Acceleration traces are shown in Figure 3.57 and impact times, velocities and peak values are summarized in Table 3.32. In this test the last contact times were difficult to determine because the view of the specimen was blocked by the vertical load frame. However, rough estimates are provided and they indicate that except for BG 1A, all other BGs lingered on the specimen after impact.

The equivalent pressure pulse (Figure 3.58) shows a slower initiation, a lower peak, and a small pulse before the main pulse, but is otherwise consistent in shape with that of an actual blast. This is caused by the initial softness of the programmer and non-simultaneity of BG hits. The maximum equivalent pressure of 1504 psi (10.4 MPa) was measured at 1.45 ms after impact. Except for a slightly slower initiation, the shape of the equivalent impulse equivalent impulse (Figure 3.59) is very similar to that of an actual explosive. The maximum equivalent specific impulse is 1616 psi·ms (11.1 MPa·ms), which is equivalent to a 1230 lb (558 kg) charge of TNT at 14.2 ft (4.33 m). The 5%-95% pulse time is 3.39 ms. These values are summarized in Table 3.33.

Physical Description of Specimen Behavior

Due to the presence of the vertical load frame, the specimen behavior was not visible through most of the test. Video measurements of displacement to supplement the potentiometer measurements were not possible. At 6.5 ms, the maximum upward axial deflection of 0.21 in (5.3 mm) was reached. Not until 7.2 ms, did the column begin to emerge beyond the vertical load frame. By 17.9 ms, a mass of spalled concrete was seen to be moving away from the column. The

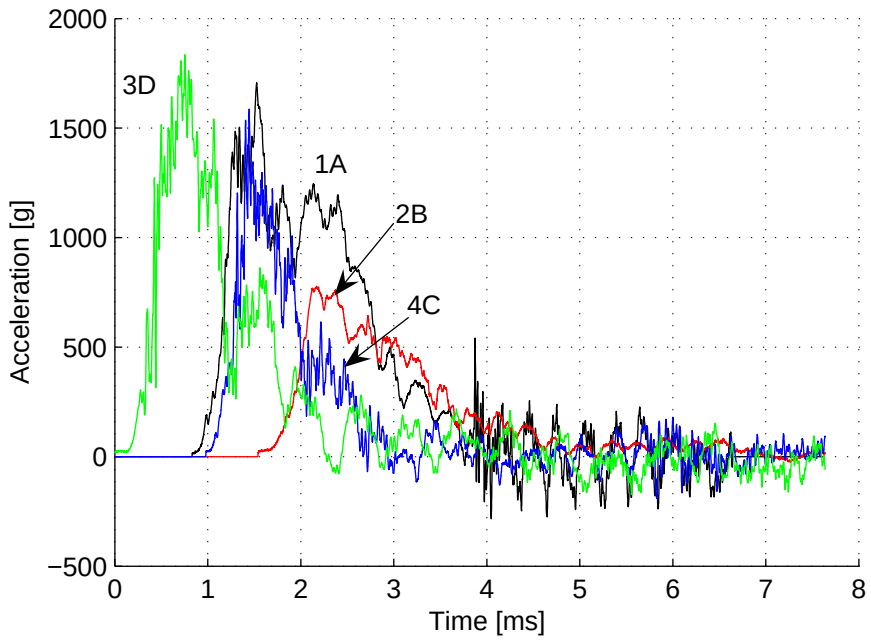

Figure 3.57: Accelerometer Readings (Test 8)

Table 3.32: BG Impact Details (Test 8)

BG	Impact Time ms	Impact Velocity m/s	Peak Time ms	Peak Value g	Last Contact ms
3D	0.00	17.6	0.754	1834	24.6
4C	0.98	17.4	1.445	1587	33.9
2B	1.54	17.7	2.170	778	33.9
1A	0.83	17.9	1.525	1707	6.6
Average		17.7			

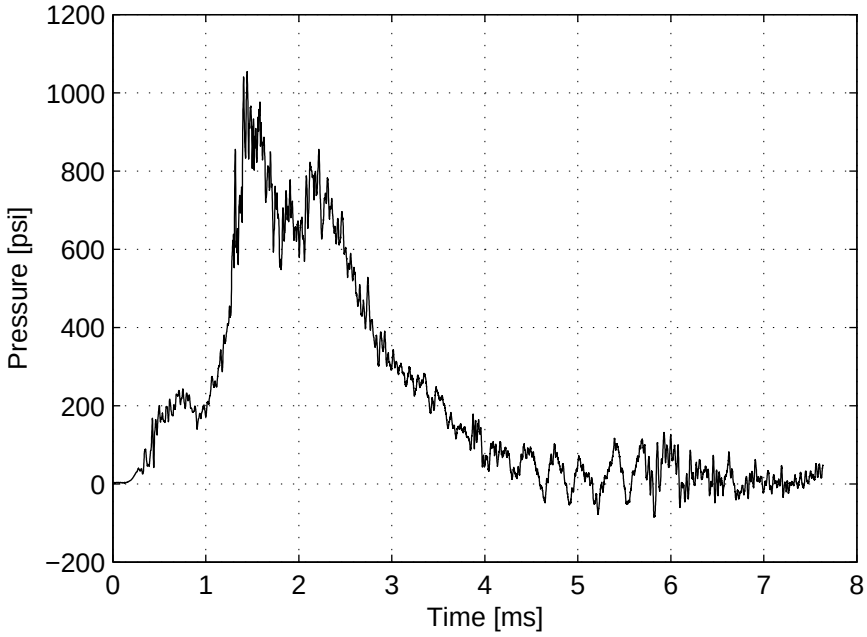

Figure 3.58: Equivalent Pressure (Test 8)

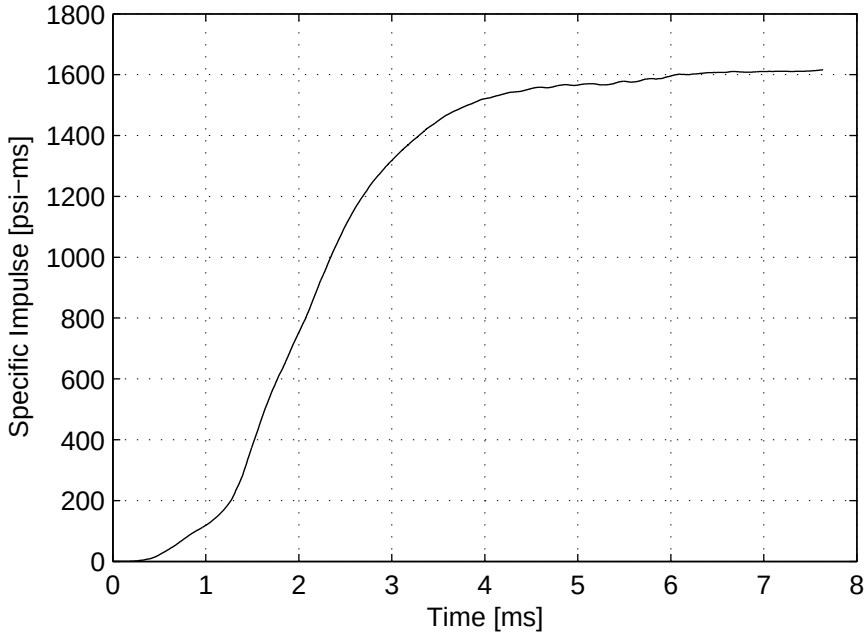

Figure 3.59: Equivalent Specific Impulse (Test 8)

Table 3.33: Equivalent Pulse Characteristics (Test 8)

Peak Pressure psi (MPa)	ms	Impulse psi·ms (MPa·ms)	Pulse Time ms	Equiv. Standoff ft (m)
1504 (10.4)	at 1.45	1616 (11.1)	3.39	14.2 (4.33)

Table 3.34: Specimen Response (Test 8)

Peak Defl. in (mm)	ms	Res. Defl. in (mm)	Damage
6.2 (157)	at 47.6	3.24 (82)	Shear damage at top and bottom

progression of this behavior is seen in Figures 3.60, 3.61, and 3.62. Graphical scaling of the video record can be used to estimate the maximum deflection at 6.2 in (157 mm) at 47.6 ms. The timing is also consistent with the maximum vertical deflection of -1.45 in (-36.8 mm) that occurs at 53.3 ms. The residual deflection is 3.24 in (82.3 mm). After the test, the column was inspected and was found to have two regions of shear failure at the top and bottom. These measured about 30 in (762 mm) and 40 in (1016 mm) respectively. The center region was relatively undamaged; the only signs of distress were minor flexural cracks. The column is shown post-test in Figure 3.63. Specimen response parameters are summarized in Table 3.34.

Figure 3.60: Incipient Damage (Test 8, 17.9 ms)

Figure 3.61: Damage Progressing (Test 8, 36.9 ms)

Figure 3.62: Advanced Damage (Test 8, 53.0 ms)

Figure 3.63: Specimen Post-Test (Test 8, removed from test fixture)

3.D Chapter Summary

The third chapter discusses the first-ever series of simulated blast tests. Because the simulated blast methodology is new, this requires the development of novel methods of data analysis: the equivalent uniform load method, which converts the loads imparted by a number of BGs to a single equivalent load and the equivalent charge method that converts this equivalent load to a representative charge size. The equivalent uniform load method is derived for a general case and it applies not only to the tests described in this chapter, but to other BG arrangements and even to field tests using real explosives. This method produces a single, rationally-obtained metric for comparing across laboratory and field tests.

The test results themselves are described in detail to provide the first-ever record of the structural behavior during a blast-like event. Unlike field blast tests, where the structural behavior is hidden by the fireball, the laboratory tests provide a view of the entire test sequence. Detailed text descriptions and video captures are provided for seven tests on retrofitted and non-retrofitted specimens. The results demonstrate once again the effectiveness of carbon fiber composite jackets in mitigating the damage caused by blast loads and lend credence to the validity of simulated blast.

4 Laboratory Characterization and Validation

This section covers developments that enable future investigators to use the blast simulation concept with confidence and ease. First, it is shown that the resulting data compare well to existing data from field tests, both qualitatively and quantitatively.

Next, attention turns to the needs of an investigator intending to use the facility. First, a methodology is developed by which the investigator can quickly and easily determine the blast generator impacting velocity settings necessary to produce a desired impulse. The predictive model is constructed from an SDOF-based theoretical development complemented by empirically-produced coefficient of restitution data. It is validated against independently obtained experimental data.

Next is developed a model of the constitutive behavior of the programmer to facilitate accurate and detailed finite element predictions and analyses of the test results. The load-deformation behavior of the programmer is first studied at low loading rates and then this baseline curve is modified via a physically-motivated dynamic increase factor. The model is in good agreement with the coefficient of restitution data and compares well to independent data. This comparison also makes it possible to characterize an oscillatory phenomenon observed in the BG acceleration traces, thus adding to the understanding of the system as a whole.

Figure 4.1: Pseudo-CSS Columns: DB8 (Left) and Test 4 (Right)

4.A Comparison to Field Data

The data resulting from blast simulations described in Chapter 3 compare well to existing data from field tests in the Divine Buffalo test series (see Section 1.C). The results from both tests are compared both qualitatively and numerically. The qualitative comparisons are drawn between post-mortem descriptions of similar specimens subjected to field and laboratory loading (Figures 4.1 and 4.2). The pseudo-CSS specimen from DB8 is compared to the one from Test 4; neither shows signs of significant damage or residual displacement. The as-built column from DB6 is compared to those from tests 2 and 7, which were tested at higher and lower levels, respectively. The columns exhibit the same failure mode in all three cases: severe shear damage at the top and bottom ends, a relatively undamaged center section, and a large permanent deformation. The tests at higher levels show increased deflection, degradation of core concrete, and spalling of cover concrete.

Figure 4.2: As-Built Columns: Test 2 (Left), DB6 (Center), and Test 7 (Right)

The numerical comparisons, in the form of a demand-damage curve, provide a strong argument for the correspondence between the two types of tests; the combined data when plotted together are indistinguishable and exhibit expected behavior: larger damage at lower standoff, lower damage for stronger retrofits, and initiation of damage at lower standoff for stronger retrofits.

The damage metric is simply defined as the residual deflection. Defining the demand metric requires more thought. While it may have been preferable to use the recorded impulse as the demand metric, the quality of field data was too poor to provide a useful means of comparison.[1] The equivalent charge concept

[1]Consider for instance, tests DB20, DB21, DB22, and DB28 (aramid-wrapped), all of which tested 14 in (356 mm) square specimens loaded by 1450 lb (758 kg) of ANFO at a 13 ft (3.96 m) standoff and elevated 3 ft (914 mm). The expected impulse in this case is 1814 psi·ms (12.5 MPa·ms) (see example in Section 1.A.1), but test data vary wildly: using the equivalent pulse methodology of Section 3.B.3 the equivalent impulse for test DB20 is 3096 psi·ms (21.3 MPa·ms), while for test DB22 it is 1438 psi·ms (9.91 MPa·ms). These fall far from the expected value and differ greatly from each other; the variance is too high for this to be a useful parameter for comparison.

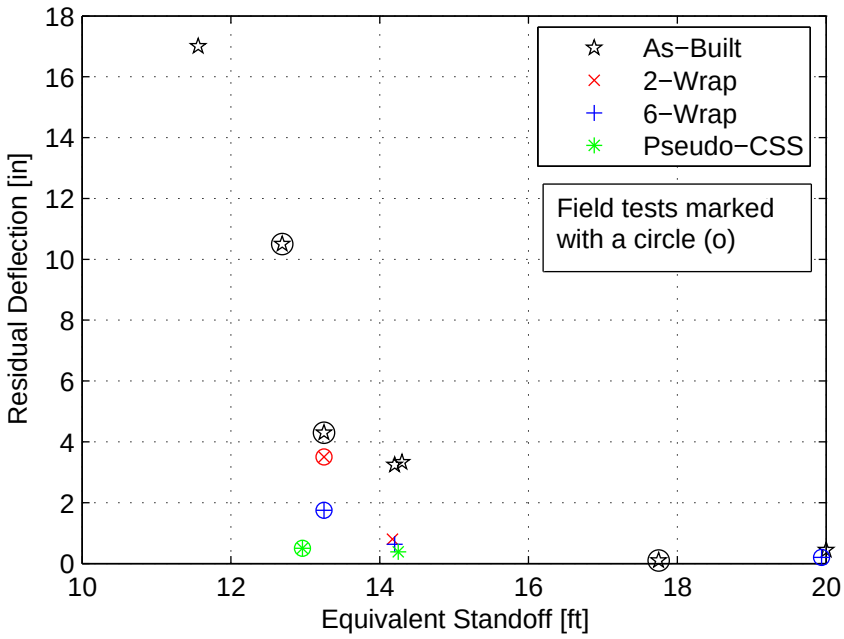

Figure 4.3: Lab and Field Comparison of All Columns

of Section 3.B.4 is used instead as the demand metric. The field specimens are loaded by charges of sizes varying from 1189 lb (539 kg) to 1284 lb (582 kg). These are also converted to an equivalent standoff by first calculating the impulse from the original charge size and standoff and then calculating the standoff at which a 1230 lb (558 kg) charge would have to be to cause the same impulse (the difference between the resulting and original standoff is small).

The equivalent standoff values previously reported in Chapter 3 for the laboratory tests and those calculated here for the field tests are combined with the residual deflection data previously reported in Section 1.C and Chapter 3. These data are presented for each specimen type in Table 4.1. The data confirm expectations, but graphical approach in the following paragraph will better elucidate the trends.

Figure 4.3 shows demand-damage points for each specimen type: as-built, two-wrap, six-wrap, and pseudo-CSS. At large standoffs all of the specimens are essentially undamaged, with residual deflections near zero. As standoff decreases,

Table 4.1: Laboratory and Field Comparison: As-Built Specimens

Type	Test	Standoff		Res. Defl.	
		ft	m	in	mm
As-Built	3	20.0	6.10	0.44	11
	DB06-2A3	17.8	5.43	≈ 0	≈ 0
	7	14.3	4.36	3.33	85
	8	14.2	4.33	3.24	82
	DB20	13.3	4.05	5.43	138
	DB06-2A3	12.7	3.87	10.5	267
	2	11.6	3.54	17	432
Two-Wrap	6	14.2	4.33	0.8	20
	DB22	13.3	4.05	3.5	89
Six-Wrap	DB08-1A3	20.0	6.10	≈ 0	≈ 0
	5	14.2	4.33	0.63	16
	DB21	13.3	4.05	1.75	44
Pseudo-CSS	4	14.3	4.36	0.38	10
	DB08-1A2	13.0	3.96	<1	<25

the residual deflection of the as-built specimen deviates from zero. At this same standoff, the retrofitted specimens are still undamaged. With a further reduction in standoff, the residual deflection of the two- and six-wrap specimens begins increasing, indicating that they are beginning to suffer damage, and that of the as-built specimen increases at a quicker rate, indicating that it has suffered near complete failure. The pseudo-CSS specimen never deviates from zero indicating negligible damage. At all load levels, the stronger retrofits suffer equal or lower damage than weaker retrofits, and in addition, stronger retrofits remain undamaged under larger loads than weaker retrofits. It is noteworthy that if the circles differentiating laboratory and field tests were removed from Figure 4.3, it would be impossible to distinguish the two types of tests from each other. That the the combined laboratory and field data fit well together and describe the expected demand-damage patterns provides a compelling argument in favor of the equivalence between the two.

4.B Impacting Mass Velocity Prediction

The theoretical methodology developed in this section allows investigators to quickly estimate the impacting velocity required for the blast generator to input a specified impulse to the specimen without needing to build an expensive and time-consuming finite element model. The model is built by satisfying conservation of momentum and an experimental coefficient of restitution (COR) relation; it is verified against the results obtained in Chapter 3. It gives an investigator an upper bound on the required velocity with errors less than 13% for the current set of columns. Loading on more flexible specimens can be estimated with a smaller error.

4.B.1 Theoretical Formulation

This formulation has been an ongoing development of mine; an earlier version was incorporated into a presentation at the Second *fib* (Federation Internationale du Beton) Congress, June 2006, in Naples, Italy [21]. The objective in this section is to predict the impacting mass velocity required to deliver a desired impulse to the specimen. This is accomplished with a pure impulse collision approach that satisfies conservation of momentum in a weak sense and a pointwise coefficient of restitution relation. Mass and impact velocity are both allowed to vary over the length of specimen. The fundamental relations are conservation of total momentum of the system,

$$\int_L m_1(x)\mathsf{v}_{1i}(x)\,\mathrm{d}x = \int_L m_1(x)\mathsf{v}_{1f}(x)\,\mathrm{d}x + \int_L m_2(x)\mathsf{v}_{2f}(x)\,\mathrm{d}x \tag{4.1}$$

and the coefficient of restitution (COR) equation

$$c_r(\mathsf{v}_{1i}(x)) = \frac{\mathsf{v}_{2f}(x) - \mathsf{v}_{1f}(x)}{\mathsf{v}_{1i}(x)} \tag{4.2}$$

where m_1 and m_2 are masses per unit length of the impacting masses and the specimen, respectively; v_{1i} is the initial velocity of the impacting mass; v_{1f} is the final

velocity of the impacting mass; and v_{2f} is the final velocity of the specimen. The coefficient of restitution c_r is determined from test data in the following section. In these experiments, c_r was determined to be a (mostly) decreasing function of impacting velocity. Since impacting velocity v_{1i} varies with x so does c_r.

The velocity functions are represented as

$$\mathsf{v}_{1i}(x) = \mathsf{v}_o \psi_1(x) \tag{4.3}$$

and

$$\mathsf{v}_{2f}(x) = \dot{z}_o \psi(x) \tag{4.4}$$

where the shape functions ψ_1 and ψ represent the variation of BG and specimen velocity, respectively, over the specimen height. The constant v_o represents the maximum velocity over the height of the column and ψ_1 is normalized to a maximum value of one. The notation used for v_{2f} agrees with that of the SDOF formulation where ψ is the shape function and z is the time component of deflection; $\dot{z}_o$ is then the time component of initial velocity.

Impulse is the change in momentum occurring during the impact (as in Equation (1.68)), which is written for a distributed mass column as

$$I = \int_L m_2(x) \mathsf{v}_{2f}(x) \, \mathrm{d}x \tag{4.5}$$

Combining Equations (4.1) to (4.5) (see derivation in Appendix A) yields the following expression:

$$\mathsf{v}_o \cdot \int_L m_1 (1 + c_r) \psi_1 \, \mathrm{d}x = I \cdot \left[\frac{\int_L (m_1 + m_2) \psi \, \mathrm{d}x}{\int_L m_2 \psi \, \mathrm{d}x} \right] \tag{4.6}$$

where the dependence on x has been omitted for clarity. Determining the impulse expected from a given velocity distribution is a simple matter of evaluating the expression for I. However, because c_r has a nonlinear dependence on velocity and is inside the integral, rearranging the expression to obtain a closed form solution for required velocity is not possible. Instead, the solution must be found iteratively.

The solution is simplified if the masses are independent of x. In this case the integral $\int_L \psi \, \mathrm{d}x$ cancels out of the expression in square brackets in Equation (4.6). This implies that the results are independent of the choice of mode shape. A further simplification can be made if the impact masses hit at the same velocity. In this case $\psi_1 = 1$, $\mathsf{v}_{1i} = \mathsf{v}_o$, and c_r is a constant (that depends on the value of v_o). This allows Equation (4.6) to be simplified to

$$\mathsf{v}_o = \frac{I \cdot (m_1 + m_2)}{(1 + c_r) \cdot m_1 \cdot m_2 \cdot L} \tag{4.7}$$

This is the same result that would have been obtained if the specimen and impact masses had been treated as point particles.

This is a pure impulse calculation; as such it does not consider any variation in pulse shape. As discussed in Chapter 1, this approach is expected to provide good accuracy if the ratio of pulse duration to structural period, t_d/T_n, is less than 0.25, which is marginally satisfied for the column tests reported in Chapter 3, as is now shown. The structural period $T_n = 2\pi\sqrt{\tilde{M}/\tilde{k}}$ is rewritten using Equations (1.41) and (1.42) as

$$T_n = 2\pi\sqrt{\frac{C_m}{C_k}\frac{mL^4}{EI}} \tag{4.8}$$

where $C_m/C_k = 1/504$ for a fixed-fixed beam, and 31/3024 for a pinned-pinned beam. Using $EI \approx 0.5EI_g$, where EI_g is the gross section stiffness, and a pulse time of $t_d = 3.5$ ms, which is larger than any of the experimentally observed pulse times, the period ratio t_d/T_n is 0.124 in the pinned end case and 0.283 in the fixed end case. In reality, because the actual boundary conditions are imperfectly fixed, the period ratio is somewhere between the two. In either case, it is close enough to 0.25 that this method has to be understood to contain a certain amount of systematic error due to the assumption of pure impulse.

In addition to this error, there is a much larger component of error due to the lack of synchronization of the BGs and the nonlinearity of COR with velocity. During an actual test, one of the BGs will hit the specimen first, which accelerates the specimen before the later BGs hit. When they do, the approach velocity is

now reduced because the specimen is travelling away from it. The lower approach velocity results in a higher COR, which means that a greater proportion of the approach velocity is transferred to the specimen. Yet transferring a greater proportion of a now reduced approach velocity suggests nothing about the ultimate change in the final velocity of the specimen. As shown by Equation (1.66) the final velocity of the specimen depends on the magnitudes of the impacting masses, the specimen, their initial velocities, and the COR.

To understand better what the effect might be, a side study was conducted; Equation (1.66) was applied to two simple cases that bound the actual behavior. The first is with all BGs hitting at the same time, as is assumed by the proposed method , and the other is with each BG hitting one after the other with no overlap, an extreme case of the actual behavior. This study determined that the proposed method can either overestimate or underestimate the actual behavior, depending on the ratio of the specimen mass to that of the total impacting mass. If this ratio is near unity, as it currently is, then for a given impacting velocity the proposed method will underestimate the impulse delivered to the specimen. Conversely, the proposed method will overestimate the velocity required to deliver a desired impulse.

4.B.2 Test Data

With the theory developed and the expected error characterized, what remains to be done is to experimentally determine the COR-velocity relation. This is done with the factory acceptance test (FAT) described in Section 2.C, which involve firing a BG with a standard mass and programmer at impact velocities from 9 to 29 m/s at a second catcher BG in a self-reacting frame (Figure 4.4). The primary purpose of these tests was to test the functioning of each BG prior to shipment to the Explosive Loading Laboratory. Sufficient data were collected to make preliminary indications about the coefficient of restitution of the programmer.

The data were reduced and analyzed by M. Gram at MTS and reported

Figure 4.4: Factory Acceptance Test Setup

to UCSD in late February, 2006 [18]. Gram subtracted the hydraulic, friction and nitrogen forces present during the collision to extract from the data the behavior that would have occurred in a pure collision. Two series of tests were carried out, each on a different programmer. In all, nine data points are available and are presented in Table 4.2 and plotted in Figure 4.5 along with an interpolating function. As velocity increases, the COR decreases and its slope becomes less negative. The data are fitted with the following quadratic curve

$$c_r(\mathsf{v}) = 0.6476 - 0.02774 \cdot (\mathsf{v}) + 5.517 \cdot 10^{-4} \cdot (\mathsf{v})^2 \qquad (\mathsf{v} \text{ in m/s}) \qquad (4.9)$$

The fitted curve has a coefficient of determination of 0.91 and the following 95% confidence bounds on the constant, linear and quadratic coefficients, respectively: (0.5072,0.7881), (-0.04445,-0.01103), and $(1.087 \cdot 10^{-4}, 9.947 \cdot 10^{-4})$. The fit is good, but there is still a need for further characterization. Tests are currently underway at the Explosive Loading Laboratory to more accurately assess the COR of the programmer. Once these tests are completed, the data can be incorporated into the methodology developed here by substituting a different function for the COR. The interpolating function has a small rise at velocities greater than about 25 m/s that is not explained by physical reasoning; it is simply an artifact of the form of

Table 4.2: Velocity-COR Relation from FAT Data

Specimen 1		Specimen 2	
Vel. [m/s]	COR	Vel. [m/s]	COR
9.260	0.448	9.045	0.426
15.212	0.374	-	-
19.828	0.330	19.637	0.285
25.760	0.308	25.406	0.282
28.017	0.318	28.520	0.299

the fitting function and the scatter of data. No effort is made to complicate the formulation to remove this effect, largely because the quadratic formulation leads to good estimates, but also because the effect is small and because new data are being collected.

This relation is valid only for the programmers used in these tests. Other programmers have been built for other tests and it is unknown whether the COR is the same for these. The extensive battery of tests currently underway to measure the COR for a variety of different programmers will likely answer this question.

4.B.3 Model Validation

For validation the predictive tool is compared to the test results of Chapter 2. It was previously argued that the model overestimates the velocity required to apply a desired impulse; this error is now quantified. For all tests but Test 3, which used only three BGs over only part of the column, the impulse produced by BGs hitting at a constant average velocity v_o is given by rearranging Equation (4.7) and by converting impulse to specific impulse with $I = i\,b\,L$ to obtain

$$i = \frac{(1 + c_r(\mathsf{v}_o))\,\mathsf{v}_o\,m_1\,m_2}{b\,(m_1 + m_2)} \tag{4.10}$$

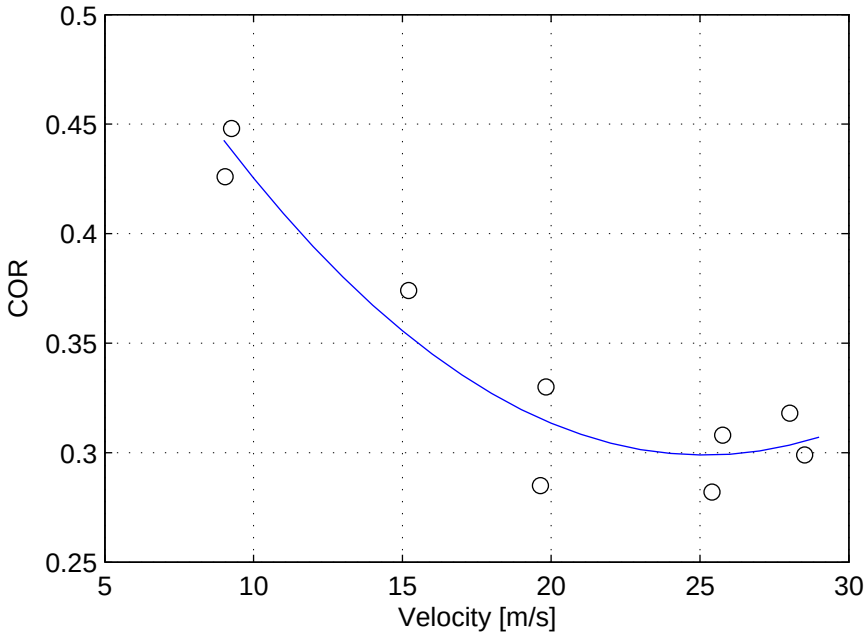

Figure 4.5: Velocity-COR Relation from FAT

where

$$m_1 = \frac{4M_{bg}}{L} \tag{4.11}$$

$$m_2 = b\,h\,\rho_v \tag{4.12}$$

and where b is the column width, L is its length, h is its depth, M_{bg} is the mass of an individual impacting mass, and ρ_v is the volumetric mass density of concrete.

In Test 3, where the BGs hit over only part of the column, the simplifications used in deriving Equation (4.7) are not valid, and the more general form of Equation (4.6) must be used. The specific impulse produced by three BGs impacting at a constant average speed v_o ($\psi_1 = 1$) is

$$i = \frac{\mathsf{v}_o \cdot (1 + c_r(\mathsf{v}_o)) \cdot \left[\int_L m_1\,\mathrm{d}x\right] \cdot \left[\int_L m_2 \psi\,\mathrm{d}x\right]}{b \cdot L \cdot \int_L (m_1 + m_2)\,\psi\,\mathrm{d}x} \tag{4.13}$$

where

$$m_1(x) = \begin{cases} \frac{3\,M_{bg}}{L - 2L_u} & L_u \le x \le L - L_u \\ 0 & \text{otherwise} \end{cases} \tag{4.14}$$

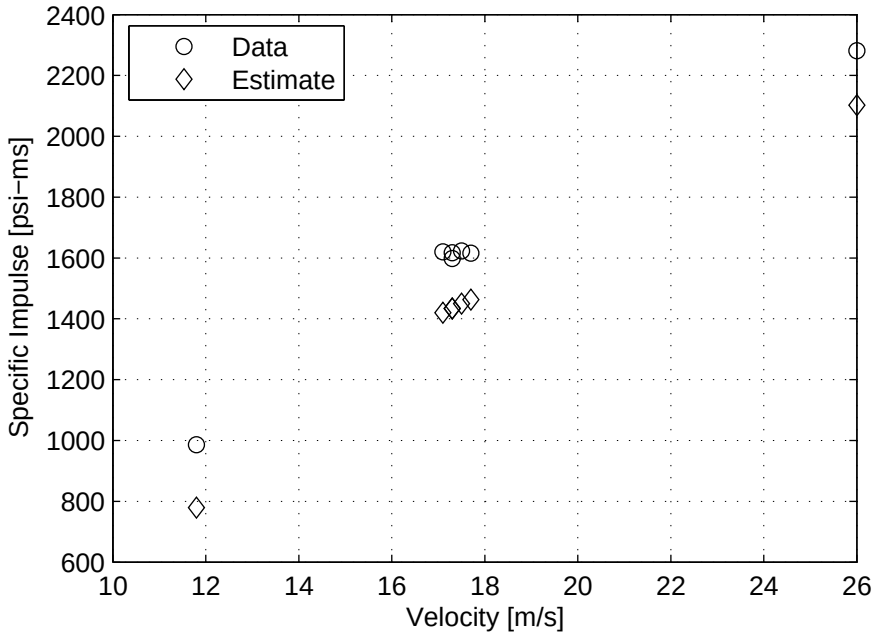

Figure 4.6: Specific Impulse Estimate Versus Actual

and where $L_u = 16.5$ in (419 mm) is the unloaded length at the top and bottom of the column and $\psi(x) = \psi_{ff}(x)$, the shape function for the fixed end beam given by Equation (1.47).

For all the column tests in Chapter 2, the recorded average impact velocity is used as input for v_o and the estimated specific impulse i is computed and compared to the equivalent specific impulse $\bar{\imath}$ (Figure 4.6). The estimated impulse falls below the recorded impulse by between 153 psi·ms (1.05 MPa·ms) to 207 psi·ms (1.43 MPa·ms) with an average difference of 180 psi·ms (1.24 MPa·ms). The percent error is larger for the lower level tests (21%), lower for mid-level tests (average of 12%), and even lower for the high level test (9%). This is consistent with the expected systematic error, which says that the predicted impulse will be lower than the actual impulse for any given velocity.

Of greater interest to future investigators is to know the error involved in estimating the required impact velocity for a desired impulse. To this end,

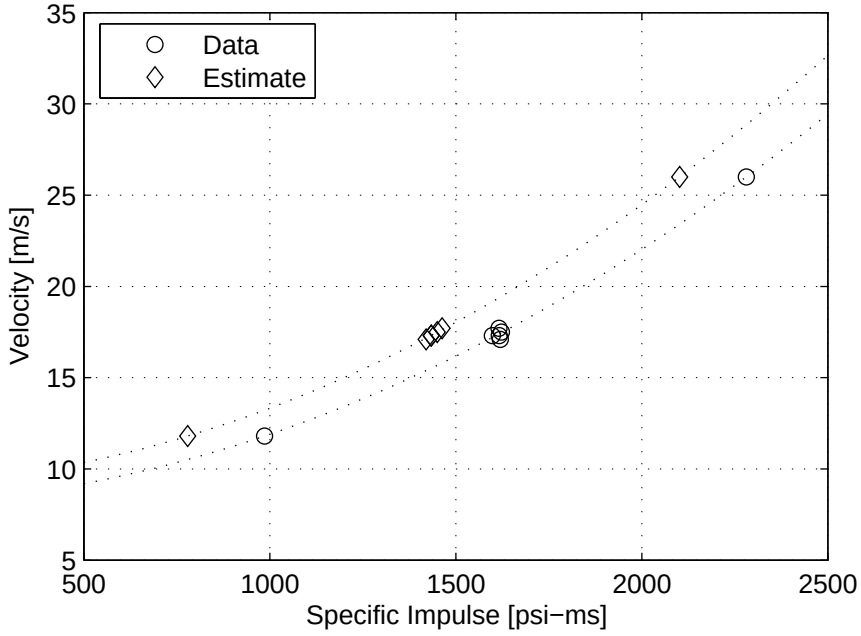

Figure 4.7: Impacting Velocity Estimate Versus Actual

the variables in Figure 4.6 are plotted in Figure 4.7 but on opposite axes and along with interpolating functions. The figure is in agreement with the expected error; the prediction overestimates the necessary velocity. To make a more useful predictive model, the error is quantified by subtracting the interpolating functions from each other; the resulting error curve is shown in Figure 4.8. Percent errors decrease with increasing impulse and are between 10% and 13%. The magnitude of the error increases with increasing impulse and can be as large as 3.2 m/s at an impulse of 2500 psi·ms (17.2 MPa·ms). With the error quantified in this way, an investigator can accurately estimate the required velocity by subtracting the estimated error from the calculated estimate. With the data currently available, the error can only be determined for ratios of total BG mass to specimen mass near unity. Further studies are required to investigate how the error relates to the masses used.

In summary, to estimate the required velocity for a desired specific im-

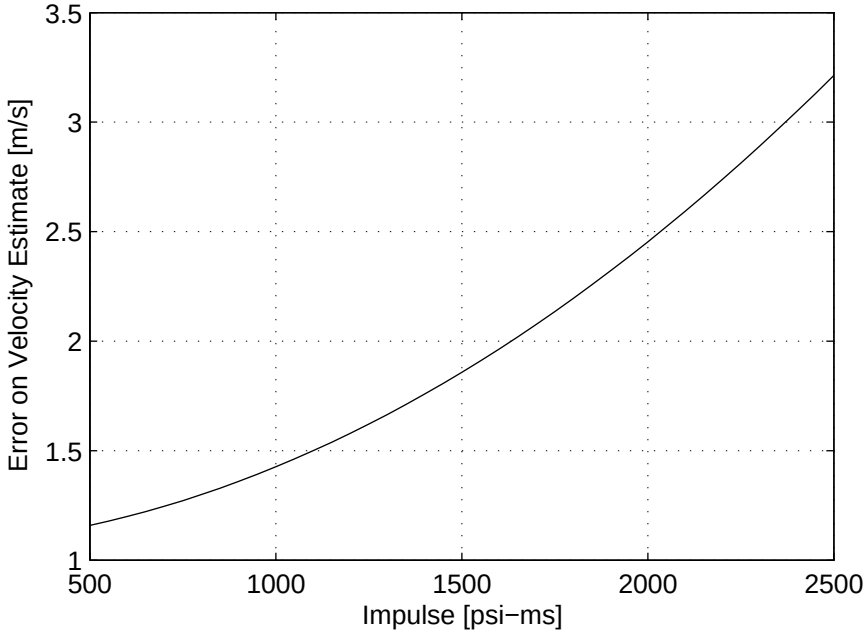

Figure 4.8: Error of Impacting Velocity Estimate

pulse, an investigator will define the masses m_1 and m_2 and iteratively solve either Equation (4.10) or Equation (4.13) for v_o, depending on whether or not the masses are constant over the column height. Both equations use the fitted COR relation given by Equation (4.9), which is only valid for the programmers used in these tests and for which studies are currently underway to refine the relation. Once a preliminary estimate is found in this way, Figure 4.8 is used to find the error correction, which is subtracted from the preliminary estimate. These results will provide very good estimates for columns of similar natural period as those in Chapter 3. To use the methodology for different specimens requires a degree of judgement on the part of the investigator. Estimates on more flexible specimens will suffer a smaller error and the error estimate will need to be reduced accordingly. Care is cautioned for stiffer specimens because the estimated velocity will be much greater than the required velocity; if this difference is not accurately taken into account, a dangerous testing environment may result.

4.C Programmer Characterization

A detailed finite element analysis of a simulated blast event requires proper modelling of the constitutive behavior of all important components. While the constitutive modelling of concrete is not fully understood and is still in the development phase there are adequate models for its behavior, e.g., the so-called K&C model discussed in Chapter 1. However, no information is currently available to model the programmers. All analyses to date have been performed in an *ad-hoc* manner. One approach has been to use a linear elastic material with a reduced impact velocity to account for viscous losses. A more sophisticated approach was later taken by K&C: using the test data presented in this chapter they made a simple conversion of the quasi-static load-deformation response to engineering stress-strain and adjusted LS-DYNA model 57 (low-density urethane foam) to match the stress-strain curve [14]. This approach is far better than the previous one, but still no consideration was made for dynamic effects, thus grossly underestimating damping losses and overestimating the energy deposited on the specimen. In all cases, the constitutive properties were determined informally by eyeballing the data.

Prior methods worked well at the time and for their intended purpose. With them we began to understand the underlying phenomena and we were able to proceed with the experimental testing. However, in the interest of completeness and to provide more accurate tools for the future, a proper constitutive model for the programmer is a necessary development.

To this end, two approaches are developed. The first is a phenomenological hysteretic approach that describes the force-deformation behavior of the programmer; it is developed fully in this chapter with extensions being discussed in the following chapter. The second is a one-dimensional material characterization based on a viscoelastic model; it is presented in the following chapter schematically as suggestions for further research.

The phenomenological model is built in two main steps. First, experimental quasi-static testing is used to establish a baseline hysteresis curve. Next, a physically-motivated dynamic increase factor is advanced and its parameters are fit using the coefficient of restitution data from the factory acceptance tests. The model is verified against independent data and in the process some features of the BG behavior are discovered.

4.C.1 Test Data

The programmer assembly was tested at the UCSD Powell Labs CalTrans SRMD test facility on March 21 and 22, 2005. The programmer was loaded a total of nineteen times at various loading rates, which because of test rig limitations were all significantly lower than those seen in blast simulations. Data were collected for force applied to and deformation suffered by the programmer. The programmer tested was identical to that used in blast simulation tests on column specimens.

The programmer assembly was placed between thick steel plates and loaded in compression by an actuator pushing upward onto a steel reaction beam. Four linear potentiometers were placed near each corner of the programmer to measure the compressive deformation of the specimen, which was taken as the average of the four readings. Force was measured directly by the actuator. The SRMD test facility was chosen because it was the only facility able to develop the force necessary to apply a large deformation to the programmer. Unfortunately, this facility does not allow direct control of specimen deformation. Instead, the actuator displacement is controlled directly and the specimen deformation is determined by a combination of the actuator displacement and that of the reaction structure. It is thus impossible to exactly control the deformation rate in such a way to subject the specimen to a constant (or zero) deformation rate. However, the deformation rates obtained showed only small variations from a constant value.

All specimens were loaded in three segments: a loading segment, a static segment in which either the force or displacement was held constant, and an un-

Table 4.3: Programmer Test Matrix

Test	Loading Ramp	Control	Disp. Rate
3,4,6	Incremental	Displacement	0.2 mm/s
7-10	Monotonic	Displacement	0.2 mm/s
11-12	Monotonic	Force	11 mm/s
13-19	Monotonic	Displacement	22 mm/s

loading segment. Some of the loading segments were incremental while others were monotonic. Most of the tests were run in displacement control, but two were run in force control. Loading rates differed as well, generally falling in two ranges: the quasi-static range (≈ 0.2 mm/s) and a low-rate dynamic range (11-22 mm/s). For comparison, simulated blast loading rates can reach up to 35 000 mm/s. Unloading rates were all in the vicinity of 0.2 mm/s, except for the force controlled tests, which were unloaded about five times faster. A test matrix summarizing the different tests is provided in Table 4.3. Three tests are missing from the test matrix: Tests 1 and 2 were low level and did not produce useful data while Test 5 suffered an instrumentation failure.

Early in the test sequence, a small damaged notch was observed (Figure 4.9) but it is of negligible relevance to the results. Surprisingly, the programmer debonded from the backing plate (Figure 4.10), resulting in the programmer material extruding beyond the edge of the plate. Loss of lateral confinement, frictional losses and additional nonlinearities are noticeable effects of this behavior, but lacking further testing and instrumentation, they are irretrievably confounded in the data. Post-test investigation of the specimen determined that the polymer was still firmly held to the backing plate indicating that the debonding phenomenon was limited only to the edges of the specimen. Thus, the effect of debonding is small.

To avoid unnecessarily encumbering the main text, the detailed data plots

Figure 4.9: Local Damage Observed in Programmer Tests

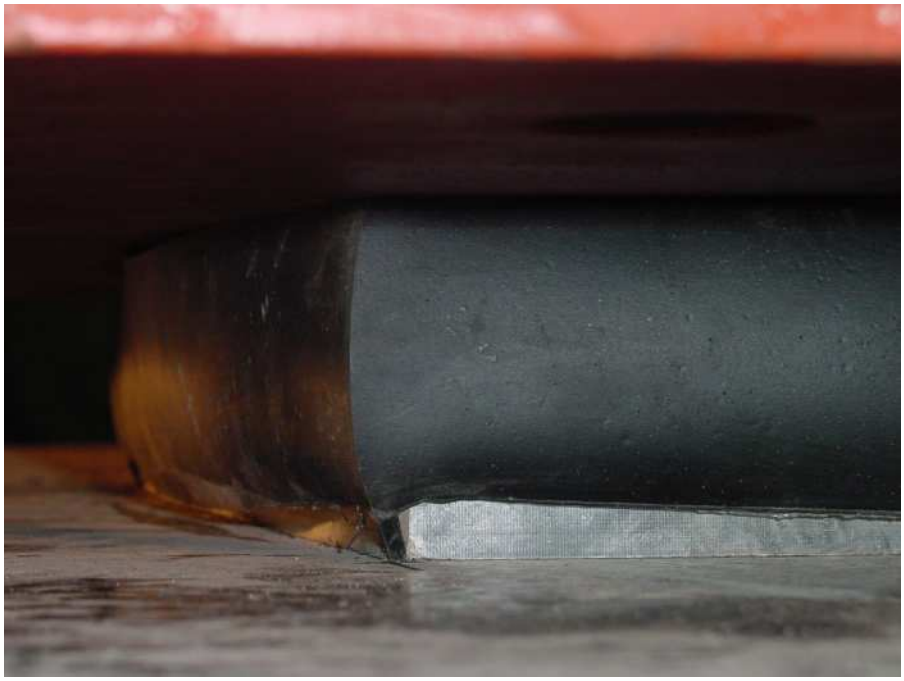

Figure 4.10: Debonding Observed in Programmer Tests

for force, deformation, average true stress, average true strain and time are provided in Appendix B. Typical characteristics of the data, such as the strain-time, stress-time and stress-strain curves, are illustrated here with results from Test 14. This test is selected only because the data clearly illustrate the phenomena described.

The true strain ε is calculated as the change in length divided by the current length: $\varepsilon = d/(\tau_o - d)$, where d is the deformation and τ_o is the original thickness of the programmer. The true stress σ is calculated as the force divided by the actual area A, which is estimated by $A = A_o(1 + \nu\varepsilon)^2$, where ν is Poisson's ratio ($\nu \approx 0.5$ for the programmer material) and A_o is the original area. Both of these calculations are clearly simplifications and are intended only to discuss general trends. The resulting stress and strain are only average values and do not represent true pointwise values.

The strain time history (Figure 4.11) shows the difficulty in applying truly constant strain rates at this facility; although the different segments of the curve are fairly straight, there is some curvature visible, especially during the relaxation phase. Toward the end of the same curve, the unloading strain rate suddenly decreases. This occurs because the actuator unloading rate exceeds the recovery rate of the material and, because the reaction system cannot develop tension, a gap opens between the reaction beam and the plate above the programmer assembly.

The stress time history (Figure 4.12) is consistent with a standard solid. This is seen most clearly during the relaxation and unloading phases. During relaxation, the stress drops exponentially to a non-zero terminal value and the force drop is exponential during unloading as well. This does not imply that the material will for sure be accurately modelled by the standard solid model, but the similarities are nonetheless useful in determining the proper viscoelastic model for the material.

The stress-strain hysteresis curve (Figure 4.13) illustrates the large effect that the pyramidal surface (Figure 2.11) has on the overall behavior of programmer.

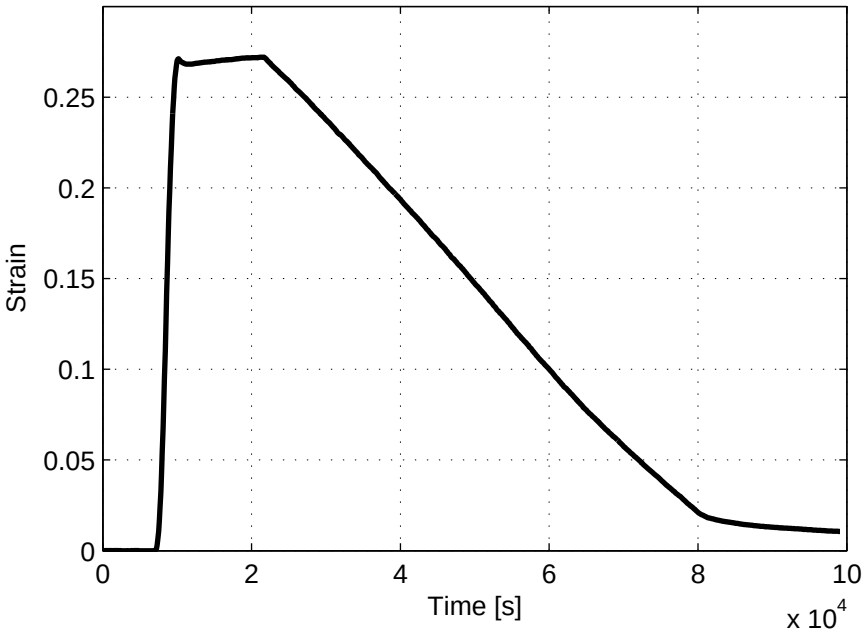

Figure 4.11: Strain Time History for Programmer Test 14

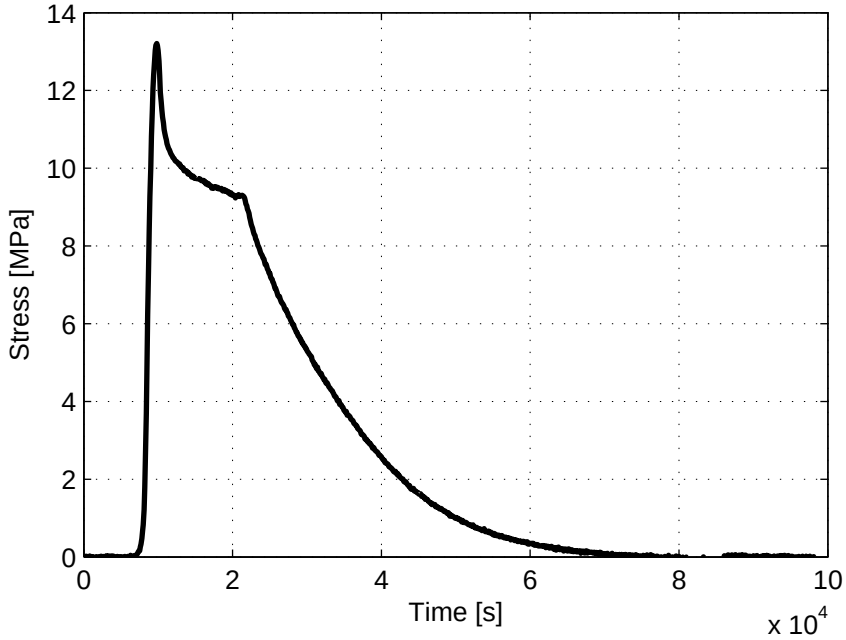

Figure 4.12: Stress Time History for Programmer Test 14

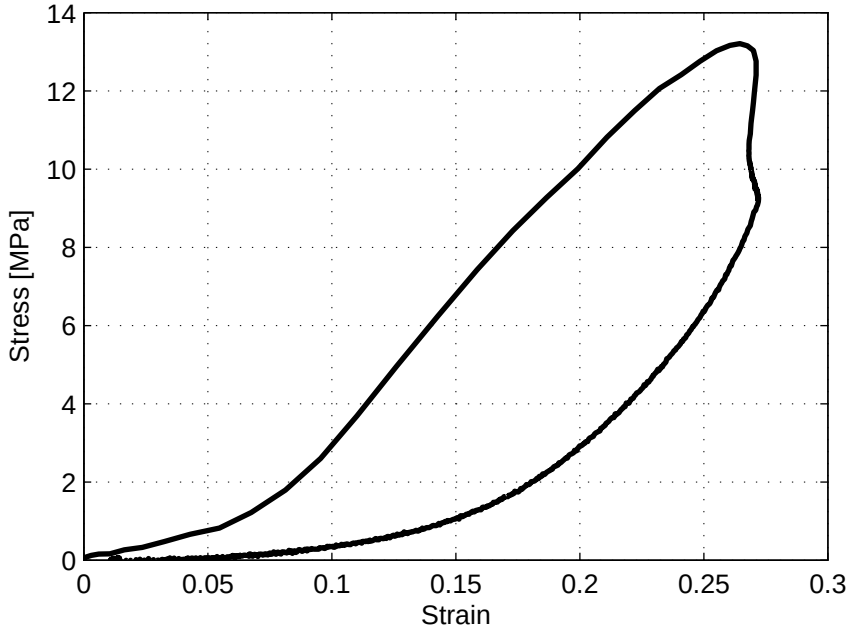

Figure 4.13: Stress-Strain Relation for Programmer Test 14

Early in the loading process, the stress-strain relation is governed by the pyramidal geometry and the specimen quickly gains stiffness as the pyramids deform, thus the curvature is highly positive. Later in the loading process, the pyramids are fully compressed and the curve is instead dominated by material properties. During this phase the curvature is slightly negative.

Unfortunately, the geometric nonlinearities introduced by the programmer's pyramidal front surface make it impossible to develop a proper viscoelastic model. (Chapter 5 is devoted in large part to initial developments in modelling the material itself.) The available data are better suited to developing a model of the force-deformation behavior of the programmer as a structure. Two curves from the quasi-static tests (Figure 4.14), one from an incrementally loaded test and the other from a monotonically loaded test, illustrate features of this behavior. The three different loading segments – loading, relaxation, and unloading – are indicated on these curves by the curve segments O-L, L-U, and U-O, respectively.

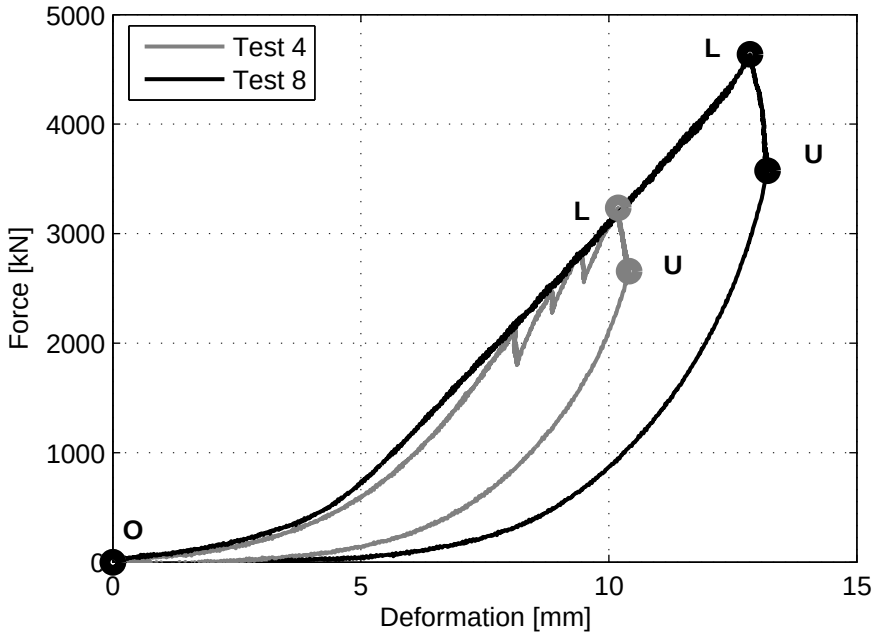

Figure 4.14: Phases of Quasi-Static Loading

The loading behavior both for the load envelope and monotonic loading has positive curvature and exhibits different small and large deformation behavior because of the effect of the pyramids and nonlinearities due to large deformations. The differences between incremental and monotonic loading are seen between the two curves; the incremental loading exemplified by Test 4 results in a sawtooth-shaped load curve because of material relaxation during the pauses in loading while the monotonic loading exemplified by Test 8 produces a much cleaner curve. The monotonic tests produce many more data points along the monotonic loading curve than do the incrementally loaded tests; only the monotonic curves are used in developing a fit to the loading curve of the test data.

Relaxation takes place along the line segment L-U as well as during pauses between loading increments. In addition to relaxation, the material exhibits some creep during these phases because the deflection of the cross beam is not fixed. As the material creeps slightly some of the force in the reaction structure is lost. This

explains the diagonal direction of the load-displacement curve during relaxation.

Lastly, unloading takes place along the line segment U-O, which lies beneath O-L. Like the loading curve, the unloading curve also has positive curvature. At the start of unloading, the force rapidly approaches zero and then flattens out to eventually reach zero at the origin. The force cannot drop below zero because the reaction structure cannot develop tension.

4.C.2 Constitutive Modelling

The phenomenological hysteresis model is intended to describe the force-deflection curve of the programmer during a simulated blast during which it undergoes only a single loading and unloading cycle at deformation rates in the tens of meters per second. Thus only this behavior is characterized; behavior such as reloading, creep, and relaxation are not addressed. In other words, the applied deformation is limited to

$$d \geq 0, \qquad 0 \leq t \leq t_d \tag{4.15}$$

$$\dot{d} \geq 0, \qquad 0 \leq t \leq t^* \tag{4.16}$$

$$\dot{d} < 0, \qquad t^* < t \leq t_d \tag{4.17}$$

where d is the deformation, $\dot{d}$ the deformation rate, t^* the time at which loading ends and unloading begins, and t_d is the pulse duration. In addition, no attempt is made to model the results of the low-rate dynamic tests; doing so would require detailed developments at loading rates that are not of interest in a simulated blast. As mentioned previously, the programmer is not modelled at the material level because it is impossible to separate the necessary material behavior from the force-deformation data; it is irretrievably confounded with the geometric behavior of the pyramids. This model is built only for the programmers used in this tests and because stresses are averaged, it is only adequate for specimens insensitive to peak pressure. Extensions to programmers of different geometry and material material, as well as to pressure-sensitive specimens, are discussed in Chapter 5.

The model is built in two steps: the first determines a baseline curve for quasi-static loading and the second determines a dynamic modification factor for the deformation rates of interest. Both are determined by nonlinear optimization techniques; the former is fit to the monotonic, quasi-static loading curves and all the unloading curves, and the latter is fit to the coefficient of restitution data developed in the factory acceptance tests. The model is verified against independent data developed during the site acceptance tests (Section 2.C).

Baseline Loading Curve

The baseline loading curve, shown for the test data in Figure 4.15, is assumed to follow a power law of the form $f_{bl} = \kappa_1(d)^{\kappa_2}$, where the constant κ_1 and the exponent κ_2 are positive fitting parameters. The loading curve accounts for the geometrical effect of the pyramid, which results in increasing stiffness with increasing deflection as well as the power law known to govern the loading behavior of rubbers [17]. The model was fit with the quasi-static, monotonic loading curves. A nonlinear regression determines the baseline loading function to be

$$f_{bl} = 28.36 \cdot \text{kN} \cdot (d)^{1.993} \qquad (d \text{ in mm}) \tag{4.18}$$

with a coefficient of determination of 0.99, indicating an excellent fit. This is seen visually as well in Figure 4.16.

Baseline Unloading Curve

The baseline unloading curve (Figure 4.17) is also assumed to follow a power law, but in this case one constrained to pass through both the origin and the point (d_o, f_o), which is the deflection and load measured at t^*, the end of the loading phase. The baseline unloading function is thus $f_{bu} = f_o(d/d_o)^{\kappa_3}$, where the exponent κ_3 is a fitting parameter. Although a reasonable fit is obtained for a function of this form, κ_3 has a small dependence on d_o. An enhanced model allows the exponent to vary linearly with d_o as $\kappa_3 = \kappa_4 + \kappa_5 \cdot d_o$, where the constants

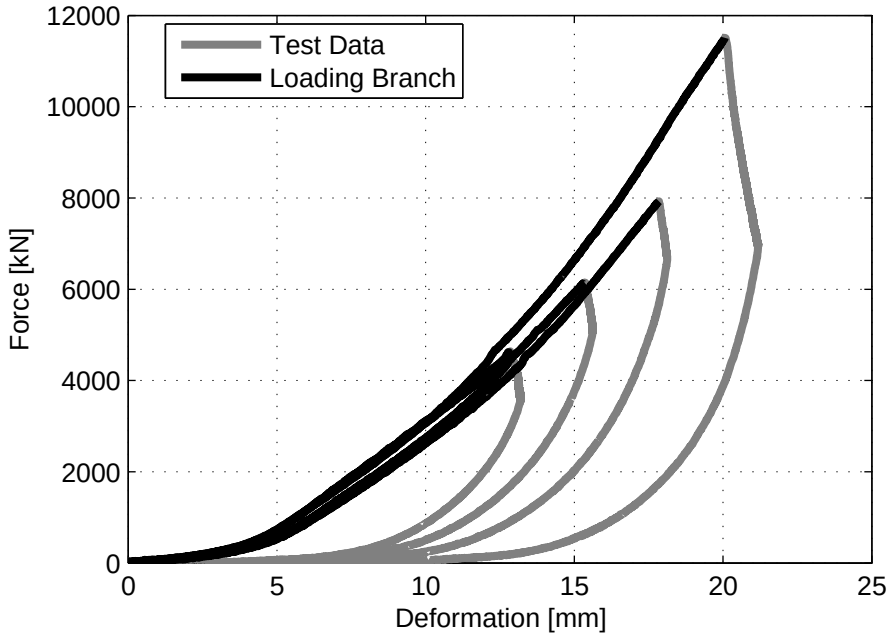

Figure 4.15: Programmer Loading Curves

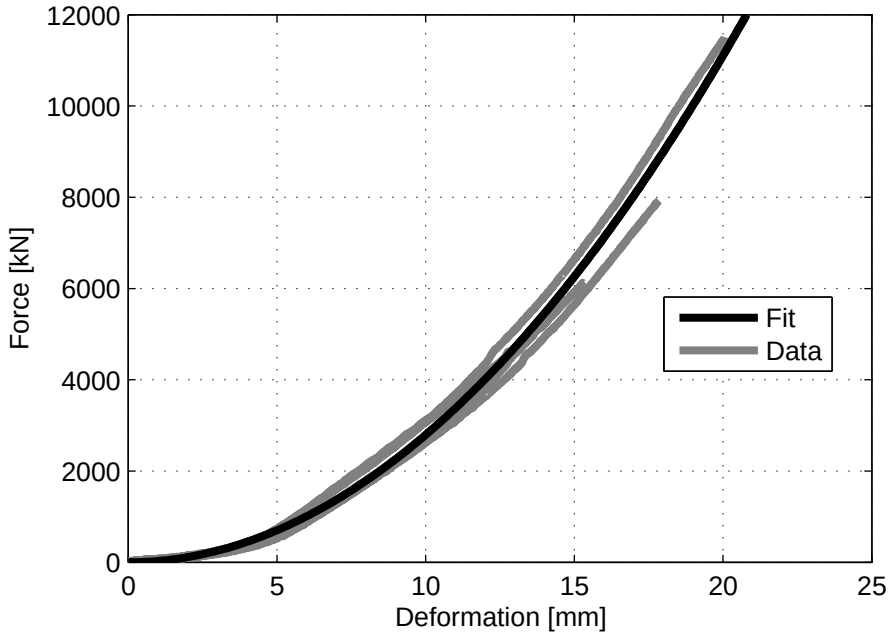

Figure 4.16: Programmer Loading Function

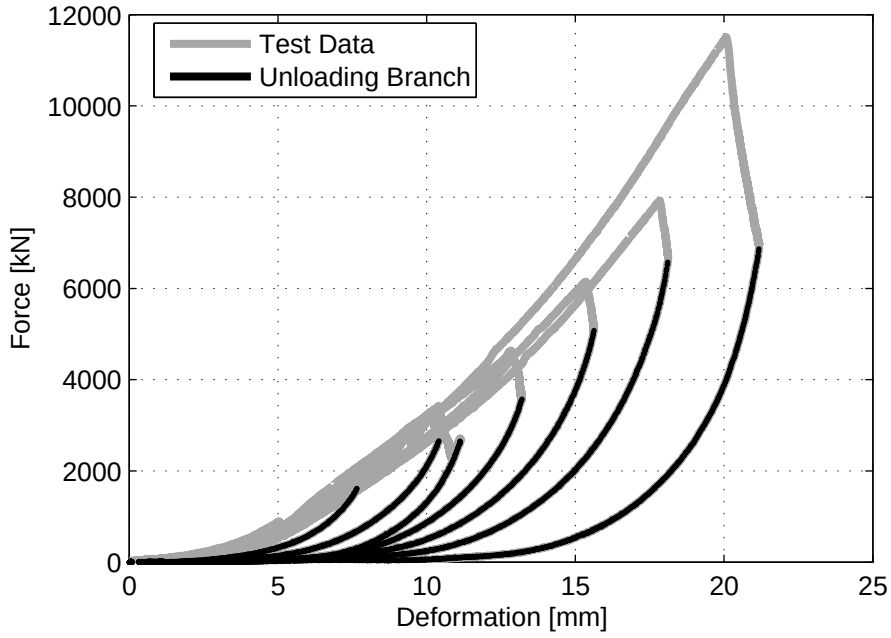

Figure 4.17: Programmer Unloading Curves

κ_4 and κ_5 are fitting parameters. Because all tests were unloaded quasi-statically, both the quasi-static and low-rate tests were used to fit the unloading function. A nonlinear regression determines the unloading behavior to be

$$f_{bu} = f_o \left(\frac{d}{d_o} \right)^{1.3181+0.3097 \cdot d_o} \qquad (d, d_o \text{ in mm}) \tag{4.19}$$

with a coefficient of determination equal to 0.99, indicating an excellent fit, which is seen visually as well in Figure 4.18.

Definition of Dynamic Modification Factors

The second stage in the model generation is to expand these base curves to the loading rates experienced in blast simulation tests by multiplying the baseline loading curve by a dynamic modification factor that varies with deformation rate $\dot{d}$. Thus the programmer force is defined as

$$f(d, \dot{d}) = F_d(\dot{d})\, f_b(d) \tag{4.20}$$

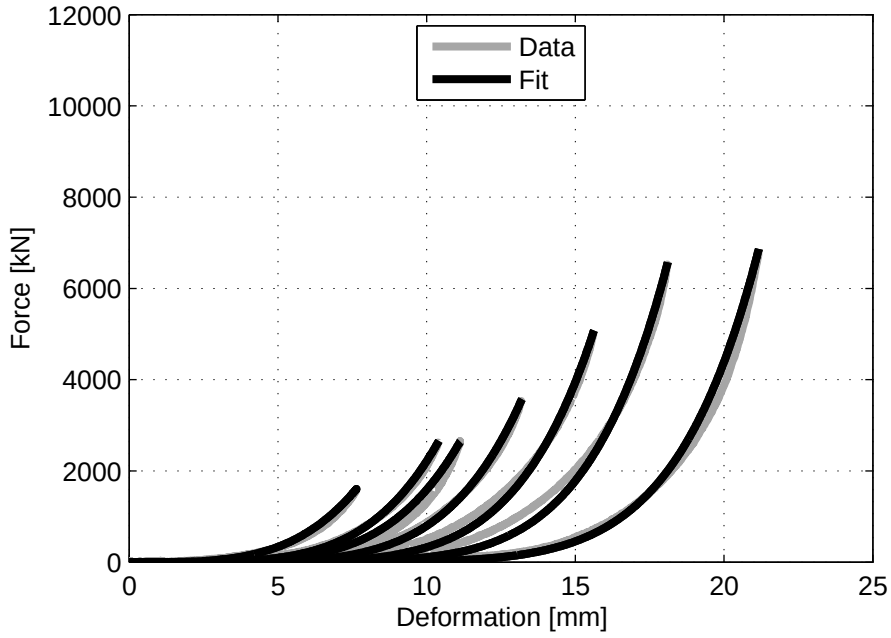

Figure 4.18: Programmer Unloading Function

where the baseline curve f_b is

$$f_b = \begin{cases} f_{bl}, & 0 \leq t \leq t^* \\ f_{bu}, & t^* < t \leq t_d \end{cases} \tag{4.21}$$

and the dynamic modification factor F_d is

$$F_d = \begin{cases} F_{dl}, & 0 \leq t \leq t^* \\ F_{du}, & t^* < t \leq t_d \end{cases} \tag{4.22}$$

Different factors are used in loading and unloading. The dynamic factor in loading F_{dl} is always greater than unity and the dynamic factor in unloading F_{du} is always between zero and unity. Thus, the loading curve is above the baseline and the unloading curve is below the baseline.

The dynamic factor for loading is equal to unity at zero deformation rate and has an initial positive slope, but due to shear thinning, at large deformation rates it decreases again and approaches one asymptotically. The following function

captures this physical behavior:

$$F_{dl} = 1 + \kappa_6 \gamma \cdot \mathrm{e}^{(-\kappa_7 \gamma)} \tag{4.23}$$

where $\gamma = \dot{d}/(30\,\mathrm{m/s})$ is a normalized deformation rate and κ_6 and κ_7 are positive model parameters. The dynamic factor for unloading must be less than one but cannot be less than zero because the contact condition between the specimen and the programmer cannot develop tension. The following function captures this behavior:

$$F_{du} = \frac{1}{1 - \kappa_8 \gamma} \tag{4.24}$$

where the parameter κ_8 will be shown to be equal to κ_6. Note that because $\gamma < 0$ during unloading the denominator is always positive and ranges from unity to infinity.

Although shear thinning and the contact condition are used to motivate the functional form of the dynamic modification factors, the resulting model is not intended to prove or disprove these assertions. Instead it is intended to model the impulse produced by a collision between an impacting mass and a specimen at the deformation rates of interest; it is against this intention that the quality of the model is measured. Accurate material modelling, such as characterization of the supposed shear thinning behavior, requires more testing and theoretical development. Such a study is proposed in Chapter 5.

The above mentioned equality between κ_6 and κ_8 is derived from the constraint that at the moment of load reversal the force-time curve must be smooth, i.e., $\dot{f}$ is continuous at t^*. (Of course f itself is also continuous; this is enforced by the equality at load reversal of both the baseline curves and the dynamic factors.) The derivative of f with respect to time is

$$\dot{f} = f_b \frac{\partial F_d}{\partial \gamma} \frac{\partial \gamma}{\partial \dot{d}} \ddot{d} + F_d \frac{\partial f_b}{\partial d} \dot{d} \tag{4.25}$$

At load reversal $\dot{d} = 0$ and the second term vanishes. Examining now the first term at load reversal, f_b is constant because $f_{bl} = f_{bu}$ by definition. The quantity

$\partial\gamma/\partial\dot{d}$ is a constant, and because neither the force nor the mass change during load reversal, the deformation rate $\ddot{d}$ is constant as well. Thus, the only quantity in the first term that can change between loading and unloading is $\partial F_d/\partial\gamma$, so the continuity requirement for $\dot{f}$ reduces to the requirement that

$$\left.\frac{\partial F_{dl}}{\partial\gamma}\right|_{\gamma=0} = \left.\frac{\partial F_{du}}{\partial\gamma}\right|_{\gamma=0} \tag{4.26}$$

Substituting the derivatives of Equations (4.23) and (4.24) into Equation (4.26) yields

$$\left.\kappa_6\,(1-\kappa_7\,\gamma)\,\mathrm{e}^{(-\kappa_7\,\gamma)}\right|_{\gamma=0} = \left.\frac{\kappa_8}{(1-\kappa_8\,\gamma)^2}\right|_{\gamma=0} \tag{4.27}$$

which when evaluated yields the condition $\kappa_6 = \kappa_8$. Thus, the dynamic behavior is represented by two independent, physically-motivated parameters and the force-time curve is guaranteed to be smooth.

Fitting of Dynamic Modification Factors

The two independent parameters κ_6 and κ_7 are determined by fitting the model to the COR data from the factory acceptance tests, which involved, as previously explained, firing one BG against another. This process is modelled as a single dimensional collision with the above programmer model determining the force between the two BGs. Using this simulation as the objective function, the parameters κ_6 and κ_7 are adjusted to minimize the sum square error between the estimated and measured COR.

The collision is modelled by an explicit time stepping algorithm where the force acting on each body is determined by the constitutive model for the programmer. The behavior is followed as the programmer compresses and decompresses. When the programmer reaches the original thickness, a gap has opened and no more force is developed. The incoming mass M_1 travels at speed v_o and the second mass M_2 is stationary. The position of the masses are given by y_1 and y_2, respectively. To generalize the formulation, a spring term k is added to represent the stiffness of the mass assembly being impacted. The spring term is equal to

zero when fitting the material parameters but can be changed to simulate a column specimen as is done in the verification phase.

At each time step the equation of motion of each mass is

$$\ddot{y}_{1,j+1} = -\frac{f(d_j, \dot{d}_j)}{M_1} \tag{4.28}$$

$$\ddot{y}_{2,j+1} = \frac{f(d_j, \dot{d}_j) - k\, y_{2,j}}{M_2} \tag{4.29}$$

where

$$d_j = y_{1,j} - y_{2,j} \tag{4.30}$$

$$\dot{d}_j = \dot{y}_{1,j} - \dot{y}_{2,j} \tag{4.31}$$

and where j represents the time step count. The kinematics of each mass are updated assuming a constant acceleration over the time step of length Δt, thus

$$\dot{y}_{i,j+1} = \dot{y}_{i,j} + \ddot{y}_{i,j+1}\, \Delta t \tag{4.32}$$

$$y_{i,j+1} = y_{i,j} + \dot{y}_{i,j}\, \Delta t + \frac{1}{2}\, \ddot{y}_{i,j+1}\, (\Delta t)^2 \tag{4.33}$$

for $i = 1, 2$. The coefficient of restitution is calculated via Equation (1.64) using as input the final velocities determined by this calculation. In this calculation, a time step of 5e-4 ms yielded converged values in a reasonable computational time.

The fit resulting from this process, shown in Figure 4.19, is good with a coefficient of determination of 0.89. In accordance with expectations it exhibits a decreased COR with increased impacting velocity and a slight positive curvature. The parameters that lead to the best fit are $\kappa_6 = 12.2295$ and $\kappa_7 = 3.8840$, thus the dynamic modification factors are

$$F_{dl} = 1 + 12.2295\, \gamma \cdot \mathrm{e}^{(-3.8840\, \gamma)} \tag{4.34}$$

and

$$F_{du} = \frac{1}{1 - 12.2295\, \gamma} \tag{4.35}$$

which are pictured in Figures 4.20 and 4.21, respectively. The loading factor reaches a maximum of just under 2.2 at a deformation rate of around 7 to 8 m/s

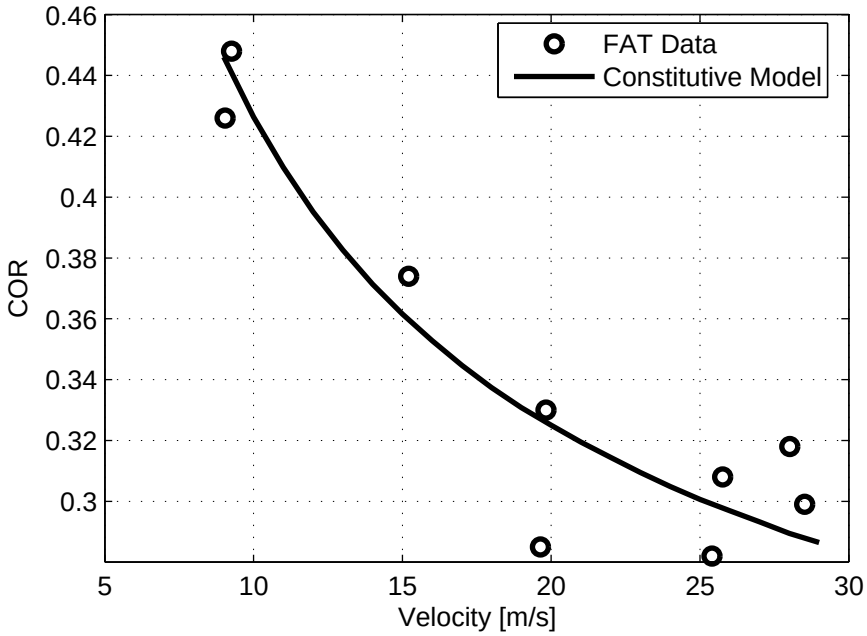

Figure 4.19: Fit of Model to FAT COR Data

and it decays slowly to just over 1.2 at a deformation rate of 30 m/s. The factor for unloading decays rapidly from 1.0 to reach 0.2 by a deformation rate of 10 m/s. By the time it reaches 30 m/s it has decayed to under 0.1. With such a rapid decay rate, the force under large deformation rate comes very close to zero thus approximating what would happen if a gap were to have opened due to the separation rate between masses exceeding the restoration rate of the material.

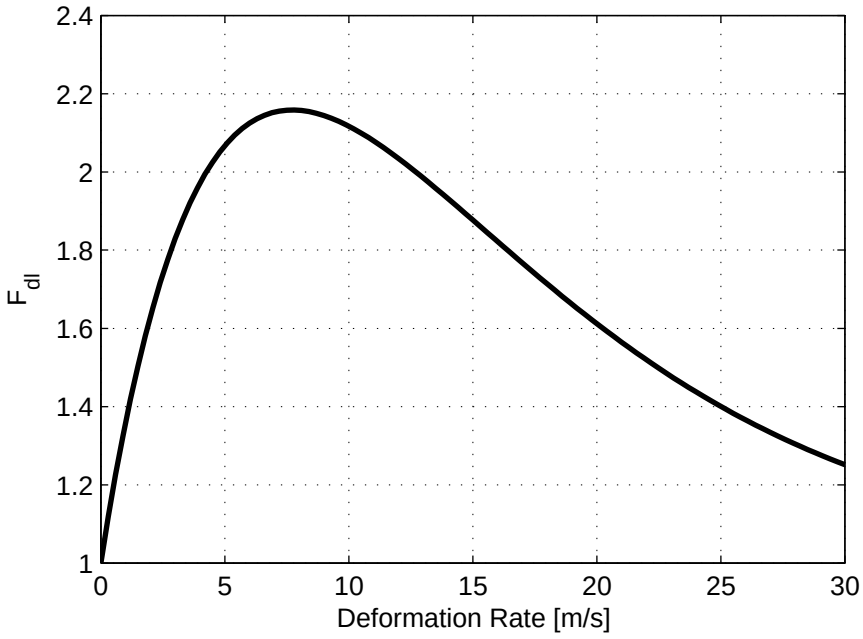

Figure 4.20: Dynamic Modification Factor for Loading

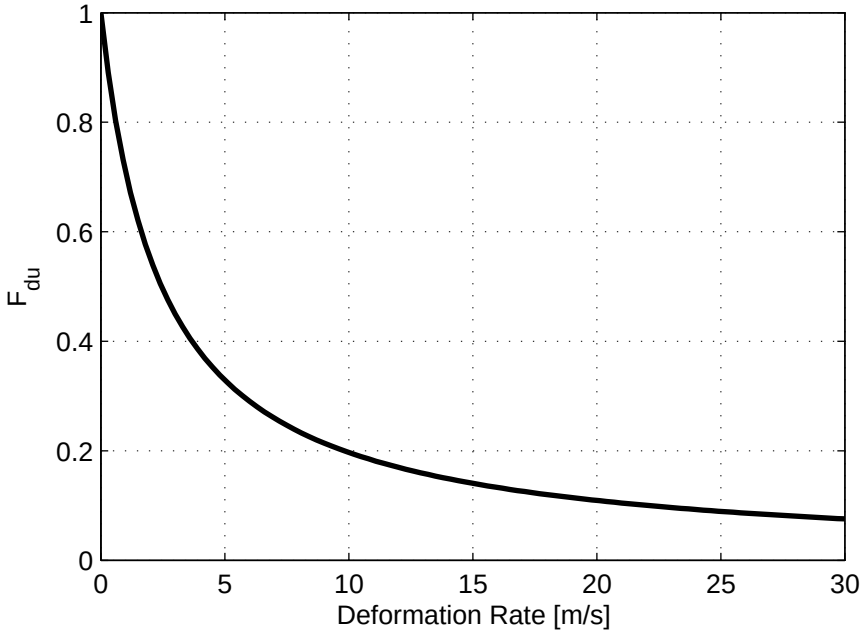

Figure 4.21: Dynamic Modification Factor for Unloading

Model Behavior

To illustrate the features of the model, a simulation is made of a 243 kg mass impacting a 217 kg mass at 15 m/s, typical of a mid-range factory acceptance test. At impact, the deformation rate (Figure 4.22) equals the impact velocity. The force curve (Figure 4.23) begins rising slowly then quickly turns upward. This reduces the deformation rate, resulting in a change in the dynamic modification factor (Figure 4.24). In fact, the dynamic factor increases at first because the initial deformation rate is beyond that at which the maximum dynamic increase occurs.

The maximum force occurs at about 0.7 ms before the deformation rate reverses at about 0.85 ms. This is unlike the baseline curve, where the maximum occurs exactly at the moment of reversal. The dynamic factor hovers around 2.0 until shortly before deformation rate reversal, when it drops quickly to one. The moment of reversal is seen when the dynamic factor crosses unity and when the actual force intersects the baseline curve. After reversal, the dynamic factor drops quickly to about 0.5 and then decreases slowly after that. The deformation rate after reversal is about three times smaller than the peak loading rate, resulting in a longer post reversal and post peak time. The force drops to zero and the pulse ends at 2.79 ms.

The impulse predicted from the model (Figure 4.25) looks remarkably similar to the impulse delivered during the tests in Chapter 3. The maximum impulse is 2341 kN·ms and the 5%-95% pulse time is 1.09 ms. Dividing the impulse by the programmer area of 14 in (356 mm) × 30 in (762 mm) yields a specific impulse of 8.64 MPa·ms (1250 psi·ms). Both the pulse durations and specific impulse are realistic. The differences in energy dissipation between the baseline and actual curves are seen clearly in the hysteresis plot (Figure 4.26) where the force curve is far above the baseline during loading and far below during unloading. This large increase in area develops the relatively low COR of 0.36. Overall, the behavior is physically reasonable and in accordance with expectations, lending

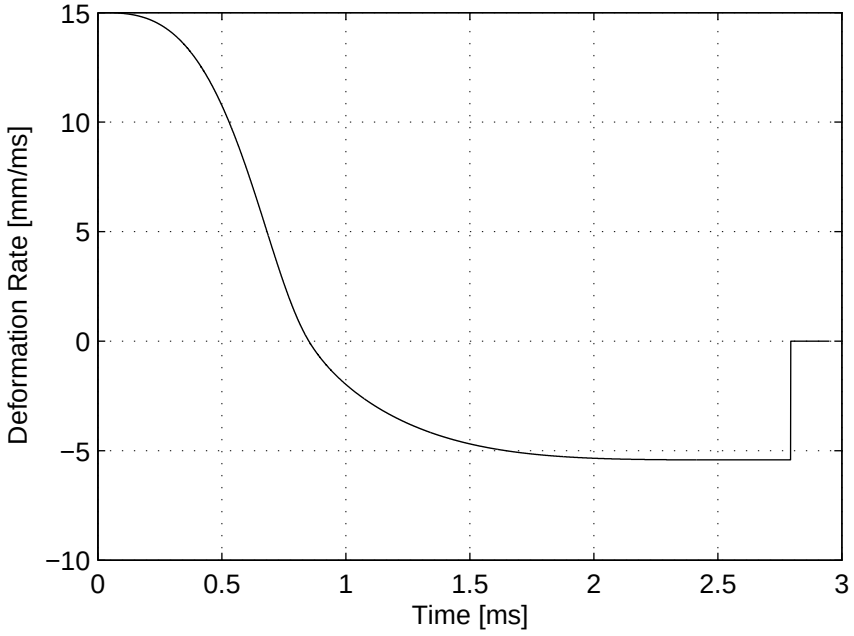

Figure 4.22: 15 m/s Calculation: Deformation Rate

credence to the model's validity.

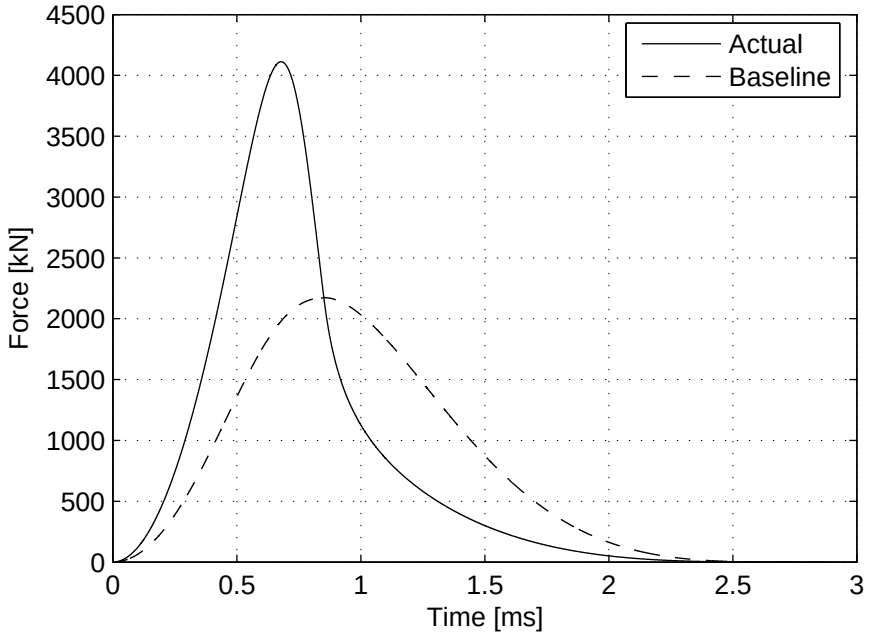

Figure 4.23: 15 m/s Calculation: Force

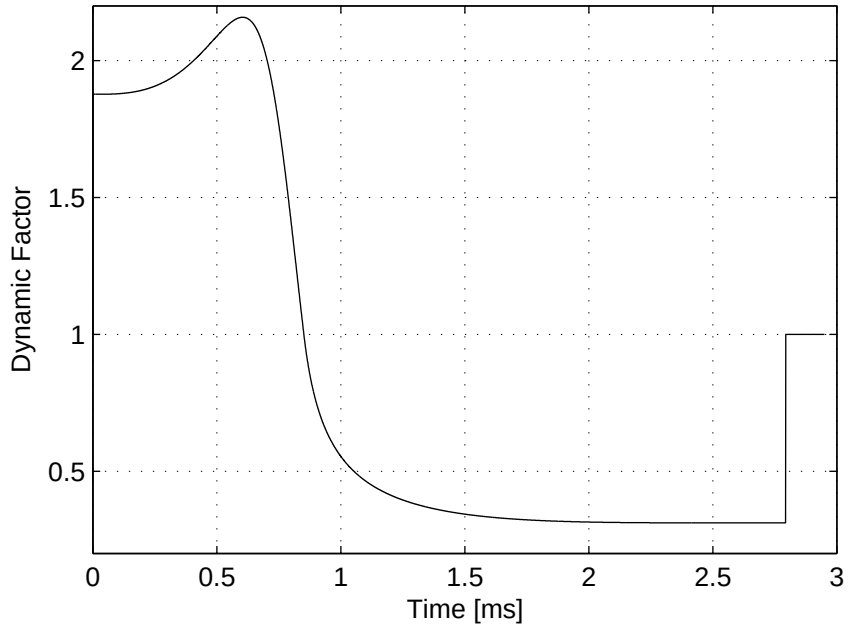

Figure 4.24: 15 m/s Calculation: Dynamic Factor

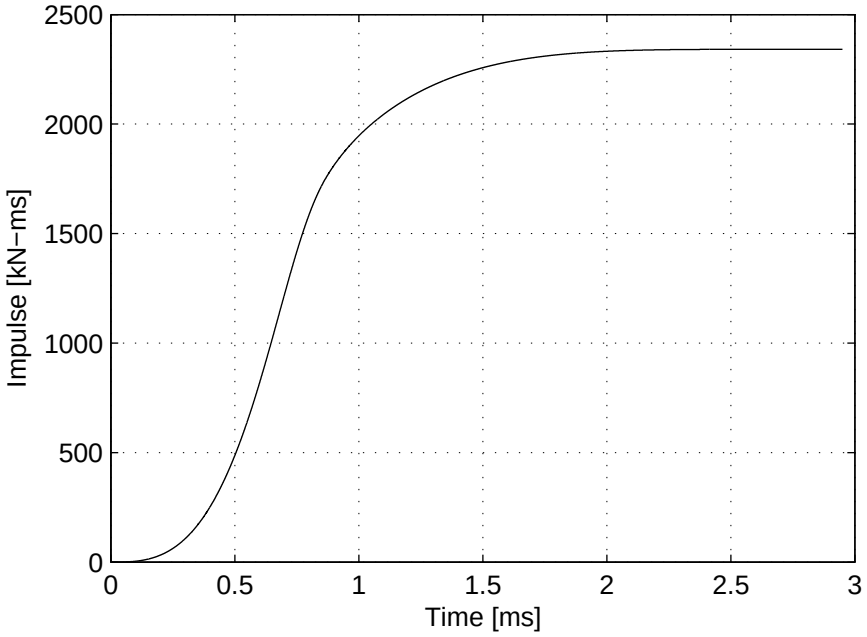

Figure 4.25: 15 m/s Calculation: Impulse

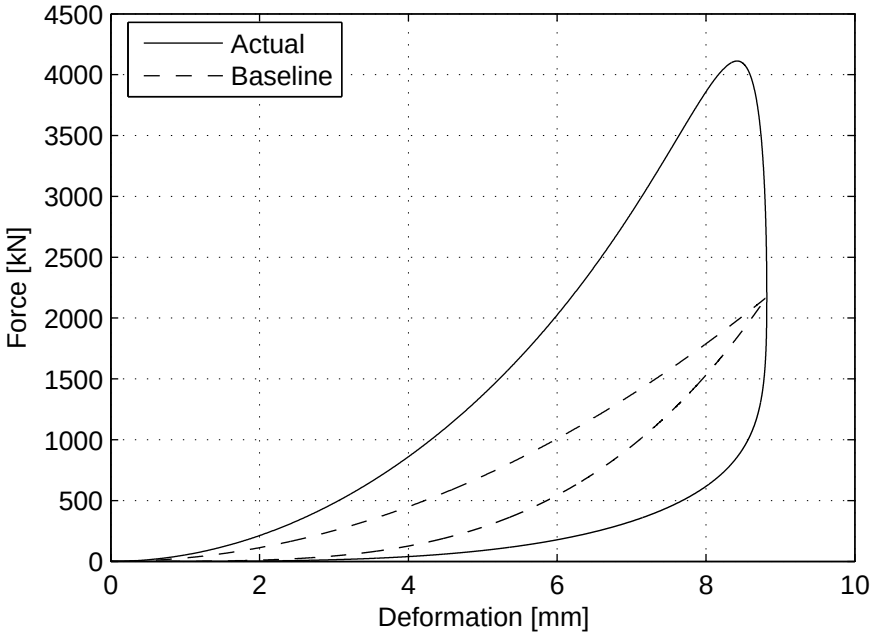

Figure 4.26: 15 m/s Calculation: Hysteresis

4.C.3 Model Validation

The model is validated against the site acceptance test (SAT) data, which are completely independent of data used to create the model. In the SAT each BG was exercised independently against a strong and stiff dummy column and acceleration traces were recorded. The BGs were exercised at various speeds; the highest speed test (impacting at 9.2 m/s) is used for verification. Both of the center BGs are expected to produce the same acceleration traces, and as shown in Figure 2.29 the data are nearly equal. The accelerations of the two BGs are averaged together for this comparison.

The test event is modelled by SDOF methods using the time stepping algorithm just developed. The column mass and stiffness are converted to equivalent SDOF quantities as is the mass of the impacting module by a method developed in this section. The column is very stiff and massive with a mass $M_2 = 2490\,\text{kg}$ and a flexural stiffness $EI = 2.872 \cdot 10^{11}\,\text{kN} \cdot \text{mm}^2$. The equivalent SDOF mass of the dummy column is given as $\tilde{M}_2 = C_m\, M_2$, where $C_m = 0.4063$ for a fixed-fixed column, thus $\tilde{M}_2 = 1012\,\text{kg}$. The equivalent SDOF stiffness of the dummy column is given as $C_k EI/L^3$, where $C_k = 204.8$ for a fixed-fixed column, thus $\tilde{k} = 1672$ kN/mm.

The modification is more involved for the BG mass. From Equation (1.40), the equivalent force delivered by the BG acting between x_{bn} and x_{tn} is

$$\tilde{f} = w \int_{x_{bn}}^{x_{tn}} \psi \, \mathrm{d}x \tag{4.36}$$

where the limits of integration are defined as in Section 3.B.3. The shape function ψ is taken as ψ_{ff}, the shape of the fixed-fixed column given by Equation 1.47. The load w is

$$w = \frac{M_{bg}\, a}{L_n} \tag{4.37}$$

where $M_{bg} = 243$ kg is the mass of the impacting module, $L_n = x_{tn} - x_{bn}$ is the tributary length of the single BG and a is the recorded acceleration. The integral in Equation (4.36) above has already been calculated in Equation (3.8). Using this

result and Equation (4.37), Equation (4.36) becomes

$$\tilde{f} = \left[\left(\frac{L}{L_n} C_{fn} \right) M_{bg} \right] a \tag{4.38}$$

where L is the length of the column and $C_{fn} = 0.2125$. Because the BG is one quarter of the height the ratio $L/L_n = 4$. The quantity in square brackets is the equivalent impacting mass

$$\tilde{M}_1 = \left(\frac{L}{L_n} C_{fn} \right) M_{bg} \tag{4.39}$$

which is $\tilde{M}_1 = 0.85 M_{bg} = 207\,\text{kg}$.

The first comparison is made between the recorded and predicted *pseudo-impulse*, or integral of acceleration (Figure 4.27). The agreement is excellent; the data produce a maximum pseudo-impulse of 1283 g·ms, while the model predicts 1297 g·ms, an error of only 1%. There are definite differences in the shapes of the impulse. The model rises smoothly to the maximum, while the data oscillate about the predicted curve. This causes the data to reach the maximum earlier than the model during one of its upswings, thus making the 5%-95% pulse times much different from each other: 1.81 ms for the data and 2.93 ms for the model. This is not cause for concern as it is but an artifact of the way pulse time is defined.

The next comparison made is between the acceleration records themselves (Figure 4.28). Comparing the estimate to the data, the peak is indeed high and early, the initial decay too quick, but the later decay rate matches well up to an oscillatory behavior in the data. The discrepancies between the two provide a number of valuable insights. First, it is important to note that the procedure used to fit the model is based on COR, which is determined largely by impulse during a collision. The pulse shape itself does not come into play, and thus the fitting procedure has no influence on the pulse shape of the model. Rather, pulse shape is determined simply as a product of the a-priori phenomenological assumptions used to build the model, most importantly the dynamic modification factor. Keeping this in mind, the agreement between the data and the model is actually quite good.

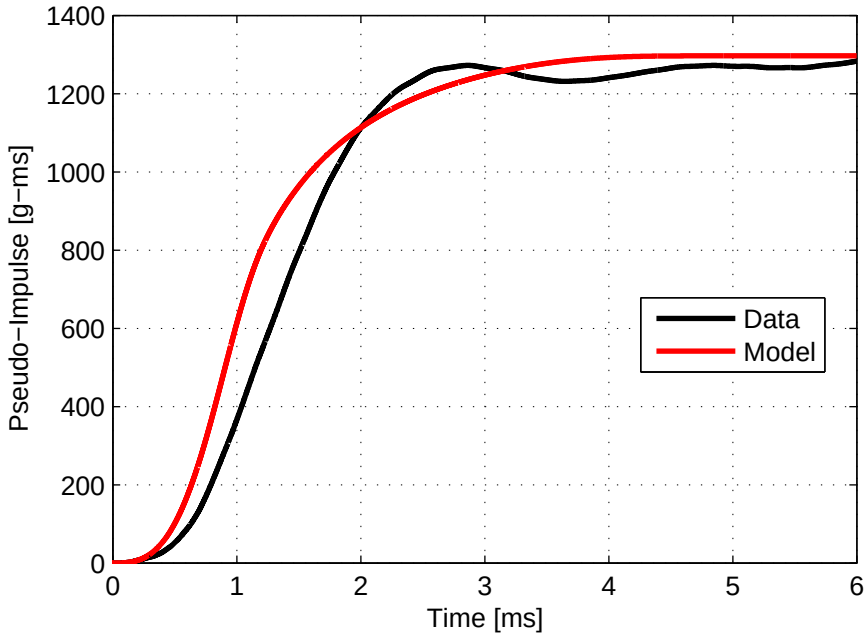

Figure 4.27: SAT Pseudo-Impulse Estimate Versus Actual

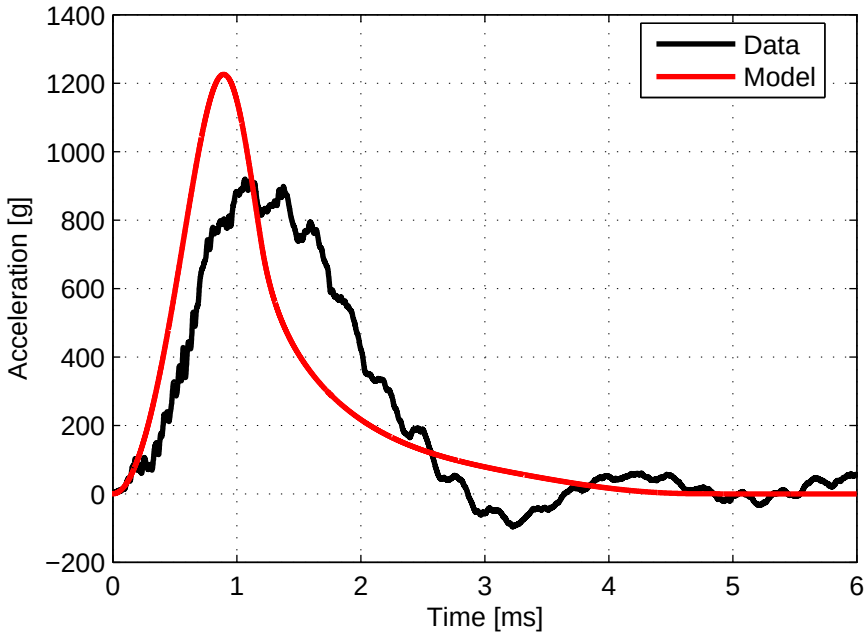

Figure 4.28: SAT Acceleration Estimate Versus Actual

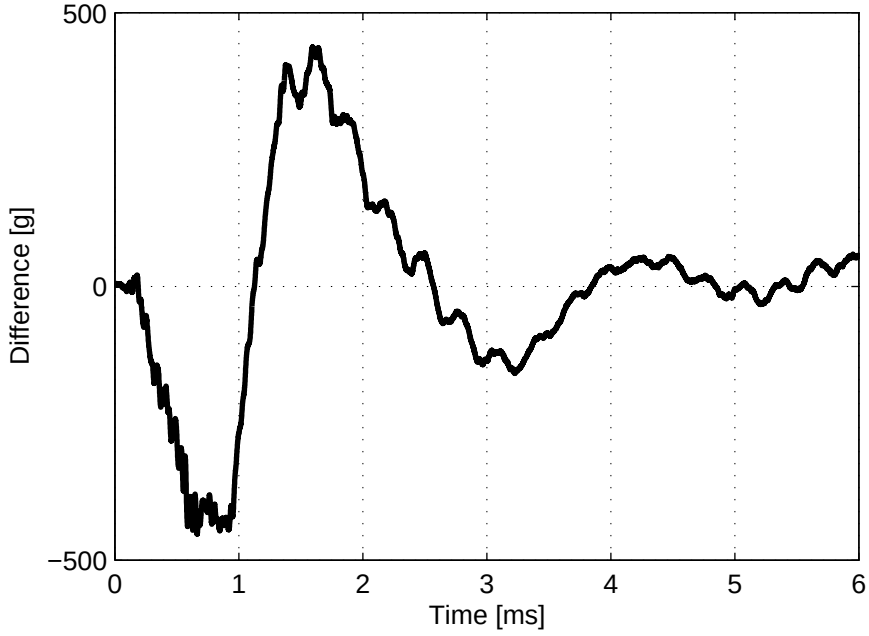

Figure 4.29: SAT Error in Acceleration Estimate

However, much of the discrepancy is due not to a failure of the model but to the nature of the recorded data, which carry an oscillatory signal superposed on the main signal. Although the cause of this signal has not been studied it is likely due to vibration of the impacting module or shock transmission through the impacting module or the oil column. When the modelled acceleration is subtracted from the recorded data (Figure 4.29), what emerges is a signal that looks very much like damped harmonic oscillation. It is more likely that the difference between the two signals is due to an unmodelled vibration phenomenon than a design error in the material model. An interesting avenue for further investigation is to determine the cause of this behavior and how it affects the loading on the structure. Fortunately for the tests herein, which are dominated by impulse, the answer makes little difference, but for specimens that are pressure sensitive, it is critically important to have an accurate answer.

4.D Chapter Summary

The fourth chapter is aimed at facilitating future research by proving the equivalence between laboratory simulations and field tests and by developing analytical tools that future investigators can use to predict and analyze results. The equivalence between field and laboratory data is shown most dramatically with a demand-damage plot formed with laboratory and field data in which the two data sets are indistinguishable. After this, two analytical tools are developed: a pre-test prediction and a structural characterization of the programmer. The former is useful for an investigator to quickly and easily determine the necessary impacting velocity to deliver a desired impulse to the specimen. The latter is useful for more detailed analyses of the simulated blast event. Both tools are derived theoretically, calibrated to experimental data, and verified against independent experimental data. In the latter case, the verification highlights some anomalies in the recorded data that improve our understanding of BG behavior by highlighting some unknown behavior that merits future investigation. The models are currently limited to programmers of the same geometry and material as those used in these tests. Extensions are discussed in the following chapter.

5 Conclusion

This chapter wraps up the dissertation. First, some ideas for future research are presented. These expand upon the programmer material model presented in the previous chapter and set the foundations for a full material characterization of the polymer. Following this, the central ideas of the dissertation are brought together and summarized.

5.A Ideas for Future Research in Programmer Modelling

The phenomenological programmer model developed in Chapter 4 was applied in the same chapter to a single degree of freedom analysis of a column. It is of interest to eventually be able to model programmers of arbitrary size, shape, and material constitution, either in a single degree of freedom or a finite element analysis. To this end, possible extensions and alternative formulations are now discussed.

As long as the pyramidal structure and material remain similar, the phenomenological model can be extended to programmers of different sizes by use of an appropriate shape factor modification. The shape factor is the area of one loaded surface divided by the area of the unloaded surfaces that are free to bulge. For instance, a block measuring 100 mm square $\times$ 10 mm thick would have a shape factor of $100^2/(4 \cdot 100 \cdot 10)$ or 2.5. Gent and Lindley [17] give methods for finding the "equivalent Young's modulus" of a specimen as a function of shape factor and they examine the shape factor modification at large deformations. Using their ap-

proach an appropriate scaling factor can be found to apply to the baseline loading and unloading curves of the programmer model. A model based on the modified baseline curves can be included directly into a single degree of freedom analysis; it can also be adapted for inclusion into a finite element model by, for instance, fitting an existing material subroutine to data generated by the programmer model.

There are two main shortcomings to approaches based on the model in Chapter 4. The first is that it neglects the stress gradients over the loaded area. Gurtman and Sallay [19] showed that due to confining effects the stress is significantly higher in the center than at the edges. The model developed in the last chapter smears this effect into an average stress, so it is of limited use if the application requires accurate knowledge of the stress profile. The second shortcoming is that because the model confounds the material and geometric behavior, it cannot be easily extended to programmers with a differently shaped front surface or made of a different material. To further extend the modelling capabilities requires the development of an accurate continuum model for the material itself. To this end, the probable nature of a successful one-dimensional theoretical model is now discussed and guidelines are provided as to the types of material tests necessary for determining the material parameters. A one-dimensional model can then be extended to a three-dimensional continuum model (e.g., Bardenhagen et al. [6]).

Some work in this direction has already been performed. Gurtman and Sallay [19], who have assisted the Explosive Loading Laboratory, have determined that the programmer material is Adiprene L-100 cured with MOCA (4,4-Methylene-Bis-Orthochloroaniline). It was necessary to conduct this material characterization because the exact material constitution was not specified in the design process; we only became interested in it afterwards. MTS, with extensive knowledge in the engineering behavior of the shock properties of rubbers, specified primarily the required hardness of the material knowing that this material would satisfy the requisite design parameters; more detailed chemical or mechanical characterization was not of concern to them. Gurtman and Sallay contacted

the manufacturer to determine the likely makeup of the material, which as stated above is Adiprene L-100 cured with MOCA. This story serves as a cautionary tale for future developments at the Explosive Loading Laboratory; newly manufactured programmers must be subject to strict material and procedural controls so that its properties can readily be determined from existing material models.

There exist no fully-accepted material models for Adiprene L-100. It is known that it is a viscoelastic material and that exhibits shear thinning (a reduction in viscosity at large strain rates). Johnson et al. [25] propose that Adiprene L-100 can be modelled by a generalized Maxwell model, which is a collection of any number of Maxwell elements in parallel. They settle on the standard solid model[1] with two elastic springs and adopt from Bardenhagen et al. [6] a damping constant that depends on strain rate as

$$\eta(\dot{\varepsilon}) = \eta_\infty + \frac{\eta_o - \eta_\infty}{[1 + (c_1\,\dot{\varepsilon})^2]^{(1-c_2)/2}} \tag{5.1}$$

where η_o is the viscosity at zero strain rate, η_∞ is the viscosity at infinite strain rates, and c_1 and c_2 are additional parameters used to adjust the degree of shear thinning. These and other parameters are fitted to experimental data. The standard solid model is a sound choice; recall that the programmer test data presented in Section 4.C.1 suggest that the material exhibits behavior consistent with such a model.

Khan et al. [26] propose a different model: an extension of the standard solid model that adds a dashpot in parallel with the standard solid model. The lone spring follows a nonlinear power rule and the viscous constants of both dashpots vary with strain rate as

$$\eta = \eta_\infty + \frac{\eta_o - \eta_\infty}{(1 + (c_3\dot{\varepsilon})^2 - (|\dot{\varepsilon}|/c_6)^{c_4})^{c_5}} \tag{5.2}$$

where η_o and η_∞ are defined as above; c_3, c_4, and c_5 are additional parameters used to adjust the degree of shear thinning; and c_6 is equal to 1e5/s. These and other

[1]The standard solid model is a specific instance of a generalized Maxwell model. It is a two-element generalized Maxwell model with one of the damping constants tending to infinity.

parameters are fitted to experimental data. Unfortunately, the model suffers from serious problems that were brought to light by both Sallay's [46] and my separate efforts at applying the model. First, the additional dashpot introduces non-physical behavior such as non-zero stress at the beginning of loading. Second the strain rate $\dot{\varepsilon}$ referred to by Equation (5.2) is defined as the strain rate across only the dashpot, not the global strain rate. While this is physically sensible, it makes the numerical application much more expensive because it involves at each time step an iterative solution of the strain rate across the dashpot. It is unclear why this complication is necessary. Nonetheless, Khan et al. have proposed sensible forms of the equations governing the viscous constants and the nonlinear springs. These equations may later prove useful in building a custom model to describe the behavior of the programmer material.

Neither reference specifies the curative used in manufacturing the Adiprene L-100 specimens. Therefore, it is unclear whether a direct application of either model would directly model the programmer. Instead, it is best to conduct independent material tests on the programmer material and to develop an appropriate viscoelastic model, using as possible starting points the useful ideas espoused by the above mentioned references. Material tests need to be conducted at stress rates up to about 500/s, which correspond to about a 28 m/s impacting velocity. This is higher than can be imposed with a stress-strain machine (as seen in Section 4.C.1) but lower than what is imposed by a Hopkinson bar test [38, Chap. 12]. Instead, drop tests need to be performed to capture the desired strain rates. In addition, slower loading-relaxation tests should be conducted to characterize the quasi-static behavior. Ideally, the loading tests are performed at a constant true strain rate, but this is near impossible in the case of the drop test. Creep tests should be conducted as well to provide a comprehensive material characterization and redundant data. Once the tests are performed, the existing material models can be assessed for their applicability to the programmer material.

Whatever model is selected, a proper numerical implementation is crucial

in solving the differential equation and fitting the parameters. Given the form of the differential equation (e.g., Equation (1.61)) it might be tempting to solve the differential equation for $\dot{\sigma}$ as a function of σ. In this way the increment of stress can be written as a function of stress in the previous time step and the equation can be solved incrementally. However, this method exhibits terrible time step instabilities, especially for large values of E/η. Instead, it is better to assume a constant strain rate over each time step and solve the differential equation for this condition. The stress is solved independently for each element in parallel; the total stress is then calculated as the sum of all elements in parallel.

In summary, future material characterization depends on first conducting a battery of material tests at the appropriate strain rates. These results can be compared with existing models for Adiprene L-100 to derive an appropriate model for the programmer behavior. Evaluation of the model under arbitrary loading paths depends on a proper numerical implementation for which some guidelines have been provided.

5.B Summary of the Dissertation

The first chapter motivates the research by providing a conceptual framework in which to understand the results. There have been a number of attacks against United States installations at home and abroad. Included in the response to these attacks are defensive technologies to mitigate the damaging effects of such bomb attacks on buildings. To meet this need by experimentally testing promising designs, the Explosive Loading Laboratory, headed by principal investigators G. Hegemier and F. Seible, enables investigators to experimentally simulate blast loading on structural specimens at a lower cost and with better data than tests using real explosives.

The bulk of the first chapter discusses fundamentals related to later developments: blast loading on buildings, analysis methods including the single degree

of freedom method, viscoelastic theory, theory of collisions, and relevant experimental work. The equivalent single degree of freedom method and the discussion on collisions figure prominently in the new methods developed in Chapters 3 and 4. Previous field experiments are mentioned for comparison to the results described in Chapter 3. Other sections provide a sound technical background to developments throughout the dissertation.

The second chapter covers the design, construction and proof testing of the Explosive Loading Laboratory, which took place between late 2002 and early 2005. The simulated blast load is applied via specially designed apparatuses called blast generators or BGs. Each BG is made of a high speed actuator that accelerates an impacting module towards the specimen. A polymer pad called the programmer, which is located on the front of the impacting module, is designed to provide a blast-like pressure pulse. The setup is housed in a self-reacting reaction structure that is isolated from the surrounding facilities. It is made of highly post-tensioned reinforced concrete and designed to suffer no tension during service. Proof tests of the BGs were conducted at the factory and once the facility was constructed, at the site. These tests are described not only to demonstrate that the BGs function as intended, but also to provide initial insight into the facility behavior and to present data that will be used in later chapters.

The third chapter discusses the first-ever series of simulated blast tests. Because the simulated blast methodology is new, this requires the development of novel methods of data analysis: the equivalent uniform load method, which converts the loads imparted by a number of BGs to a single equivalent load and the equivalent charge method that converts this equivalent load to a representative charge size. The equivalent uniform load method is derived for a general case and it applies not only to the tests described in this chapter, but to other BG arrangements and even to field tests using real explosives. This method produces a single, rationally-obtained metric for comparing across laboratory and field tests.

The test results themselves are described in detail to provide the first-

ever record of the structural behavior during a blast-like event. Unlike field blast tests, where the structural behavior is hidden by the fireball, the laboratory tests provide a view of the entire test sequence. Detailed text descriptions and video captures are provided for seven tests on retrofitted and non-retrofitted specimens. The results demonstrate once again the effectiveness of carbon fiber composite jackets in mitigating the damage caused by blast loads and lend credence to the validity of simulated blast.

The fourth chapter is aimed at facilitating future research by proving the equivalence between laboratory simulations and field tests and by developing analytical tools that future investigators can use to predict and analyze results. The equivalence between field and laboratory data is shown most dramatically with a demand-damage plot formed with laboratory and field data in which the two data sets are indistinguishable. After this, two analytical tools are developed: a pre-test prediction and a structural characterization of the programmer. The former is useful for an investigator to quickly and easily determine the necessary impacting velocity to deliver a desired impulse to the specimen. The latter is useful for more detailed analyses of the simulated blast event. Both tools are derived theoretically, calibrated to experimental data, and verified against independent experimental data. In the latter case, the verification highlights some anomalies in the recorded data that improve our understanding of BG behavior by highlighting some unknown behavior that merits future investigation. The models are currently limited to programmers of the same geometry and material as those used in these tests. Extensions are discussed in the following chapter.

The fifth and final chapter includes this summary and ideas for future research in programmer modelling. The programmer characterization in the previous chapter is based on average global response of a programmer of a specific shape. To determine stress profiles with more detail and to calculate the behavior of programmers of arbitrary shape requires a more detailed material characterization. To this end, appropriate viscoelastic material models are selected from the

literature and discussed. An appropriate testing battery is proposed and numerical issues are mentioned. This sets the stage for a more sophisticated understanding of the laboratory behavior.

The main contribution of this work is in the analytical and experimental tools and confidence it brings to a nascent field of simulated blast testing. With the work presented here, future investigators can be confident that their results correlate with the results that would be obtained under real blast testing, and they have tools that enable them to conduct experiments and analyze test results. This work sets the stage for decades of fruitful research.

A Derivations

Equation (1.61)

Equation (1.61), the governing equation for the standard solid model presented in Chapter 1 is derived. Two equations govern the behavior of the proposed solid:

$$\dot{\varepsilon} = \frac{\dot{\sigma}_m}{E_1} + \frac{\sigma_m}{\eta} \tag{A.1}$$

$$\sigma = \sigma_m + E_2\,\varepsilon \tag{A.2}$$

The first is the governing equation for the Maxwell element (σ_m is the stress in the Maxwell element) and the second is the equilibrium of the entire model. First, Equation (A.1) is rearranged to obtain

$$\dot{\sigma}_m = E_1\left[\dot{\varepsilon} - \frac{\sigma_m}{\eta}\right] \tag{A.3}$$

Then Equation (A.2) is solved for σ_m

$$\sigma_m = \sigma - E_2\,\varepsilon \tag{A.4}$$

and differentiated to obtain

$$\dot{\sigma}_m = \dot{\sigma} - E_2\,\dot{\varepsilon} \tag{A.5}$$

Equations (A.3) and (A.5) are set equal to each other to obtain

$$\dot{\sigma} - E_2\,\dot{\varepsilon} = E_1\left[\dot{\varepsilon} - \frac{\sigma_m}{\eta}\right] \tag{A.6}$$

This is combined with Equation (A.4) to obtain

$$\dot{\sigma} - E_2\,\dot{\varepsilon} = E_1\left[\dot{\varepsilon} - \frac{\sigma - E_2\,\varepsilon}{\eta}\right] \tag{A.7}$$

which when rearranged yields the governing equation for the standard solid model (Equation (1.61))

$$\dot{\sigma} + \frac{E_1}{\eta}\,\sigma = (E_1 + E_2)\,\dot{\varepsilon} + \frac{E_1\,E_2}{\eta}\,\varepsilon \tag{A.8}$$

Equation (4.6)

Equation (4.6) is derived by considering the collision between a distributed mass against a specimen. The five governing equations (Equations (4.1) to (4.5)) are discussed in the main text and are repeated here for reference:

$$\int_L m_1(x)\mathsf{v}_{1i}(x)\,\mathrm{d}x = \int_L m_1(x)\mathsf{v}_{1f}(x)\,\mathrm{d}x + \int_L m_2(x)\mathsf{v}_{2f}(x)\,\mathrm{d}x \tag{A.9}$$

$$c_r(\mathsf{v}_{1i}(x)) = \frac{\mathsf{v}_{2f}(x) - \mathsf{v}_{1f}(x)}{\mathsf{v}_{1i}(x)} \tag{A.10}$$

$$\mathsf{v}_{1i}(x) = \mathsf{v}_o\psi_1(x) \tag{A.11}$$

$$\mathsf{v}_{2f}(x) = \dot{z}_o\psi(x) \tag{A.12}$$

$$I = \int_L m_2(x)\mathsf{v}_{2f}(x)\,\mathrm{d}x \tag{A.13}$$

First, Equation (A.10) is solved for v_{1f}

$$\mathsf{v}_{1f} = \mathsf{v}_{2f} - c_r\,\mathsf{v}_{1i} \tag{A.14}$$

and substituted into Equation (A.9) to obtain

$$\int_L m_1\mathsf{v}_{1i}\,\mathrm{d}x = \int_L m_1(\mathsf{v}_{2f} - c_r\,\mathsf{v}_{1i})\,\mathrm{d}x + \int_L m_2\mathsf{v}_{2f}\,\mathrm{d}x \tag{A.15}$$

which after rearranging becomes

$$\int_L m_1\mathsf{v}_{1i}(1 + c_r)\,\mathrm{d}x = \int_L \mathsf{v}_{2f}(m_1 + m_2)\,\mathrm{d}x \tag{A.16}$$

Equation (A.11) is substituted into the left hand side and Equation (A.12) into the right hand side of Equation (A.16) to obtain

$$\mathsf{v}_o\int_L m_1(1 + c_r)\psi_1\,\mathrm{d}x = \dot{z}_o\int_L (m_1 + m_2)\psi\,\mathrm{d}x \tag{A.17}$$

In the only step that is not entirely obvious Equation (A.13) is rearranged to obtain the following identity

$$1 = \frac{I}{\int_L m_2 \, \mathsf{v}_{2f} \, \mathrm{d}x} \tag{A.18}$$

Equation (A.12) is substituted into Equation (A.18) to obtain

$$1 = \frac{I}{\dot{z}_o \int_L m_2 \psi \, \mathrm{d}x} \tag{A.19}$$

which is multiplied on the right hand side of Equation (A.17) to obtain

$$\mathsf{v}_o \int_L m_1 (1 + c_r) \psi_1 \, \mathrm{d}x = I \cdot \left[\frac{\int_L (m_1 + m_2) \psi \, \mathrm{d}x}{\int_L m_2 \psi \, \mathrm{d}x} \right] \tag{A.20}$$

after cancellation of the $\dot{z}_o$ term. This is the sought after result in Equation (4.6).

B Programmer Test Data

This appendix contains test data from the programmer tests described in Section 4.C.1. For each test eight different plots are provided, four in force-deformation space and four in stress-strain space. In force-deformation space plots are provided for force-time, deformation-time, force-deformation, and deformation rate-time. In stress-strain space they are provided for stress-time, strain-time, stress-strain, and strain rate-time. All these are true, not engineering values. Calculation of stress and strain are described in the main text (p. 179). The strain rate is calculated numerically from the calculated strain. The deformation and deformation rate plots show both the deformation suffered by the programmer as well as the deflection recorded for the actuator. The difference is the deflection of the reaction structure that influenced the ability to apply a constant deformation rate. The plots are presented four to a page and begin on the following page.

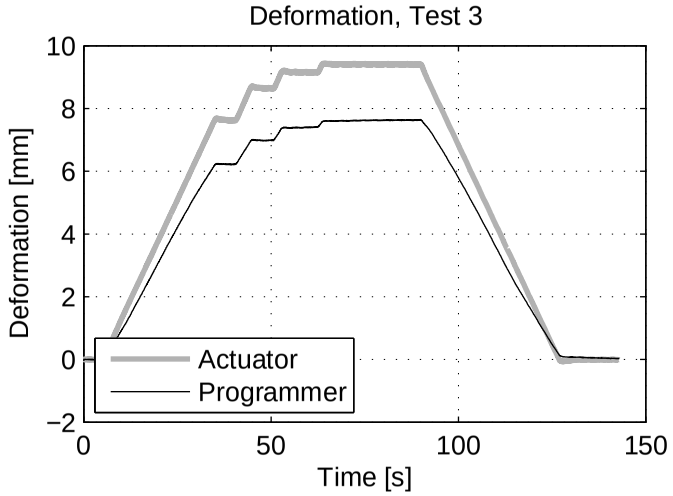
Deformation, Test 3
Deformation [mm]
Time [s]
Actuator
Programmer

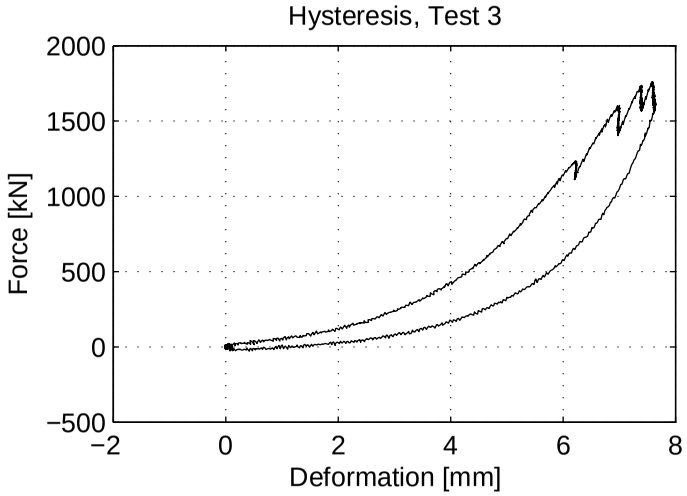
Hysteresis, Test 3
Force [kN]
Deformation [mm]

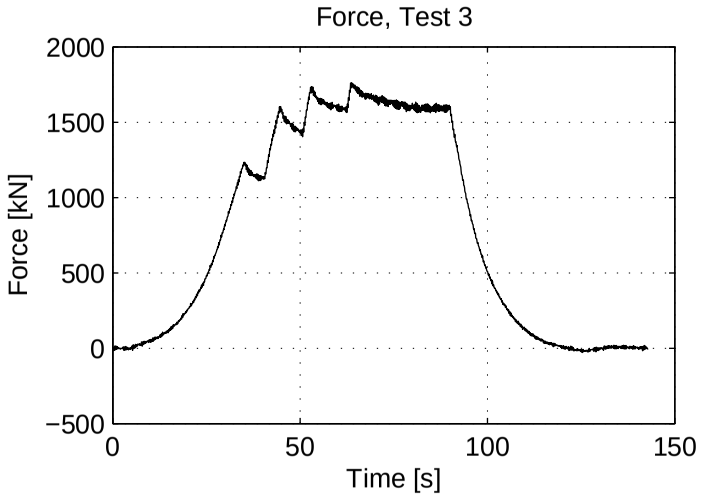
Force, Test 3
Force [kN]
Time [s]

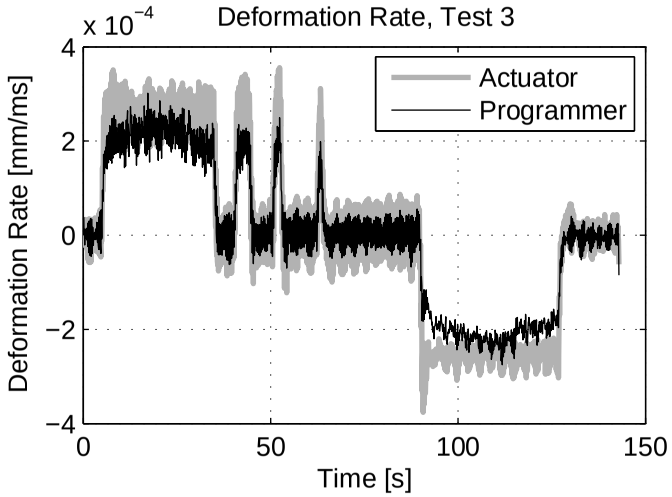
x 10^-4
Deformation Rate, Test 3
Deformation Rate [mm/ms]
Time [s]
Actuator
Programmer

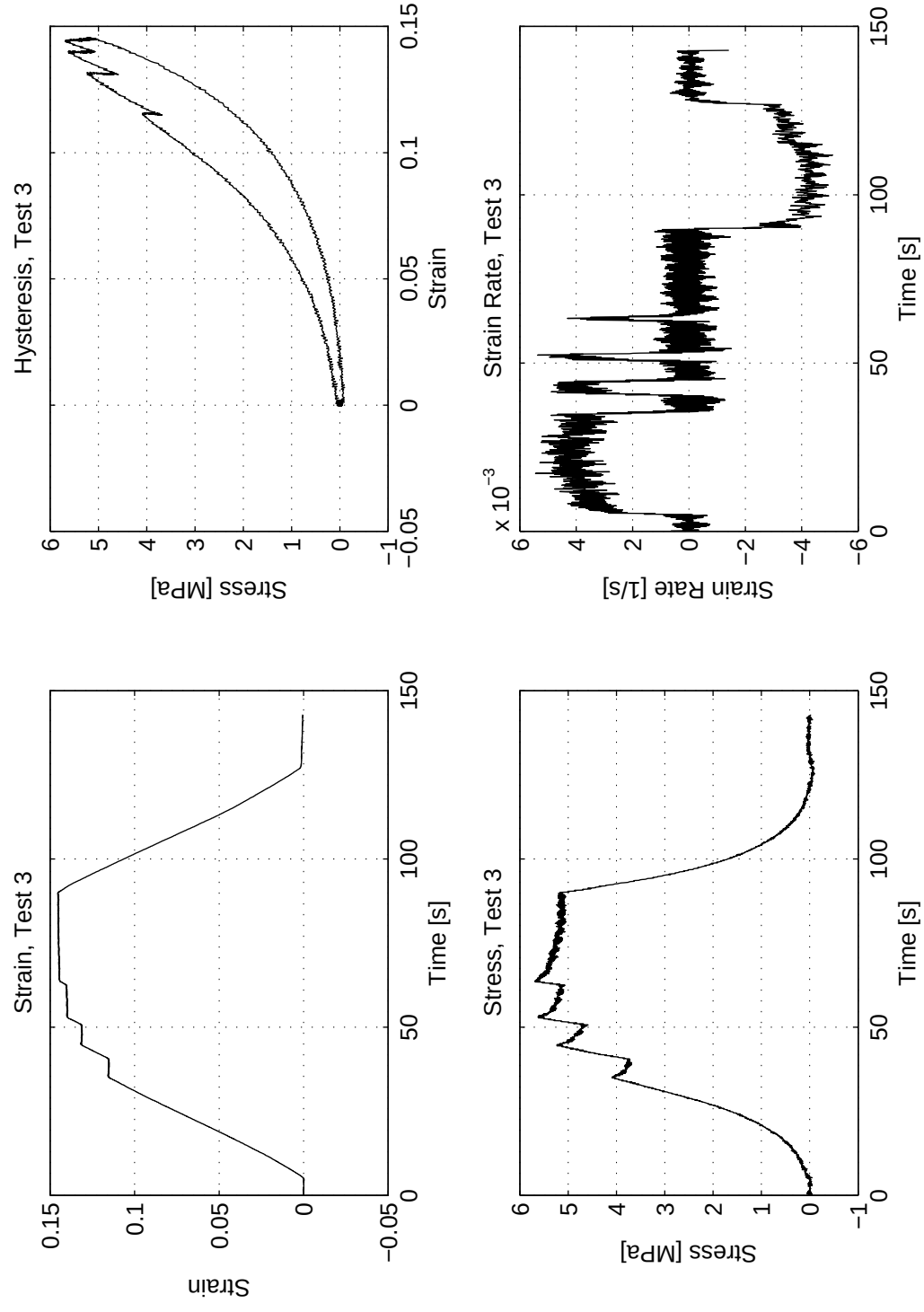
Hysteresis, Test 3
Stress [MPa]
Strain
Strain, Test 3
Strain
Time [s]
Strain Rate, Test 3
x 10^-3
Strain Rate [1/s]
Time [s]
Stress, Test 3
Stress [MPa]
Time [s]

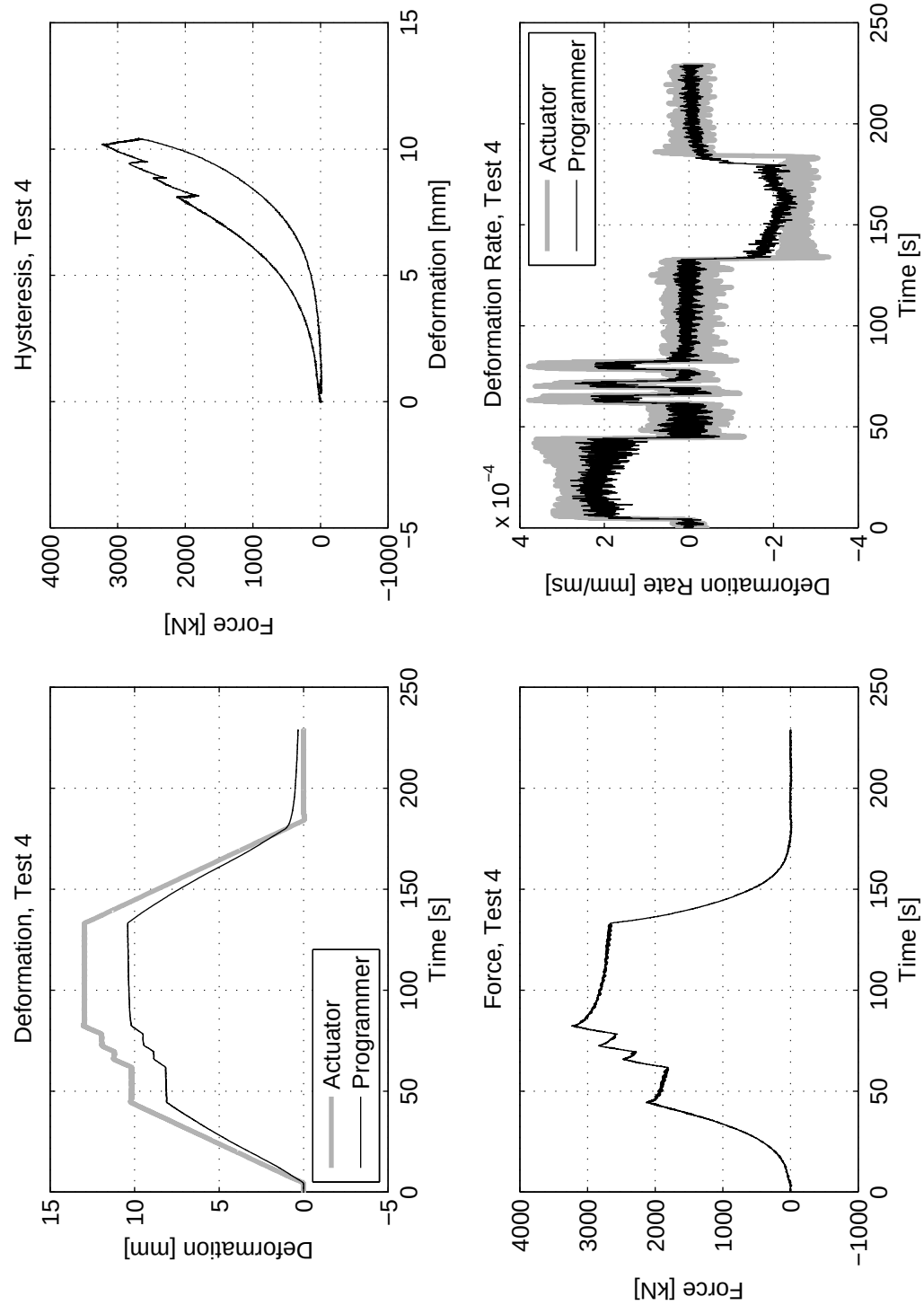
Hysteresis, Test 4
Force [kN]
Deformation [mm]
Deformation, Test 4
Deformation [mm]
Time [s]
Actuator
Programmer
Deformation Rate, Test 4
x 10^-4
Deformation Rate [mm/ms]
Force, Test 4

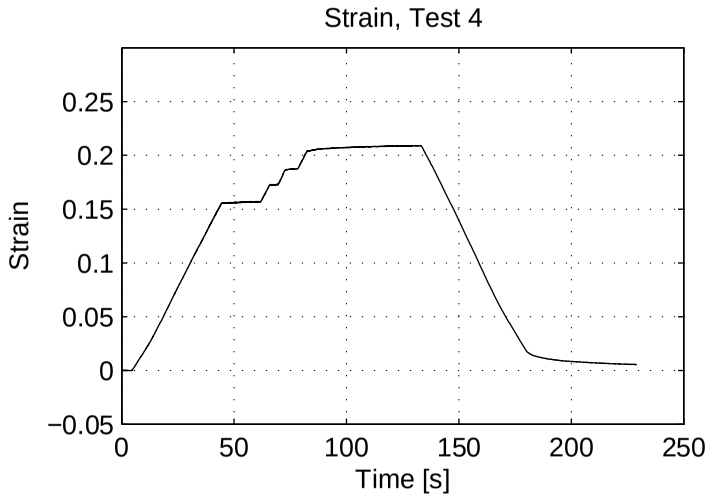
Strain, Test 4
Strain
Time [s]
0.25
0.2
0.15
0.1
0.05
0
−0.05
0
50
100
150
200
250

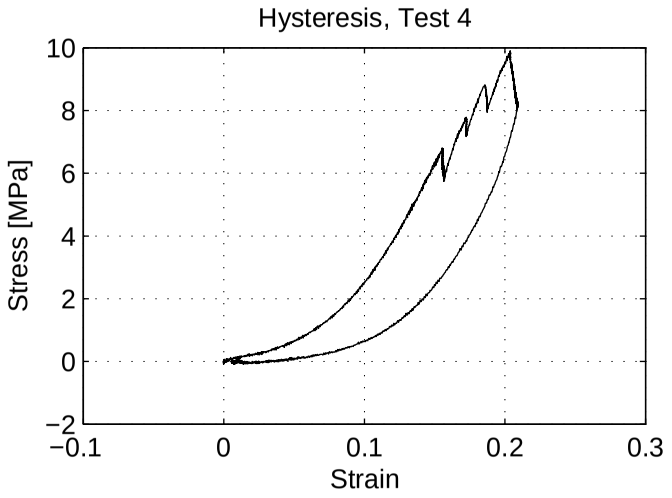
Hysteresis, Test 4
Stress [MPa]
Strain
10
8
6
4
2
0
−2
−0.1
0
0.1
0.2
0.3

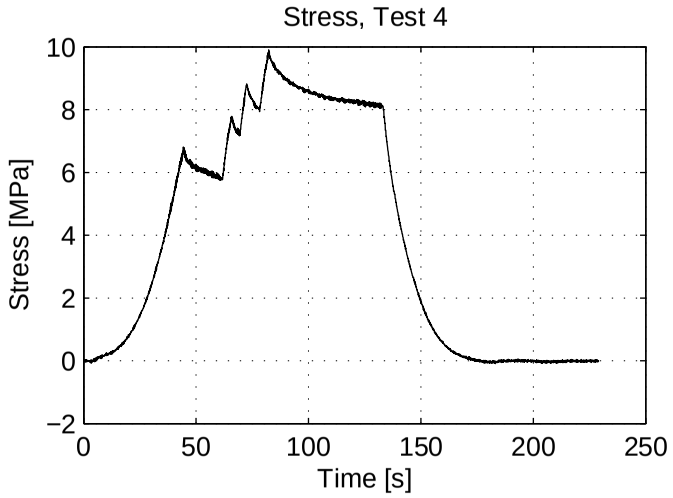
Stress, Test 4
Stress [MPa]
Time [s]
10
8
6
4
2
0
−2
0
50
100
150
200
250

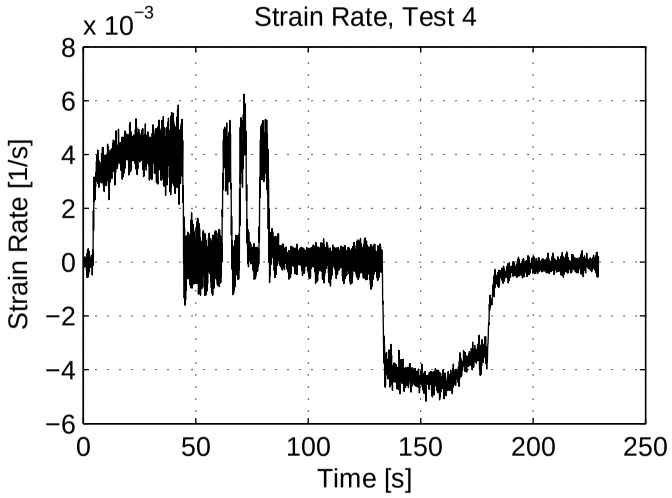
Strain Rate, Test 4
x 10−3
Strain Rate [1/s]
Time [s]
8
6
4
2
0
−2
−4
−6
0
50
100
150
200
250

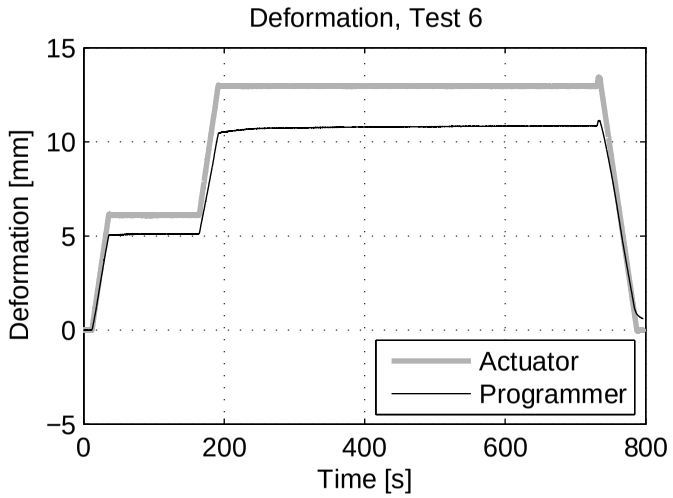
Deformation, Test 6
Deformation [mm]
Time [s]
Actuator
Programmer

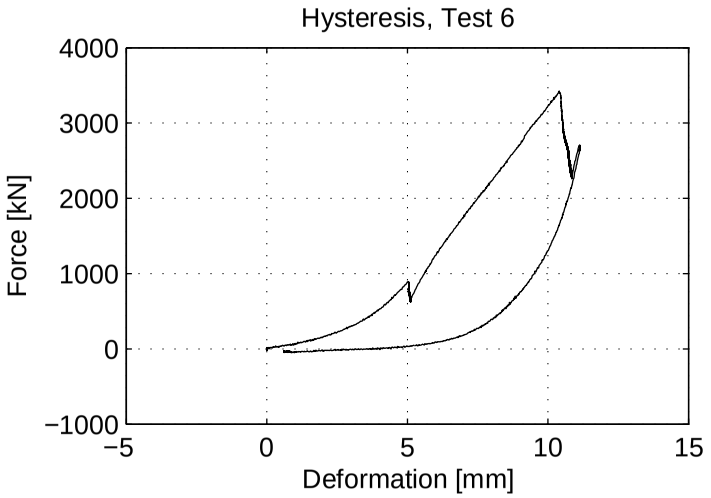
Hysteresis, Test 6
Force [kN]
Deformation [mm]

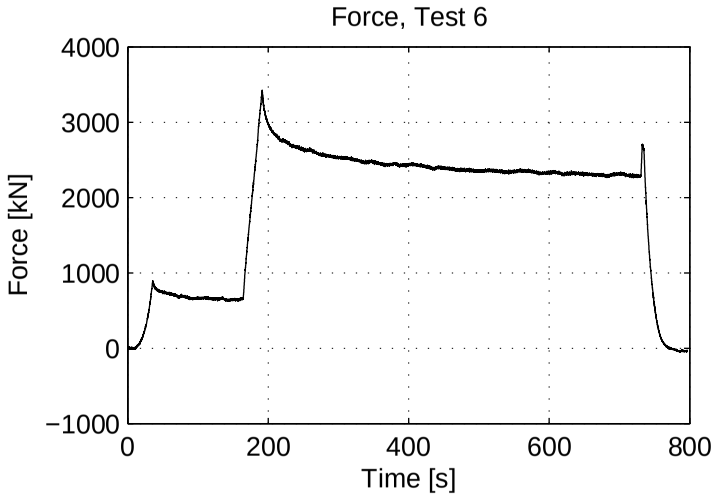
Force, Test 6
Force [kN]
Time [s]

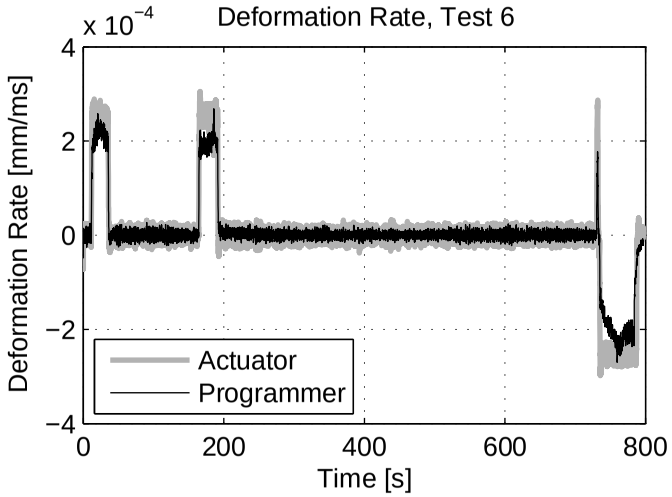
x 10^-4
Deformation Rate, Test 6
Deformation Rate [mm/ms]
Time [s]
Actuator
Programmer

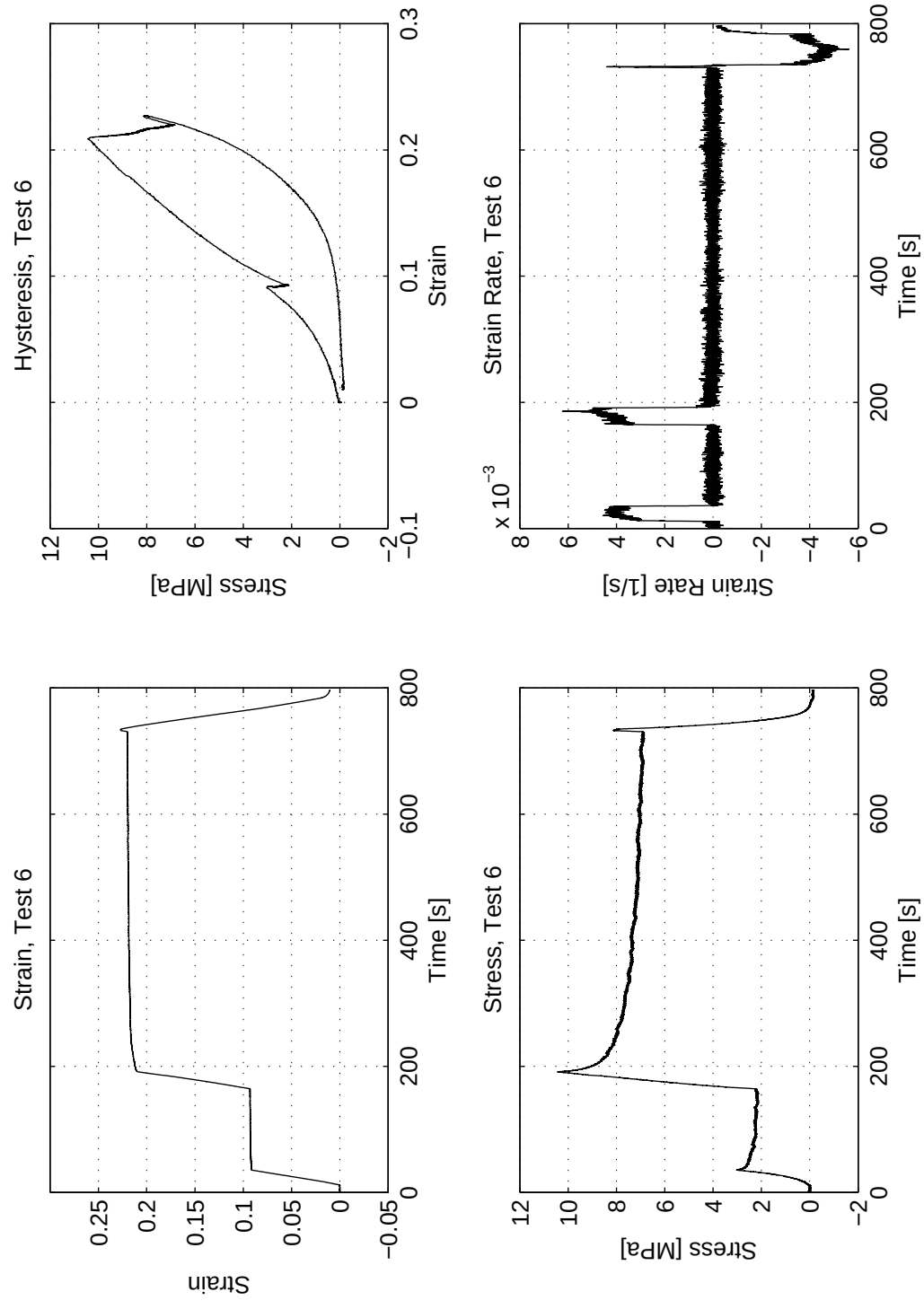
Hysteresis, Test 6
Stress [MPa]
Strain
Strain Rate, Test 6
x 10^-3
Strain Rate [1/s]
Time [s]
Strain, Test 6
Strain
Time [s]
Stress, Test 6
Stress [MPa]
Time [s]

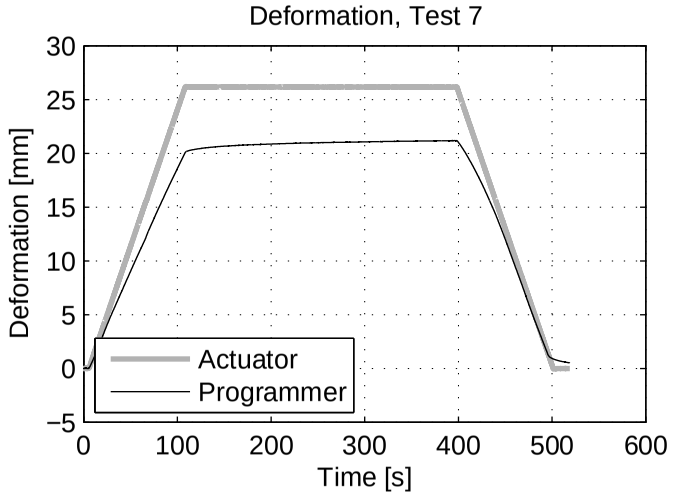
Deformation, Test 7
Deformation [mm]
Time [s]
Actuator
Programmer

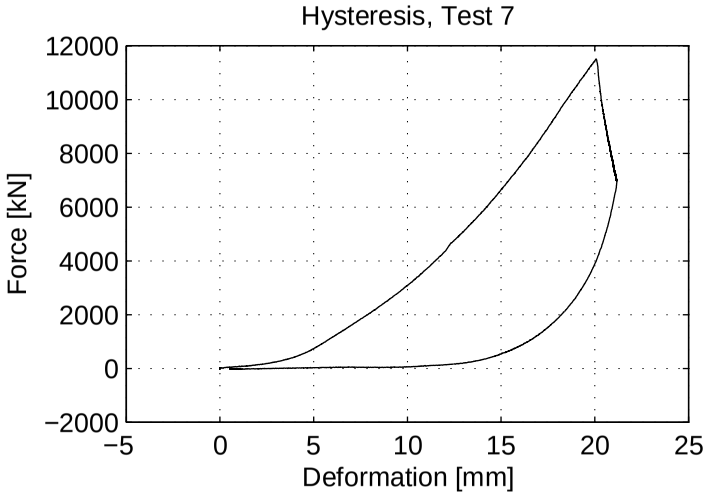
Hysteresis, Test 7
Force [kN]
Deformation [mm]

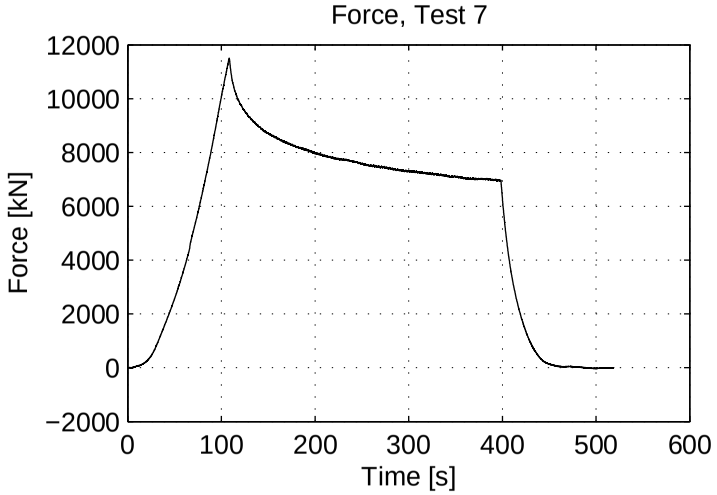
Force, Test 7
Force [kN]
Time [s]

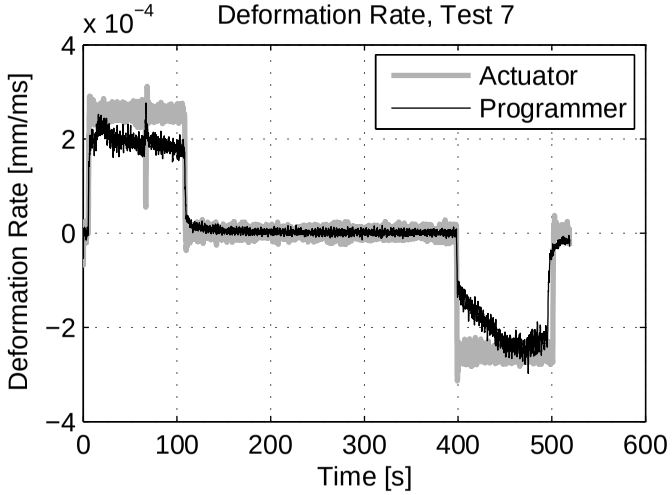
x 10^-4
Deformation Rate, Test 7
Deformation Rate [mm/ms]
Time [s]
Actuator
Programmer

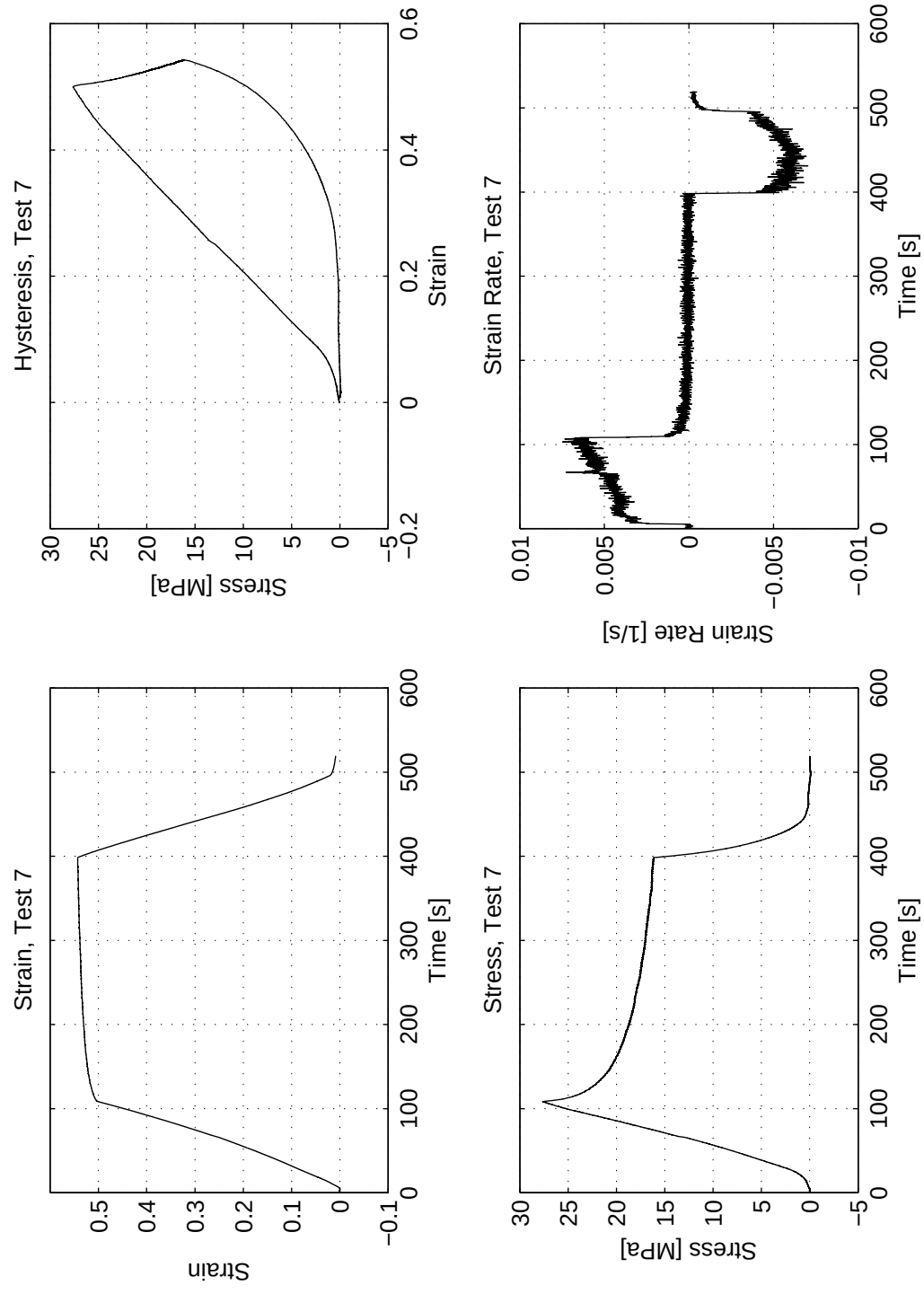
Hysteresis, Test 7
Stress [MPa]
Strain
Strain, Test 7
Strain
Time [s]
Strain Rate, Test 7
Strain Rate [1/s]
Time [s]
Stress, Test 7
Stress [MPa]
Time [s]

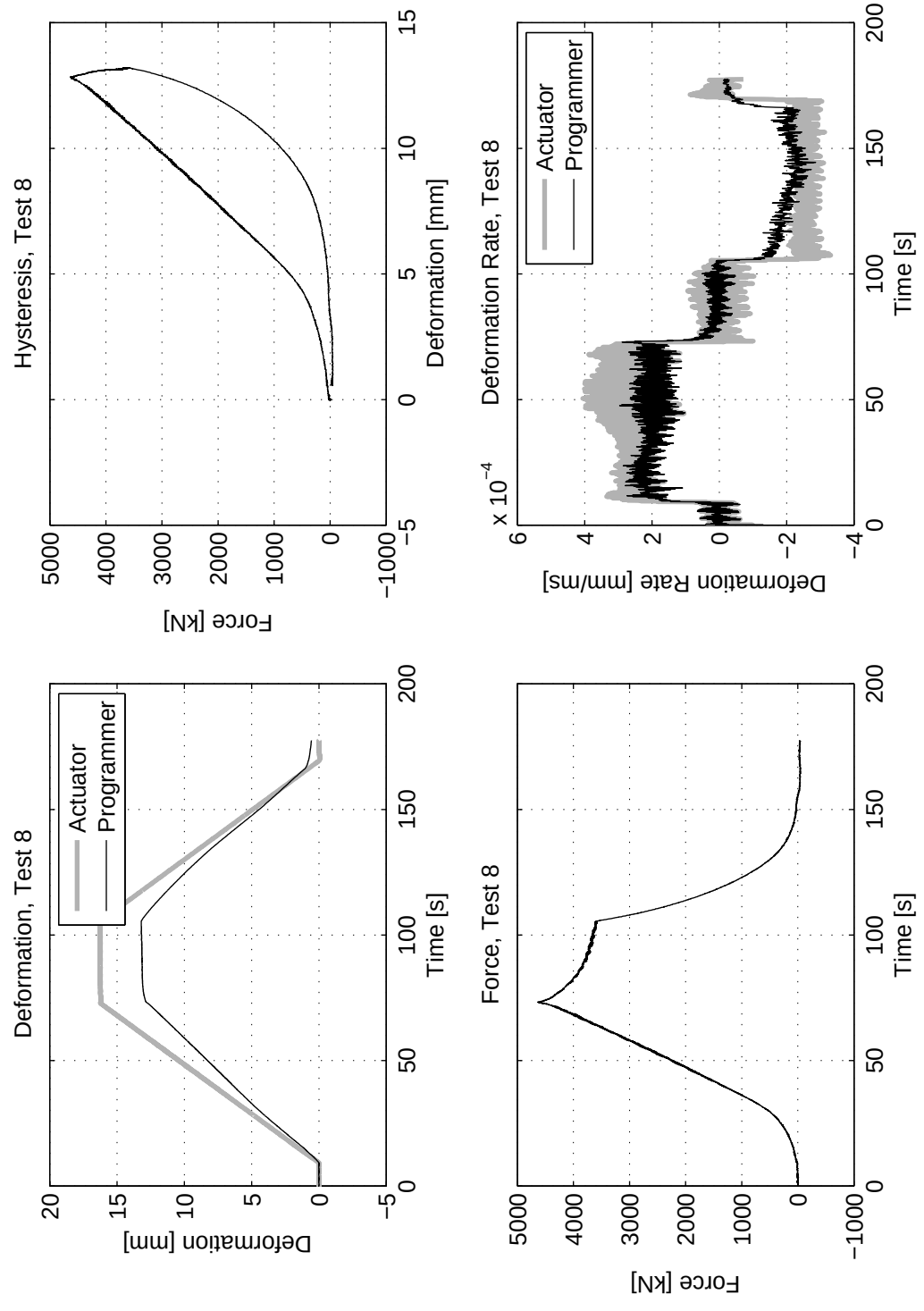
Hysteresis, Test 8
Force [kN]
Deformation [mm]
Deformation, Test 8
Actuator
Programmer
Deformation [mm]
Time [s]
Deformation Rate, Test 8
x 10^-4
Deformation Rate [mm/ms]
Force, Test 8
Force [kN]

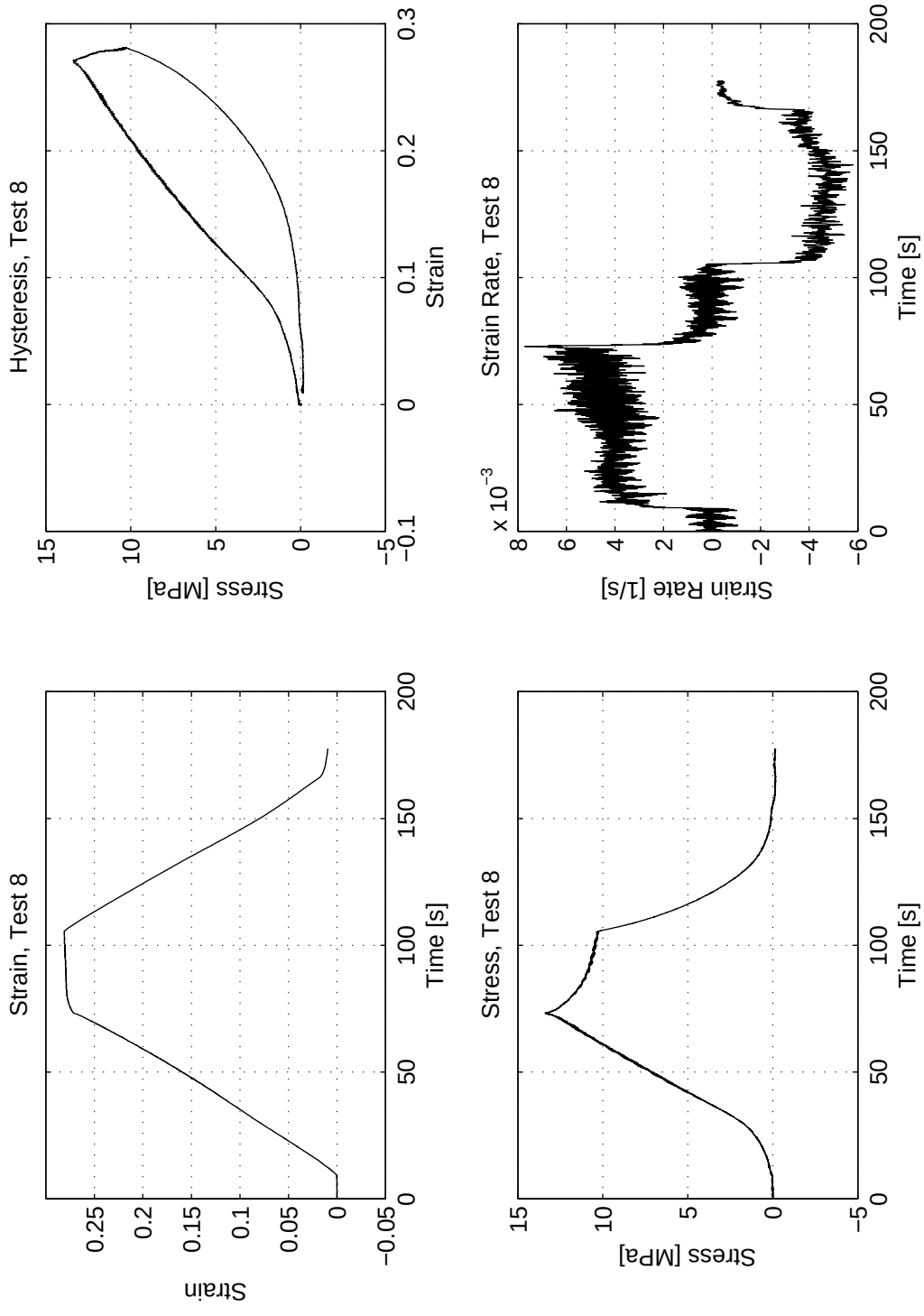
Hysteresis, Test 8
Stress [MPa]
Strain
Strain, Test 8
Strain
Time [s]
Strain Rate, Test 8
x 10^-3
Strain Rate [1/s]
Time [s]
Stress, Test 8
Stress [MPa]
Time [s]

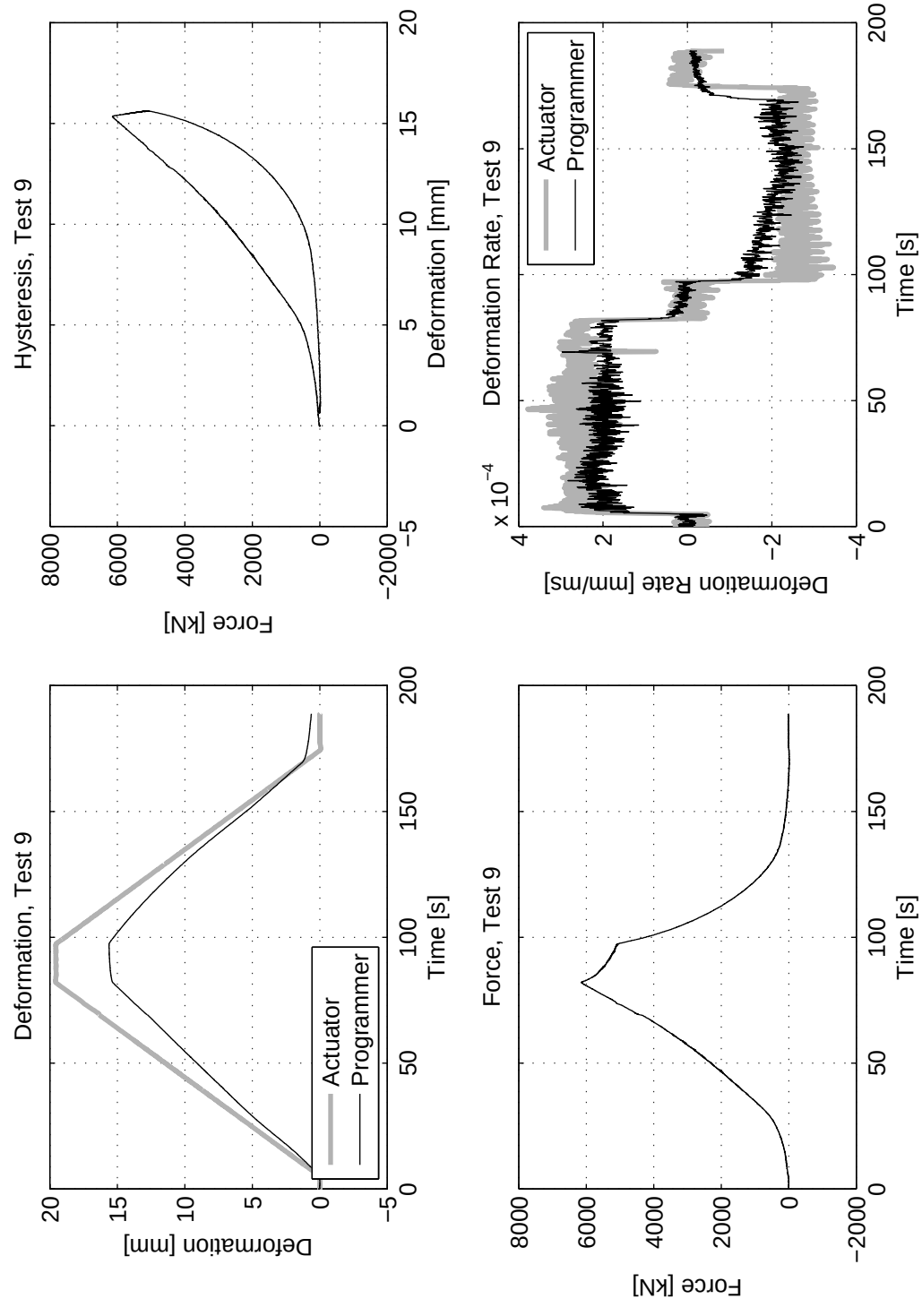
Hysteresis, Test 9
Force [kN]
Deformation [mm]
Deformation, Test 9
Deformation [mm]
Time [s]
Actuator
Programmer
Deformation Rate, Test 9
x 10^-4
Deformation Rate [mm/ms]
Force, Test 9

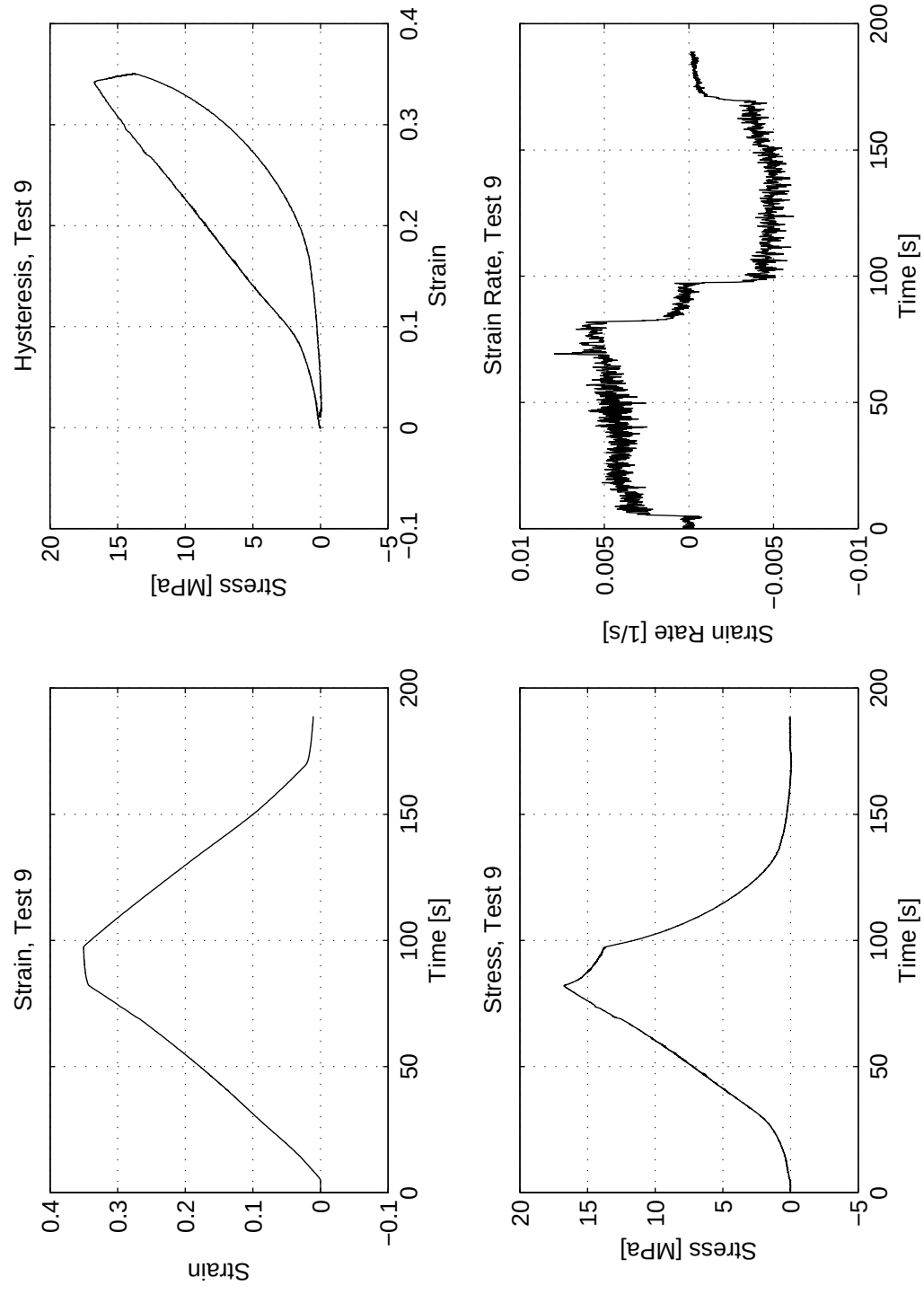
Hysteresis, Test 9
Stress [MPa]
Strain
Strain, Test 9
Strain
Time [s]
Strain Rate, Test 9
Strain Rate [1/s]
Time [s]
Stress, Test 9
Stress [MPa]
Time [s]

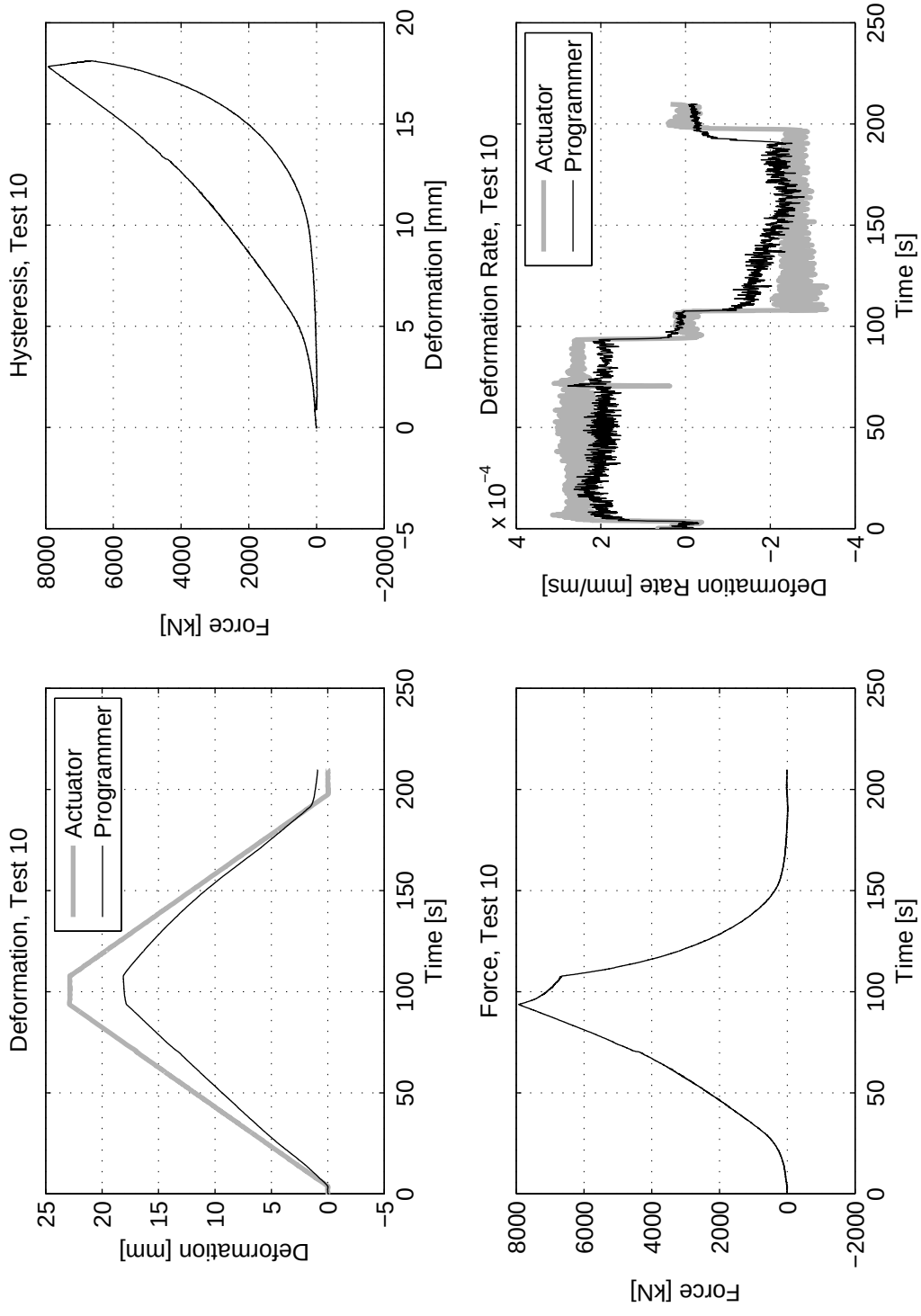
Hysteresis, Test 10
Force [kN]
Deformation [mm]
Deformation Rate, Test 10
x 10^-4
Deformation Rate [mm/ms]
Time [s]
Actuator
Programmer
Deformation, Test 10
Deformation [mm]
Force, Test 10

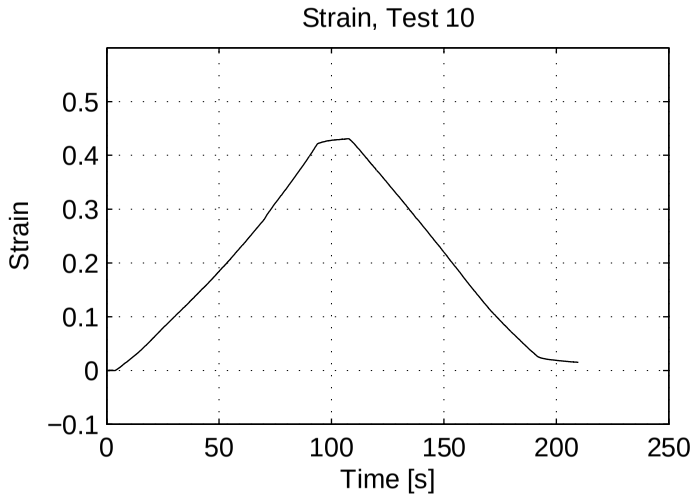
Strain, Test 10
Strain
Time [s]
0.5
0.4
0.3
0.2
0.1
0
−0.1
0
50
100
150
200
250

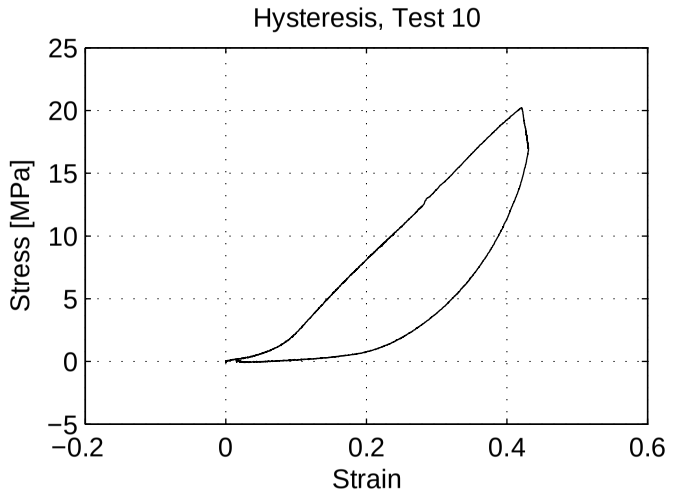
Hysteresis, Test 10
Stress [MPa]
Strain
25
20
15
10
5
0
−5
−0.2
0
0.2
0.4
0.6

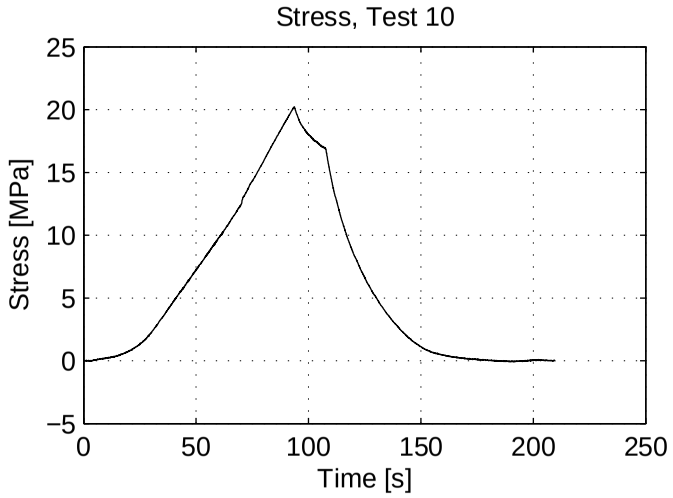
Stress, Test 10
Stress [MPa]
Time [s]
25
20
15
10
5
0
−5
0
50
100
150
200
250

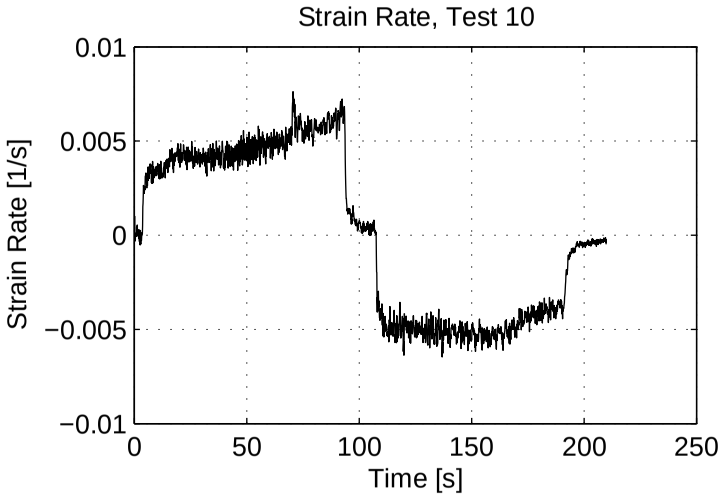
Strain Rate, Test 10
Strain Rate [1/s]
Time [s]
0.01
0.005
0
−0.005
−0.01
0
50
100
150
200
250

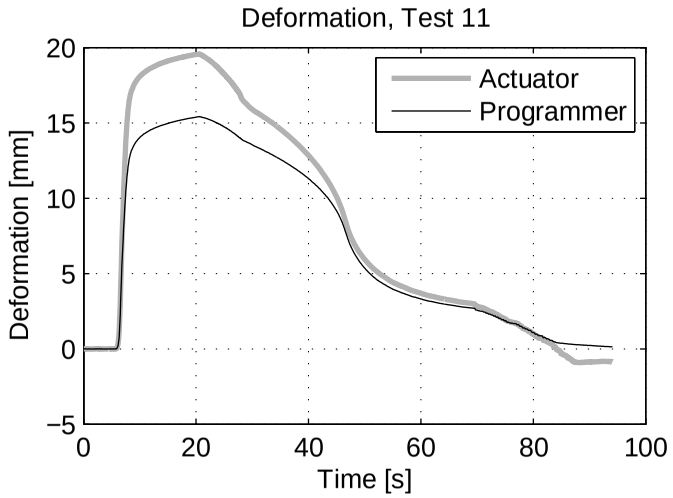
Deformation, Test 11
Actuator
Programmer
Deformation [mm]
Time [s]

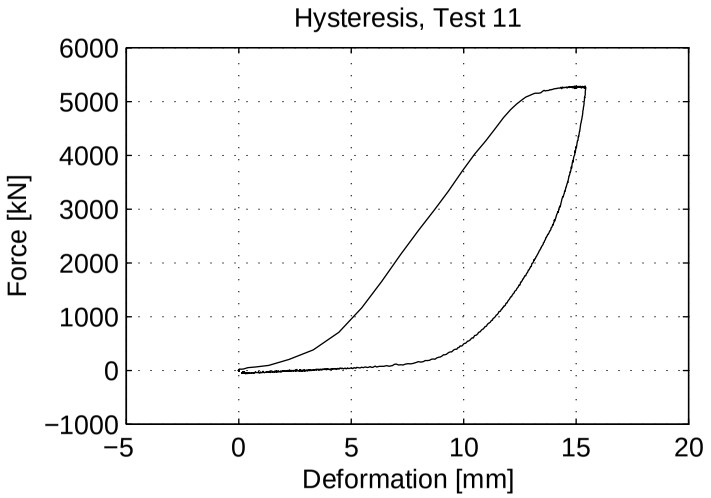
Hysteresis, Test 11
Force [kN]
Deformation [mm]

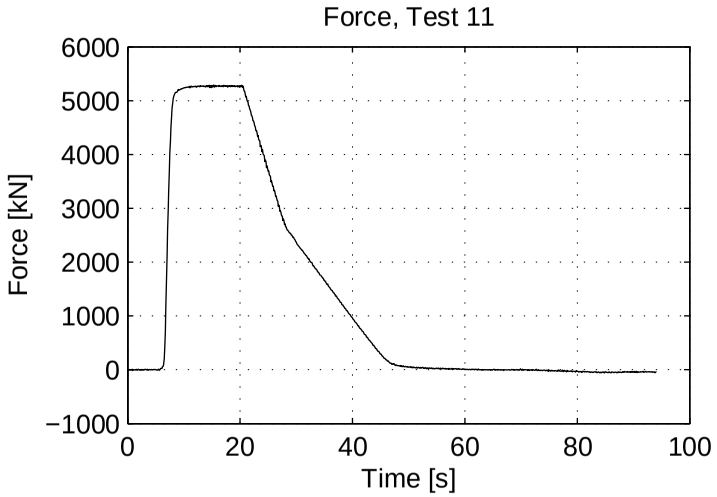
Force, Test 11
Force [kN]
Time [s]

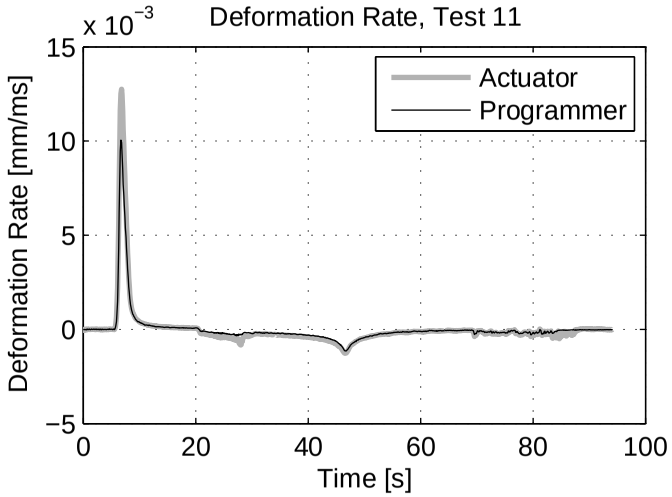
x 10^-3
Deformation Rate, Test 11
Actuator
Programmer
Deformation Rate [mm/ms]
Time [s]

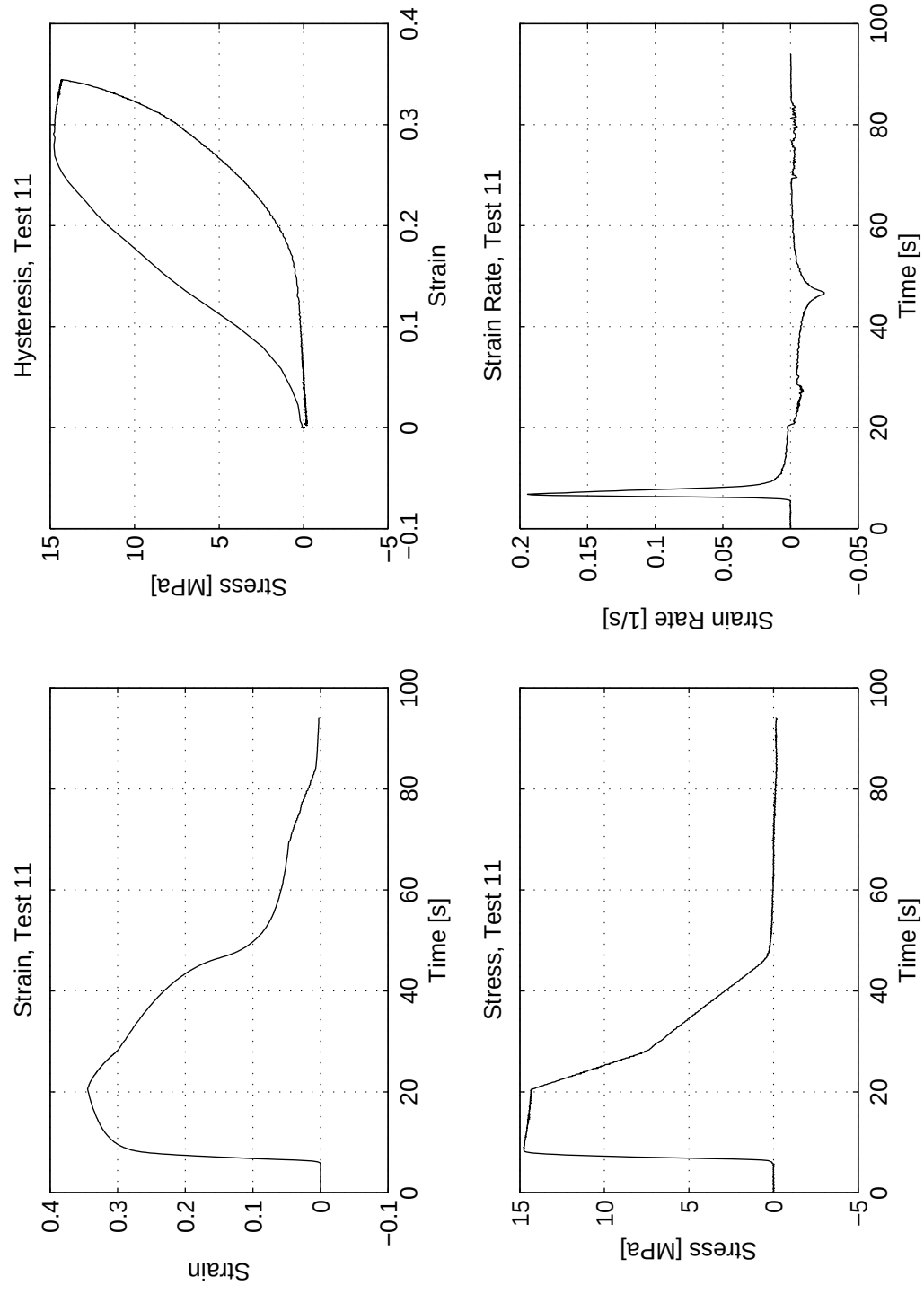
Hysteresis, Test 11
Stress [MPa]
Strain
Strain Rate, Test 11
Strain Rate [1/s]
Time [s]
Strain, Test 11
Strain
Time [s]
Stress, Test 11
Stress [MPa]
Time [s]

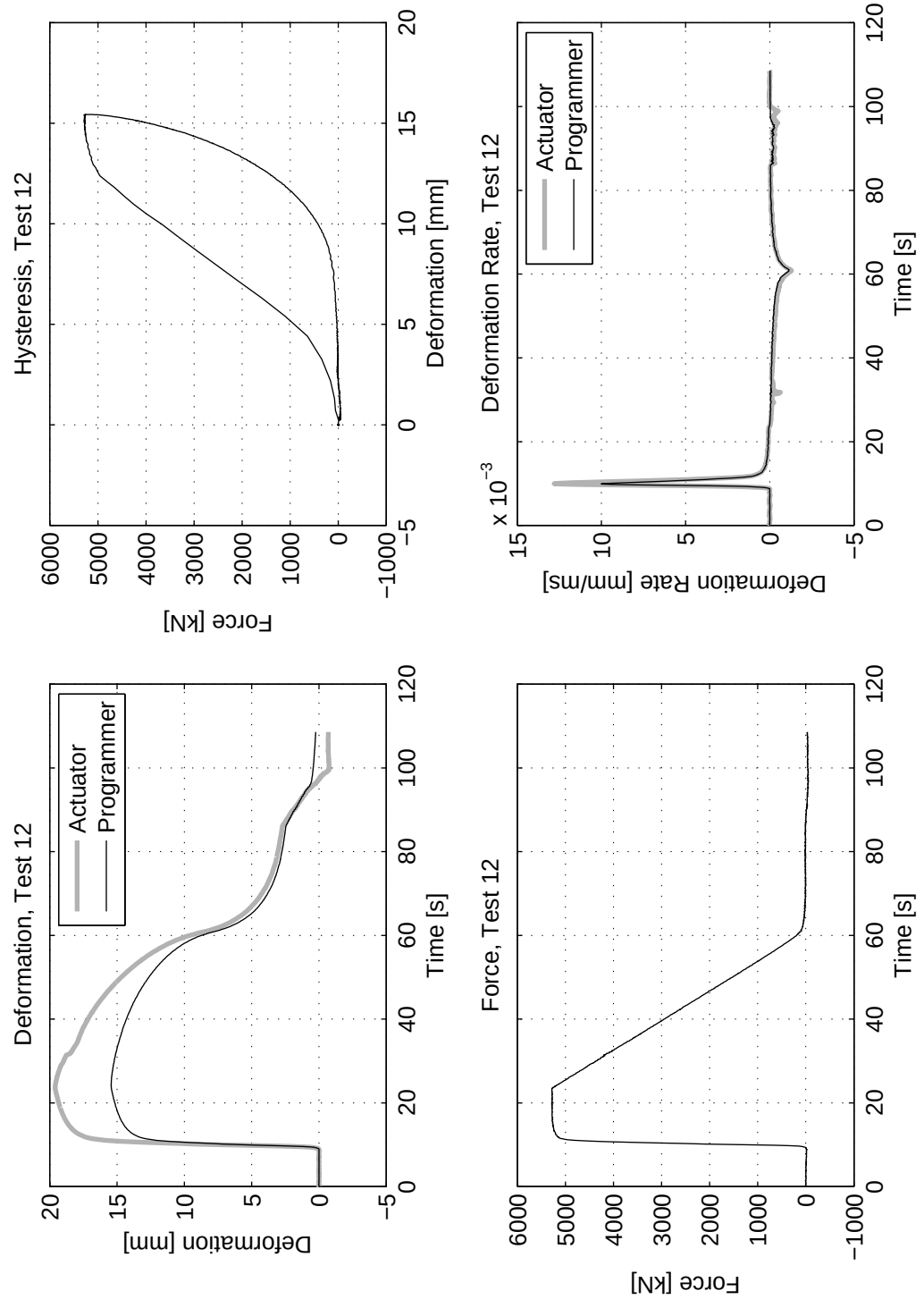
Hysteresis, Test 12
Force [kN]
Deformation [mm]
Deformation, Test 12
Actuator
Programmer
Deformation [mm]
Time [s]
Deformation Rate, Test 12
x 10^-3
Deformation Rate [mm/ms]
Force, Test 12

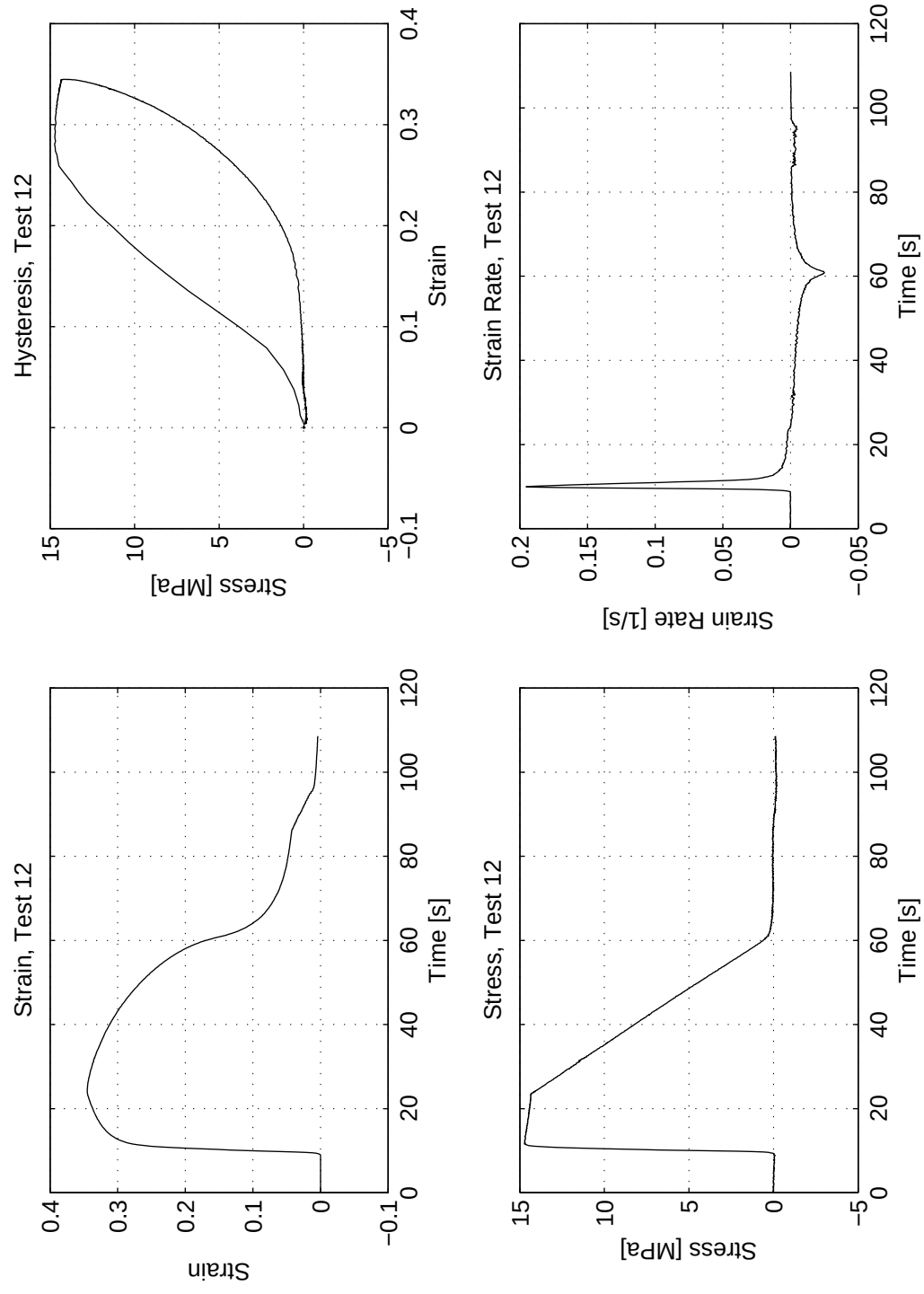
Hysteresis, Test 12
Stress [MPa]
Strain
Strain Rate, Test 12
Strain Rate [1/s]
Time [s]
Strain, Test 12
Strain
Time [s]
Stress, Test 12
Stress [MPa]
Time [s]

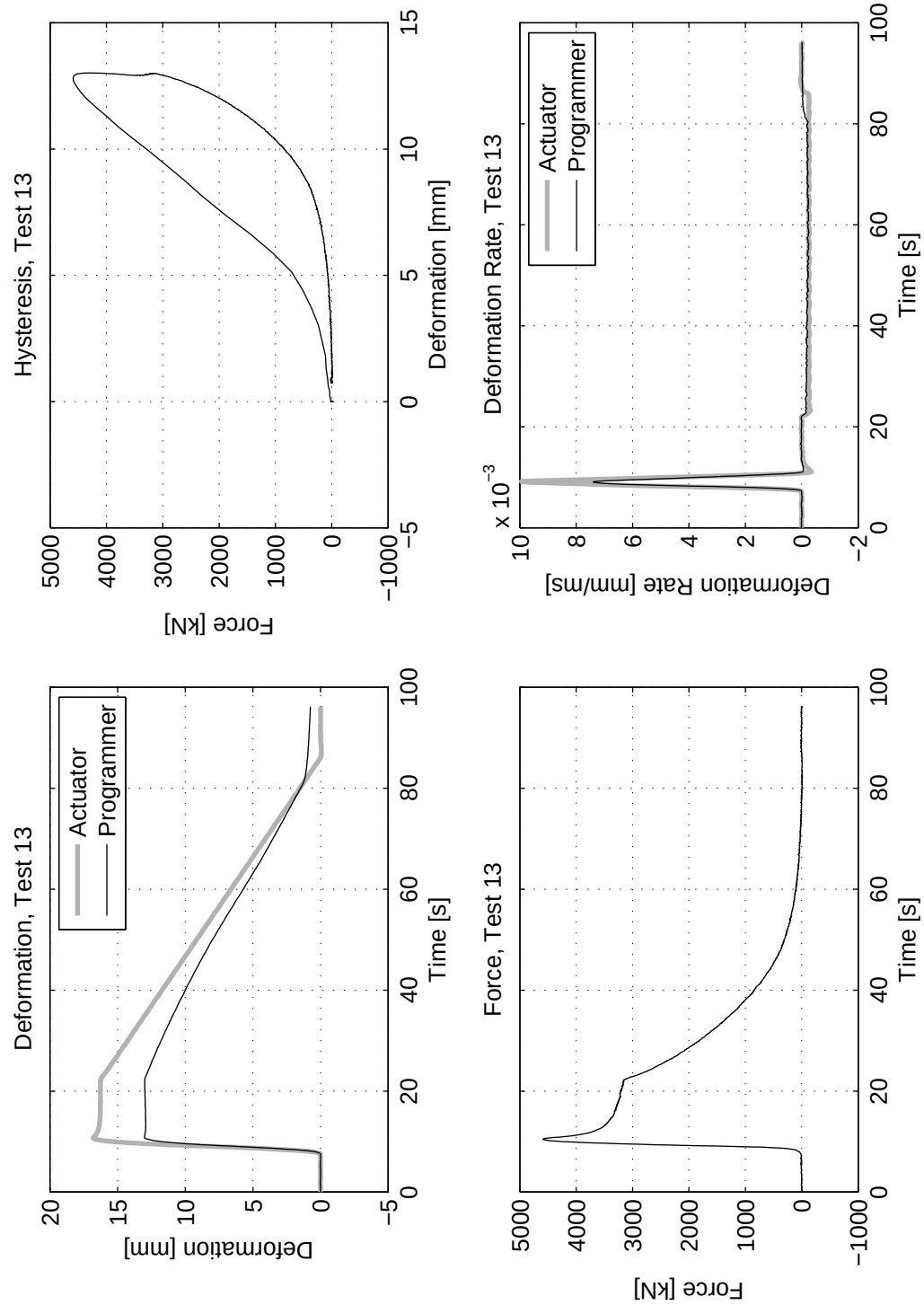
Hysteresis, Test 13
Force [kN]
Deformation [mm]
Deformation, Test 13
Actuator
Programmer
Deformation [mm]
Time [s]
Deformation Rate, Test 13
x 10^-3
Deformation Rate [mm/ms]
Force, Test 13

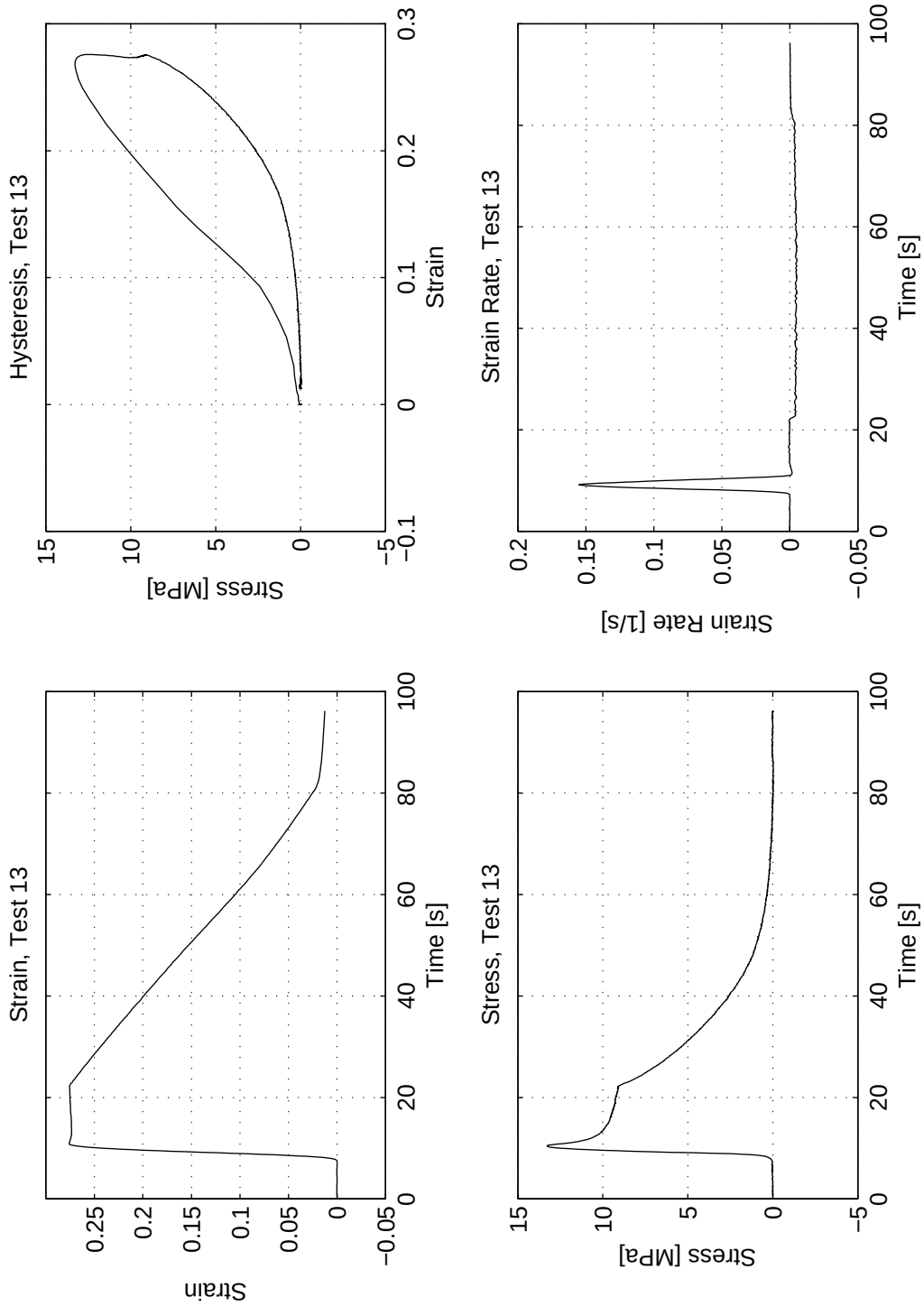
Hysteresis, Test 13
Stress [MPa]
Strain
Strain Rate, Test 13
Strain Rate [1/s]
Time [s]
Strain, Test 13
Strain
Time [s]
Stress, Test 13
Stress [MPa]
Time [s]

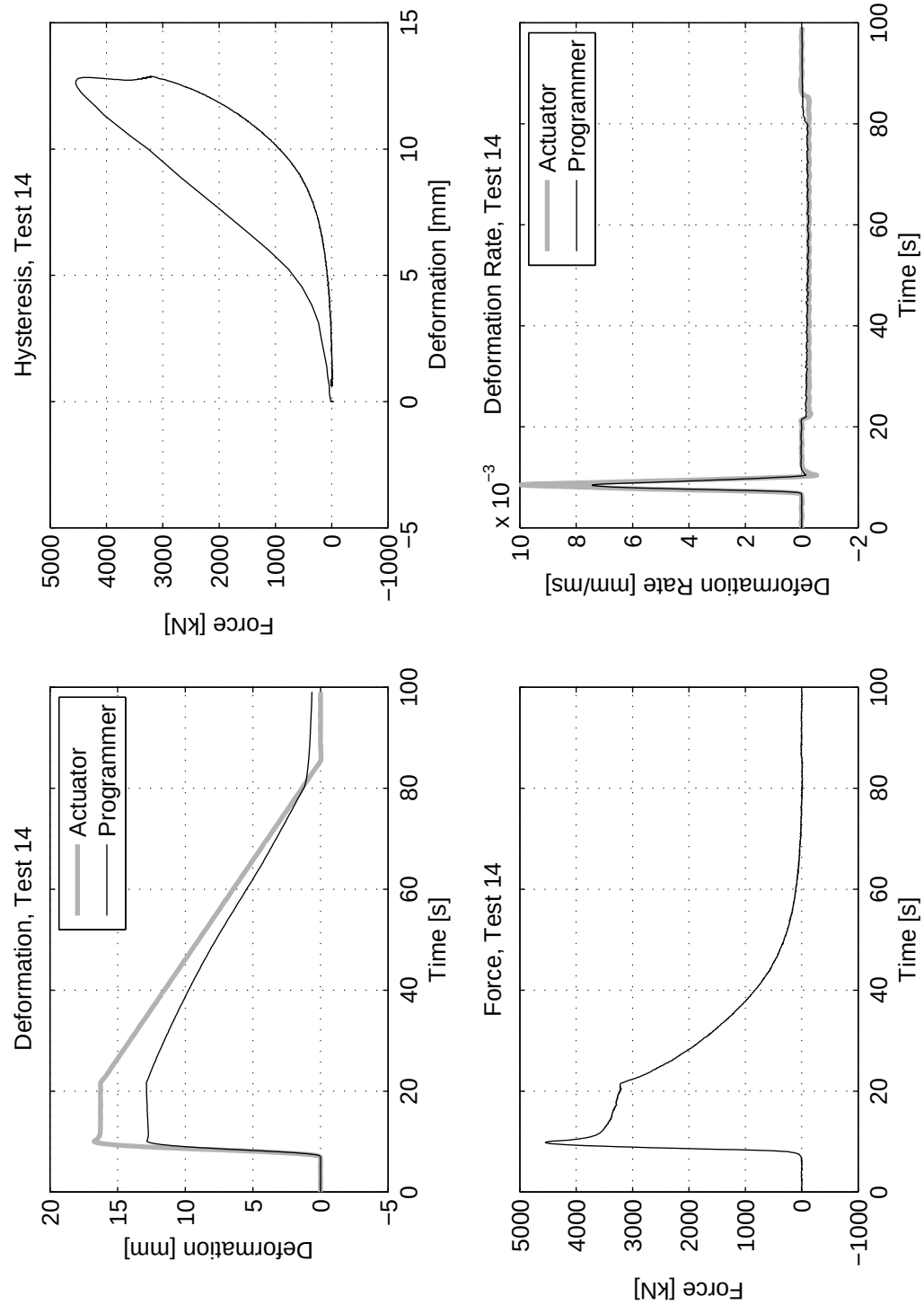
Hysteresis, Test 14
Force [kN]
Deformation [mm]
Deformation, Test 14
Actuator
Programmer
Deformation [mm]
Time [s]
Deformation Rate, Test 14
x 10^-3
Deformation Rate [mm/ms]
Force, Test 14

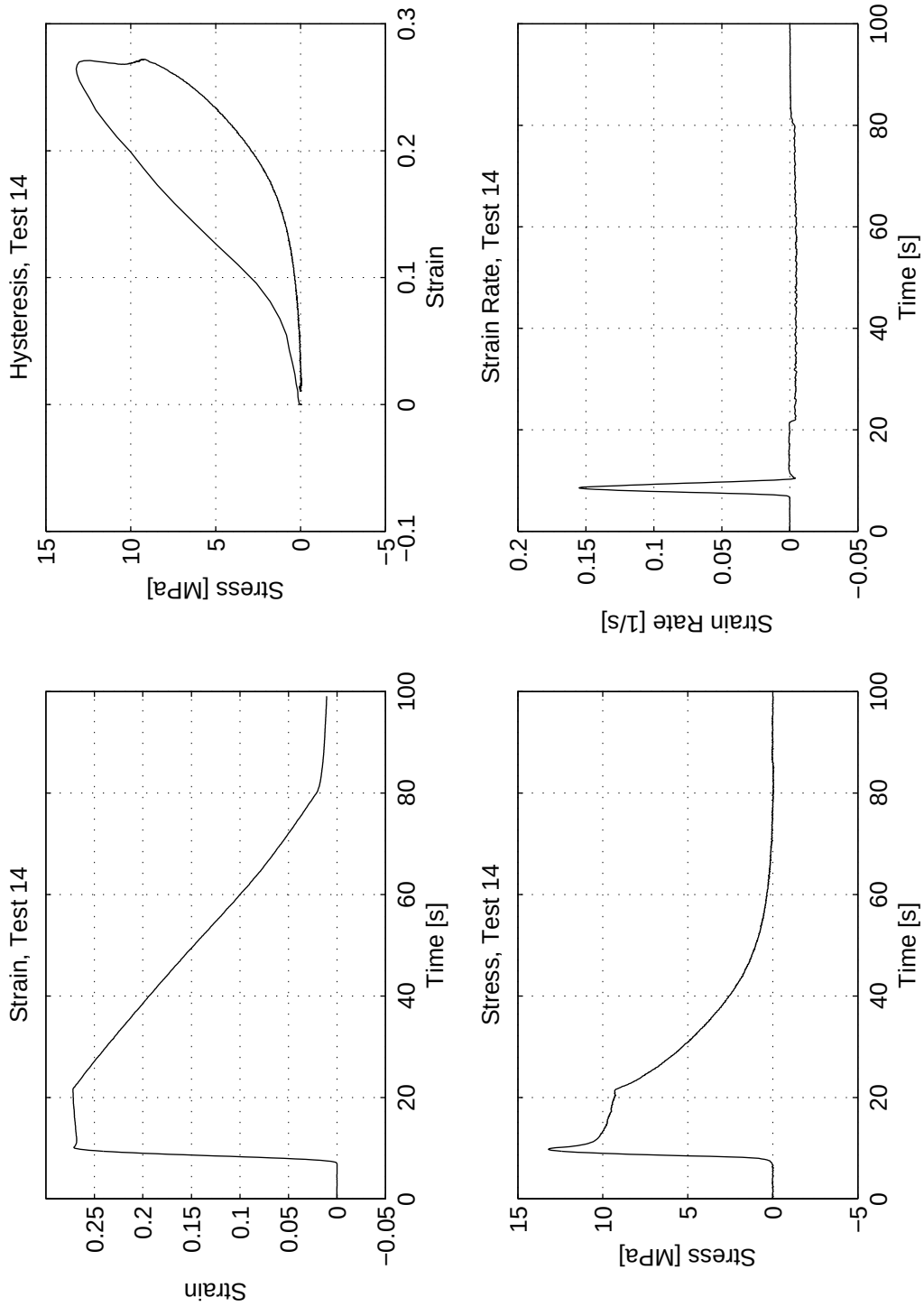
Hysteresis, Test 14
Stress [MPa]
Strain
Strain Rate, Test 14
Strain Rate [1/s]
Time [s]
Strain, Test 14
Strain
Time [s]
Stress, Test 14
Stress [MPa]
Time [s]

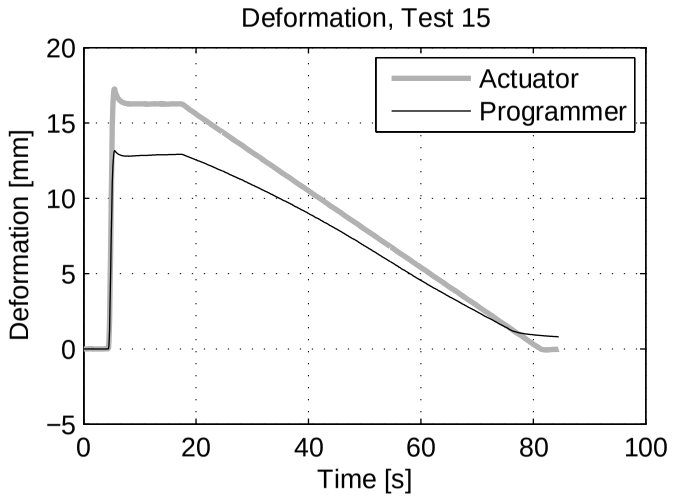
Deformation, Test 15
Actuator
Programmer
Deformation [mm]
Time [s]
20
15
10
5
0
−5
0
20
40
60
80
100

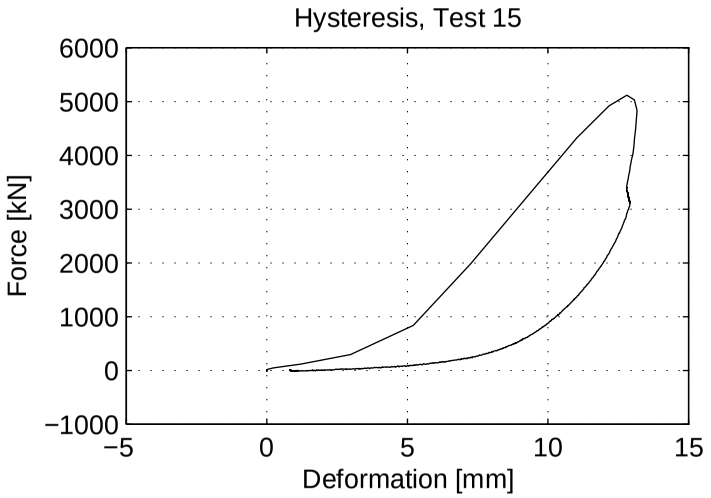
Hysteresis, Test 15
Force [kN]
Deformation [mm]
6000
5000
4000
3000
2000
1000
0
−1000
−5
0
5
10
15

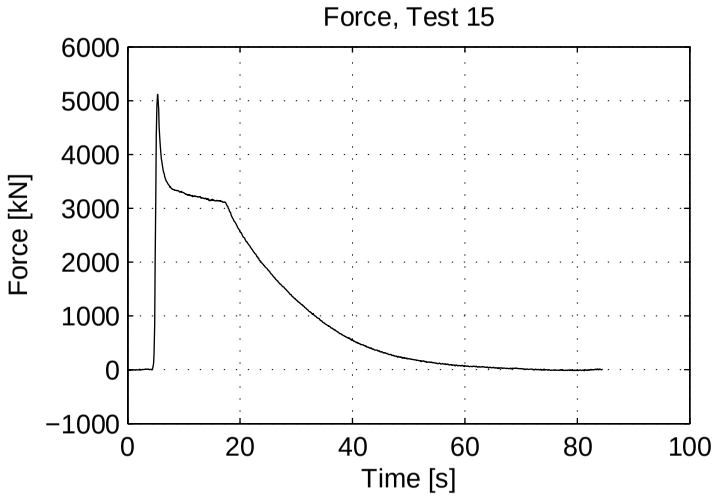
Force, Test 15
Force [kN]
Time [s]
6000
5000
4000
3000
2000
1000
0
−1000
0
20
40
60
80
100

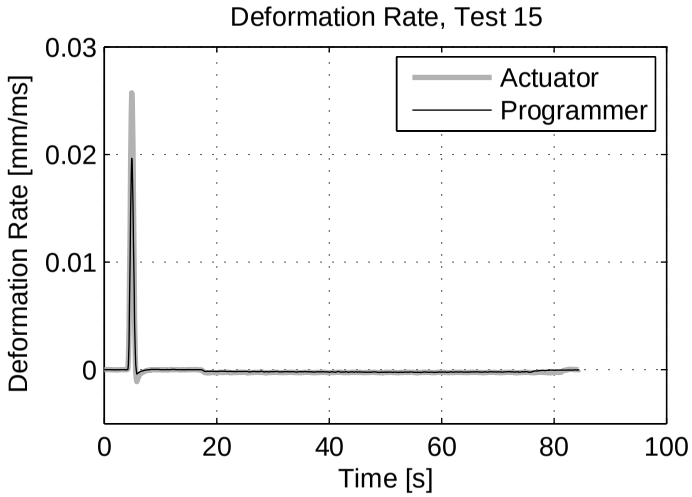
Deformation Rate, Test 15
Actuator
Programmer
Deformation Rate [mm/ms]
Time [s]
0.03
0.02
0.01
0
0
20
40
60
80
100

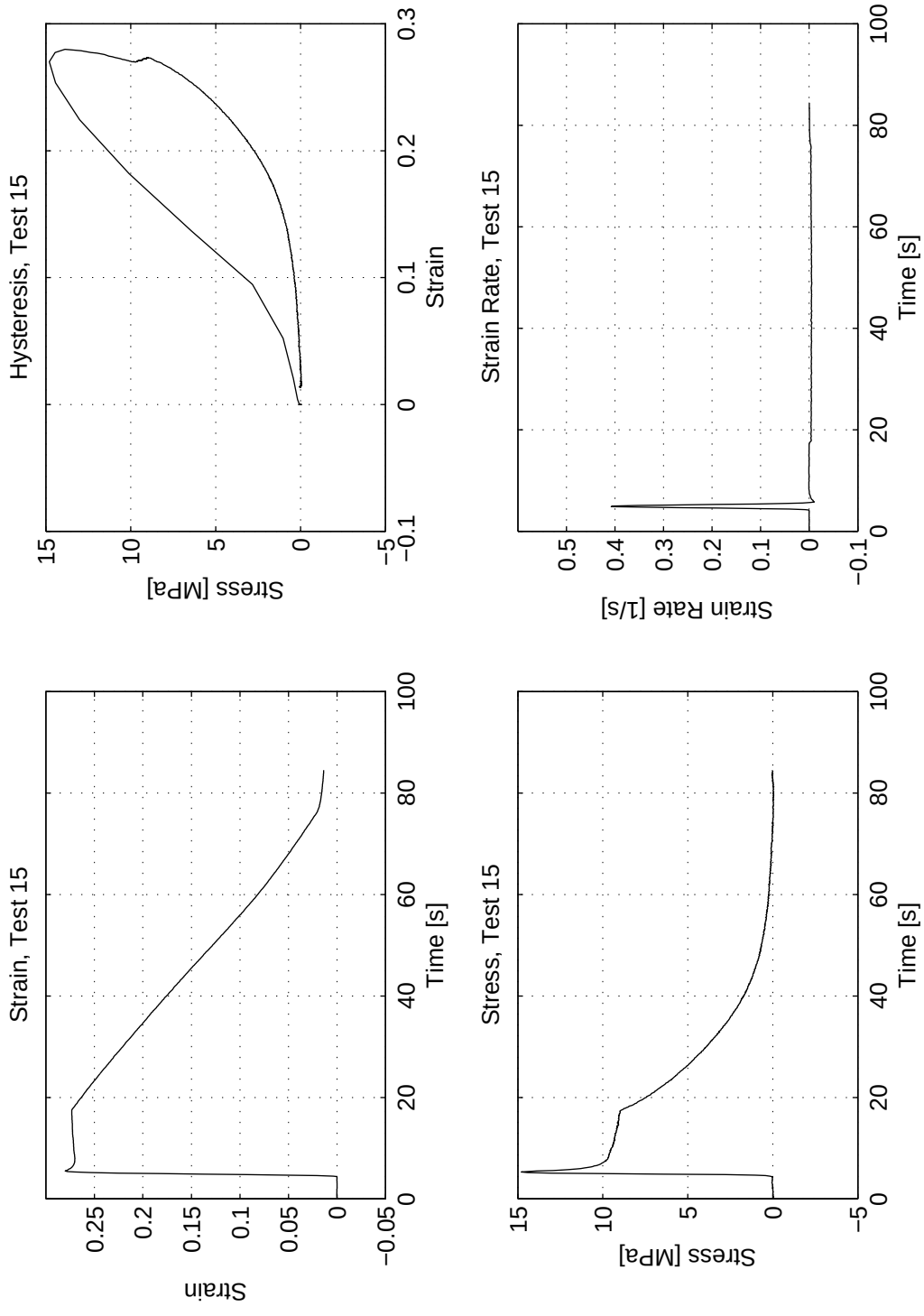
Hysteresis, Test 15
Stress [MPa]
Strain
Strain Rate, Test 15
Strain Rate [1/s]
Time [s]
Strain, Test 15
Strain
Time [s]
Stress, Test 15
Stress [MPa]
Time [s]

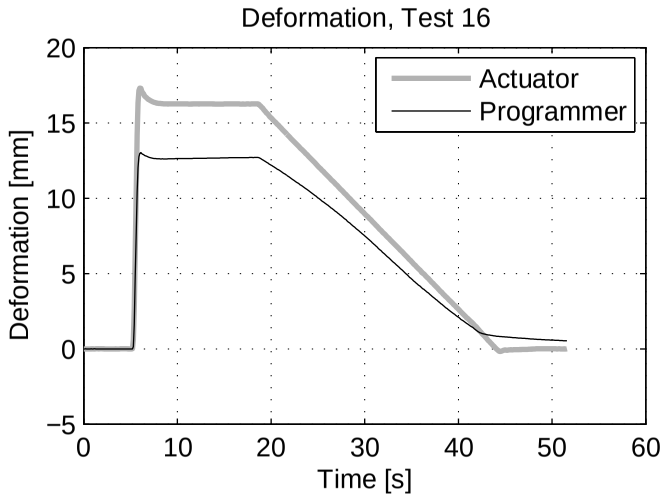
Deformation, Test 16
Actuator
Programmer
Deformation [mm]
Time [s]
20
15
10
5
0
−5
0
10
20
30
40
50
60

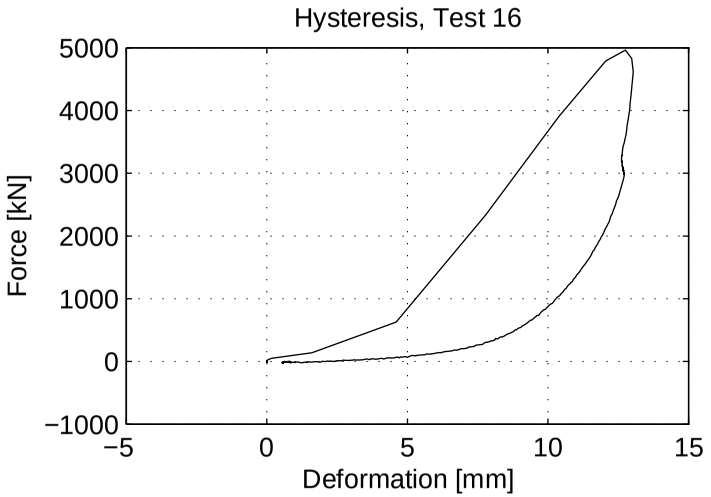
Hysteresis, Test 16
Force [kN]
Deformation [mm]
5000
4000
3000
2000
1000
0
−1000
−5
0
5
10
15

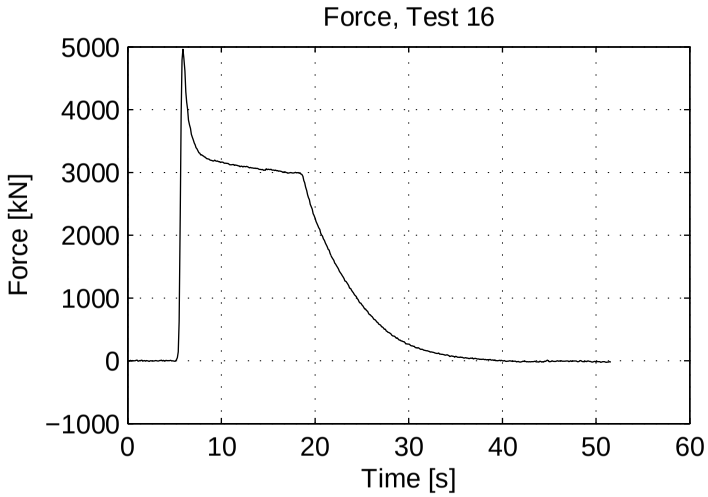
Force, Test 16
Force [kN]
Time [s]
5000
4000
3000
2000
1000
0
−1000
0
10
20
30
40
50
60

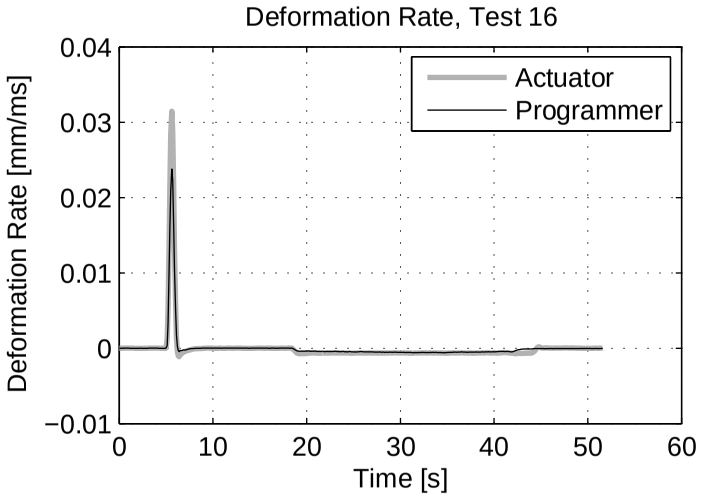
Deformation Rate, Test 16
Actuator
Programmer
Deformation Rate [mm/ms]
Time [s]
0.04
0.03
0.02
0.01
0
−0.01
0
10
20
30
40
50
60

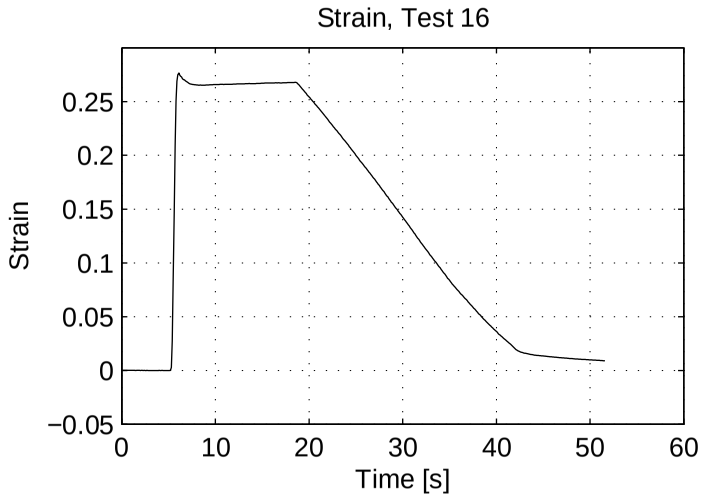
Strain, Test 16
Strain
Time [s]
0.25
0.2
0.15
0.1
0.05
0
−0.05
0
10
20
30
40
50
60

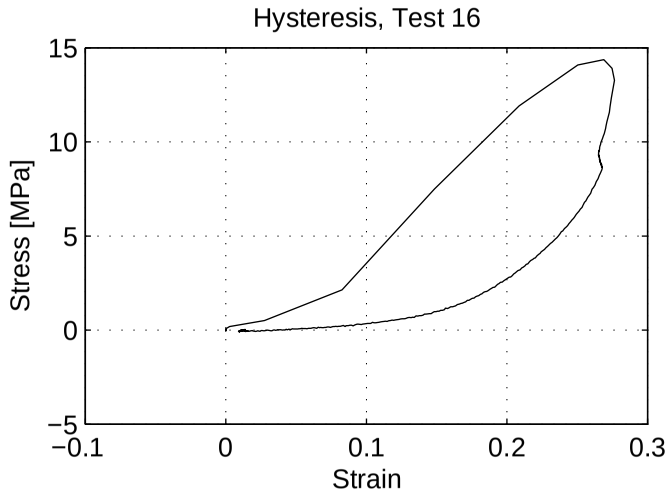
Hysteresis, Test 16
Stress [MPa]
Strain
15
10
5
0
−5
−0.1
0
0.1
0.2
0.3

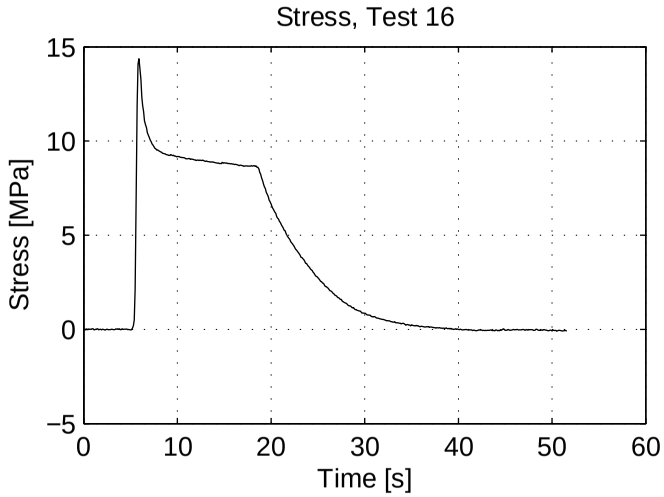
Stress, Test 16
Stress [MPa]
Time [s]
15
10
5
0
−5
0
10
20
30
40
50
60

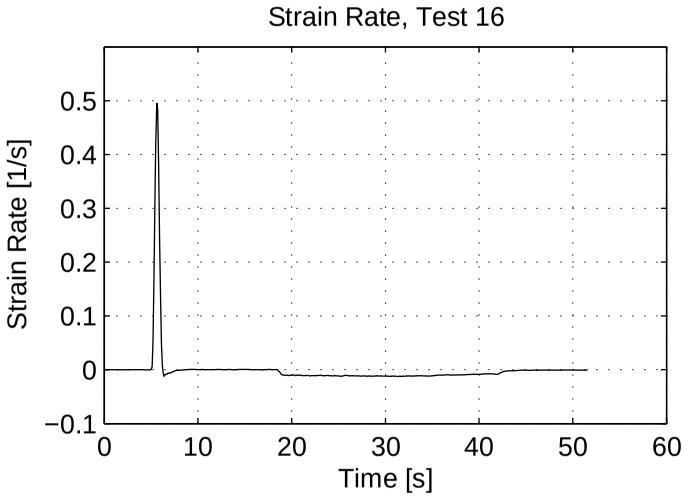
Strain Rate, Test 16
Strain Rate [1/s]
Time [s]
0.5
0.4
0.3
0.2
0.1
0
−0.1
0
10
20
30
40
50
60

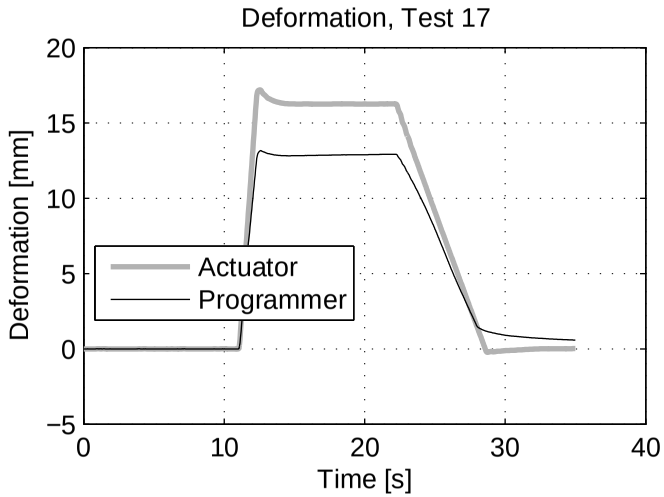
Deformation, Test 17
Deformation [mm]
Time [s]
Actuator
Programmer

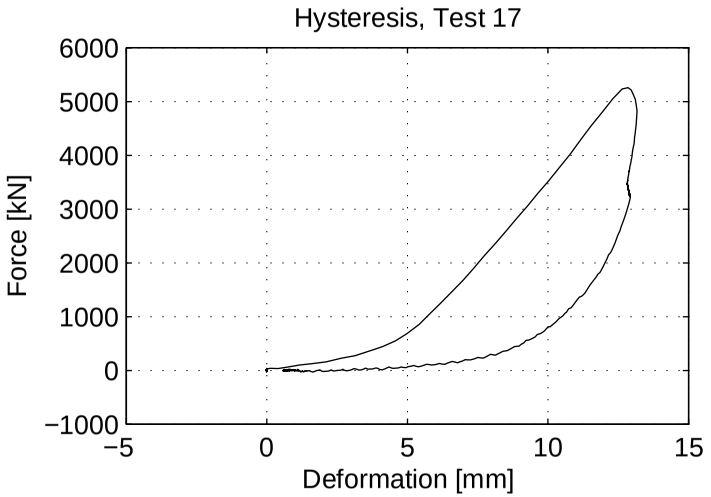
Hysteresis, Test 17
Force [kN]
Deformation [mm]

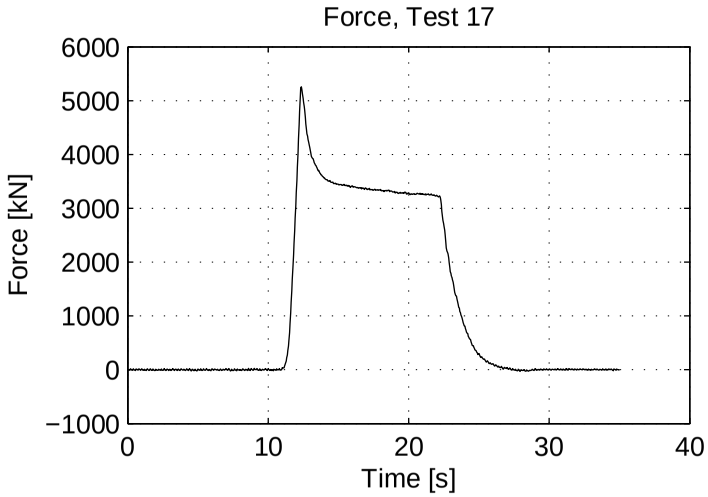
Force, Test 17
Force [kN]
Time [s]

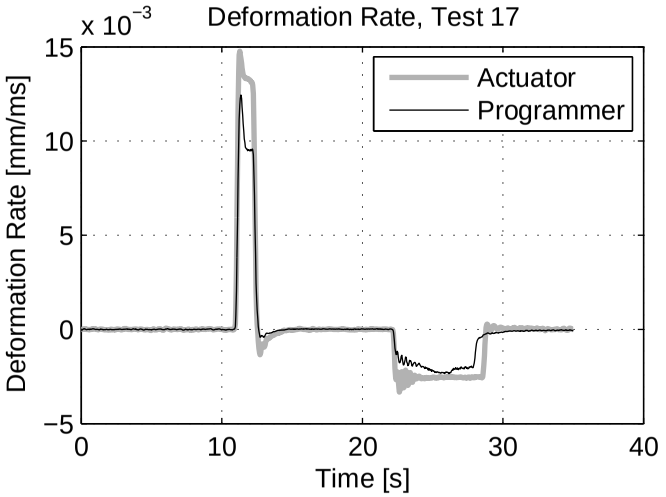
x 10^-3
Deformation Rate, Test 17
Deformation Rate [mm/ms]
Time [s]
Actuator
Programmer

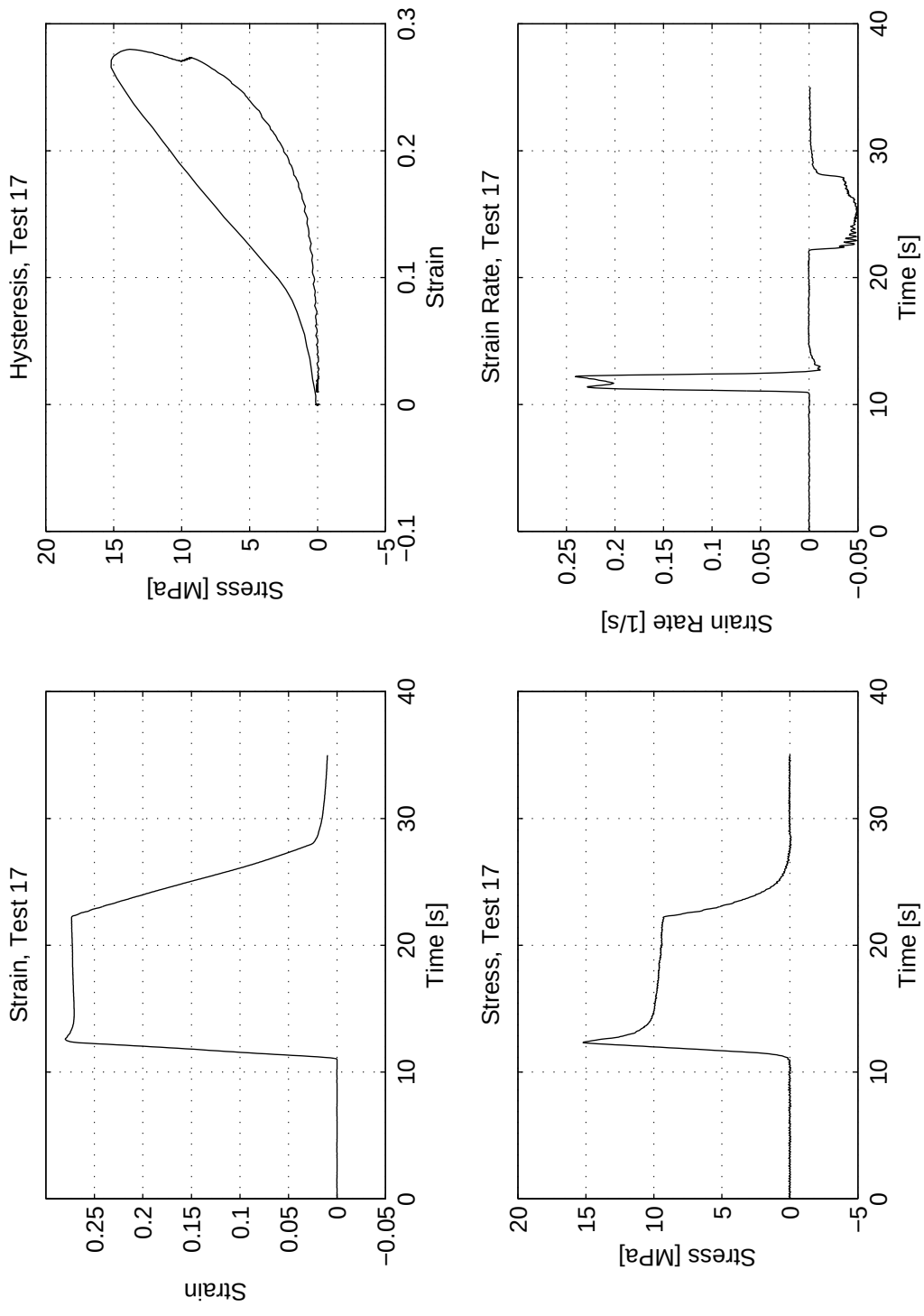
Hysteresis, Test 17
Stress [MPa]
Strain
Strain, Test 17
Strain
Time [s]
Strain Rate, Test 17
Strain Rate [1/s]
Time [s]
Stress, Test 17
Stress [MPa]
Time [s]

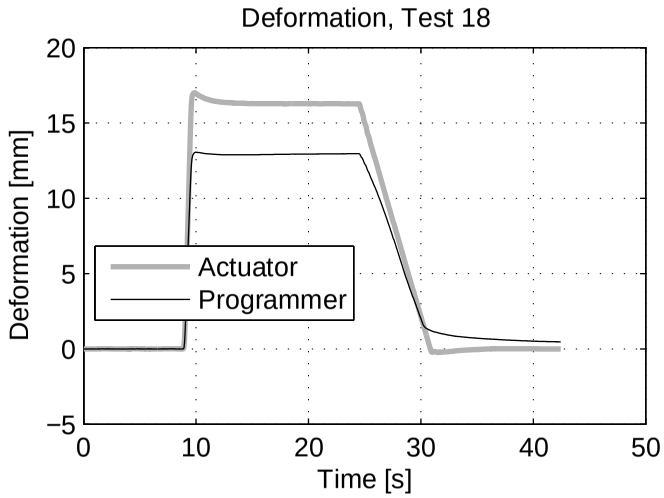
Deformation, Test 18
Deformation [mm]
Time [s]
Actuator
Programmer

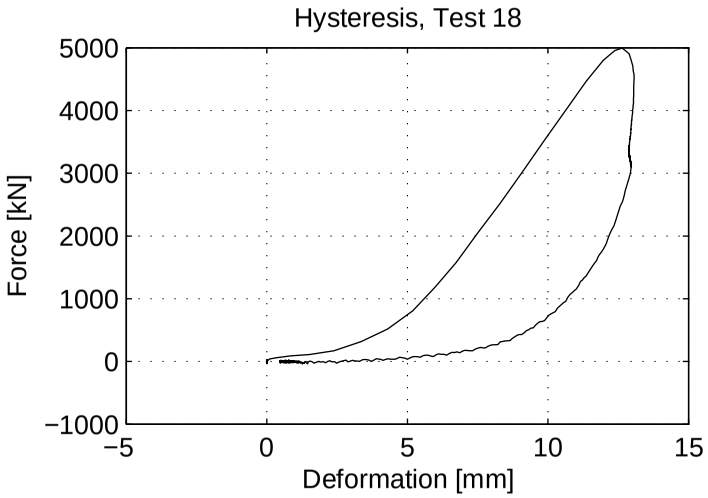
Hysteresis, Test 18
Force [kN]
Deformation [mm]

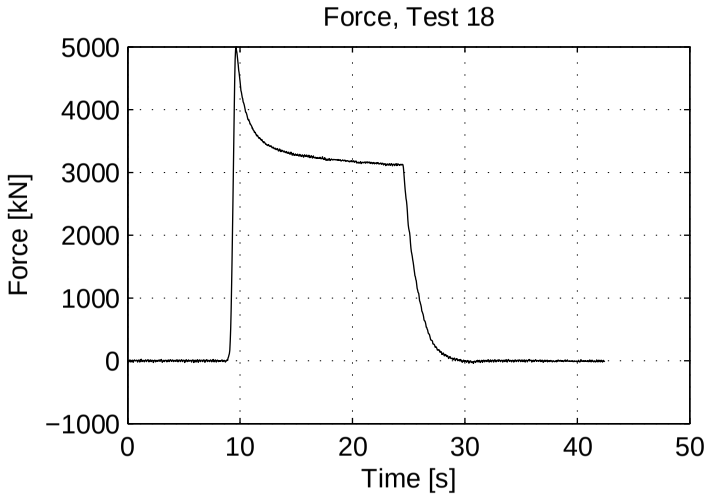
Force, Test 18
Force [kN]
Time [s]

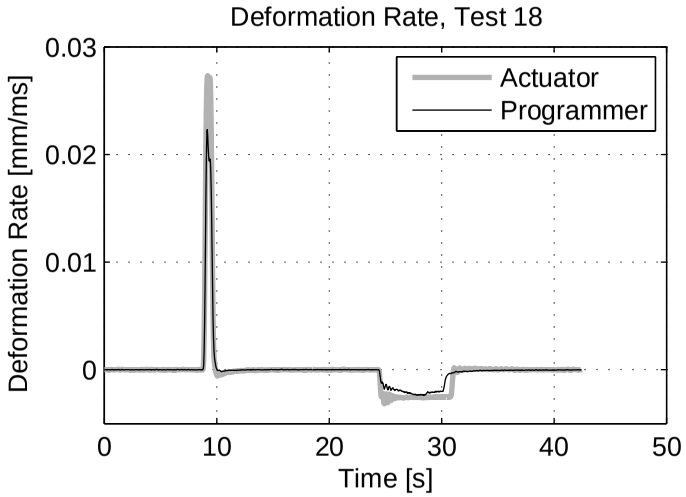
Deformation Rate, Test 18
Deformation Rate [mm/ms]
Time [s]
Actuator
Programmer

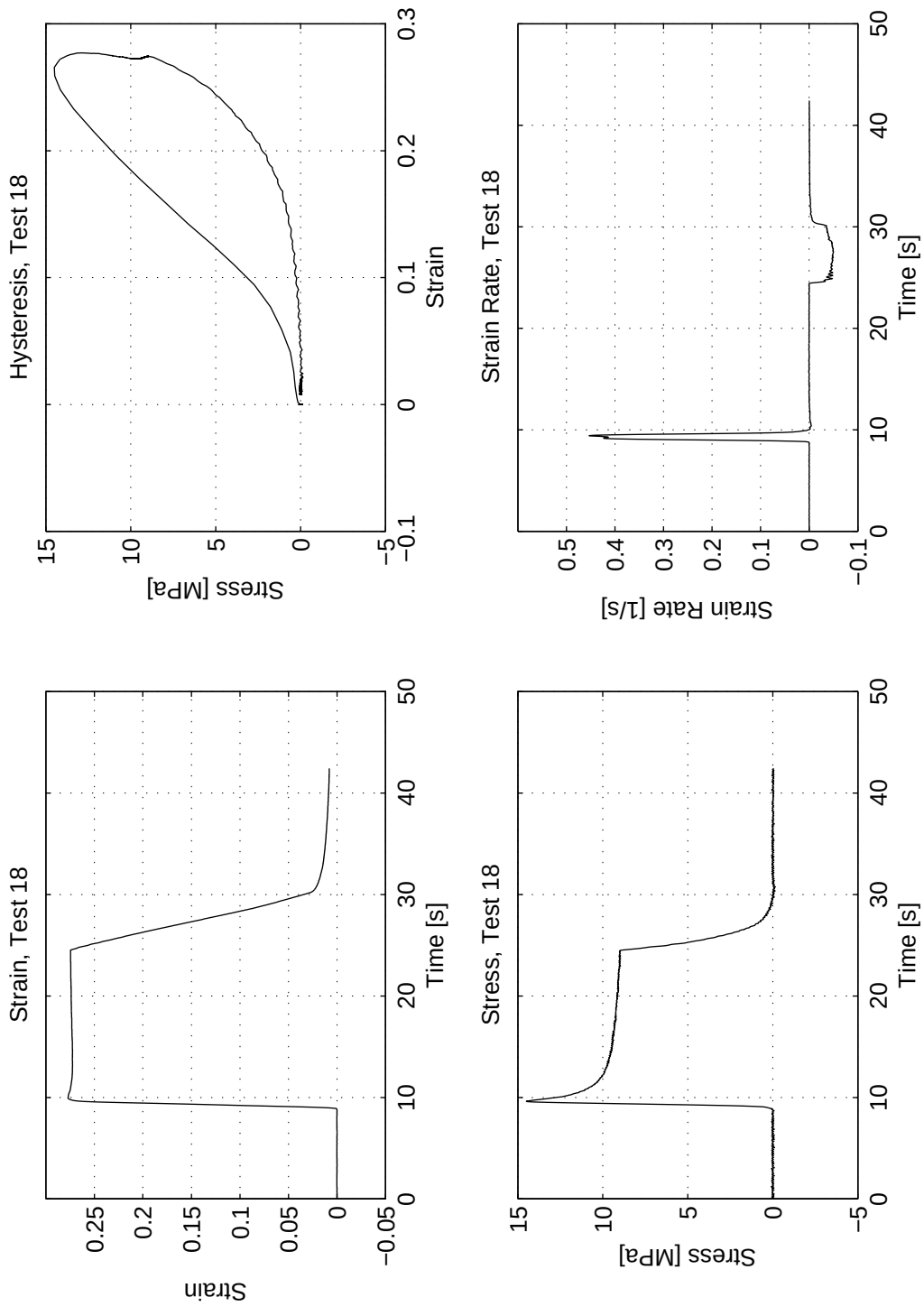
Hysteresis, Test 18
Stress [MPa]
Strain
Strain, Test 18
Strain
Time [s]
Strain Rate, Test 18
Strain Rate [1/s]
Time [s]
Stress, Test 18
Stress [MPa]
Time [s]

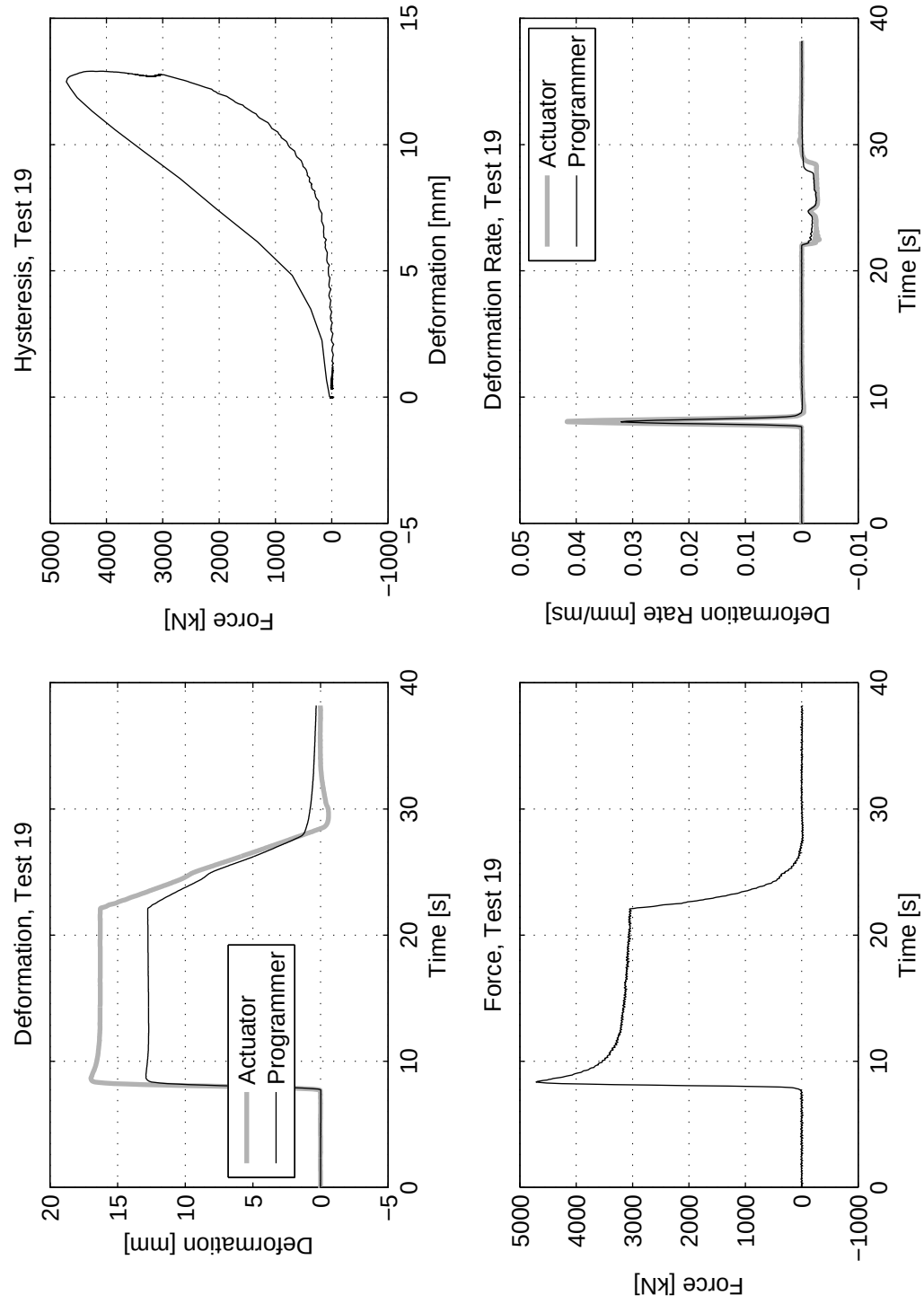
Hysteresis, Test 19
Force [kN]
Deformation [mm]
Deformation, Test 19
Deformation [mm]
Time [s]
Actuator
Programmer
Deformation Rate, Test 19
Deformation Rate [mm/ms]
Force, Test 19

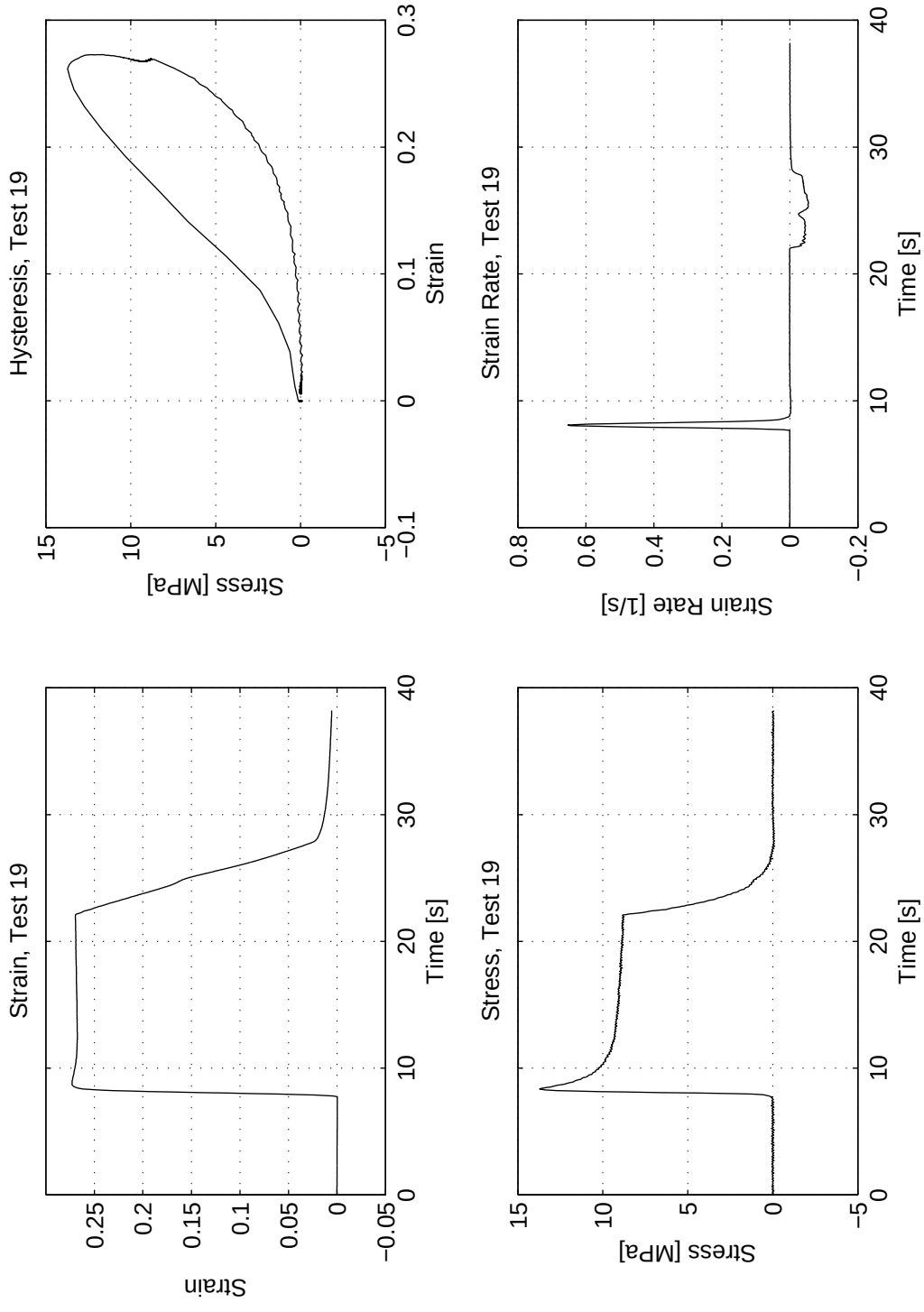
Hysteresis, Test 19
Stress [MPa]
Strain
Strain, Test 19
Strain
Time [s]
Strain Rate, Test 19
Strain Rate [1/s]
Time [s]
Stress, Test 19
Stress [MPa]
Time [s]

References

[1] ABAQUS, Inc. (2003). *ABAQUS Analysis User's Manual*. Pawtucket, RI.

[2] American Concrete Institute (1995). *Building Code Requirements for Structural Concrete and Commentary*. ACI 318-05.

[3] ASTM International (2005). Annual book of ASTM standards.

[4] Attaway, S. W., Matalucci, R. V., Key, S. W., Morrill, K. B., Malvar, L. J., and Crawford, J. E. (2000). Enhancements to PRONTO3D to predict structural response to blast. Sandia Report SAND2000-1017, Sandia National Laboratories. Export Controlled.

[5] Bache, T. C. (2004). Personal communications. Stuctural Group.

[6] Bardenhagen, S., Harstad, E., J.C. Foster, J., and Maudlin, P. (1996). Viscoelastic models for polymeric composite materials. In *Proceedings of the Conference of the American Physical Society Topical Group on Shock Compression of Condensed Matter*, pages 327–330. American Institute of Physics.

[7] Biggs, J. M. (1964). *Introduction to Structural Dynamics*. McGraw-Hill.

[8] Chen, W. F. (1982). *Plasticity in Reinforced Concrete*. McGraw Hill.

[9] Chopra, A. K. (1995). *Dynamics of Structures: Theory and Applications to Earthquake Engineering*. Prentice-Hall.

[10] Clough, R. W. and Penzien, J. (1993). *Dynamics of Structures*. McGraw-Hill.

[11] Conrath, E. J., Krauthammer, T., Marchand, K. A., and Mlakar, P. F., editors (1999). *Structural Design for Physical Security: State of the Practice*. American Society of Structural Engineers.

[12] Crawford, J. E., Malvar, L. J., Morrill, K. B., and Ferritto, J. M. (2001). Composite retrofits to increase the blast resistance of buildings. Technical report, K&C, Burbank, CA , USA. Presented at 10th Intl. Symp. on Interaction of the Effects of Munitions with Structures.

[13] Crawford, J. E., Malvar, L. J., Wesevich, J. W., Valancius, J., and Reynolds, A. D. (1997). Retrofit of reinforced concrete structures to resist blast effects. *ACI Structural Journal*, 94(4):371–377.

[14] Explosive Loading Laboratory (2004). Explosive loading laboratory testing for blast mitigation: Infrastructure development and blast simulator design. Technical report, UCSD, Department of Structural Engineering, 9500 Gilman Dr #0085, La Jolla CA, 92093-0085, USA. Internal document delivered to sponsoring agency.

[15] Explosive Loading Laboratory (2005). Explosive loading laboratory testing for blast mitigation: Blast simulator commissioning and construction. Technical report, UCSD, Department of Structural Engineering, 9500 Gilman Dr. #0085, La Jolla, CA, 92093-0085, USA. Internal document delivered to sponsoring agency.

[16] Gelfand, I. and Fomin, S. (2000). *Calculus of Variations*. Dover.

[17] Gent, A. N. and Lindley, P. B. (1959). The compression of bonded rubber blocks. *Proc Instn Mech Engrs*, 173(3):111–122.

[18] Gram, M. (2006). Personal communications. MTS Systems Corporation.

[19] Gurtman, G. and Sallay, J. (2005). Characterization of UCSD blast simulator programmer material. Technical report, Science Applications International Corporation, San Diego, CA, USA.

[20] Hegemier, G. A., Seible, F., Lee, C.-S., and Rodriguez-Nikl, T. (2003). FRP-based blast retrofit design strategies - laboratory tests on rectangular RC columns - part II. Research Report SSRP-2002/17, UCSD Structural Engineering, La Jolla, CA, USA.

[21] Hegemier, G. A., Seible, F., Rodriguez-Nikl, T., and Arnett, K. (2006). Blast mitigation of critical infrastructure components and systems. In *Proceedings of the Second fib Congress*, Naples, Italy.

[22] Hegemier, G. A., Seible, F., Rodriguez-Nikl, T., Lee, C.-S., Budek, A. M., and Dieckmann, L. (2002). FRP-based blast retrofit design strategies - laboratory tests on rectangular RC columns. Research Report SSRP-2002/04, UCSD Structural Engineering, La Jolla, CA, USA.

[23] Howie, I. and Karbhari, V. M. (1995). Effect of two sheet composite wrap architecture on strengthening of concrete due to confinement: I - experimental studies. *Journal of Reinforced Plastics and Composites*, 14(9):1008–1030.

[24] Hyde, D. (1992). ConWep: Conventional weapons effects. Available at <https://pdc.usace.army.mil/software/conwep> as of 7 September 2006.

[25] Johnson, J., Dick, J., and Hixson, R. (1998). Transient impact response of three polymers. *Journal of Applied Physics*, 84(5):2520 – 2529.

[26] Khan, A. S., Lopez-Pamies, O., and Kazmi, R. (2005). Thermo-mechanical large deformation response and constitutive modeling of viscoelastic polymers over a wide range of strain rates and temperatures. *International Journal of Plasticity*, 22(4):581–601.

[27] Kleiber, M., editor (1998). *Handbook of Computational Solid Mechanics*. Springer-Verlag.

[28] Krauthammer, T. (2004). Blast effects and progressive collapse. In *Proc. International Conf. On Planning, Design, and Construction of Hardened and Protective Facilities (HARDFAC)*, Kuala Lumpur, Malaysia.

[29] Krauthammer, T., Assadi-Lamouki, A., and Shanaa, H. M. (1993a). Analysis of impulsively loaded reinforced concrete structural elements–I. Theory. *Computers & Structures*, 48(5):851–860.

[30] Krauthammer, T., Assadi-Lamouki, A., and Shanaa, H. M. (1993b). Analysis of impulsively loaded reinforced concrete structural elements–II. Implementation. *Computers & Structures*, 48(5):861–871.

[31] Lee, C.-S. (2006). *Modeling of FRP-Jacketed RC Columns Subject to Combined Axial and Lateral Loads*. PhD thesis, University of California, San Diego.

[32] Livermore Software Technology Corporation (2005). *LS-DYNA Keyword User's Manual*. Livermore, CA.

[33] MacGregor, J. G. (1992). *Reinforced Concrete: Mechanics and Design*. Prentice-Hall, 2nd edition.

[34] Malvar, L. J., Crawford, J. E., Wesevich, J. W., and Simons, D. (1997). A plasticity based concrete model for DYNA3D. *Int. J. Impact Engng*, 19(9–10):847–873.

[35] Malvar, L. J., Morrill, K. B., and Crawford, J. E. (2004). Numerical modeling of concrete confined by fiber-reinforced composites. *Journal of Composites for Construction*, 8(4):315 – 322.

[36] Mander, J. B., Priestley, M. J. N., and Park, R. (1988). Theoretical stress-strain model of reinforced concrete columns. *Journal of Structural Engineering*, 114(8):1804–1826.

[37] Marchand, K. A. (1999). *Structural Design for Physical Security: State of the Practice*, chapter 2. American Society of Civil Engineers.

[38] Meyers, M. A. (1994). *Dynamic Behavior of Materials*. John Wiley.

[39] Morrill, K. B., Malvar, L. J., Crawford, J. E., and Attaway, S. (2000). RC column and slab retrofits to survive blast loads. In Elgaaly, M., editor, *Proc. Structrures Congress 2000: Advanced Technology in Structural Engineering*. American Society of Civil Engineers.

[40] Nanni, A. and Bradford, N. M. (1995). FRP jacketed concrete under uniaxial compression. *Construction and Building Materials*, 9(2):115–124.

[41] Ottosen, N. S. and Ristinmaa, M. (2005). *The Mechanics of Constitutive Modeling*. Elsevier.

[42] Paulay, T. and Priestley, M. J. N. (1992). *Seismic Design of Reinforced Concrete and Masonry Buildings*. John Wiley & Sons.

[43] Perrault Structural Products (2004). BLast Information System (BLIS) database. U.S. Department of Defense, Technical Support Working Group.

[44] Priestley, M. J. N., Seible, F., and Calvi, G. M. (1996). *Seismic Design and Retrofit of Bridges*. John Wiley & Sons.

[45] Read, H. and Hegemier, G. (1984). Strain softening of rock, soil and concrete - a review article. *Mechanics of Materials*, 3:271–294.

[46] Sallay, J. (2006). Personal communications. Science Applications International Corporation.

[47] Seible, F., Burgueño, R., Abdallah, M. G., and Nuismer, R. (1995a). Advanced composite carbon shell systems for bridge columns under seismic loads. In *Proc. National Seismic Conference on Bridges and Highways*. Federal Highway Administration and California Department of Transportation.

[48] Seible, F., Priestley, M. J. N., Hegemier, G. A., and Innamorato, D. (1997). Seismic retrofit of RC columns with continuous carbon fiber jackets. *Journal of Composites for Construction*, 1(2):52–62.

[49] Seible, F., Priestley, M. J. N., and Innamorato, D. (1995b). Earthquake retrofit of bridge columns with continuous fiber jackets, Vol II, Design guidelines. Research Report ACTT-95/08, UCSD Structural Engineering, La Jolla, CA, USA.

[50] Seismic Energy Products (2004). QC results for seismic isolation bearings: Explosive Loading Laboratory at Camp Elliot, University of California, San Diego. Technical Report R19066-A, 2447 Santa Clara Av, Ste. 301, Alameda, CA, 94501.

[51] Smith, P. D. and Hetherington, J. G. (1994). *Blast and Ballistic Loading of Structures*. Butterworth-Heinemann.

[52] Tang, M. J., Britt, J. R., Abernathy, R. A., and Leone, M. G. (2000). Blast tool evaluation. Technical Report CT 99-23, New Mexico Tech: Energetic Materials Research and Testing Center, Socorro, New Mexico.

[53] Teng, J. G., Chen, J. F., Smith, S. T., and Lam, L. (2002). *FRP Strengthened RC Structures*. John Wiley & Sons.

[54] U.S. Department of Defense (2002). *Unified Facilities Criteria (UFC): DoD Minimum Antiterrorism Standards for Buildings*. UFC 4-010-01.

[55] U.S. Department of the Air Force (2000). *Installation Force Protection Guide*. Date approximate.

[56] U.S. Department of the Army (1986). *Fundamentals of Protective Design for Conventional Weapons*. TM 5-855-1.

[57] U.S. Departments of the Army, the Navy and the Air Force (1990). *Structures to Resist the Effects of Accidental Explosions.* Report Number TM 5-1300 / NAVFAC P-397 / AFR 88-22.

[58] Wang, Y. C. and Restrepo, J. I. (2001). Investigation of concentrically loaded reinforced concrete columns confined with glass fiber-reinforced polymer jackets. *ACI Structural Journal*, 98(3):377–385.